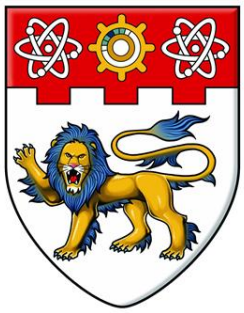

NANYANG TECHNOLOGICAL UNIVERSITY

STRUCTURAL BEHAVIOR OF REINFORCED CONCRETE FRAMES SUBJECTED TO PROGRESSIVE COLLAPSE

YU JUN

SCHOOL OF CIVIL AND ENVIRONMENTAL ENGINEERING

2012

STRUCTURAL BEHAVIOR OF REINFORCED CONCRETE FRAMES SUBJECTED TO PROGRESSIVE COLLAPSE

YU JUN

School of Civil and Environmental Engineering

A thesis submitted to the Nanyang Technological University in partial fulfillment of the requirement for the degree of Doctor of Philosophy

2012

ACKNOWLEDGEMENT

I would like to express my deeply gratitude and appreciation to my supervisor, Professor Tan Kang Hai, for his warm encouragement, invaluable advice, patient guidance and support throughout my PhD study in NTU. His passion for research will always inspire me in my future career and life. I am very fortunate to conduct research under his supervision.

I would also like to sincerely thank Dr. Yuan Weifeng, Mr. Yang Bo, Mr. Liu Junxian, Mr. Kang Shaobo, Mr. Nguyen Minh Phuong and Mr. Pham Xuan Dat for their kind help, constructive discussions and critical comments. Also, I appreciate the reminiscent life with all FERGAN members in NTU.

Special thanks should also extend to the technical staff from Protective Engineering and Construction Technology Laboratory, in particular, Mr. Chelladurai Subasanran, Mr. Jee Kim Tian and Mr. Tui Cheng Hoon for their assistance in the course of the experimental work.

Finally, I am indebted to my parents and my brother for their unceasing support and encouragement throughout the study. Without them it is impossible to complete this work.

TABLE OF CONTENTS

ABSTRACT

With the threat of terrorist attack looming large, the ability of a building to mitigate progressive collapse is of key interest to government agencies. Alternate load path (ALP) approach is one of the direct methods to assess progressive collapse resistance by introducing a column removal scenario.

An experimental program, comprising eight reinforced concrete (RC) beam-column sub-assemblages and seven RC frames, was carried out to investigate structural behavior and progressive collapse resistance of RC frame members subjected to a middle column removal scenario (MCRS), in particular, large-deformation behavior. Each sub-assemblage specimen consisted of a two-bay beam, a middle beam-column joint (just above a removed column) and two end-column stubs. Each frame specimen comprised a two-bay, a middle joint and two side columns, and most of frame specimens also include beam extensions. With increasing two-bay beam deflection, three different structural mechanisms, i.e. flexural action, compressive arch action (CAA) and catenary action, can be sequentially mobilized in a load-deflection history. Flexural action capacity is determined with a conventional plastic hinge mechanism. CAA is developed accompanied by beam axial compression and catenary action is mobilized when beam axial force changes from compression to tension.

On top of flexural action capacity, both CAA and catenary action can significantly increase structural resistance, suggesting large potential of structures. However, compared with CAA, catenary action involves much large deflections and requires large rotation capacities of RC beams. In the sub-assemblage tests, the effects of specimen detailing, top and bottom reinforcement ratios at the middle joint regions, and span-to-depth ratios of two-bay beams on structural behavior were investigated. In the frame tests, the effects of boundary conditions of the frame specimens and specimen detailing are studied. In particular, three special detailing techniques were introduced, targeting at increasing beam-end rotation capacities.

An analytical model was proposed for evaluating CAA capacity and corresponding maximum axial compression throughout beams. This is because CAA can be

mobilized with enhanced structural resistance at relatively smaller deflections and thereby it is more attractive for buildings with high protective levels. The proposed model is able to consider the effects of imperfect boundary conditions (including axial and rotational restraint stiffness, and connection gaps), geometric and material properties on CAA capacity as well as maximum axial compression. Based on parametric studies, the conditions appropriate for incorporating CAA into structural design are suggested.

During the tests, it is found that large discontinuity occurred at the beam-column connections due to severe concrete crushing and cracking as well as bar fracture at catenary action stage. Therefore, to simulate structural behavior more realistically, it is necessary to isolate beam-column joints as independent elements from beams and columns to capture discontinuity. Accordingly, a component-based joint model was proposed. The joint model consists of a series of components, each of which represents a load transfer path from the adjoining beams to a joint panel. The systematic calibration procedure on each component was provided as well. Finally, macromodel-based finite element analysis by using fiber beam elements and the proposed joint model show good agreement between numerical and experimental results.

LIST OF FIGURES

LIST OF TABLES

LIST OF SYMBOLS

a_{s1}, a_s	Distance from the utmost tension fiber of concrete to the centroid of tension reinforcement at the beam end and the middle joint interface, respectively
a'_{s1}, a'_s	Distance from the extreme compression fiber of concrete to the centroid of compression reinforcement at the beam end and the middle joint interface, respectively
A_s, A_s'	Area of tensile and compression reinforcement, respectively
A_b	Nominal cross-sectional area of a reinforcing bar
b	Width of a beam section
b_j	Width of a middle joint
c, c_1	Neutral axis depth at the middle joint interface and at the beam end, respectively
c_N	Neutral axis depth to formulate a compressive spring at a join interface
C'_c, C_c	Concrete compressive force acting at the beam end and the middle joint interface, respectively
C'_s, C_s	Steel compressive force acting at the beam end and the middle joint interface, respectively
d	Effective depth of a beam section
d_b	Diameter of a reinforcing bar
E_c	Elastic modulus of concrete

E_s	Elastic modulus of steel reinforcement
E_h	Hardening modulus of reinforcement
f_s	Applied stress at the loaded end of a bar
f_{se}	Maximum elastic stress at the elastic region of a bar
f_y , f_u	Yield strength and ultimate tensile strength of reinforcement
f_c' , f_t	Compressive and tensile strength of concrete, respectively
f_{scr}'	Stress of compression reinforcement corresponding to extreme compression fiber of concrete attaining the ultimate strain
f_y'	Artificial yield strength of reinforcement in a simplified bilinear constitutive model
F_s	Force of a diagonal spring in a joint panel
F_t	Force in a tensile branch of a bar force-slip spring
F_c	Force in a compressive branch of a bar force-slip spring
h	Depth of a beam section
k_{bb} , k_{bt}	Bar force-slip springs at the bottom and top of a beam-joint interface
k_{bs}	Interface shear spring at a beam-joint interface
k_s	Shear panel spring in a component-based joint model
K_a , K_r	Stiffness of axial and rotational restraints
l	Total net span length of sub-assemblages
l_n	Net span length of a one-bay beam

l_1	Crack width at an end of a sub-assemblage
l_{embd}	Physical embedment length of a bar
l_e	Available elastic length in which elastic bond strength is allowed to develop
l_{erq}	Required elastic length in which a bar stress can increase from zero to the maximum elastic applied stress
l_{ed}	Elastic development length, the shortest length in which the bar stress can increase from zero to the yield strength
l_{yrq}	Required inelastic length, in which the bar stress can increase from the yield strength to the maximum inelastic stress
l_{eq}	Equivalent embedment length of an anchored bar with a hook
L_n	Net span length of a single-bay beam
L	Total net span length of a sub-assemblage
M_{u1}, M_u	Bending moments acting on the beam end and on the joint interface, respectively
M	Bending moment at a beam section
N	Axial force at a beam section
$N_{\max}$, N_a	Experimental and analytical maximum axial compression at compressive arch action stage, respectively
N_0	Maximum axial compression used for comparison reference
P	Progressive collapse (or vertical) resistance of sub-assemblages (or beams)

P_0	Compressive arch action capacity used for comparison reference
P_f	Calculated flexural capacity based on plastic hinge mechanism
P_{caa} , P_a	Experimental and analytical capacity of compressive arch action
s_{ext}	Slip due to bar extension
s_0	Slip at the free end of an anchored bar
s_1	Slip corresponding to the ultimate bond stress in Eligehausen's local bond-slip model
S_t	Slip in a tensile branch of a bar force-slip spring
S_c	Slip in a compressive branch of a bar force-slip spring
t	Outward lateral displacement of each beam end due to linear elastic axial restraint
t_0	Gap between axial restraints and beam ends
T' , T	Steel tensile force acting at beam end and joint interface, respectively
V	Shear force at a middle joint interface
α	Enhancement factor of structural capacity due to compressive arch action
β	Ratio of the net span length of a single-bay beam to the total net span length of a sub-assemblage, i.e. l_n / l
β_1	Ratio of the depth of the equivalent rectangular stress block to the neutral-axis depth

γ_a , γ_r	Relative axial and rotational restraint stiffness at beam ends, respectively
δ	Beam deflection or displacement at the middle joint
ε_{cu}	Ultimate compressive strain of concrete, assumed as 0.003
ε'_s	Strain of compression reinforcement
ε_y	Yield strain of steel reinforcement
ε_s , ε_{end}	Strain at the loaded end and strain at the bar center for a continuous under axial tension, respectively
ε_u	Strain corresponding to ultimate tensile strength of steel reinforcement
ε'_{scr}	Strain of compression reinforcement corresponding to extreme compression fiber of concrete attaining the ultimate strain
ε_{sh}	Strain at the start of hardening phase
θ	Rotation at a beam section
θ_r , θ_{gr}	Local and global rigid rotation at a beam section
τ_p , γ	Shear stress in a joint panel and shear distortion of a joint panel
τ_{ET}	Average elastic bond strength for a bar in tension
τ_{YT}	Average inelastic bond strength for a bar in tension
τ_{EC}	Average elastic bond strength for a bar in compression
τ_{YC}	Average inelastic bond strength for a bar in compression
τ_u	Ultimate bond stress in Eligehausen's local bond-slip model

τ_e	Elastic bond stress at the free end of a bar
τ	Bond stress along a bar
φ	Rotation at the end support
ω	Mechanical reinforcement ratio

CHAPTER 1 INTRODUCTION

1.1 Research Background

Progressive collapse is a situation where local failure is followed by collapse of adjoining members, which in turn causes additional collapse (Allen and Schriever 1972). ASCE Standard 7-05 defines progressive collapse as "the spread of local damage, from an initiating event, from element to element resulting, eventually, in the collapse of an entire structure or a disproportionately large part of it". It is also known as disproportionate collapse. From an analytical point of view, progressive collapse occurs when a structure has its load pattern or boundary conditions changed so that other structural elements are loaded beyond their capacity and consequently fail (Krauthammer et al. 2002).

Dusenberry and Juneja (2002) summarized that there have been totally three waves of interest in progressive collapse: following the Ronan Point collapse in England in 1968, there was a flurry of interest in the subject of progressive collapse. A second wave of interest followed the terrorist attack on the Alfred P. Murrah Federal Building USA, in 1995. Interest now is at the highest level as structural engineering communities world-wide respond to the collapses of the WTC towers in the New York City and of a portion of the Pentagon in Washington, all resulting from a coordinated terrorist attack in September 2001. Building owners and government agencies are also interested in evaluating the progressive collapse potential of existing buildings and in designing new buildings to resist this type of collapse.

Since the Ronan Point collapse event, design considerations to improve the integrity, robustness and resilience of structures to resist progressive collapse have been incorporated into building codes (ACI 318-05; EN 1991-2-7 2006) and design guidelines (DoD 2010; GSA 2003; NIST 2007). After Alfred P. Murrah Federal Building event and 9-11 event, more specific structural analysis is required for buildings with a certain level of protection in design guidelines (DoD 2010; GSA 2003). The design methodology in these codes and design guidelines can be broadly classified into *indirect* and *direct* methods (Ellingwood and Leyendecker 1978). The indirect method specifies a minimum level of connectivity among various

structural components, and no structural analysis is required. The indirect method is threat-independent, but it is not equally effective for all threats. In GSA 2003 and UFC 4-023-03 (DoD 2010), the indirect method is implemented by tie force approach, in which the building is mechanically tied together, enhancing continuity, ductility, and development of tensile membrane action and catenary action. The specifications in tie force approach was originally employed by the British in their building codes after the Ronan Point failure (Ministry of Hoursing and Local Government 1968) and has been continually referred to in the current Eurocode (EN 1991-2-7 2006). NISTIR 7396 (NIST 2007) reported that the indirect method (including tie requirements and seismic detailing) is widely used in practice to reduce the likelihood of progressive collapse of buildings in the event of abnormal loading. However, because progressive collapse is a rare hazard, the actual effect of the indirect method is rarely verified by real disasters or test results.

The direct design falls into two general categories (Ellingwood and Leyendecker 1978): (1) *Specific local resistance method* and (2) *Alternate load path (ALP) method*. The former seeks to provide sufficient strength to resist failure from a specific threat. An example of this is the hardening of a building's first floor perimeter columns to withstand a specified abnormal load without exceeding a specified level of damage. It requires that a specific normative load (threat) be identified; unfortunately, there is no assurance that the building will perform adequately for threats other than the one specifically considered (Ellingwood et al. 2009). The latter (i.e. ALP method) allows local failure to occur, but seeks to provide ALPs so that damage is absorbed and major collapse is averted. The ALP method provides a formal check of the capability of a structural system to resist the removal of specific elements, such as columns and load-bearing walls. It does not require characterization of the threat causing a loss of the elements, and is, therefore, a threat-independent approach (GSA 2003).

In UFC 4-023-03 (DoD 2010), the ALP method shall not be applied to structural elements or connections that cannot provide the required longitudinal, transverse, or peripheral tie strength. With ALP method, designers must show that a structure is capable of bridging over a removed structural element and that the resulting extent

of damage does not exceed the damage limits. This indicates that the ALP is provided by the *flexural resistance* of structural members, and catenary action or tensile membrane action provided by ties is regarded as the second defense against progressive collapse. Furthermore, the approaches and the criteria employed in ASCE 41-06 *Seismic Rehabilitation of Existing Buildings* (ASCE 2007) are adopted and adapted into UFC 4-023-03, so that linear static (LS) analysis and nonlinear static (NLS) analysis can be conducted rationally by engineers. As progressive collapse is a dynamic and nonlinear event, the load cases for the static procedures require the use of factors to account for inertial and nonlinear effects. It is assumed that LS analysis is equivalent to the results of nonlinear dynamic (NLD) analysis through multiplying the loads with load increase factors (LIF) and NLS analysis is equivalent to the results of NLD analysis through multiplying the loads with dynamic increase factors (DIF).

The review of design methods against progressive collapse shows that the performance of structures designed by both indirect method and ALP method should be evaluated by introducing initial damage, currently by *fictitiously removing a single column or a load-bearing wall in each scenario*. Moreover, both methods seek ALPs to avoid global collapse due to local damage. The indirect method relies on catenary action or tensile membrane action provided by horizontal ties when flexural members (i.e. beams or slabs) are under large deformations, and the ALP method depends on the flexural resistance of structural members. However, the effectiveness of both design methods needs to be verified by experimental data. More importantly, the existing structures were designed without considering the requirements specified in the latest UFC 4-023-03 (DoD 2010), then how about their structural behavior after initial damage? This further challenges engineers to envision the behavior of a structural system following the occurrence of an abnormal event.

On the other hand, for progressive collapse scenarios induced by blast loading, the idea of considering the immaculate removal of a column as a damage scenario while leaving the rest of a building undamaged, is not realistic (Krauthammer 2003). This is because an explosive event near a building will cause extensive localized

damage, affecting more than a single column. To be realistic, the progressive collapse potential should be evaluated on the damaged structure determined at the end of nonlinear blast-structure interaction. However, it is challenging to determine the level of threat (i.e. explosive weight and standoff) in design guidelines (Stevens et al. 2009a). Furthermore, the assessment of progressive collapse potential of a building with a blast analysis is very complicated and time-consuming, not suitable for practicing engineers. Therefore, to avoid blast analysis and facilitate design against progressive collapse, the column removal scenario is a good starting point to increase structural integrity and robustness. The structural performances of different components (including beams, slabs, columns and connections, etc) under a column loss scenario can provide more insight to simplified numerical modeling, which can be further incorporated to conduct more comprehensive numerical simulations with computational-efficiency. To this end, it is imperative to experimentally investigate structural behavior of structural components under a column removal scenario.

So far, experimental data for structural behavior under a column removal scenario is very limited, especially for reinforced concrete (RC) structures. There were only a few tests conducted to study structural mechanisms of RC structures under column-removal scenarios (Orton 2007; Regan 1975; Sasani et al. 2007; Sasani and Kropelnicki 2008; Sasani and Sagiroglu 2008; Su et al. 2009; Yi et al. 2008) before our research group started the research in this field. Meanwhile, more insights towards the structural behavior of RC members were attained through the research on RC slabs at large displacements but for different research purposes (Foster et al. 2004; Guice and Rhomberg 1988; Park and Gamble 2000).

1.2 Objectives of This Research

Experimental data are essential to verify practice for mitigating progressive collapse and to study mechanisms of structures subjected to a column removal scenario. Previous studies (Izzuddin and Elghazouli 2004; Orton 2007; Regan 1975; Sasani and Kropelnicki 2008) indicate that with increasing deflections, beams could sequentially undergo flexural action (i.e. conventional beam action), compressive arch action (CAA) and catenary action, and failure was concentrated near beam-column joint interfaces (i.e. in beam-column connections). However, there is a lack

of systematic research on structural behavior of RC beams, joints and frames subjected to a column removal scenario. As a result, an experimental program will be conducted to investigate the structural behavior of RC frames and the performance of beam-column connections and joints under *a middle column removal scenario*. To extend the findings from the tests, an analytical model is proposed to study CAA, and a joint model is developed to consider the possible failure at beam-column connections and joint panels. In summary, the objectives of this research are as follows:

- To investigate the effects of *reinforcement ratios* at the beam sections near a middle joint just above a removed column, the *span-to-depth ratio* of beams and the *arrangement of stirrups* in beams on structural behavior of eight simplified RC sub-assemblages. Each sub-assemblage consists of a two-span beam, a middle beam-column joint and two end column stubs. The restraints from remaining unaffected structures to the two-bay beam which is above the removed column are simplified into two end column stubs. The main interest is structural behavior of the *two-bay beams* and the *middle joints* in this series of tests.

- To investigate the effects of *reinforcement detailing* and *boundary conditions* of RC frames on structural behavior of RC *frames* and two *side joints*. More realistic boundary conditions are introduced in the tests on seven RC frames so that each frame comprises a two-span beam, a middle beam-column joint, two side columns and two side joints. The frames are designed with both conventional and special detailing.

- To develop an analytical model for compressive arch action (CAA) of RC beams. With adequate lateral restraints, CAA of RC beams can be mobilized prior to catenary action. The presence of axial compression in beams at CAA stage could enhance structural resistance even at a relatively small deflection. Therefore, it is very beneficial and promising to be incorporated into the ALP method. An analytical model will be developed based on a first principle considering boundary conditions, geometrical and material parameters of beams. Subsequently, the effects of imperfect boundary

conditions, longitudinal reinforcement ratios and beam span-to-depth ratios on CAA of RC beams will be investigated.

- To develop a beam-column joint model that can be incorporated into macro model-based finite element analysis, in which beams and columns are modeled by fiber elements. The joint model, namely, component-based joint model, consists of a set of equivalent nonlinear springs that represent the load transfer paths from surrounding structural members to the joint. A new tensile bar stress-spring model will be proposed with consideration of embedment length and bar stress states of reinforcing bars.

1.3 Scope of Work

Current work is mainly concerned with reinforced concrete (RC) frames, beams and joints without considering the contributions from slabs. The membrane action of RC slabs is outside the scope of the current work. Moreover, the frames concerned are located in the middle of a two-dimensional multi-bay perimeter frame and the removed column is a middle column. Therefore, the effect of transverse beams on RC joints is excluded, and the columns adjacent to the removed one are assumed to be able to sustain the increased axial loads and transfer the lateral force from the two-bay beam after load redistribution.

The experimental program will be conducted quasi-statically to obtain nonlinear static behavior of RC structures rather than dynamic behavior, although progressive collapse is a dynamic event. This is because static tests can provide more details and insights towards the development of different structural mechanisms. Moreover, the test results are able to consider both material and geometric nonlinearity, and the derived static resistance can be converted to dynamic resistance through dynamic increase factors (DIF) (DoD 2010).

The size effect of specimens will not be studied although the specimens are one-half scaled. This is because that one-quarter scale is regarded as the minimum scale for joint specimens fabricated with conventional deformed bars and aggregate concrete mix (Abrams 1987), and shear behavior is not dominant under a column removal scenario. Therefore, the size effect can be ignored in this research.

1.4 Layout of the thesis

The thesis consists of eight chapters and one appendix. The contents of the following chapters are briefly described as follows:

Chapter 2 elaborates the indirect method and the ALP method in code provisions and reviews previous research on progressive collapse resistance and structural behavior of RC framed structures under column removal scenarios. Finally, the joint modeling techniques on RC beam-column joints are reviewed.

Chapter 3 presents the objectives of the experimental program on simplified RC sub-assemblages and RC frames and the links between these two series of tests. Additionally, Chapter 3 elaborates the specimen design, the test set-up and the instrumentation for each series of tests, as well as the ways to conduct material tests. The test results of simplified RC sub-assemblages are comprehensively discussed in Chapter 4 at structural level, cross-sectional level and fiber level. The test results of RC frames are systematically discussed in Chapter 5, including the behavior of two-bay beams, side columns and side joints.

Chapter 6 shows the development of an analytical model on compressive arch action (CAA) of RC beams and parametric studies conducted on CAA. Chapter 7 presents the component-based joint model, in particular, the formulation of tensile bar force-slip springs with consideration of embedment length and stress state of bars. The joint model is then incorporated into macro model-based finite element analysis (FEA).

Chapter 8 concludes the research work and gives the recommendations for future work. Appendix A introduces the detailed process of evaluating the values of stiffness of imperfect boundary restraints in the tests.

CHAPTER 2 LITERATURE REVIEW

2.1 Overview

To mitigate progressive collapse, efforts are directed at both code provisions and research work. In the introductory chapter, design approaches in different codes are briefed. This chapter will give more details on code provisions, mainly on the indirect method and the alternate load path (ALP) method. Besides, the research work to be reviewed is related to reinforced concrete (RC) frames under column loss scenarios, in particular, to compressive arch action and catenary action of RC beams. Finally, joint modeling techniques are reviewed since it is necessary to model joints explicitly at catenary action stage.

2.2 Design approaches to mitigate progressive collapse

Based on the lessons learned from case studies (NIST 2007) that involved progressive collapse of buildings due to extreme loading, methods of mitigating progressive collapse are incorporated in most building codes or standards (ASCE 7-05; EN 1991-2-7 2006; NIST 2007), as shown in **Fig. 2.1**. It should be noted that both the indirect method and the ALP method improve structural robustness and resistance against progressive collapse, but they are largely predicated on initial damage to a single primary structural element, and specific local resistance method is mainly used to design columns or load-bearing walls. However, since it is typically difficult to determine specific threats and the number of damaged primary structural elements may be more than one, a modified specific local resistance approach was developed in UFC 4-023-3 to enhance the performance of perimeter columns and walls for the first and second story (DoD 2010; Stevens et al. 2011).

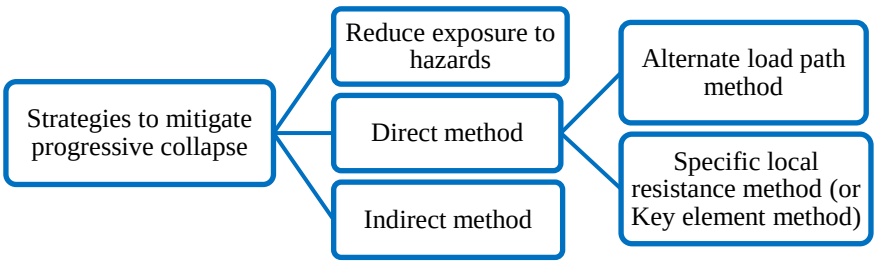

Fig. 2.1: Design approaches to prevent progressive collapse

2.2.1 Indirect method and code provisions

The indirect method is a prescriptive approach of providing a minimum level of connectivity among various structural components and little additional structural analysis is required by designers. Its application is accomplished by specifying minimum tie forces or general structural integrity.

The indirect method has been used in the UK since the early 1970s, immediately following the Ronan Point collapse, and is deemed to be effective in protecting building occupants during extreme loading events (Moore 2002). Recently, the U.K. approach (BS 8110:1997) has been inherited by Eurocode (EN 1991-1-7 2006) and adopted, in part, by the U.S. Department of Defense in UFC 4-023-04 (DoD 2010).

2.2.1.1 Tie force method

In BS 8110, Eurocode EN 1991-1-7 and UFC 4-023-03, the indirect method is achieved by specifying tie requirements, including horizontal and vertical ties. The horizontal ties comprise internal longitudinal ties, internal transverse ties and peripheral ties, as indicated in **Fig. 2.2**. This is often called "tying a building together" by using an integrated system of ties in three directions along the principle lines of structural framing, as illustrated in **Fig. 2.2**.

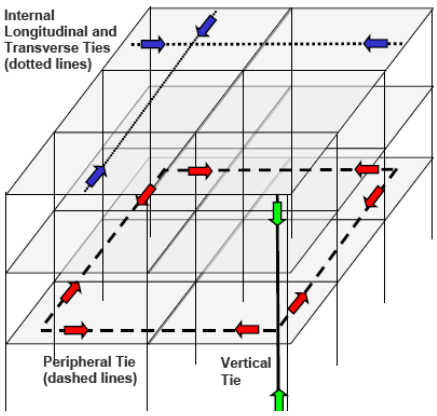

Fig. 2.2: Schematic of tie forces in a frame structure (UFC 4-023-03)

Table 2.1 succinctly summarizes the approaches to specify the magnitudes of horizontal and vertical tie forces for RC framed structures in three codes. The comparisons show that the ways to determine required tie strength in BS 8110-1

and EN 1991-1-7 are more empirical, while the approach in UFC 4-023-03 is more analytical. Moreover, both BS 8110-1 and EN 1991-1-7 allow that ties can be placed in beams, whereas UFC 4-023-03 suggests that ties must be placed beside beams rather than in beams or within the area directly above beams, unless they can be shown capable of a 0.20-rad rotation. This is because a common concern with the tie force approach is the potential inability of steel connections and some RC members and joints to provide horizontal tie-force capacity after significant rotations (Stevens et al. 2011).

Table 2.1 Strength of ties required in building codes for RC framed structures

Ties	BS 8110-1: 1997*	BS EN 1991-1-7:2006	UFC 4-023-03
Interior ties	Greater of $1.0F_t$, or $\frac{g_k+q_k}{7.5}\frac{l_r}{5}F_t$, where F_t = the lesser of $(20+4n_0)$ or 60 kN/m; l_r is the greater of the distances between the centers of columns, frames, or walls supporting any two adjacent floor spans in the direction of the tie under consideration;	Greater of 75 kN, or $T_i = 0.8(g_k + \psi q_k)sL$; where s is the spacing of ties and L is the span of tie, the same as l_r used in BS 8110-1: 1997; Ψ is the relevant factor in the expression for combination of action effects for the accidental design situation.	$F_i = 3w_F L_1$ (kN/m), where $w_F = 1.2g_k + 0.5q_k$ and L_1 is the same as l_r used in BS 8110-1: 1997
Peripheral ties	$1.0F_t$	Greater of $T_i = 0.4(g_k + \psi q_k)sL$, or 75 kN.	$F_p = 6w_F L_1 L_P$ (kN), where L_P = 0.91 m; w_F and L_1 are the same as those for interior ties, but in the building perimeters
Vertical ties	Maximum design ultimate dead and imposed load received by the column from any one story	Columns and walls carrying vertical actions should be able to resist an accidental design tensile force equal to the largest design vertical permanent and variable load reaction applied to the column from any one story.	Vertical ties must have design strength in tension equal to the largest vertical load received by the column from any one story, using the tributary area and the floor load w_F.

* g_k = characteristic dead load per unit area of the floor or roof;

q_k = characteristic imposed floor or roof load (or live load) per unit area.

n_0 = number of stories including ground and basement;

2.2.1.2 Structural integrity

Good engineering judgment, design and construction practice should ensure redundancy, ductility and continuity, which are requisites for structural robustness and integrity. This view is adopted in a number of standards, for instance, ACI 318-05, which has recommendations for reinforcement continuity and connection detailing under the heading of "structural integrity" rather than "progressive collapse". In Chapter 7 of ACI 318-05, the integrity of reinforcement provisions is specified as follows (ACI 2005):

> ***7.13.1*** *– In the detailing of reinforcement and connections, members of a structure shall be effectively tied together to improve integrity of the overall structure.*
>
> ***7.13.2.2*** *— Beams along the perimeter of the structure shall have continuous reinforcement consisting of:*
>
> *(a) at least* ***one-sixth*** *of the tension reinforcement required for negative moment at supports, but not less than two bars; and*
>
> *(b) at least* ***one-quarter*** *of the tension reinforcement required for positive moment at midspan, but not less than two bars*
>
> ***7.13.2.4*** *— In other than perimeter beams, when stirrups as defined in 7.13.2.3 are not provided, at least* ***one-quarter*** *of the positive moment reinforcement required at midspan, but not less than two bars, shall be continuous or shall be spliced over or near the support with a Class A tension splice or a mechanical or welded splice satisfying 12.14.3, and at noncontinuous supports shall be terminated with a standard hook.*

From the viewpoint of multi-hazards, if the elements of a structure resisting progressive collapse have larger capacities due to severe wind and seismic demands in design, the structure would have a higher probability of confining initial local damage and preventing progressive collapse. This is because compared to gravity-loads-dominant design, wind and seismic design require structural members to have larger capacities, toughness, integrity and ductility. After forensic investigations on the collapse of the Murrah Federal Building, Sozen et al. (1998), Corley et al. (1998) and Corley (2002) recommended that seismic detailing, in particular the special

moment frame detailing (such as spiral reinforcement in columns, continuous reinforcement in transfer girders and continuous bars achieved with full capacity mechanical butt splices in spandrel beams), can significantly reduce the degree of direct-induced damage and subsequent progressive collapse. Hayes Jr et al. (2005) examined the effects of alternative seismic design and strengthening, respectively, of the Murrah Federal Building on its resistance to collapse and pointed out that improvements in blast and progressive collapse resistance can result from some good seismic design strengthening measures, in particular from strengthened perimeter elements.

2.2.2 Alternate load path method

The ALP method (also called *notional load path method* in Eurocode) of evaluating the progressive collapse potential is performed by removing one or several major structural bearing elements of a structure (i.e., introducing an initiating damage) and analyzing the remaining structure to determine if this initiating damage propagates. The method does not require characterization of the threat causing the loss of particular elements. Therefore, it is a threat-independent approach and the solution is valid for any type of hazards that causes member loss.

The procedures to analyze remaining structures include linear-elastic static (LS), nonlinear static (NLS), linear-elastic dynamic and nonlinear dynamic (NLD) analysis. Advantages and disadvantages of these analysis approaches were summarized and compared by Marjanishvili (2004). Moreover, the procedures LS, NLS and NLD have been employed in GSA guidelines (2003) and UFC 4-023-03 (DoD 2010). In essence, progressive collapse is a dynamic and nonlinear event. As a result, a LS procedure requires the use of a load increase factor (LIF) to account for both dynamic and nonlinear effects, and a NLS procedure requires a dynamic increase factor (DIF) to account for just inertial effects (Marchand et al. 2009). The extensive analysis shows that DIF is a function of rotation ductility. With increasing rotation ductility, DIF decreases (Marchand et al. 2009). Their results show that DIFs for RC buildings range from 1.00 to 1.40, rather than 2 which is used by both GSA guidelines (2003) and the old version of UFC 4-023-03 (DoD 2005).

In the building codes and design guidelines (BS 8110-1:1997; UFC 4-023-03 2010; BS EN 1991-1-7:2006; GSA 2003), only one column is removed each time for analysis. For a framed building, the available column removal scenarios are shown in **Fig. 2.3**, including corner column, penultimate column, internal column, near penultimate column, edge column and near edge column scenarios (Stevens et al. 2009b). UFC 4-023-03 accounts for most scenarios except the *near penultimate column scenario*. GSA 2003 considers fewer scenarios, merely including corner column, edge column and near penultimate column scenarios. The load combinations after column removal in different codes are summarized in **Table 2.2**.

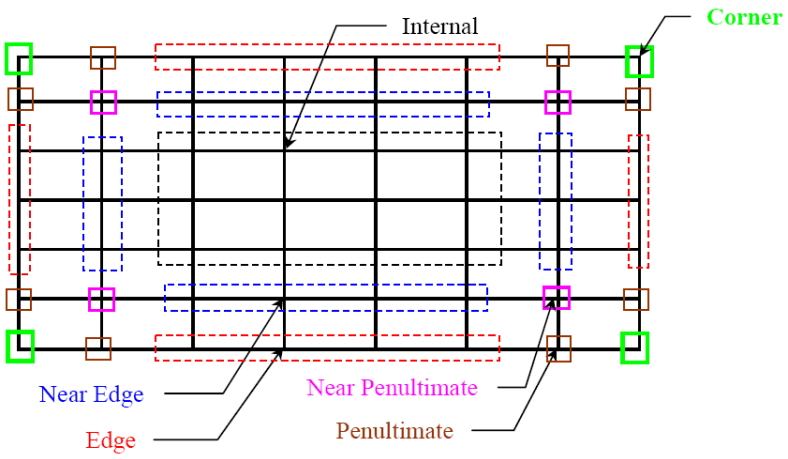

Fig. 2.3: Scenarios of removal of columns (Stevens et al. 2009b)

Table 2.2 Load combinations for ALP method

Codes	**Load combinations after column removal***
BS 8110-1:1997	1.05(D + L/3 + W_n / 3) Except for storage buildings, where 1.0L should be used.
BS EN 1991-1-7: 2006	Not specified
ASCE 7-05	(0.9 or 1.2)D + 0.5L + 0.2S
GSA 2003	2(D + 0.25L) Static analysis; D + 0.25L Dynamic analysis;
UFC 4-023-03 (2010)	Ω_L [(0.9 or 1.2)D + (0.5L or 0.2S)] for linear static analysis; Ω_N [(0.9 or 1.2)D + (0.5L or 0.2S)] for nonlinear static analysis; (0.9 or 1.2)D + (0.5L or 0.2S) for nonlinear dynamic analysis, together with lateral loads applied to structure side

* D = dead load, L = live (imposed) load, W_n = wind load, S = snow load; Ω_L = load increase factor, seen in Table 3-4 of UFC 4-023-03, Ω_N = dynamic increase factor, seen in Table 3-5 of UFC 4-023-03; In UFC 4-023-03, gravity loads for floor areas away from the removed column is (0.9 or 1.2)D + (0.5L or 0.2S).

After column removal, possible ALPs include flexural action and catenary action, in which flexural action is also named Virendeel action (Sasani et al. 2007). However, BS 8110-1, EN 1991-1-7 and GSA 2003 do not discuss whether the ALP method involves flexural (Virendeel action) or catenary action. Additionally, neither BS 8110-1 nor EC 1991-1-7 specifies the acceptance criteria of the ALP method. So far, most design tools cannot account for catenary action; therefore, these analyses are predicated on the ultimate bearing capacity of structure elements being limited by the yield strength of materials. On the contrary, UFC 4-023-03 (DoD 2010) explicitly specifies that the ALP method relies on the flexural strength of structural members. In addition, the acceptance criteria and the modeling parameters in ASCE 41 Seismic Rehabilitation of Existing Buildings (ASCE 2007) are adopted and adapted into UFC 4-023-03 to make the requirement more explicit for engineers.

Izzuddin et al. (2008) proposed a simplified assessment framework to appraise the progressive collapse potential of multi-story buildings due to sudden column loss. After column removal, the structural response at a higher level (say, the whole building) can be obtained by assembling the structural response at a lower level (say, the floor system). Likewise, the structural response of a floor system can be obtained from the integrated responses of corresponding beams and connections as well as slabs. At each assessment level, the *pseudo-static response*, which is transformed from *nonlinear static response*, can be used to consider dynamic effects and assess the robustness and the progressive collapse potential. The nonlinear static response of the lowest level, such as beams and connections, can be ascertained either by simplified analytical models or by detailed numerical models. As a result, the nonlinear static response of the lowest level is the foundation of the whole simulation process. ALPs at any higher levels rely on the nonlinear static response of the lowest level, and ALPs could include both flexural action and catenary action, depending on the ductility limit of the beams and the connections in question. Compared with code provisions (e.g. GSA 2003 and UFC 4-023-03), Izzuddin et al's proposed framework offers greater flexibility to engineers.

In summary, the ALP method may be viewed as a tool to ensure redundancy in the gravity load-resisting system rather than as a simulation of structural response after

an initial damage (NIST 2007). Regarding dynamic response, although the ALP method does not consider dynamic effects to structures arising from an impact or a blast, it does capture the influence of column failure occurring over a relatively short duration to the response time of the structures (Izzuddin et al. 2008). Briefly, this method forms the first proposal of a quantifiable model for designing robust buildings (Gurley 2008).

2.2.3 Comparisons between indirect method and ALP method

The indirect method and the ALP method should be checked by analysis to ascertain whether ALPs exist around hypothetically collapsed regions after introducing initial damage. The tie force method relies upon catenary action to redistribute loads following damage of a column, for example, as used for providing robustness to steel-framed buildings (Byfield and Paramasivam 2007a; b). In turn, the studies on ALPs of structures can be used as design guidelines for developing rules to achieve minimum levels of continuity and ductility or tie forces required by the indirect design approach. In the case of buildings of load-bearing wall construction, the notional removal of a section of wall, one at time, is likely to be the most practical strategy to adopt (EN 1991-1-7:2006), since the flexural resistance due to arch action could be increased.

In design practice conforming to UFC 4-023-03 (DoD 2010), for Option 1 of Occupancy Category II and for Occupancy Category IV, the ALP method is an alternative option when the required vertical tie capacity cannot be achieved. However, the ALP method cannot be used for elements when the horizontal tie force capacity is inadequate.

In this research, the interest in ALPs is more performance-based. That is, with increasing deformation of frames, what kind of ALPs will develop and how they sequentially transit from one to the other? The specimens to be designed satisfy both *tie force requirements* in EN 1991-1-7 and *integrity requirements* in ACI 318-05.

2.2.4 Dynamic increase factor

Due to the dynamic nature of progressive collapse, nonlinear static structural resistance must be divided by dynamic increase factors (DIF) of acting loads to evaluate progressive collapse resistance. In the design guideline of UFC 4-023-03, the DIF model employed for RC structures is shown in Eq. (2-1).

$$\text{DIF} = 1.04 + \frac{0.45}{\theta_{pra} / \theta_y + 0.48} \tag{2-1}$$

where θ_{pra} is the plastic rotation angle, and θ_y is the yield rotation of RC members. Note that the ratio of θ_{pra} / θ_y is defined as ductility measure, equal to rotation ductility minus one.

With the frame work proposed by Izzuddin et al. (2008), DIFs of an RC member or assembly can be evaluated by the ratio of *pseudo-static resistance* to *quasi-static resistance* for any given deflection. By assuming the deflection (or displacement) ductility equal to rotation ductility, relationship between of the DIFs and ductility measure can be constructed (Izzuddin and Nethercot 2009). For example, **Fig. 2.4** shows the nonlinear static and the pseudo static structural responses as well as the variations of DIF vs. ductility for an elastic-plastic system. It can be seen that with increasing ductility after yielding, DIF monotonically decreases.

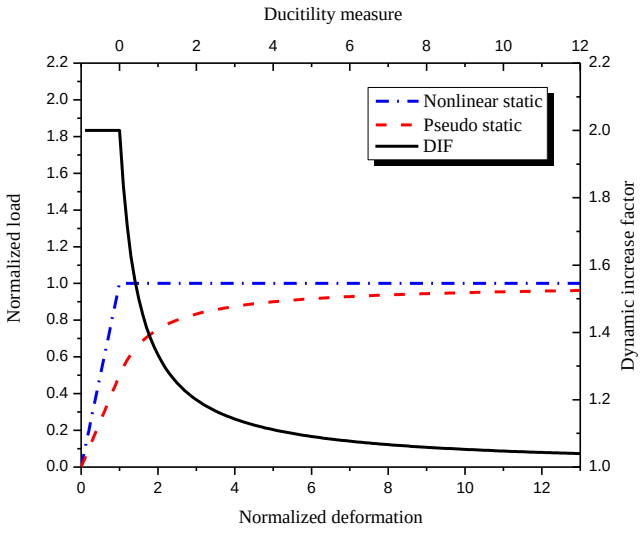

Fig. 2.4: Characteristic responses and DIF for elastic-plastic system

Fig. 2.5 shows that the predictions of the relationship of DIF vs. ductility by using two approaches are close to each other, indicating that the DIF model (or Eq. (2-1)) for RC structures in UFC 4-023-3 corresponds to elastic-plastic structural performance under static loading. More precisely, bilinear structural performance with strength hardening at plastic stage was used to derive Eq. (2-1) (Izzuddin and Nethercot 2009). However, if this model is utilized for other types of nonlinear structural performance, the predictions of DIF may be overly conservative or unsafe.

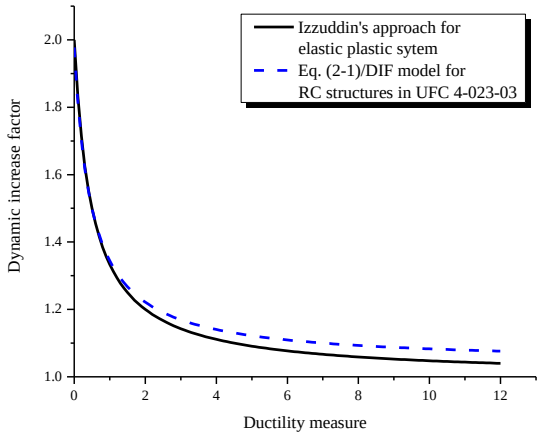

Fig. 2.5: Comparison of DIF models

Fig. 2.6 shows the variations of DIFs vs. ductility for two different types of nonlinear responses. It can be seen that DIF does not monotonically decreases with increasing ductility. For example, when the normalized deformation exceeds around 6, DIF increases with ductility, as shown in **Fig. 2.6(a)**. At this stage, using Eq. (2-1) to predict DIF is unsafe. Similar phenomenon can also be found in **Fig. 2.6(b)**.

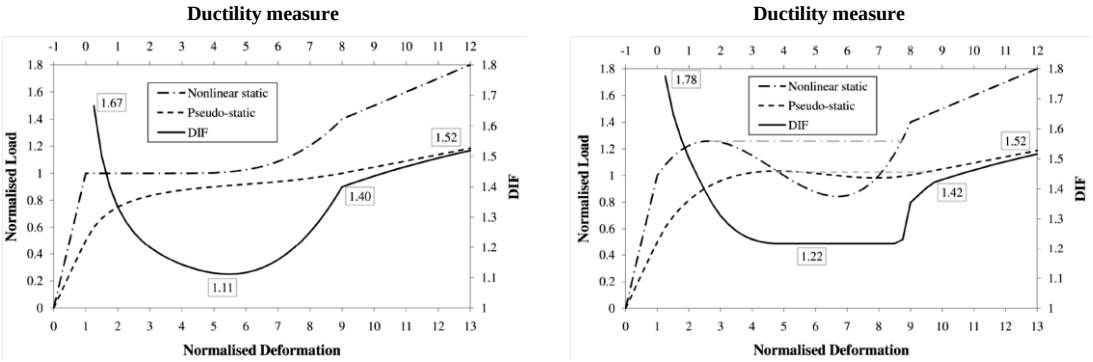

(a) elastic-plastic with catenary action (b) Snap through with catenary action

Fig. 2.6: Characteristic responses and DIF for different nonlinear systems (Izzuddin and Nethercot 2009)

In summary, DIFs depend not only on structural ductility but also on types of nonlinear structural performance (Izzuddin and Nethercot 2009). However, the DIF model for RC structures in UFC 4-023-03 can only be applied to structures with elastic-plastic or bilinear structural performance.

2.3 Typical alternate load paths of RC frames

The available ALPs for RC framed structures include Vierendeel action, compressive arch action and catenary action. Vierendeel action can be characterized by relative vertical displacement between beam ends and double curvature deformations of beams and columns (Sasani et al. 2007). It utilizes the flexural resistance of beam and column members to redistribute loads.

Compressive arch action (CAA) of beams can be elucidated by analogy with compressive membrane action of RC slabs, as illustrated in **Fig. 2.7**. The surrounding slabs laterally restrain the interior slab, allowing the development of internal compressive thrust which enhances the flexural strength at critical sections of the slab. As a result, the structural resistance was larger than that predicted by yield line theory (Welch 2000). Likewise, with adequate lateral restraints at both ends of a beam, CAA in the beam can be mobilized. Furthermore, due to the presence of axial compression, the structural resistance of the beam will be greater than that determined by the conventional three-plastic-hinge mechanism.

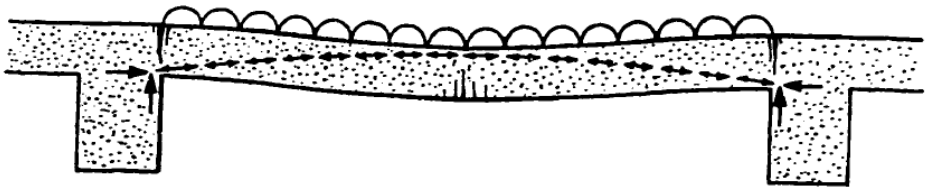

Fig. 2.7: Compressive force forming arch action (Ockleston 1958)

For framed structures with initial damage, the flexural yield strength of remaining structural elements will develop first at deflections not too much greater than in-service deflections. If this capacity is sufficient to meet the existing gravity load requirements, then there is no need to go further; otherwise, catenary action may develop, as shown in **Fig. 2.8**. For all ALPs, catenary action represents the last line

of defense against progressive collapse because it is mobilized only after large deformations have developed. Meanwhile, catenary action always involves large horizontal forces transferred to joints that may require special connections and column design (Gurley 2008). **Fig. 2.8** also indicates that the structural resistance provided by catenary action depends on the development of axial tension and the rotations of beams. The larger axial tension and the larger beam-end rotations could result in greater structural resistance. Axial tension forces are transferred from the two-bay beams directly above the removed column to the surrounding structures, which can in turn provide adequate lateral restraints to the two-bay beams without causing column failure.

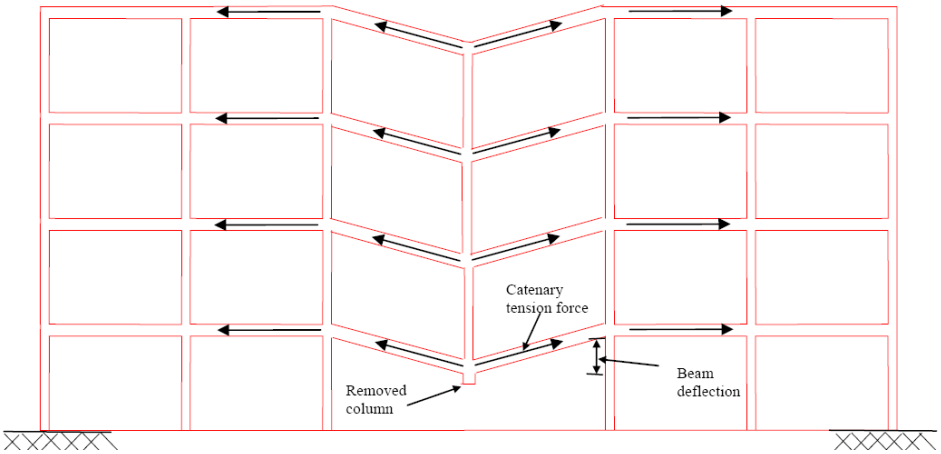

Fig. 2.8: Catenary tension force (Orton 2007)

2.4 Research on RC frames under column loss scenarios

The aforementioned ALPs of structures mobilized under column loss scenarios can be used to mitigate progressive collapse. However, very limited experimental data exist as the basis of assessing each ALP. Moreover, the nonlinear static performance at lower structural levels (say, beam-column sub-assemblages) can be further utilized to appraise the progressive collapse potential via the framework proposed by Izzuddin et al. (2008).

On the other hand, catenary action is a mechanism associated with large deformations, which have not been documented fully through tests and numerical validations. There are very few previous studies on catenary action of RC beams.

Most of the experimental studies are concerned with catenary action of steel beams at ambient and elevated temperatures and at column loss scenarios (Byfield et al. 2007; Byfield and Paramasivam 2007a; b; Demonceau 2007; Izzuddin 2005; Yin and Wang 2005). Therefore, in this section, the very limited tests on RC frames under column loss scenarios and analytical work will be reviewed.

2.4.1 Laboratory tests

Tests on precast floor strips in Imperial College, London

Regan (1975) reported catenary tests on precast floor strips conducted in Imperial College in London, as shown in **Fig. 2.9**. The specimens ranged from 356 mm to 711 mm wide and 5.4 m long with a central joint between two 2.7 m planks representing the lost support. The specimens comprised a 50 mm thick precast panel and a 50 mm thick cast-in-place topping. Details of the ties between the panels varied. For almost all the tests, there was an initial compressive arch phase, which was "snapped through" due to instability and was followed by a catenary action phase, e.g. specimen #4 and #14 in **Fig. 2.10**. The majority of beams failed by tearing out of the bottom bars near the supports at a deflection of 5 to 7% of the double span length (test #5 in **Fig. 2.10**). However, some specimens were able to yield in flexure at the supports before tearing out of the bottom bars. In these cases, the failure loads were much higher and the ultimate deflection was nearly 10% of the span length (test #3 in **Fig. 2.10**). The strips eventually failed by fracturing of the end rebar due to rotation at the support. For most tests, catenary action started at around 150 to 175 mm of displacement, greater than the strip depth of 100 mm. Due to insufficient anchorage and poor continuity of specimens, not all of them could develop catenary action successfully. Finally, Regan (1975) concluded that the successful development of catenary action requires that the members in question possess not only *tensile strength* but also *ductility*, which is largely determined by the detailing of longitudinal reinforcement.

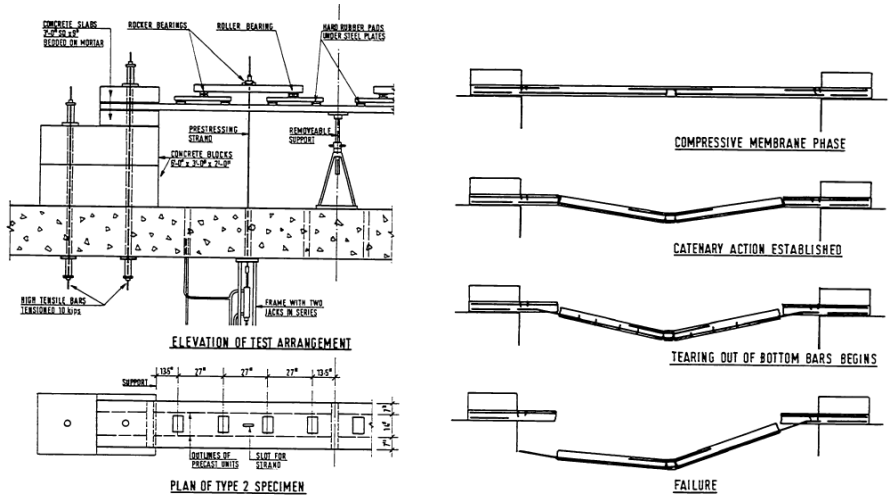

Fig. 2.9: Catenary action tests of precast floor strips (Regan 1975)

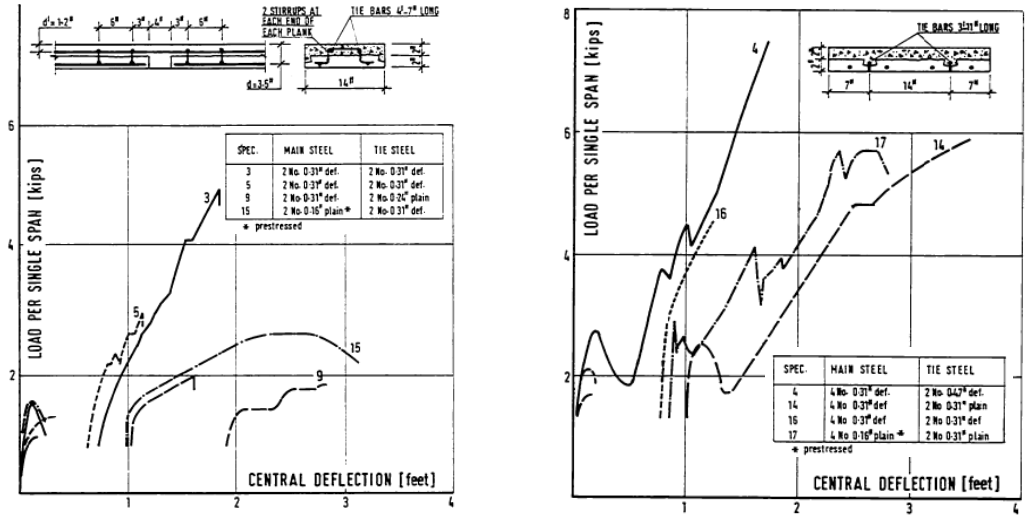

Fig. 2.10: Results of catenary action test of precast floor strips (Regan 1975)

Orton's test in University of Texas, Austin

Orton (2007) conducted a series of tests to investigate the application of carbon fiber reinforcement polymer (CFRP) on retrofitting RC beams without continuous reinforcement to develop catenary action. The test specimens were half-scaled models with a 12 in. (305 mm) by 6 in. (152 mm) cross-section, a 9 in. (229 mm) by 8½ in. (216mm) column stub, and a 30 ft (9 m) length of beams. They were designed in accordance with ACI 318-71 to represent a double-span RC beam after the removal of a middle column. Both negative and positive moment reinforcement were not continuous. To compare the results of CFRP retrofitting, one beam was designed in accordance with ACI 318-05 to provide continuous reinforcement. **Figs.**

2.11(a) and **(b)** show the detailing of specimens with and without continuous longitudinal reinforcement, respectively. The beam contained #3 stirrups with 90 ° hooks to preclude shear failure during testing. Three point loads spaced at 6 ft (1.8 m) apart were applied vertically upward until failure occurred. Axial restraints were provided at both ends.

Fig. 2.12 indicates that the two beams initially experienced CAA followed by catenary action because the mobilized beam axial forces changed from compression to tension. Moreover, the capacity of catenary action of NR-2 (around 5.0 kip) significantly exceeded that of CAA, as shown in **Fig. 2.12(a)**. However, due to fracture of reinforcing bars, the capacity of catenary action of CR-1 (around 3.5 kip) was smaller than that of CAA (around 5.0 kip). Orton illustrated that the reinforcing bar fracture was caused by the high rotation demand at the sections close to the joint.

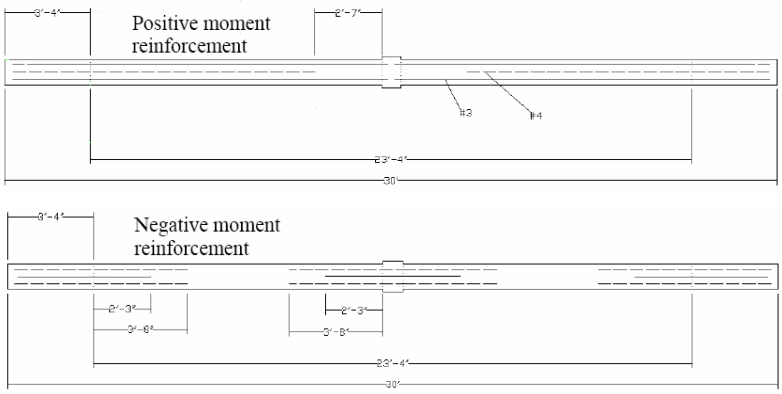

(a) NR-2 with discontinuous reinforcement

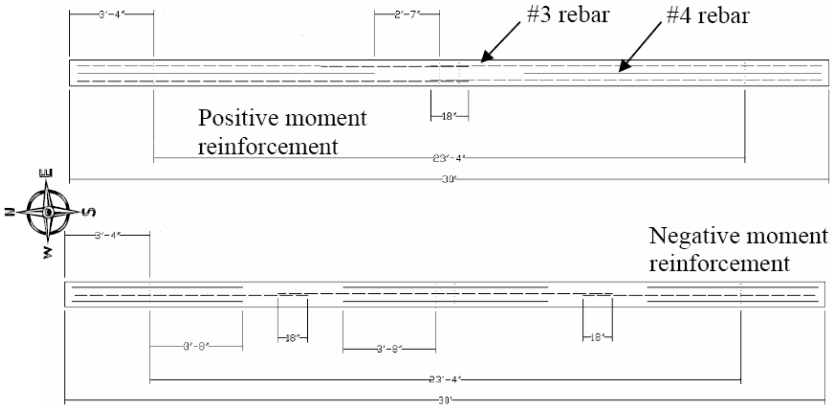

(b) CR-1 with continuous reinforcement

Fig. 2.11: Detailing of test specimens in Orton's tests (Orton 2007)

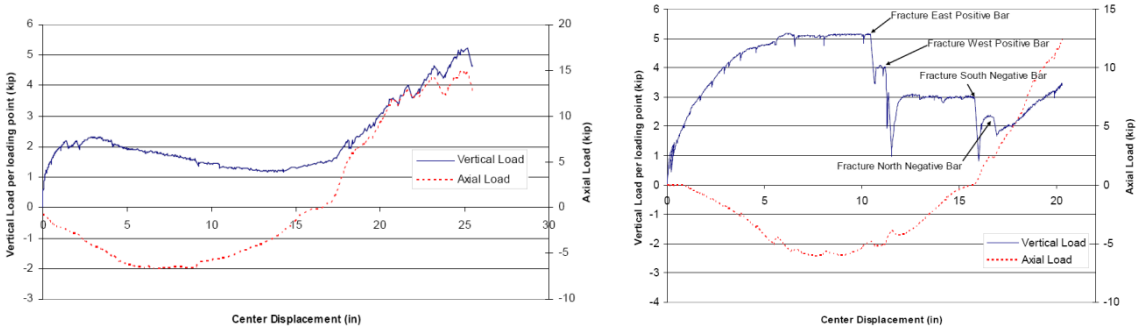

(a) NR-2 (b) CR-1

Fig. 2.12: Vertical and axial loads vs. displacement in Orton's tests (Orton 2007)

The failure modes of two beams were shown in **Fig. 2.13**. Cracks opened up widely and the beam deflected as a mechanism comprising rigid blocks connected at the hinge locations. Compared with the specimen detailing shown in **Fig. 2.11**, it can be found that all the locations with severe cracks and bar fracture coincided with the ends of discontinuous reinforcement.

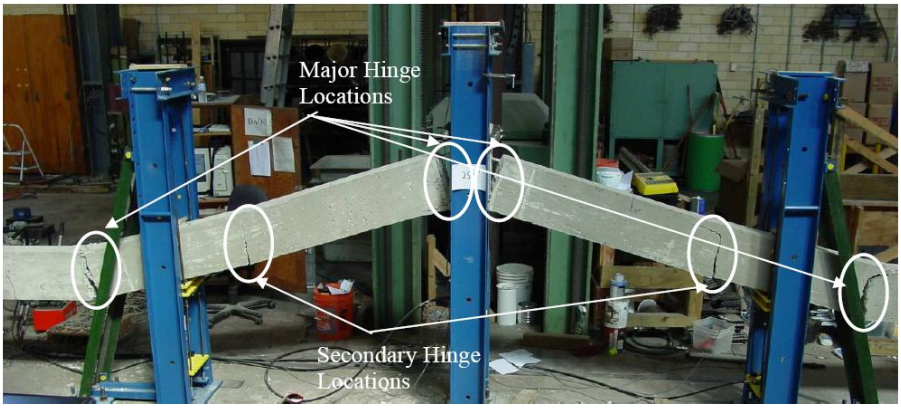

(a) Specimen NR-2

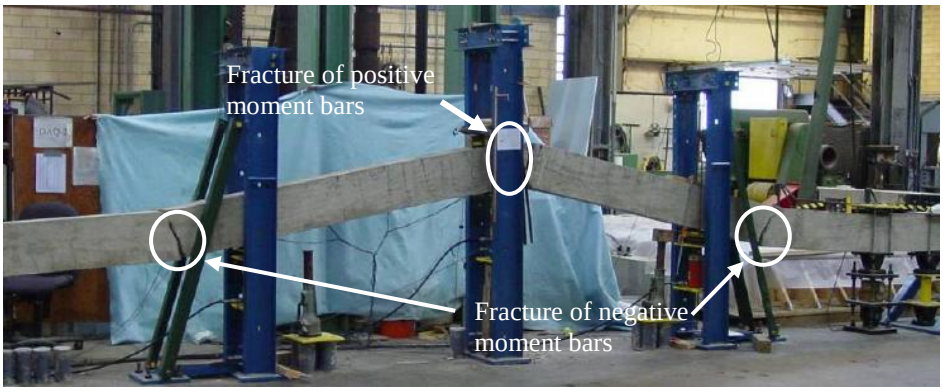

(b) Specimen CR-1

Fig. 2.13: Failure modes of beams in Orton's tests (Orton 2007)

Sasani's test in North Eastern University

Sasani and Kropelnicki (2008) tested a 3/8 scaled RC perimeter beam under a middle column removal scenario. The prototype beam was designed in accordance with ACI 318-02, which specifies integrity requirements. The detailing of the test beam is shown in **Fig. 2.14**, and the beam was assumed to model the mechanism to bridge over the lost column with fixed boundary conditions at both ends. The beam was 7.5 in. (190.5 mm) in depth and 137.25 in. (3486 mm) in length. Loading was applied by displacement control mode at the mid-span. However, in that test, the vital information of the variations of axial forces across the beam sections were not measured nor evaluated.

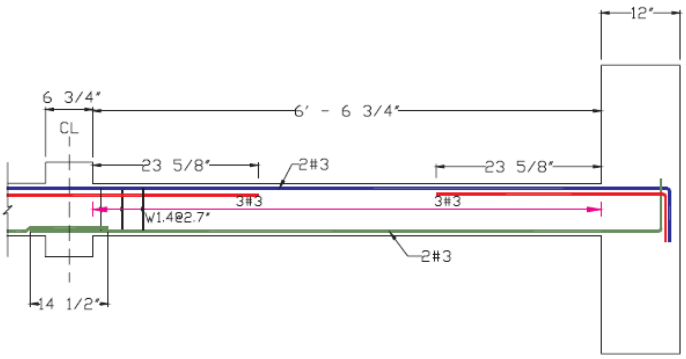

Fig. 2.14: Detailing of the test beam (Sasani and Kropelnicki 2008)

Fig. 2.15(a) shows the vertical force versus the displacement at the middle joint. At vertical displacements of about 6.0 in. (150 mm) and 7.5 in. (190 mm), the two bottom bars fractured, followed by catenary action at around 5.5% of the span. In spite of the fracture of bottom bars, the beam had significant residual strength and deformation capacity. By satisfying the integrity requirements of ACI 318-02, catenary action developed in the top reinforcement. However, the test did not show that the structural capacity due to catenary action could exceed that due to CAA. **Fig. 2.15(b)** represents the failure at the beam-column connection following the fracture of the second bar and severe concrete crushing.

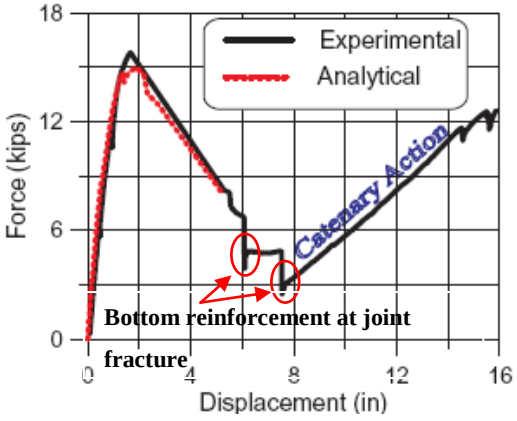

(a) Force and displacement relationships

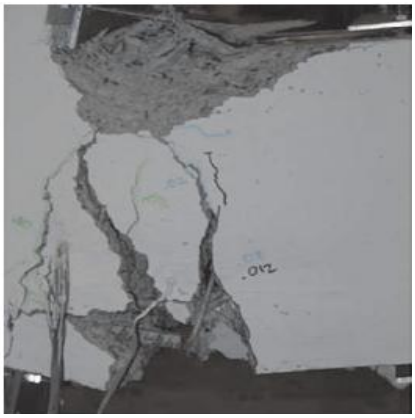

(b) Damage at connection after bar fracture

Fig. 2.15: Results of Sasani's test (Sasani and Kropelnicki 2008)

Yi et al.'s test in Hunan University, China

Yi et al. (2008) tested a one-third-scaled, four-bay and three-story RC frame under a middle column removal scenario. The specimen was designed in accordance with the concrete design code of China, which is generally similar to ACI 318-02. The beam sections were 200 mm deep and 100 mm wide with 2D12 bars at both top and bottom layers. The cross-section of columns was 200 mm by 200 mm. The other dimensions of the specimen are shown in **Fig. 2.16**. A constant vertical load was applied to the top of the middle column by a servo-hydraulic actuator to simulate the gravity load of the upper floors and the failure of the middle column of the first story was simulated by unloading a mechanical jacking system, as shown in **Fig. 2.16**. The frame collapse, defined as the rupture of steel bars in the beams, occurred at a vertical unloading displacement of 456 mm that corresponded to a beam chord rotation of 10.3^{o}. The structural mechanisms in the load-displacement history are indicated in **Fig. 2.17**. The calculated capacity of the frame based on the plastic limit state was approximately 70% of the tested failure capacity if catenary effects were also included. The overall failure mode in **Fig. 2.18(a)** indicates that the adjacent bays were able to provide adequate axial restraints to the two-bay beams to mobilize catenary action. Also, the large rotation and the axial tension resulted in the fracture of bottom bar near the middle joint interface, as shown in **Fig. 2.18(b)**.

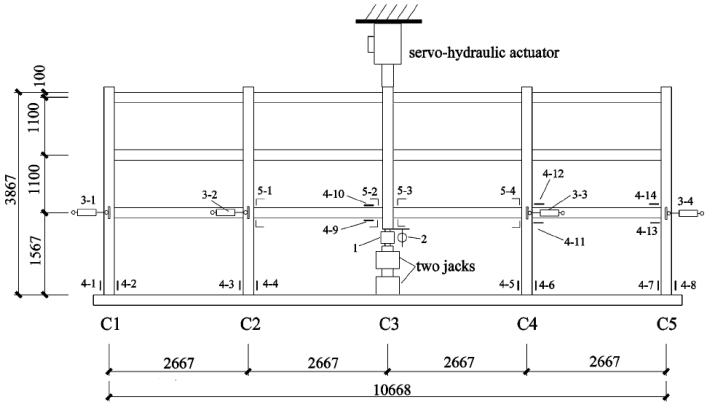

Fig. 2.16: Specimen dimensions and the test set-up (Yi et al. 2008)

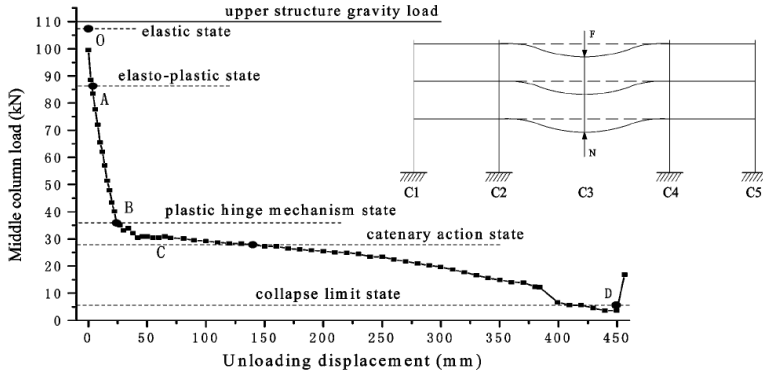

Fig. 2.17: Middle column load vs. unloading displacement (Yi et al. 2008)

(a) overall mode (b) Local mode

Fig. 2.18: Failure mode of the RC frame (Yi et al. 2008)

Su et al.'s tests in Hebei Polytechnic University, China

Su et al. (2009) tested twelve RC beam-column sub-assemblages to investigate their capacities due to CAA against progressive collapse. In the tests, the sub-assemblages were restrained longitudinally against axial deformation. The tests indicated that the CAA due to axial restraints at beam ends can significantly

enhance the flexural strength of a beam subjected to vertical loads. The CAA capacities were 50% to 160% larger than the flexural capacities estimated without considering axial restraints. Moreover, CAA was observed to be a function of the flexural reinforcement ratio and the beam span-to-depth ratio. However, the tests were not conducted to mobilize large catenary action.

2.4.2 Field tests

Other than the reported laboratory tests, two field tests were reported in the literature to investigate structural response of RC buildings under column loss scenarios in the context of overall structural behavior instead of member or sub-assemblage behavior.

Sasani et al. (2007) evaluated the progressive collapse potential of an actual 10-story RC structure following the explosion of an exterior column. Before the demolition of the University of Aransas Medical Center dormitory by implosion, Column B5 in the first story was exploded (suddenly removed), as indicated in **Fig. 2.19**. The building floor system consisted of one-way slabs supported by transverse frames. After the column removal, Vierendeel action of the transverse frame whose exterior column was removed was identified as the major mechanism for the redistribution of loads in this structure, as illustrated in **Fig. 2.20**. That is, because of moment connections, the beams and the columns above the removed column deformed in double curvature. The large axial stiffness of the columns above led to almost an identical vertical movement of different floors. The experimental permanent vertical displacement of joint B5 in the second floor and the fifth floor was 6.6 mm and 6.0 mm, respectively.

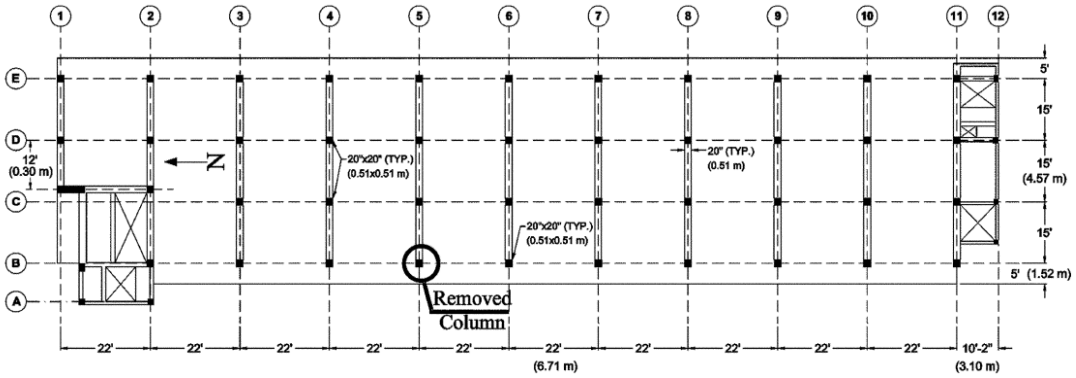

Fig. 2.19: Plan view of the structure (Sasani et al. 2007)

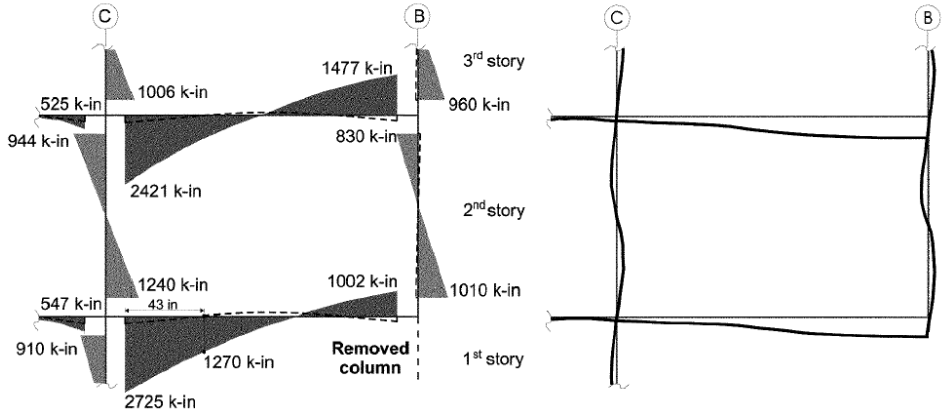

Fig. 2.20: Bending moment diagram and deformed shape of frame in axis 5 (Sasani et al. 2007)

Sasani and Sagiroglu (2008) reported the evaluation of progressive collapse resistance of Hotel San Diego following the sudden removal of two adjacent exterior columns, as shown in **Fig. 2.21**. The hotel had a nonductile RC frame structure with hollow clay tile exterior infill walls. The floor system consisted of one-way joists running in longitudinal direction, as shown in **Fig. 2.21**. After the column removal, bidirectional Vierendeel (frame) action of the transverse and the longitudinal frames was identified as a major mechanism for the redistribution of loads in this structure. That is, the beams that connected a joint above a removed column to an adjacent supported joint deformed in double curvature, which in turn developed sufficient shear forces to redistribute gravity loads. The maximum measured vertical displacement of the structure after the removal of two adjacent columns was only about 6.4 mm, directly above the removed columns.

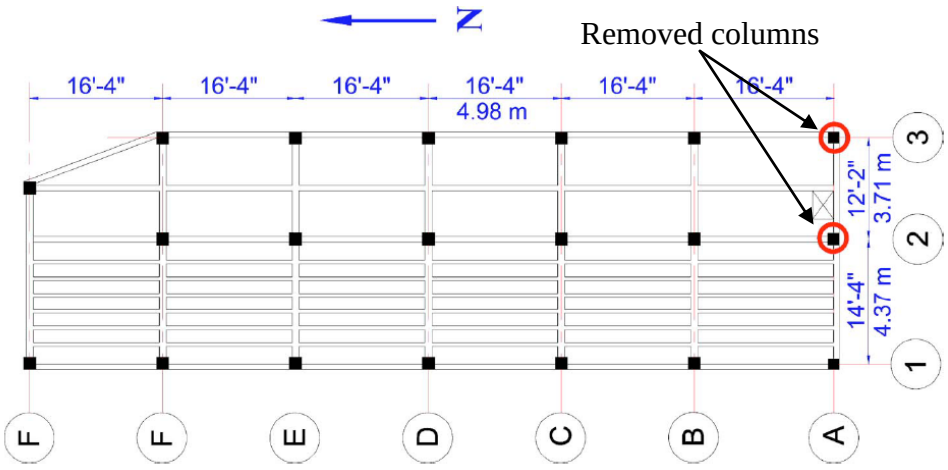

Fig. 2.21: Typical plan of Hotel San Diego—South annex (Sasani and Sagiroglu 2008)

2.4.3 Analytical and numerical studies

Izzuddin and Elghazouli (2004) proposed an analytical model for lightly-reinforced members subject to axial restraints, which accounts for compressive arch action and catenary action, bond-slip, yielding, and rupture of steel reinforcement as well as the effect of elevated temperature. The model could simulate the whole load-deformation history of lightly-reinforced concrete members. However, due to its assumptions, this model cannot be simply applied to RC beam-column sub-assemblages which have moderate to high reinforcement ratios.

Bao et al. (2008) conducted a macromodel-based simulation of progressive collapse of RC framed structures under column loss scenarios. In this model, beams and columns were simulated with fiber elements and joints with a macromodel, which consisted of a series of spring elements. The validity of the developed macromodel was verified through the comparison of high-fidelity finite-element analyses. It was found that inelastic joint models could more accurately characterize the nonlinear behavior associated with the transfer of forces through the beam-column joint—which thereby provided the capability to capture the large deformation response associated with progressive collapse. However, the calibration of those springs in the joint model was directly obtained from the database in seismic research. Therefore, it is likely that the spring properties could not reflect the actual behavior

under column loss scenarios since loading conditions and boundary conditions of progressive collapse are quite different from seismic loads.

Santafé Iribarren et al. (2011) employed multilayered beam elements in dynamic progressive collapse simulations to study the structural response of a multi-story planar frame subjected to a sudden column removal. Bilinear constitutive models were used for concrete in compression and steel reinforcement. Systematic parametric studies were carried out to investigate the influence of ultimate strain of concrete and steel, reinforcement ratio, column removal time, removed column locations and the load combinations on structural performance. When the ultimate strain of steel is reached, i.e. at bar fracture, the frame is regarded as collapse. All fractures are initiated from the top bars at the negative bending moment region, which is different from finds in experimental research (Orton et al. 2009; Sasani and Kropelnicki 2008; Yi et al. 2008; Yu and Tan 2011b; 2012b). This is probably because the numerical analysis failed to capture the concentrated cracks at joint interfaces. It was found that a higher ultimate strain of steel, reinforcement ratio and strain rate effects can result in greater progressive collapse resistance. Moreover, longer removal times can lead to no collapse after column loss, indicating that the sudden column loss idealization (considering an instantaneous column removal) offers an upper bound of the deformations obtained through an event dependent approach. Finally, it was found the scenario of corner column removal is more collapse-prone than that of interior column removal. This is because the former scenario only relies on flexural resistance of the assembly above the removed column, but the latter scenario can use compressive arch action and catenary action, which provide larger structural resistance than flexural mechanism.

Kim and Yu (2012) used fiber-based beam elements to analyze RC frames subjected to column loss and assumed that beam-column connections had adequate strength to sustain the catenary force induced in beams at large deformations. Accordingly, fracture of bars was not considered. The frames in parametric studies were designed with and without seismic loads in accordance with ACI 318-02. With seismic loads, beams are designed with larger cross-sections, greater reinforcement ratios and continuous top and bottom bars throughout the entire beam spans,

whereas without seismic loads, bottom bars are discontinuous in the beam-column joints. In fact, this non-seismic design violates the integrity requirements for reinforcement in ACI 318-02, but it can be regarded as old-fashioned non-seismic design. Definitely, under the same gravity loads, the performance of non-seismic-designed frames is inferior to that of seismic-designed frames. It is found that the development of catenary action is proportional to the amount of the reinforcement, but not related to the ultimate strength of concrete. In the analysis, the effect of stirrups was converted to the confinement to concrete. That is, a higher volume ratio of stirrups results in a greater compressive strength and ductility of concrete. By this way, the fewer amount of stirrups corresponds to earlier mobilization of catenary action. However, due to severe cracking at joint interfaces, it is suspicious whether the confinement from stirrups works effectively.

2.5 Beam-Column Joint Modeling

Because both material and geometric nonlinearity as well as discontinuities, such as bar fracture, bar pull-out and concrete crushing and spalling, are involved in the load-deformation history of RC frames under column loss scenarios, in particular at catenary action stage. Therefore, it is logical to separate joints (including *joint panels* and *connections*) from beams and columns and to treat them as independent elements.

To simplify the finite element analysis of structures, beam-column joints are usually assumed as rigid or pin. However, the actual joint behavior is in between a pin and a rigid support. Thus, taking the real behavior of beam-column joints into analysis is more accurate. Besides, in some cases, such as under seismic or abnormal loads, beam-column joints are more vulnerable.

So far, there have not been any publications on the tests of RC beam-column joints under catenary action. On the contrary, there are many research works on the tests and modeling of RC beam-column joints under cyclic loading over the past four decades. However, all the mechanisms of joints can be decomposed into some basic components, such as tension of reinforcing bars, compression of concrete, bond-slip relationship, and shear panel behavior. Thus, the approach adopted by researchers

for beam-column joints under seismic (cyclic) loading is of benefit to the modeling of joints under catenary action.

2.5.1 Types of beam-column joint modeling

The methods to develop RC beam-column joint model can be divided into four groups: statistical models, continuum finite element models, component-based super-element models, and strut-and-tie models (Mitra 2007).

Statistical models can identify the design parameters that determine the behavior of beam-column joints, but they fail to provide any meaningful insight into why these design parameters affect the joint response (Mitra 2007). To improve understanding of the joint response mechanisms, a nonlinear continuum modeling may be used, but it is not computationally efficient and is restricted to research use only.

To obtain insight into the beam-column joint behavior and computational efficiency, a component-based modeling approach has been applied to RC structures (Bao et al. 2008; Fleury et al. 2000; Lowes and Altoontash 2003; Mitra and Lowes 2007) under seismic loading and progressive collapse. With this approach, the complicated joint behavior is decomposed into behavior of several components, such as bond-slip, interface shear and shear panel behavior. These components can be represented as equivalent nonlinear springs which describe the uniaxial force-displacement relationship of each component. In this sense, the accuracy of component-based joint models highly depends on the force-displacement relationships adopted for the equivalent springs and the number of components included in the analysis. Therefore, the key point of this type of modeling is to extract the characteristics of these equivalent springs and to calibrate them based on test results. For frames under column removal scenarios, beam-column joints function as conventional rotational springs in flexural action. However, these joints play a more complex and important in compressive arch action and catenary action because large axial forces are transferred into joints other than bending moments. Consequently, it is hard to represent a joint as a certain spring, and it is logical to use a combination of uniaxial behavior of components to simulate complicated and varied joint behavior. In this thesis, the component-based modeling approach will

be employed and research work will be dedicated to developing a bar stress-slip relationship that satisfies both the loading and the boundary conditions under column loss scenarios. The component method will be reviewed in the next section.

A particular strut-and-tie model (STM) of a system provides a lower bound on the strength of the system, since neither compatibility requirements nor explicit material constitutive relationships are considered in developing an STM. However, strut-and-tie models are widely used by engineers to dimension and detail RC structures at "disturbed" regions and this design methodology is included in most structural design codes around the world (ACI 318-05; EN 1992-1-1 2004).

2.5.2 Component method concept

The origin of "component method" is to consider any joint as a set of individual basic components and it was initially developed from studies conducted on steel joints. The principles of the *Component Method* are based on the experimental and analytical work by Zoetemeijer (1983) which was conducted from 1974 to 1983. Thereafter, the method was developed further by a number of researchers, but the work of Tschemernegg and his co-workers at the University of Innsbruck, Austria, was particularly important. This work was carried out in the 1980s and 90s and was summarized in the paper (Tschemmernegg and Humer 1988). Furthermore, Jaspart (2000) combined available component data to a practical design concept for steel joints at ambient temperature.

The application of the component method requires the following steps (Jaspart 2000): 1) identification of active components for a joint; 2) evaluation of the mechanical characteristics of individual basic components; 3) "assembly" of the components to represent the mechanical characteristics of the whole joint.

Recently, the *idea* of the component method has been applied to RC joints more widely (Bao et al. 2008; Fleury et al. 2000; Lowes and Altoontash 2003; Lowes et al. 2003; Mitra and Lowes 2007). Details of their work will be discussed in the next section. However, compared with steel or composite steel joints, the available components for RC joints are more limited. Moreover, the component properties in

RC joints, such as bond-slip and shear panel behavior, are more complicated than those in composite steel joints.

2.5.3 Component-based modeling of RC joint

Mitra (2007) classified the component-based modeling of RC joints into two categories: Implicit models and explicit macroscopic models, in which the explicit macroscopic models are similar to the concept of component method.

Implicit models: The stiffness and strength loss due to joint damage is modeled by modifying beam and column elements. Typically, nonlinear springs or plastic hinges or both are added at the member ends. Such models are useful to determine the overall impact of nonlinear joint action on structural response. On the one hand, these models are difficult to calibrate since the joint action involves adjacent beams and columns. On the other hand, these models are computationally less demanding and can be easily incorporated into any finite element program. Since these models do not consider an explicit representation of the joint region, they do not satisfy the joint kinematics and thus cannot be used for detailed investigation of mechanisms governing the inelastic joint behavior. In this approach, usually only one of the primary inelastic response mechanisms observed in joints (shear or bar-slip) is considered.

Explicit macroscopic models: These models consider an explicit representation of a joint region. For joints under seismic loads, inelastic mechanisms governing the joint behavior such as bar-slippage through a joint and shear failure in a joint core, form the backbone for these models. These models satisfy joint kinematics and can be used as separate macroscopic elements in frame models composed of line elements. The models in this category vary in their level of discretization of a joint region, complexity, robustness and accuracy. That is, more precise simulation on joints may require more detailed discretization.

The crucial steps in explicit macroscopic models (or component-based models) are to extract the pertinent components and to calibrate them with test results performed on components. Some examples of this type of joint models are shown in

Table 2.3. It can be found that the connection behavior is represented by components of bar stress-slip springs and interface springs, and the joint core behavior is represented by a shear panel spring or a pair of rotational springs. However, available calibrations on these components are mainly obtained from structures under cyclic loading. For structures under column loss scenarios (or progressive collapse), new calibrations are needed because the components are likely to work in different stress states.

Table 2.3 Typical explicit macroscopic models

The schematic diagram of joint models	Brief Description
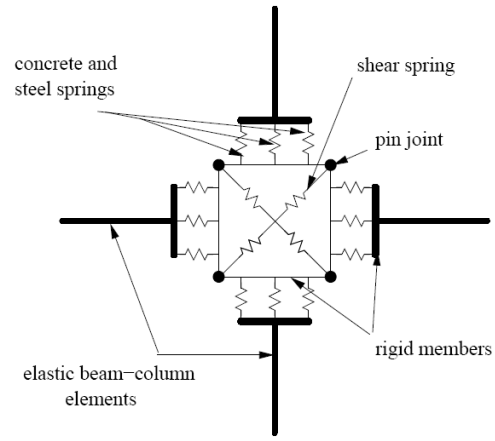 (a) Youssef-Ghobarah joint model(2001)	The impact of bar-slip within a joint and concrete crushing at the joint perimeter is represented using three concrete and three steel springs at each face of the connection region between the beams and columns and the joint panel. The steel springs characterize the relationship between the force in the steel bars and the slip. The concrete springs represent the relationship between the axial force on the concrete strut and the axial displacement of the strut. The shear springs demonstrate the shear response in the joint core.
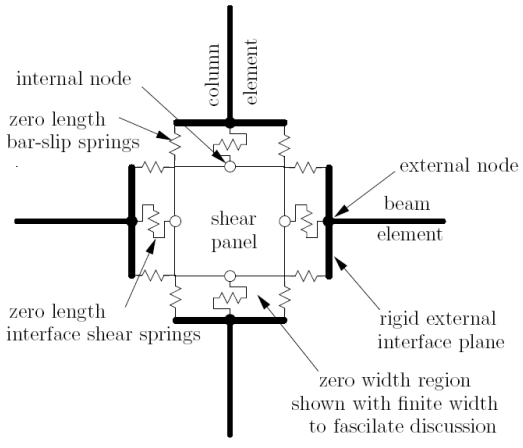 (b) Lowes-Altoontash joint model (2003)	This joint model comprises of eight zero-length bar-slip springs, four interface shear springs and a panel that deforms only in shear. The shear panel component simulates strength and stiffness loss due to shear failure of the joint core, bar-slip springs simulate stiffness and strength loss due to anchorage zone damage, and interface-shear springs simulate reduced capacity of shear transfer at the joint perimeter due to crack opening. The deformation of a component is based on the displacement at the four internal DOFs in the shear panel, along with the combination of displacements at 12 exterior DOFs.

Table 2.3 Typical explicit macroscopic models (continued)

The schematic diagram of joint models	Brief Description
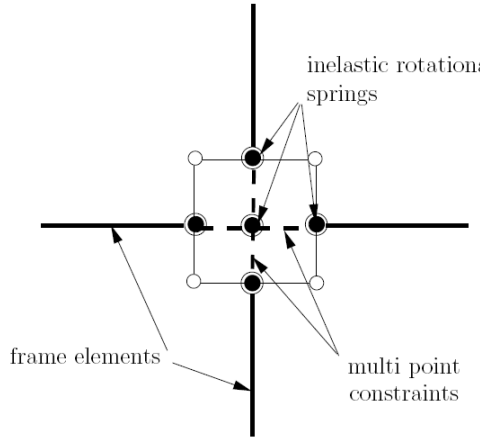 (c) Altoontash-Deierlein joint model (2003)	The joint load-deformation response is determined by a shear panel and a set of rotational springs that connect the shear panel to the frame elements. The shear panel is assumed to deform only in shear and is represented by an internal central node with *four* DOFs. The three DOFs correspond to rigid body motions and the fourth DOF is used to define the shear distortion of the joint. The rotational springs at the external nodes of shear panel represent the bar-slip behavior between the reinforcing steel and concrete with the material inelasticity in the plastic hinge region.
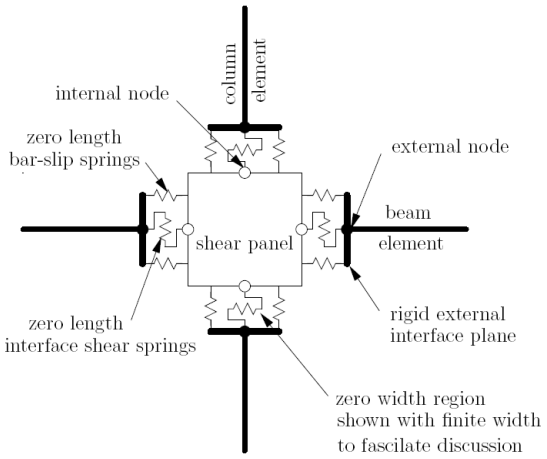 (d) Mitra-Lowes joint model (2007)	This joint model is the modification of Lowes-Altoontash model. Based on Lowes-Altoontash model, a new element formulation was proposed to improve simulation of joint response mechanisms in this model. It assumes that the joint shear is transferred through a confined concrete strut and simulates strength loss due to load history and joint damage following yielding of beam longitudinal steel. Finally, modifications are made to enable better simulation of anchorage zone response. This model has been developed as a joint element in OpenSees (Mazonni et al. 2006).
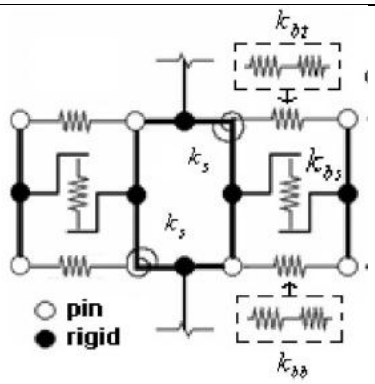 (e) Bao et al. joint model (2008)	This joint model is conceptually similar to Lowes-Altoonash joint model. At each joint interface, there are two bar force-slip springs (k_{bt} & k_{bb}) and one interface shear spring (k_s); at the joint core, there are two rotational springs to represent shear panel behavior. The joint model, with each component calibrated by the approaches proposed by Lowes et al. (2003), is incorporated into frame analysis under column loss scenarios.

2.6 Summary

Although progressive collapse is a disaster at very low possibility, the detrimental effect and the consequences cannot be neglected, especially due to the increasing threat of terrorist attacks. Currently, some building codes have incorporated design guidelines to mitigate progressive collapse, including indirect and direct methods. However, member and joint behavior under alternate load paths (ALPs) is not well understood, in particular, the effects of pertinent parameters on beam and joint behavior following column removal and subsequent catenary action. Previous research works show that after the loss of one primary column, so-called two-span beams may experience flexural action, compressive arch action and catenary action. Nevertheless, there is a lack of systematic research on identifying the critical parameters that will affect the development of each ALP and on how to incorporate the beneficial effect due to the ALPs into design. Moreover, the beam-column joints could be vulnerable in the process of developing ALPs. For example, the development of catenary action depends on the robustness of beam-column joints (or connections). Thus the influence of different detailing on the joint behavior is worthy of investigation. To facilitate structural analysis under progressive collapse, accurate and robust joint models are needed.

Based on literature review, some conclusions can be arrived as follows:

(1) As design guidelines, both indirect method and ALP method should be verified by removing a column. UFC 4-023-03 has explicitly specified that the ALP method should rely on flexural resistance of structure members, i.e. conventional plastic-hinge mechanism. However, GSA 2003 and EN 1991-1-7 do not indicate whether the ALP is governed by flexural yield capacity or catenary action. Additionally, the tests on catenary action of RC beam column sub-assemblage are still very rare.

(2) A limited number of studies on RC frames or sub-assemblages under column loss scenarios show that with increasing deflections of beams whose both ends are axially restrained, compressive arch action (CAA) and catenary action can be sequentially mobilized on top of conventional plastic-hinge mechanisms

(named as flexural action). It should be noted that CAA and catenary action are associated with the development of axial compression and tension, respectively.

(3) The reviewed laboratory tests indicated that the development of catenary action resulted in failure concentrated at beam-column connections. The failure included severe concrete cracking, concrete crushing and bar fracture, which were ascribed to large beam-end rotations. Therefore, the beam-column joints, consisting of connections and joint panels, are quite vulnerable.

(4) By analogy with studies on beam-column joint modeling under seismic loading, the component-based joint model can be also used for structures under column loss scenarios, but new calibrations at component level are required.

To improve the understandings towards the development of ALPs of RC structures under column loss scenarios, an experimental program was launched in Nanyang Technological University, as described in Chapter 3.

CHAPTER 3 EXPERIMENTAL PROGRAM ON REINFORCED CONCRETE SUB-ASSEMBLAGES AND FRAMES UNDER A COLUMN REMOVAL SCENARIO

3.1 Introduction

The alternate load path (ALP) method is used to evaluate progressive collapse resistance by removing one or several major structural bearing elements and analyzing the remaining structures to determine if this initiating damage propagates from elements to elements.

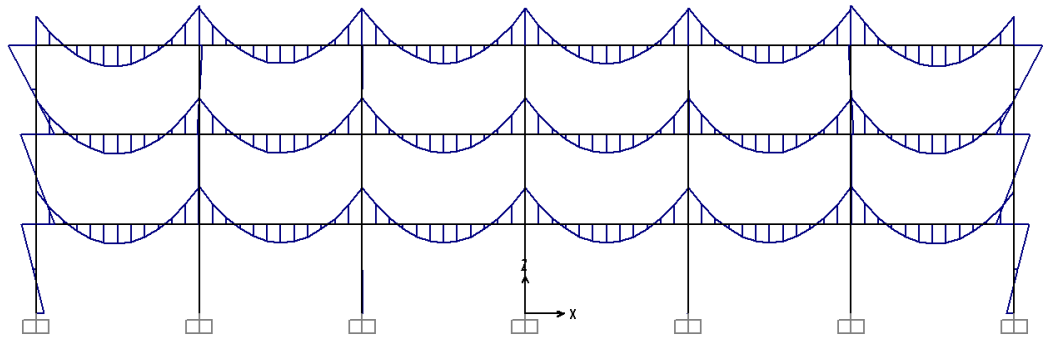

(a) Before the removal of a middle column

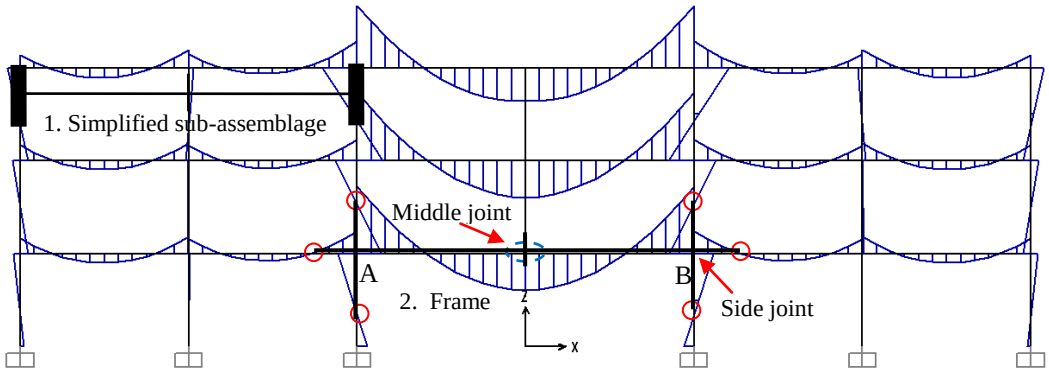

(b) After the removal a middle column

Fig. 3.1: Bending moment diagram of a frame

Fig. 3.1 shows a change of the bending moment diagram of a typical frame due to the removal of a middle column with linear elastic analysis. After the removal of the middle column, the bending moment near the middle joint at the center of AB changes direction, and the bending moments at side joint A and B increase

significantly. All these changes may not be considered in conventional design. Prior to any possible collapse, however, the frame will endeavor to balance the amplified gravity loads via different ALPs. The amplified gravity loads result from doubling of span (associated with the loss of a middle column) and dynamic effect (associated with the *sudden* loss of a supporting force). Each ALP corresponds to a structural mechanism. To demonstrate the structural mechanisms of the two-bay beam AB, a beam-column sub-assemblage was extracted at the locations of the contra-flexural points of bending moments. Then the sub-assemblage specimens were quasi-statically tested in the Protective Engineering Laboratory of Nanyang Technological University. However, in accordance with UFC 4-023-03 (DoD 2010), static resistance of structures against progressive collapse can be converted to dynamic resistance with a dynamic increase factor, which depends on the rotation ductility of RC members. So far, only a few published papers refer to experiment work on progressive collapse resistance and structural behavior of RC structures subjected to a middle column removal scenario (Orton et al. 2009; Sasani and Kropelnicki 2008; Su et al. 2009; Yi et al. 2008). Therefore, the sub-assemblage tests in our test program can explore more detailed information on structural behavior of RC frames under a middle column removal scenario and serve as useful and valuable numerical benchmark tests for other researchers to validate their models.

In this experimental program, two series of RC specimens, namely, simplified RC beam-column sub-assemblages and RC beam-column frames, were designed and tested to failure. The former was designed with simplified boundary conditions so that the RC beams and the middle joints are the research focus, as shown in **Fig. 3.1(a)**. The latter was designed with more realistic boundary conditions so that the behavior of the whole frames and the side joints can be studied, as highlighted in **Fig. 3.1(b)** with side joints A and B.

3.2 Objectives of experimental program

The experimental program was conducted to study the structural behavior of *RC sub-assemblages and frames* as well as the behavior of *beam-column joints* (including middle joints and side joints) subjected to a middle column removal

scenario. The reversal of the bending moments at the middle joints places them in a very unfavorable situation. Moreover, with increasing deflection of two-bay beams, beam axial forces are mobilized, initially in compression and subsequently in tension. These factors are beyond the considerations of conventional design and may result in failure at the middle joints. However, it is not easy to apply such combined loads (i.e. bending moments and axial forces) on isolated joints because the beam axial forces vary in magnitude and direction throughout the whole loading history of RC beam-column sub-assemblages and frames. Therefore, the joint behavior was studied in the simplified sub-assemblage and frame tests.

The objectives for the structural behavior of sub-assemblages and frames comprise the following:

(1) To investigate the development of different structural mechanisms (i.e. flexural action, compressive arch action, and catenary action) of RC sub-assemblages subjected to a middle column removal scenario;
(2) To study the effects of seismic detailing, the bottom and top reinforcement ratios at joint regions and the beam span-to-depth ratio on structural behavior of RC sub-assemblages;
(3) To investigate the effects of boundary conditions on the structural behavior of RC frames under a middle column removal scenario;
(4) To investigate whether several proposed detailing techniques can help improve the structural resistance of RC frames against progressive collapse.

The objectives for the joint behavior are as follows:

(1) To investigate the behavior of the middle and side joints of RC sub-assemblages;
(2) To provide experimental results for validating a proposed component-based joint model.

3.3 Design of specimens

The specimens are on-half scaled due to the limitations of lab facilities. The prototype of test specimens is assumed to be located at the middle of a multi-bay

perimeter frame, as shown in **Fig. 3.2**. For a public building, perimeter frames are most vulnerable due to ease of accessibility. The perimeter frame is located in a 5-story commercial building, of which the ground story is 4.0 m high and a typical story is 3.3 m high. The spans at two orthogonal directions are 6 m. The live load is 4.8 kN/m^2, and the total dead load including self-weight is 7.1 kN/m^2. A uniform dead load of 2.0 kN/m is used for non-structural exterior components acting on the perimeter frames. As a result, the unfactored dead load and live load on the perimeter frames are 23.3 kN/m and 14.4 kN/m, respectively. For seimic consideration, it is assumed that the builing is located in Site D, short period and one-second period spectral response acceleration parameters are 0.5 and 0.2, respecitvely, and the occupancy important factor is equal to 1.0. Accroding to ASCE 7-05, the seismic design category is taken as D and the buiding is designed as a special moment-resisting frame with a base shear coefficient of 0.034 in two orthogonal directions.

The building is designed to minimize the differences of longitudinal reinforcement of frames based on sesimic and non-seismic design, repectively. Non-seismic design is mainly based on gravity loads, but *seismic design* takes lateral seismic force as the main action on top of gravity loads. Typically, seismic design will require enlarged sections of structural members and increased longitudinal reinforcement ratios to resist lateral shear forces. Therefore, for the same dead loads and live loads, builidngs with greater structural capaicties based on seismic design will definitely have higher resistances to mitigate progressive collpase compared with gravity-design. In this test program, the interest is in whether *seismic detailing* rather than *seismic design* can increase structural resistance against potential progressive collapse. *Seismic detailing* is defined as the special detailing to specify the arrangement of stirrups in beams and columns and hoops in joints as well as the requirement of lap-splice of bars, to increse structural integrity and rotation capacity.

In **Fig. 3.2(b)**, the directly-affected part (enveloped by red dash lines) is just located above the removed column and the adjacent frames (enveloped by green dash lines) are indirectly-affected due to subsequent load redistribution. Assuming the two columns adjacent to the removed column do not fail and the remaining building

have sufficient lateral restraint stiffness, the shaded part in **Fig. 3.2(b)** becomes the most critical element in the whole building due to the combined effects of doubling of span and amplified gravity loads.

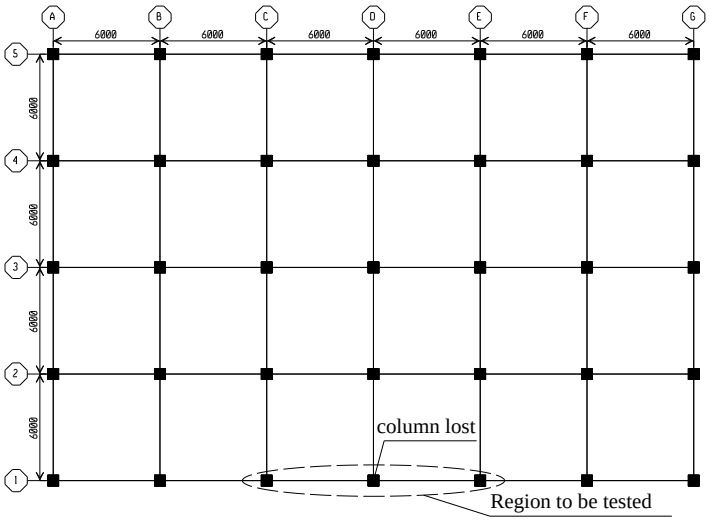

(a) Plan view of the prototype building (unit: mm)

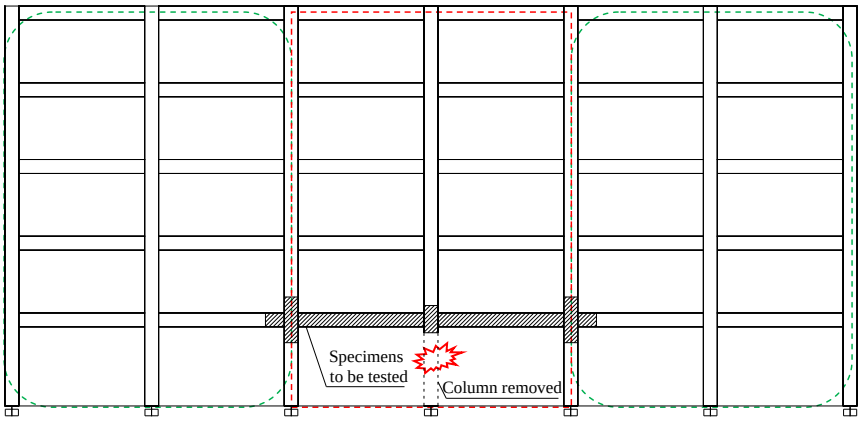

(b) Front view of the prototype building

Fig. 3.2: Location of the prototype of test specimens

3.3.1 Specimens of RC beam-column sub-assemblages

Based on foregoing loads, prototype frames were designed in accordance with ACI 318-05 (American Concrete Institute 2005), with seismic and non-seismic detailing, respectively. One-half scale model of the prototypes was constructed for specimens. The geometric dimensions of the prototypes and the specimens are listed in **Table 3.1**. However, to simplify the boundary conditions and focus on the structural mechanisms of the beams and the middle joint, the beam and column extensions at

two ends of the two-bay beam (in **Fig. 3.2**) were replaced by two enlarged column stubs (in **Fig. 3.3**), which were 400 mm wide by 450 mm deep. This design could provide sufficient anchorage for the longitudinal reinforcement in the affected beams. Since the specimens were scaled down, concrete chippings with the maximum aggregate size less than 10 mm were used. To maintain good bond and anchorage, deformed longitudinal reinforcing bars were used. Due to symmetry, the detailing of one-half of both specimens S1 and S2 is shown in **Figs. 3.3(a)** and **(b)**, respectively.

Table 3.1 Geometric properties of prototypes and specimens

Prototype &Specimen	Beam net span (mm)	Beam size (mm)		Middle column size		Reinforcement ratio at the middle joint*		Detailing
		Depth	Width	Depth	Width	Top	Bottom	
Prototype 1	5500	500	300	500	500	0.85% (2T20+1T25)	0.48% (2T20)	Seismic
Specimen S1	2750	250	150	250	250	0.90% (1T13+2T10)	0.49% (2T10)	Seismic
Prototype 2	5500	500	300	500	500	0.71% (3T20)	0.48% (2T20)	Non-seismic
Specimen S2	2750	250	150	250	250	0.73% (3T10)	0.49% (2T10)	Non-seismic

*Concrete covers of prototypes and specimens were 40 mm and 20 mm, respectively; reinforcement ratio is calculated by $\rho = A_s / bd$, where b and d are the width and the effective depth of beam sections.

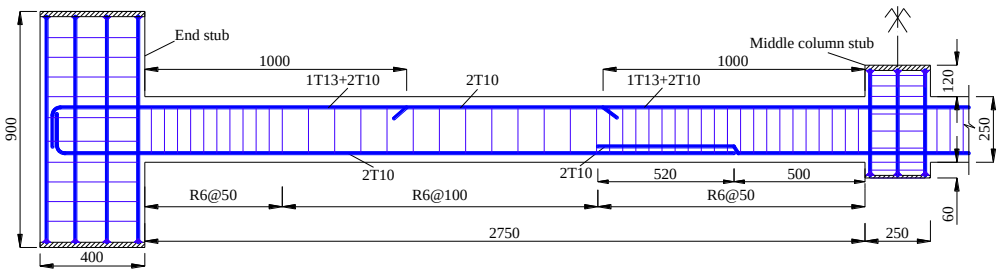

(a) Seismic specimen S1

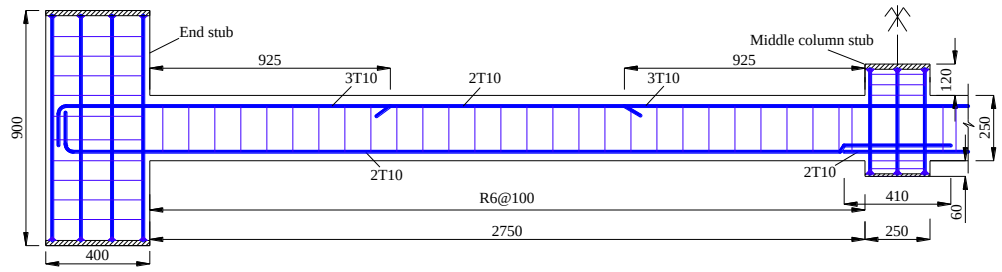

(b) Non-Seismic specimen S2

Fig. 3.3: Detailing of simplified sub-assemblages S1 and S2

The top reinforcement ratio at the middle joint and at the beam ends was 0.90% (1T13+2T10) and 0.73% (3T10) for specimens S1 and S2, respectively. The bottom reinforcement ratio for both specimens was 0.49% (2T10). Note that "T" represents high-yield strength deformed reinforcement with a nominal yield strength of 460 MPa. One of the top rebars was curtailed at specified positions for two specimens, as shown in **Fig. 3.3**. The bottom reinforcment was lap-spliced to invetigate whether the lap-splice would affect the development of catenary action. According to ACI 318-05, the tension splice of S1 was Class B splice (i.e. splice length equals to 1.3 times the development length l_d of reinforcement) and that of S2 was Class A splice (i.e. splice length equals to l_d). All stirrups were designed as two-legged R6 hoops with a 135^o hook. "R" represents low-yield strength round reinforcement with a nominal yield strength of 250 MPa. For S1, the stirrups were distributed at 50 mm on centers in the plastic hinge regions (2 times the beam depth from a joint interface) and in the lap-spliced regions, and at 100 mm in the other regions, as shown in **Fig. 3.3(a)**. The stirrups inside the middle joint of S1 consisted of three-legged R6 with a center-to-center spacing of 40 mm.

To obtain general structural behavior of RC sub-assemblages and the effects of key parameters on them under a middle column removal scenario, six more specimens (denoted S3 to S8) were designed and tested. **Fig. 3.4** and **Table 3.2** show the detailing of S3 to S8 of which the geometric dimensions remained the same as S1 and S2. After a middle column is removed, due to a reversal of the bending moment near the middle joint under gravity loads, the top and bottom reinforcement ratios at the middle joint interfaces become critical parameters. Previous research (Su et al. 2009; Yu and Tan 2012a) indicated that the beam span-to-depth ratio is a critical parameter that significantly affects compressive arch action of RC sub-assemblages. As a result, S3, S4 and S5 were used to investigate the effect of the bottom reinforcement ratio at the middle joint interfaces, with a respective ratio of 0.49%, 0.82% and 1.24%. S4 and S6 were used to investigate the effect of the top reinforcement ratio, whereas S4, S7 and S8 were used to study the effect of beam span-to-depth ratio.

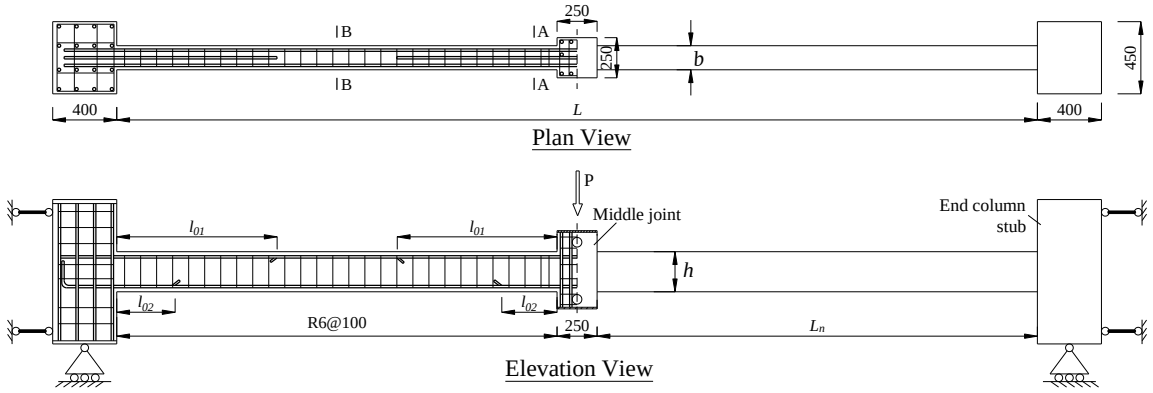

Fig. 3.4: Typical detailing of simplified sub-assemblages S3 to S8

Table 3.2 The geometric properties of sub-assemblage specimens*

Test	L_n	L/h	Position of rebar curtailment (mm)		Longitudinal reinforcement†				Bottom rebars at middle joints‡
					A-A section		B-B section		
			l_{01}	l_{02}	Top	Bottom	Top	Bottom	
S1-0.90/0.49/23S	2750	23	1000	N/A	1T13+ 2T10 (0.90%)	2T10 (0.49%)	2T10 (0.49%)	2T10 (0.49%)	continuous
S2-0.73/0.49/23	2750	23	925	N/A	3T10 (0.73%)	2T10 (0.49%)	2T10 (0.49%)	2T10 (0.49%)	lap-spliced
S3-1.24/0.49/23	2750	23	1000	345	3T13 (1.24%)	2T10 (0.49%)	2T13 (0.82%)	2T10+ 1T13 (0.90%)	lap-spliced
S4-1.24/0.82/23	2750	23	1000	N/A	3T13 (1.24%)	2T13 (0.82%)	2T13 (0.82%)	2T13 (0.82%)	continuous
S5-1.24/1.24/23	2750	23	1000	N/A	3T13 (1.24%)	3T13 (1.24%)	2T13 (0.82%)	3T13 (1.24%)	continuous
S6-1.87/0.82/23	2750	23	1000	345	3T16 (1.87%)	2T13 (0.82%)	2T16 (1.25%)	2T13 (0.82%)	lap-spliced
S7-1.24/0.82/18.2	2150	18.2	780	N/A	3T13 (1.24%)	2T13 (0.82%)	2T13 (0.82%)	2T13 (0.82%)	continuous
S8-1.24/0.82/13.4	1550	13.4	560	N/A	3T13 (1.24%)	2T13 (0.82%)	2T13 (0.82%)	2T13 (0.82%)	continuous

*: The beam sections are 150 mm wide and 250 mm deep for all specimens, i.e., b = 150 mm and h = 250 mm; the concrete cover thickness was 20 mm for all specimens;

†: The value in brackets is reinforcement ratio, calculated by A_s / bd, where b=150 mm and d=215 mm; A- A and B-B sections are referred to **Fig. 3.4**.

‡: The lap splice lengths for bottom bars of specimen S3 and S6 are 410 mm and 530 mm, respectively. The lap-spliced position is through the middle joint.

In the notations of sub-assemblages listed in **Table 3.2**, the first numeral after the dash stands for the percentage of top reinforcement in the middle joint regions and the beam ends, the second numeral indicates the percentage of bottom

reinforcement in the middle joint regions and the beam ends, and the third numeral denotes the beam span-to-depth ratio. The alphabet "S" at the end of a notation indicates seismic detailing. For example, S1-0.73/0.49/23S indicates specimen S1 designed with seismic detailing, a top reinforcement ratio of 0.73% and a bottom reinforcement ratio of 0.49% at the joint regions and the beam ends, and a beam span-to-depth ratio of 23. S7-1.24/0.82/18.2 shows that specimen S7 had non-seismic detailing, a top reinforcement ratio of 1.24%, a bottom reinforcement ratio of 0.82% at both the joint regions and the beam ends, and a beam span-to-depth ratio of 18.2.

To represent the structural behavior of typical RC beams, the curtailments of top and bottom reinforcement were considered as well. The tests on specimens S1 and S2 (Yu and Tan 2011a) indicated that the arrangement of beam stirrups (according to seismic or non-seismic detailing) did not affect the structural behavior of RC sub-assemblages under a middle column removal scenario. Therefore, the beam stirrups for specimens S3 to S8 remained constant (R6@100 mm) in accordance with non-seismic detailing, as shown in **Fig. 3.4**.

The tests on S1 and S2 also showed that the lap-splice of bottom reinforcement at the middle joint, with Class A splice according to ACI 318-05, satisfied the requirements on continuity of longitudinal reinforcement, and the lap-splice did not affect the overall behavior except the local failures, such as cracks, pullout and fracture of reinforcing bars near the middle joint interfaces. These local failures could be used to study the effect of detailing on load transfer mechanisms within joints. Therefore, in specimens S3 and S6, lap-splice was employed.

3.3.2 Specimens of RC beam-column frames

In this batch of specimens, two side columns each with a beam extension were used to replace the end column stubs in the 1st series of sub-assemblages. The geometric dimensions of the beams and the columns were kept the same as the sub-assemblages. Therefore, the geometric shapes of the frame specimens are similar to the 2-D frames highlighted in **Fig. 3.1(b)**.

In the tests of beam-column sub-assemblages, three primary parameters, viz. bottom reinforcement ratio (BRR), top reinforcement ratio (TRR) in the joint regions, and beam span-to-depth ratio (L/h), have been investigated. Therefore, in the tests on RC frames, these three parameters remained constant, and the research focus was on the detailing and the boundary conditions of the frame specimens, as shown in **Table 3.3**. The bottom and the top reinforcement ratios at the middle and side joints were 0.82% and 1.24%, respectively, the same as those of S4-1.24/0.82/24. The beam span-to-depth ratios of F1 to F7 were 24, the same as that of S4 as well.

In the notation of frame specimens, "CD" stands for conventional design and "SD" for special design. "NS" and "WS" represent non-seismic and seismic detailing, respectively. "EX" indicates exterior joints in specimens without beam extensions, such as specimens F3 and F4. For the specimens with special detailing, "MR" means middle reinforcement layer used throughout a specimen, "PD" indicates partially debonded bottom reinforcing bars in the joint regions, and "PH" represents partial hinges set at a distance away from the joint interfaces.

Table 3.3 Test plan for RC frame specimens

Parameters	Conventional Design				Special Design		
	F1-CD-NS	F2-CD-WS	F3-CD-NS-EX	F4-CD-WS-EX	F5-SD-MR	F6-SD-PD	F7-SD-PH
BRR	0.82% (2T13)	0.82% (2T13)	0.82% (2T13)	0.82% (2T13)	0.82% (2T13)	0.82% (2T13)	0.90% (1T13+2T10)
TRR	1.24% (3T13)	1.24% (3T13)	1.24% (3T13)	1.24% (3T13)	1.24% (3T13)	1.24% (3T13)	1.24% (3T13)
Detailing	Non-Seismic	seismic	Non-seismic	seismic	Non-seismic, **(1)**	Non-seismic, **(2)**	Non-seismic, **(3)**
L/h	24	24	24	24	24	24	24
Beam Extension	Y	Y	**N**	**N**	Y	Y	Y
Stirrups in beams	2R6@100	2R6@50+ 2R6@100	2R6@100	2R6@50+ 2R6@100	2R6@100	2R6@100	2R6@100

(1) Two additional reinforcing bars are placed at the mid-depth of a section;

(2) Sleeves were used to cover bottom bars at joint region to eliminate the bond between bars and concrete; therefore, bottom reinforcing bars become partially debonded.

(3) Top and bottom bars were bent to form a partial pin connection at beam ends and near joints.

The detailing of the frame specimens is shown in **Figs. 3.5(a)** to **(g)**. F1 and F3 were designed with conventional non-seismic detailing, and F2 and F4 with conventional seismic detailing. Accordingly, the arrangement of stirrups of F2 and F4 differed from that of F1 and F3. F1 and F2 included beam extensions at both ends of a two-bay beam, but F3 and F4 did not have any beam extensions. To mobilize catenary action, large deflections of RC beams have to occur. However, the rotation capacity of RC beams is limited, so special detailing was used, endeavoring to *improve the beam end rotation capacity*. For specimen F5, after severe cracks and bottom reinforcing bar fracture near both middle joint interfaces, the effective beam depth was significantly reduced. Thus, F5 with a shallow effective beam depth and an additional layer of reinforcement at the mid-sections was able to rotate easily, achieving a higher tensile force. The tests on sub-assemblages indicated that severe strain concentration occurred near the middle joint interfaces, resulting in premature fracture of bottom bars without fully utilizing the steel material strength. Therefore, debonding technique was used, attempting to diffuse strain concentration in the steel reinforcement. For specimen F6, plastic sleeves were introduced to weaken the bond of bottom reinforcing bars at the joint region. For specimen F7, a "pin detail" was designed near each end of the single-bay beam at 250 mm away from the joint interfaces, akin to the seismic concept of "strong columns and weak beams". The pins would facilitate the beam end rotation, so that catenary action could be more easily mobilized without premature fracture of longitudinal bars.

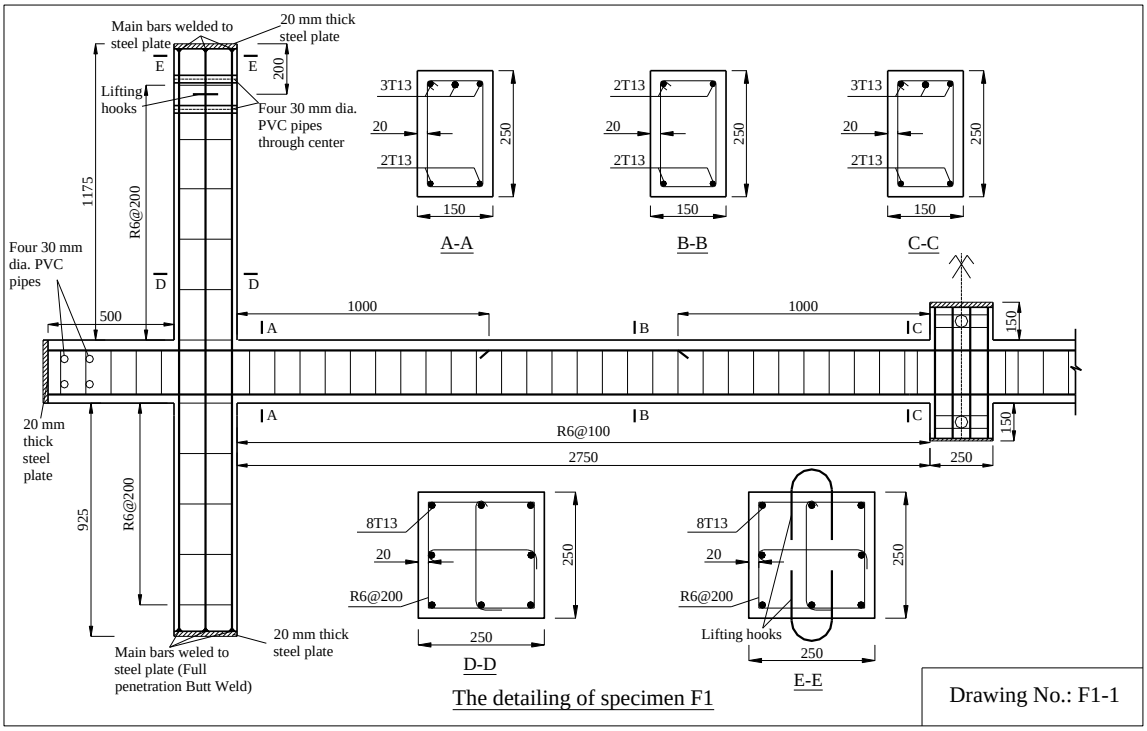

(a) Specimen F1

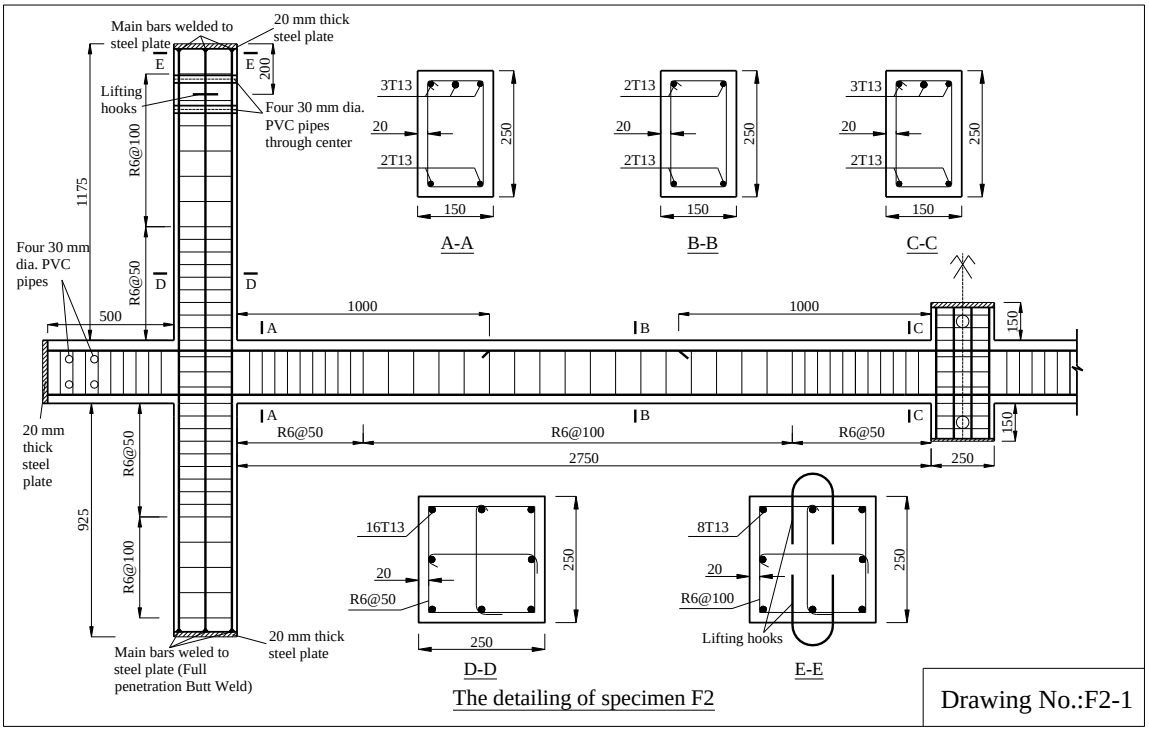

(b) Specimen F2

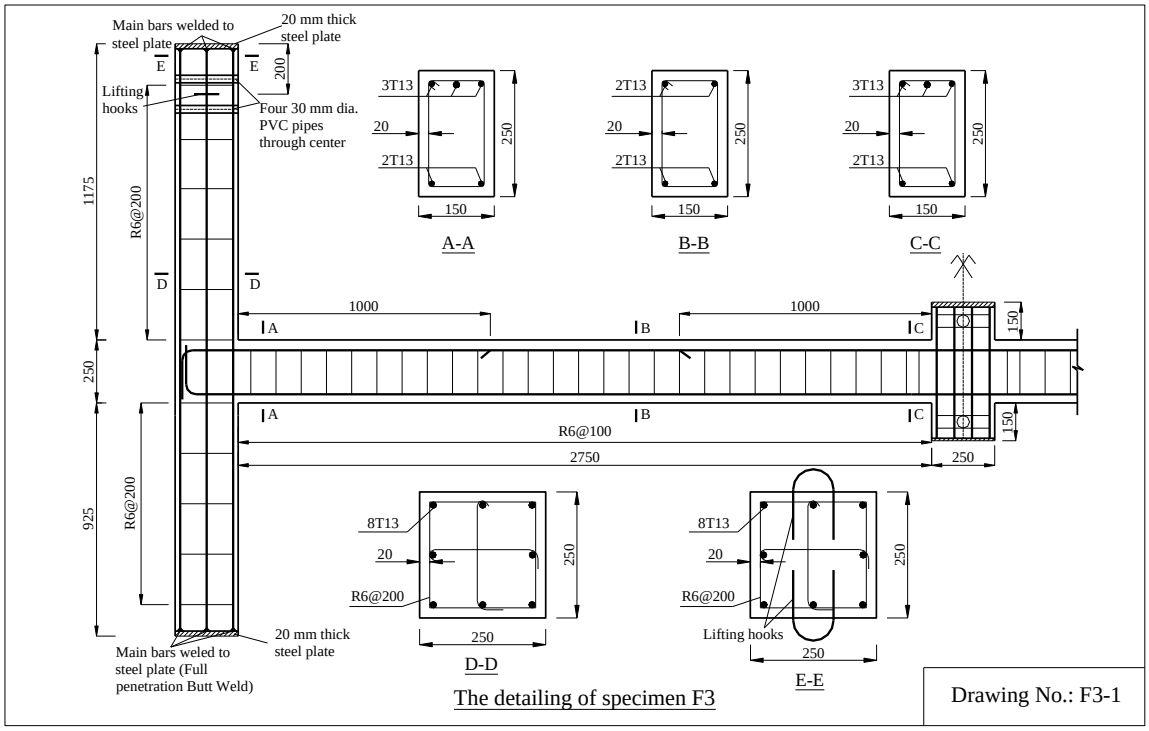

(c) Specimen F3

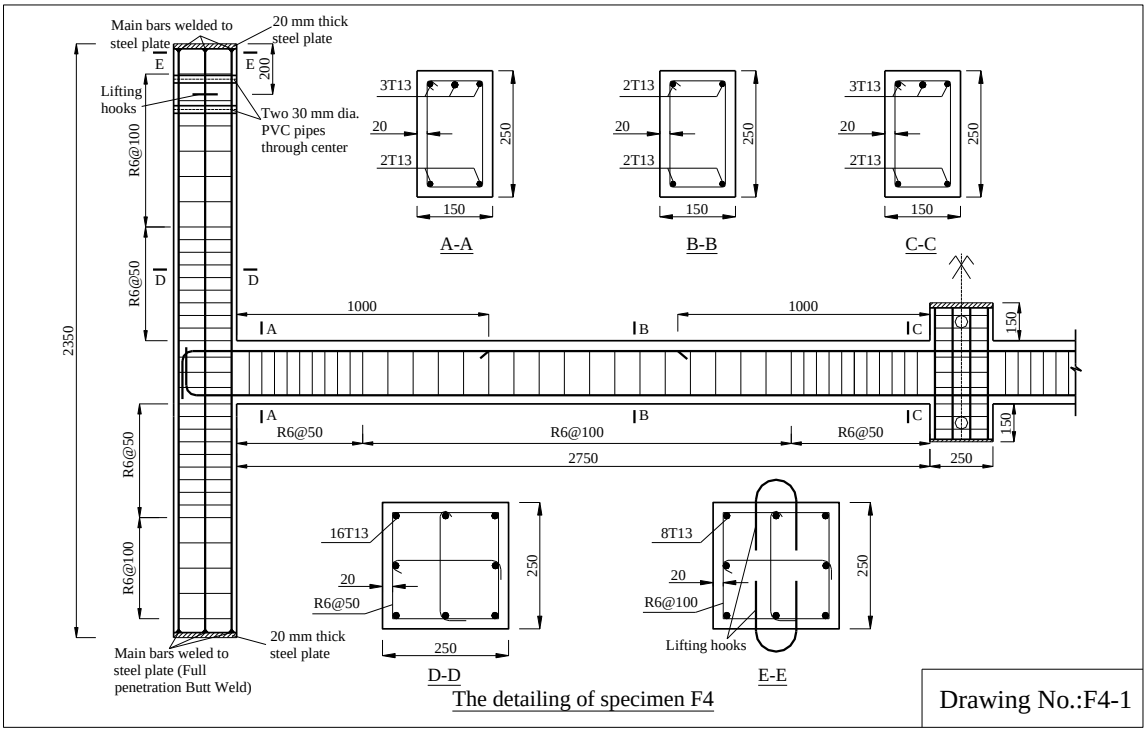

(d) Specimen F4

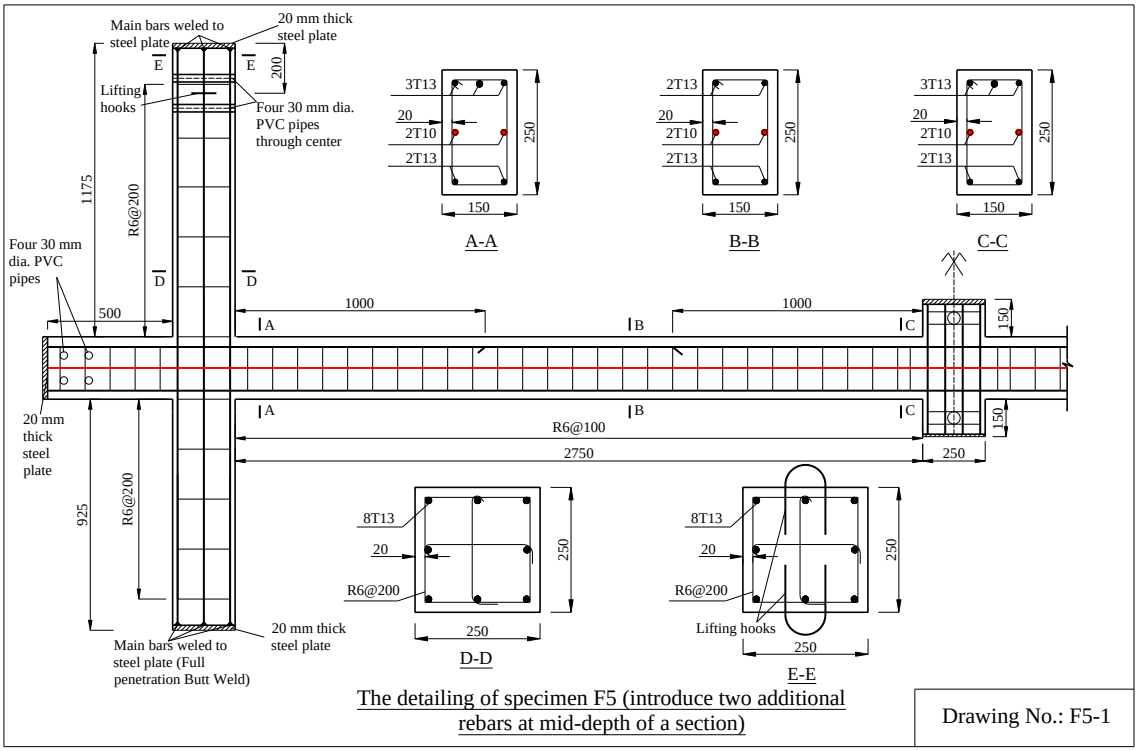

(e) Specimen F5

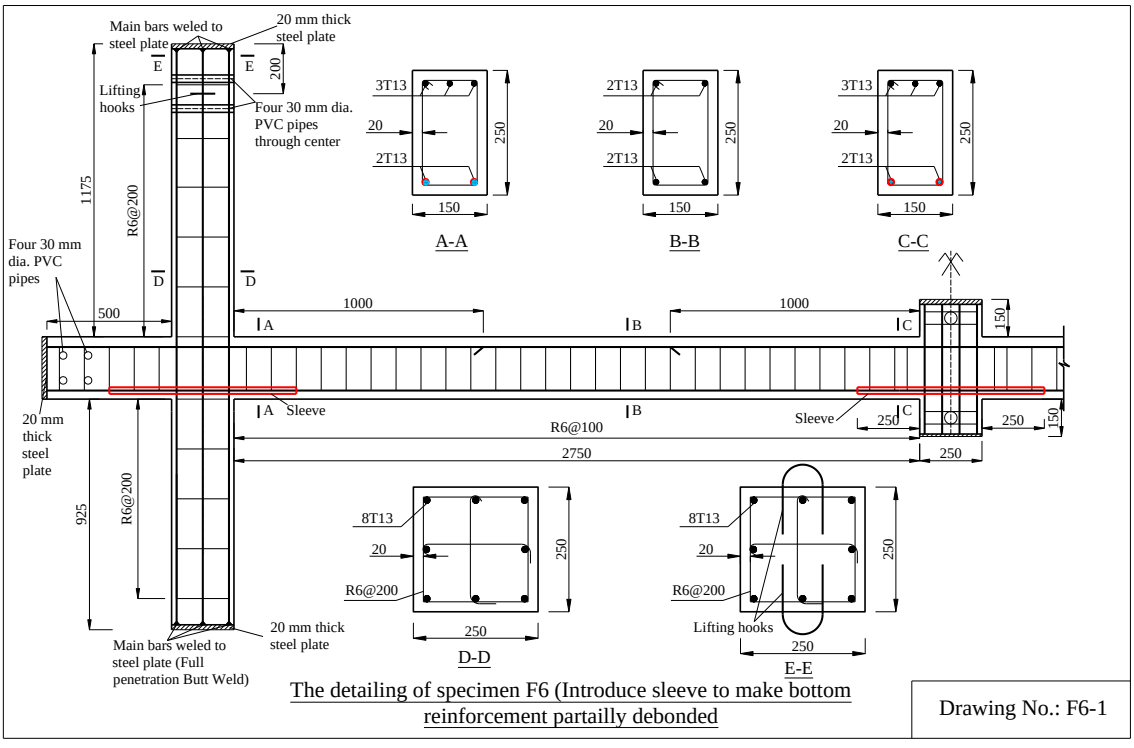

(f) Specimen F6

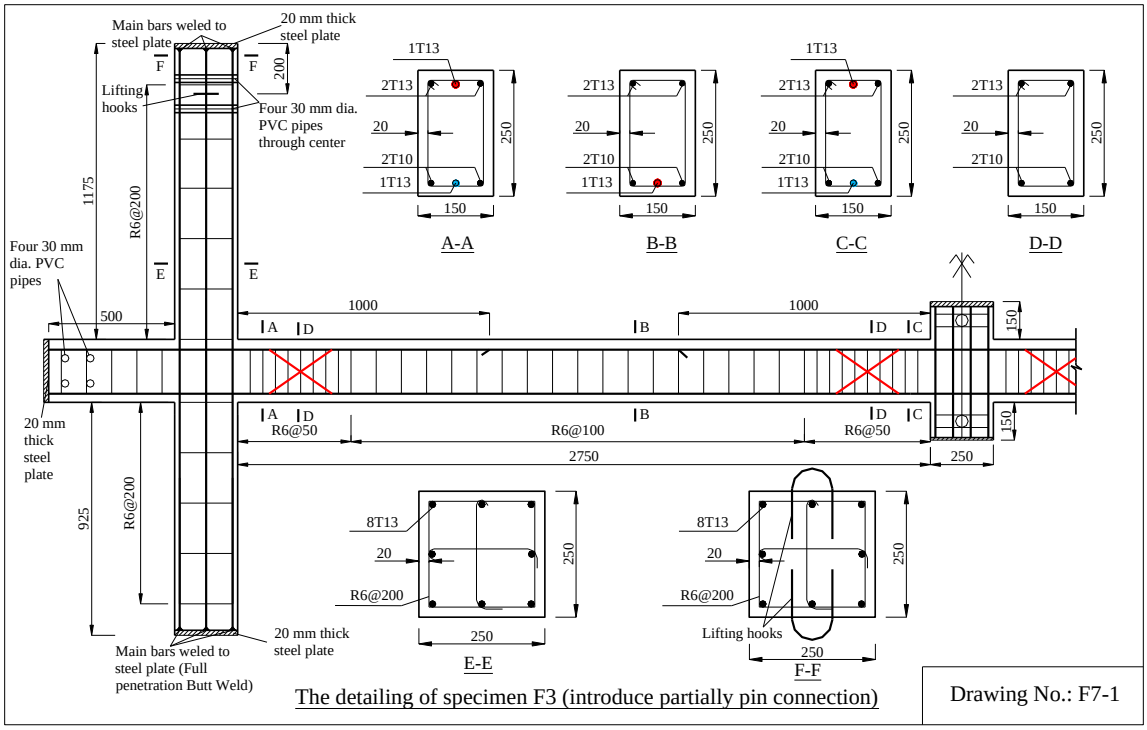

(g) Specimen F7

Fig. 3.5: Detailing of frame specimens

3.4 Design of test set-up

A statically-determinate test set-up was initially designed for sub-assemblage specimens S1 and S2. Thereafter, the test set-up was updated by adding a rotational restraint at the middle joint position. The improved test set-up was used for sub-assemblage specimens S3 to S8. Finally, the sub-assemblage test set-up was further modified for frame tests.

3.4.1 Test set-up for sub-assemblage specimens S1 and S2

Fig. 3.6 shows the test set-up for specimens S1 and S2. To simulate the axial restraints of indirectly-affected frames to a directly-affected frame, the ends of specimens were respectively connected to a steel A-frame and a reaction wall through two horizontal pin connections. In the vertical direction, each end of the specimens was supported by a pin connection seated on three steel rollers, as shown in **Fig. 3.7(a)**. The steel rollers were used to eliminate the effect of horizontal forces on vertical support reaction forces. Therefore, the measurements of vertical and

horizontal reaction forces were independent of each other. Compression load cells were placed at the bottom of the vertical supports, as indicated in **Fig. 3.7(a)**. Two tension/compression load cells were installed in horizontal restraints towards the A-Frame side, as shown in **Fig. 3.7(b)**. Strain gages were mounted at horizontal restraints towards the reaction wall, as shown in **Fig. 3.7(c)**. The load was applied at the top of the middle joint through a hydraulic actuator with displacement control until the specimens completely failed. The actuator was reacted against a steel portal frame. The applied force was measured by a built-in load cell of the actuator. Since all the reaction forces and the applied load were measured, the test system was statically determinate. Because the specimens were quite slender, two lateral restraints were installed at both sides of the middle joint to prevent out-of-plane failure. Steel plates with a steel roller were mounted onto the specimens to minimize friction when they came into contact with the flanges of I-section columns of lateral restraints, as shown in **Fig. 3.7(d)**. The steel rollers could move down together with the specimens so that they could function during the whole loading history.

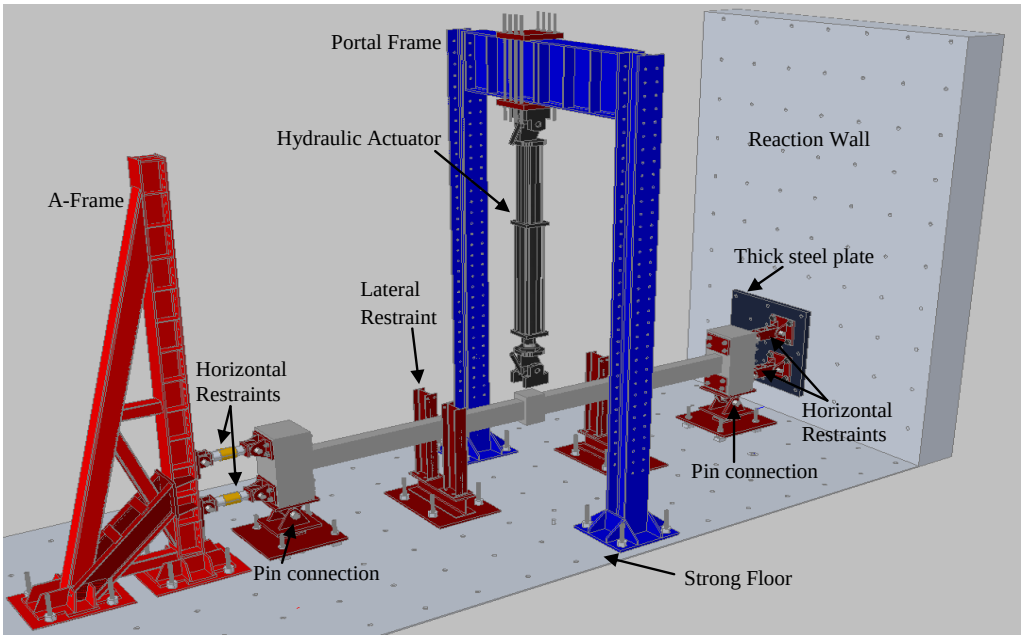

Fig. 3.6: Test set-up for specimens S1 and S2

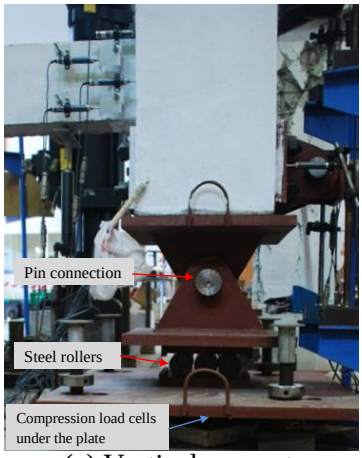

(a) Vertical support

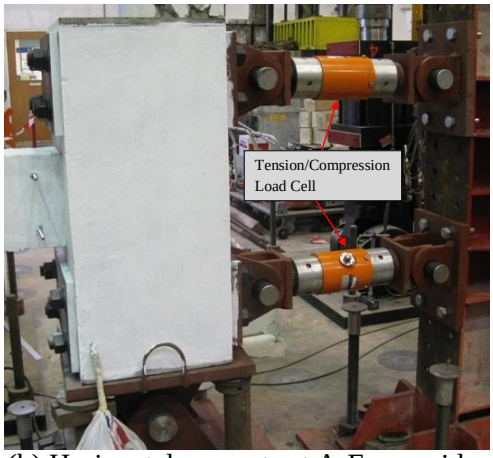

(b) Horizontal supports at A-Frame side

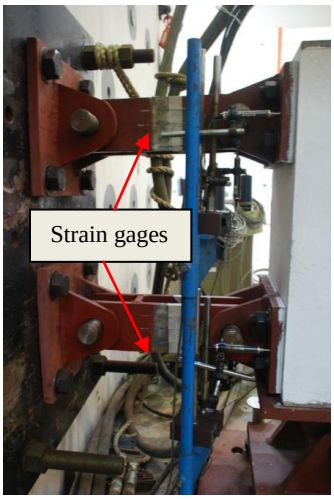

(c) Horizontal supports at RW side

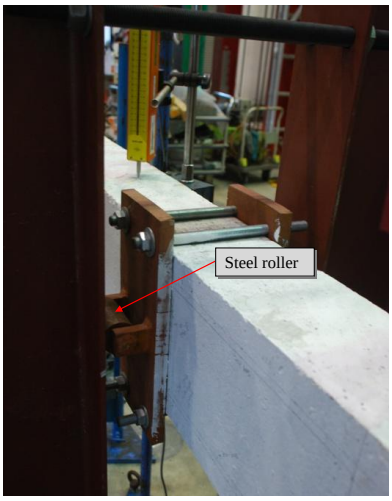

(d) The lateral restraint

Fig. 3.7: Details of test set-up for specimens S1 and S2

3.4.2 Test set-up for sub-assemblage specimens S3 to S8

Fig. 3.8 shows that the test set-up for sub-assemblage specimens S3 to S8. It is quite similar to the one for S1 and S2. However, the new test set-up was improved at these two parts: (1) adding a rotational restraint at the middle joint position; and (2) installing tension/compression load cells at horizontal pin-pin connections that connected one end column stub and a reaction wall to directly measure horizontal reaction forces. During the test, the load was imposed by the actuator with displacement control at a rate of 0.1 mm/sec until a specimen failed.

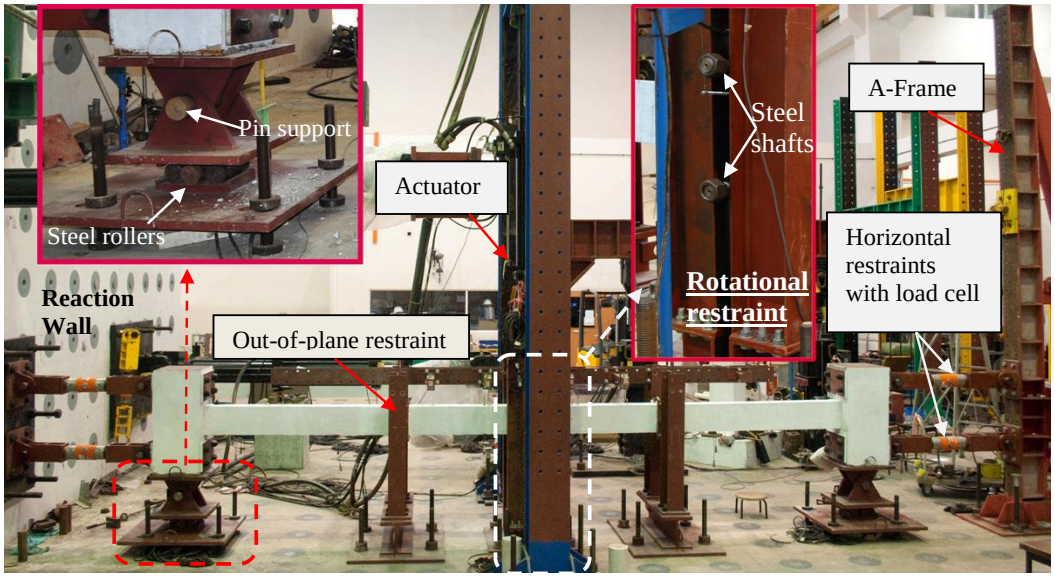

Fig. 3.8: Test set-up for specimens S3 and S8

The experimental results of S1 and S2 showed that once the cracks at one side of the middle joint was more developed than the other side due to non-uniformity of material and imperfection of cast geometry, cracks in the subsequent loading process would be concentrated at the weaker side. Due to the lack of a rotational restraint at the middle joint, inevitably, the joint tended to rotate towards the more severely cracked side. The test on a multi-story frame (Yi et al. 2008) showed that the rotation of the middle joint was restrained by the column connected to the upper story. Therefore, a rotational restraint at the middle joint was installed in the test rig. As highlighted in **Fig. 3.8**, two steel shafts, going through precast holes in the middle joint, were located in the gap of two steel columns. During the initial loading process, the two shafts could move freely along the gap without touching the flanges of the upright steel columns. However, when bottom reinforcing bars were fractured or pulled out at one side of the middle joint, the shafts would come into contact with the steel column flanges, giving rise to a force couple which acted against the rotation of the middle joint. After the bottom bars at both sides of the middle joint were fractured or yanked out, the force transfer at both joint interfaces were quite symmetrical, and the rotational restraint did not provide any force couple. Friction in vertical direction was generated when the shafts came into contact with column flanges. However, since lubricant was applied on the surfaces of the column

flanges and all the vertical reaction forces were measured directly by load cells, the influence of friction on the applied load could be eliminated.

3.4.3 Test set-up for frame specimens F1 to F7

Fig. 3.9 shows the test set-up for the frame specimens. The top ends of two columns were respectively anchored to a reaction wall and a steel A-frame via a horizontal pin-pin connection. The bottom ends of two columns were respectively supported by a pin connection seated above the ground. These boundaries indicate the restraints between adjacent stories. Specimens F1, F2, F5, F6 and F7 include beam extensions at both ends. The beam extensions represented the axial restraints from adjacent beams to the frame with a removed column. **Fig. 3.9(a)** shows that the beam extensions were respectively anchored into the reaction wall and the steel A-frame through a horizontal pin-pin connection as well. However, for specimens F3 and F4 without any beam extension, it was unnecessary to install the lower horizontal connections, as shown in **Fig. 3.9(b)**. A tension/compression load cell was installed in each pin-pin connection, so that the corresponding horizontal reaction forces could be measured. A load pin was installed in each bottom pin support, and the load pin could measure the horizontal forces that were transferred into the supports. A concentrated load was then applied at the top of a middle joint through a hydraulic actuator reacting against a steel portal frame. The load was imposed with displacement control at a rate of 0.1 mm/sec until a specimen failed. Two transverse frames were installed on both sides of the middle joint to prevent out-of-plane movement of the slender specimens. Moreover, a rotational restraint was installed at the middle joint position to prevent joint rotation due to asymmetric damage of concrete or fracture of reinforcing bars at either side of the middle joint.

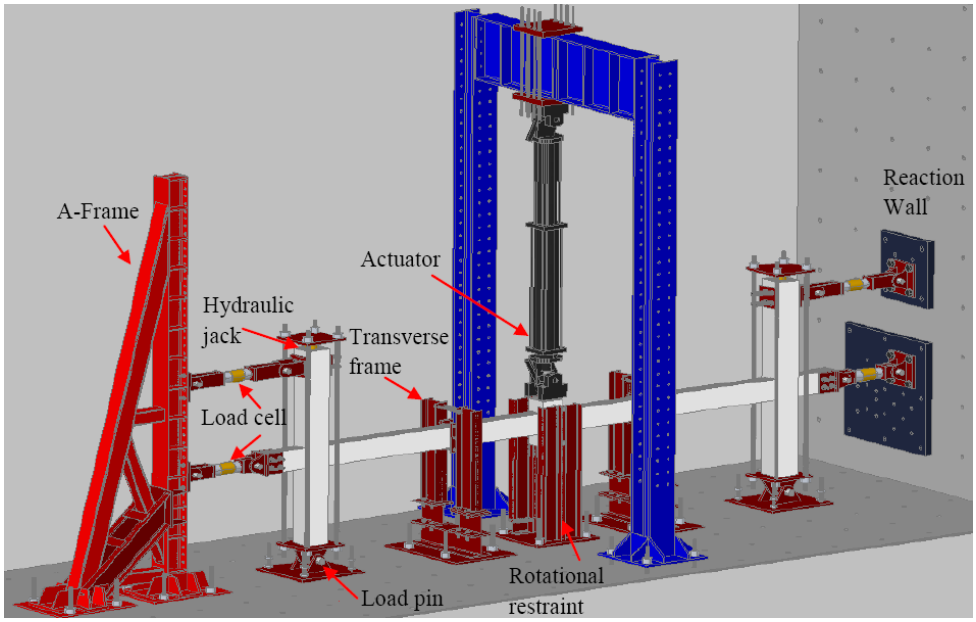

(a) For specimens F1, F2, F5, F6 and F7

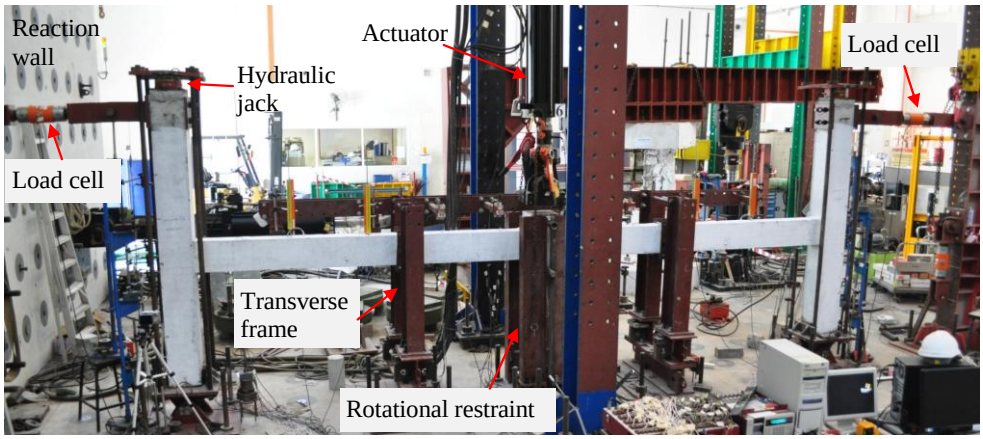

(b) For specimens F3 and F4

Fig. 3.9: Test set-up for RC frames

To consider the effect of column axial force on the behavior of frames and side joints, a hydraulic jack was installed at the top of each side column to apply a constant axial load along the side columns. For each test, the axial stress was $0.6f_c'$ and $0.4f_c'$ at the side columns towards the reaction wall and the A-frame, respectively. The axial load was achieved by using four high-strength steel rods that connected a top steel plate and the bottom pin support. When a hydraulic jack was pumped to apply a force, the top steel plate tended to move upwards but was pulled in by the four steel rods. As a result, the four steel rods were in tension to apply a

compression force on a side column. Since the hydraulic jack, the four rods, the top and bottom steel plates could form a self-equilibrium system, the applied load would not significantly affect the readings of load cells and load pins.

3.5 Instrumentation

Detailed instrumentation was planned to obtain the overall deflections of two-bay beams for all specimens, lateral drift profiles of columns for frame specimens, local deformations near the joint interfaces, deformations of side joint panels, boundary movements, and strains over longitudinal reinforcing bars.

3.5.1 Instrumentation system for RC sub-assemblages

Fig. 3.10 shows the instrumentation system for RC beam-column sub-assemblages. The instrumentation system comprised five parts: 1) six line displacement transducers and six linear variable differential transformers (LVDTs) to measure vertical displacements along the entire "two-bay" beam to determine the overall deflection curves (L_1 to L_{12} as shown in **Fig. 3.10**); 2) four LVDTs at each end of the specimens to measure the movements of end supports so as to ascertain the stiffness of axial and rotational restraints at specimen ends (L_{13} to L_{16} and L_{33} to L_{36} as shown in **Fig. 3.10**); 3) four LVDTs at specified regions to measure the rotations of local regions, for instances, the regions near the middle joint and the beam ends (L_{17} to L_{32} in **Fig. 3.10**); 4) Strain gages attached to reinforcing bars at specified sections to shed light on the variations of internal forces in the beams; 5) load cells to measure reaction forces to make the test set-up statically-determinate, as shown in **Fig. 3.7(b)** and **Fig. 3.8**. The measured forces and displacements of beams were used to calculate the cross-sectional internal forces (i.e. axial force, shear force and bending moment) throughout the beams according to the force equilibrium of the specimens at their deformed configurations.

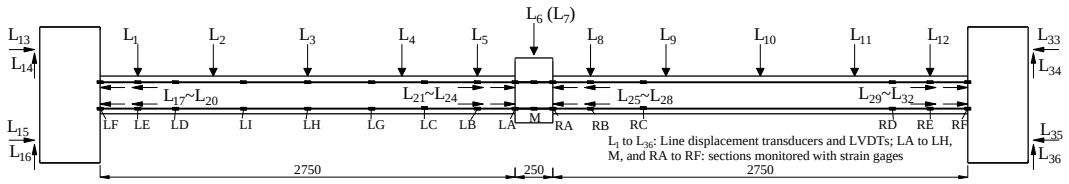

Fig. 3.10: Layout of instrumentation for sub-assemblage specimens

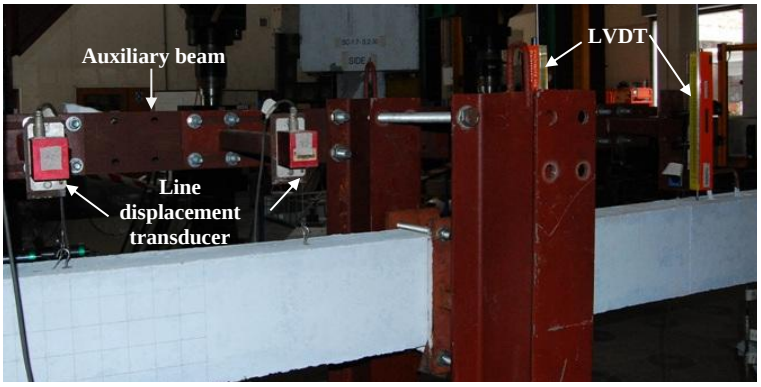

(a) Measurement on displacement along a beam

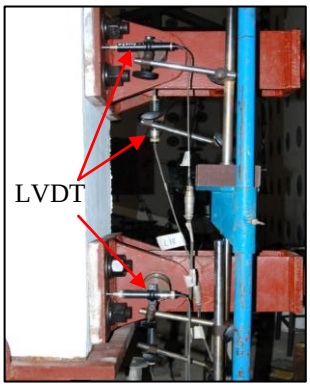

(b) Measurement of end movement

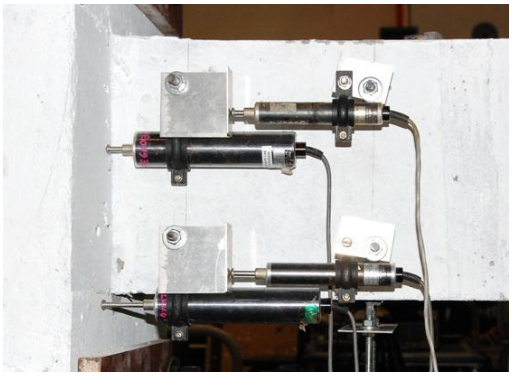

(c) Measurement on local rotations near the end column stub interfaces

(d) Measurement on local rotations near the middle joint interfaces

Fig. 3.11: The details of instrumentation for sub-assemblages

The instrumentation shown in **Fig. 3.11(a)** was used to measure the beam deflection curve at each load step. An auxiliary beam was designed to install line displacement transducers. Additionally, the movements at the specimen ends were measured to ascertain the stiffness of axial and rotational restraints, as shown in **Fig. 3.11(b)**. Finally, local rotations near the end column stub and middle joint interfaces were measured to determine the rotation capacity of RC beams, as shown in **Figs. 3.11(c)** and **(d)**, respectively.

3.5.2 Instrumentation system for RC frames

The instrumentation for the two-bay beams of RC frames was quite similar to the one for sub-assemblages, as shown in **Fig. 3.12**. In the notation of instrumentation, "R" denotes right side and "L" stands for left side. The instrumentation system for RC frames included: line displacement transducers (LDTs) and LVDTs were used to measure overall deflection curves of the two-bay beams (say, by R1 to R6), the movements at the ends of beam extensions (say, by R23 and R24) and the rotations of local regions (say, by R7 to R14), as shown in **Fig. 3.12(a)**; strain gages were attached to measure strains throughout reinforcing bars; load cells and load pins were employed to measure horizontal reaction forces; moreover, additional instrumentation for RC frames was to measure distortion of the side joint panels and column drift profiles, as highlighted in **Fig. 3.13**.

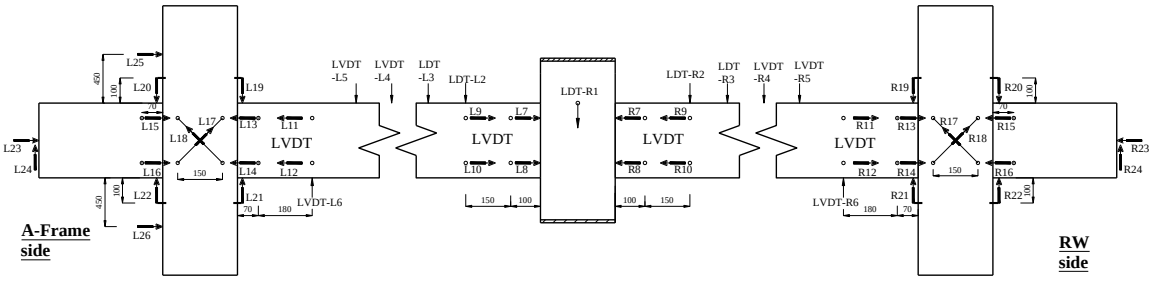

(a) For specimens F1, F2, F5, F6 and F7

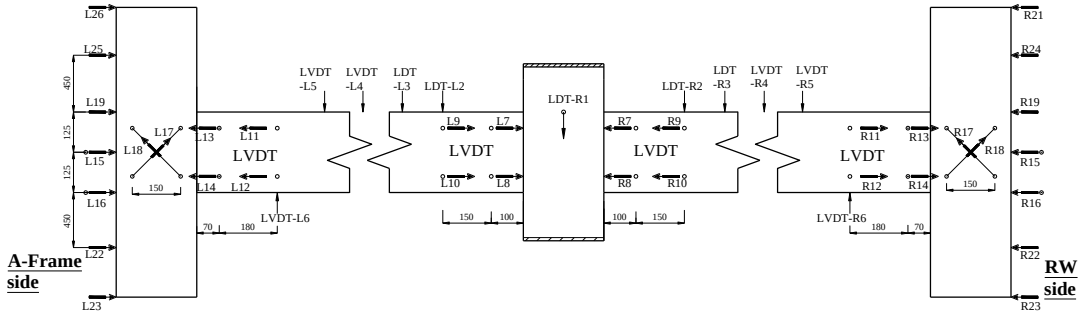

(b) For specimens F3 and F4

Fig. 3.12: Arrangement of instrumentation for RC frames

Fig. 3.13(a) shows that the lateral deflections of the side columns were measured by LVDTs, and the shear distortion of the joint panels were measured by two orthogonal potential meters. Because F3 and F4 did not include beam extensions and only the top and bottom ends of the side columns were restrained, the lateral deflections of the columns should be relatively larger. Consequently, more LVDTs

were installed to measure the lateral deflections of the columns, as shown in **Fig. 3.13(b)**.

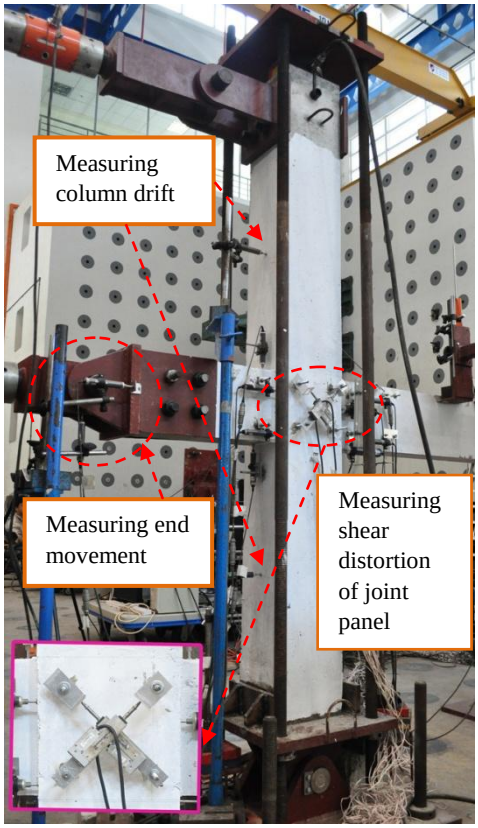

(a) For specimens F1,F2, F5 to F7

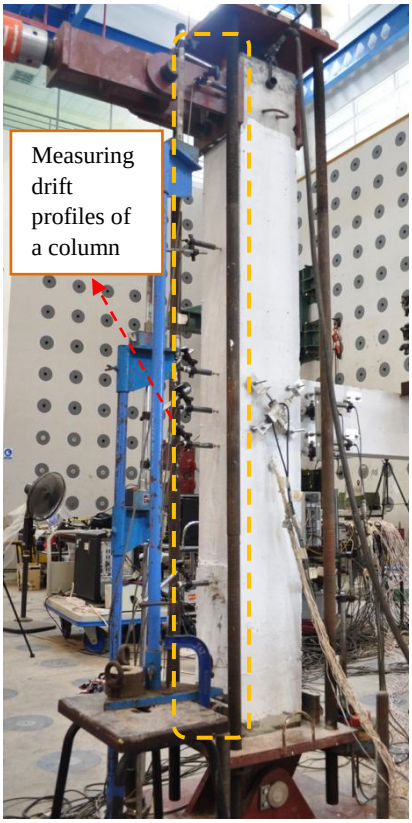

(b) for specimens F3 and F4

Fig. 3.13: Detailed instrumentation at side columns and joints

3.6 Material tests

During the stage of fabricating steel cages, several reinforcing bar samples were selected from the same batch of the bars used for sub-assemblage or frame specimens. During the casting of the specimens, concrete cylinders with 300 mm height and 150 mm diameter were cast on-site and later cured under the same condition as that for sub-assemblage or frame specimens. Reinforcing bar samples were used for tensile tests to determine the yield strength, elastic modulus, tensile strength and fracture strain of bars. Compressive cylinder and split-cylinder tests were conducted to determine the compressive and tensile strength of concrete, respectively. All the material tests were conducted in accordance with corresponding ASTM specifications. To obtain the entire compressive stress-strain curve of concrete during the compressive cylinder tests, three linear differential

variable transducers (LVDT) were installed along the circumference of the cylinders with 100 mm gage length, as shown in **Fig. 3.14**.

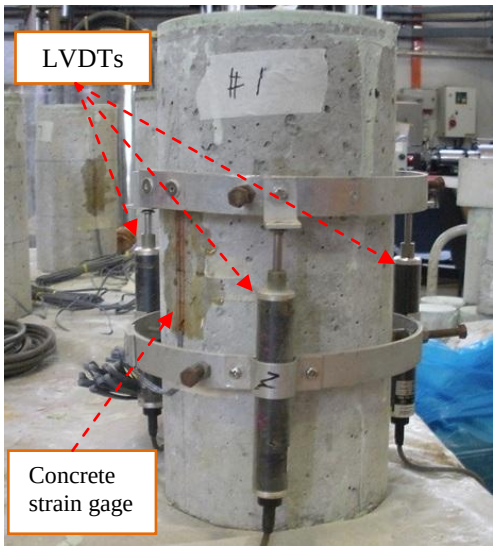

Fig. 3.14: Instrumentation in compressive concrete cylinder tests

3.7 Summary

In this chapter, the test program on reinforced concrete beam-column frames is presented. The designed specimens were categorized into two batches according to their boundary conditions. The boundaries of the first series of sub-assemblage specimens were simplified by using column stubs so that the research interest can be concentrated on the structural mechanisms of two-bay beams, the middle joint behavior and the effects of critical parameters on structural behavior of the beams. The parameters comprised the top and bottom reinforcement ratios at middle joint interfaces and the beam span-to-depth ratio. The boundaries of the second series of specimens, i.e., frame specimens, were more realistic so as to represent the restraints from surrounding structures. Other than F3-CD-NS-EX and F4-CD-WS-EX, the other frame specimens included two beam extensions. The horizontal restraints at both ends of the side columns represented the restraints from different stories, and the horizontal axial restraints at the beam extension ends represented the restraints from adjacent beams on frames with removed columns. The tests on frame specimens focus on the structural behavior of the whole frames and the side joints in the loading history. For frame specimens, besides conventional detailing,

three other types of detailing were proposed, aiming at improving structural capacity under a middle column removal scenario.

Following specimen design, a statically-determinate test set-up was designed with a systematic arrangement of instrumentation. Based on detailed measurements of forces and deformations, structural mechanisms and joint behavior under a middle column removal scenario can be observed and investigated.

CHAPTER 4 EXPERIMENTAL RESULTS OF RC BEAM-COLUMN SUB-ASSEMBLAGES

4.1 Introduction

Following the specimen design, test set-up and instrumentation introduced in Chapter 3, experimental results of RC beam-column sub-assemblages under a middle column removal scenario will be presented in this chapter. The variations of structural behavior and load transfer mechanisms are comprehensively illustrated at structural level (relationships of applied load and horizontal reaction force to middle joint displacement), cross-sectional level (the variations of forces at a section) and fiber level (distribution of longitudinal reinforcement strains).

4.2 Experimental results of specimens S1 and S2

The design and detailing of specimens S1-0.90/0.49/23S and S2-0.73/0.49/23 are introduced in section 3.3.1. The notation of S1-0.90/0.49/23S indicates that the top and the bottom reinforcement ratios at the middle joint region and the beam ends of S1 were 0.90% and 0.49%, respectively, and the beam span-to-depth ratio was 23. "S" denotes seismic detailing. The test set-up and the instrumentation for S1 and S2 are shown in **Figs. 3.6** and **3.10**. When the tests were stopped at fracture of top reinforcing bars at one beam end, the middle joint displacements (MJD) for the two specimens reached around 600 mm, slightly greater than 10% of total span length (5750 mm).

In this section, the material properties of concrete and reinforcing bars for S1 and S2 are introduced first. Thereafter, the test results will be demonstrated at three inter-related levels, i.e. structural, sectional and fiber levels, to develop a physical understanding of the global and the local behavior. In this manner, the development and the variations of different mechanisms along the beams could be traced closely. Note that all the test results have excluded the effect of specimen self-weight.

4.2.1 Material properties for specimens S1 and S2

The material tests included tensile tests for reinforcement, compressive cylinder and split-cylinder tests for concrete. The methods to conduct material tests are referred to section 3.6. The material properties of reinforcing bars and concrete are listed in **Table 4.1**. To more precisely simulate concrete behavior with constitutive models, besides compressive and tensile strength, the initial modulus of elasticity, which is defined as the secant modulus between point 1 when the axial compressive strain is 50 millionths and point 2 when the compressive stress reaches 40% of ultimate concrete strength according to ASTM C469-02, was also provided. Note that the fracture strain of bars is selected as the strain at the ultimate tensile strength, and the bar stress is evaluated according to the nominal cross-sectional areas of bars. The stress-strain relationships of T10 and T13 bars are shown in **Fig. 4.1(a)**. The compressive stress-strain relationship of concrete is shown in **Fig. 4.1(b)**.

Table 4.1 Material properties of reinforcing bars and concrete

Tested Items		Nominal Diameter (mm)	Elastic modulus (MPa)	Yield strength (MPa)	Ultimate strength (MPa)	Fracture strain (%)*	Bar type
Longitudinal reinforcing bars	T10†	10	182611	511	731	12.32	Deformed
	T13	13	185763	527	640	10.76	Deformed
Stirrups	R6‡	6	178500	310	422	14.00	Smooth
Concrete (150 mm (dia.) × 300 mm (height))		Compressive strength: 31.2 MPa Splitting tensile strength: 3.2 MPa Initial modulus of elasticity: 27,663 MPa					

*All reinforcement strength is based on the nominal diameter of reinforcement and the gage length of reinforcement is 200 mm;

† "T" denotes high-yield strength reinforcement with a nominal yield strength of 460 MPa;

‡ "R" denotes low-yield strength reinforcement with a nominal yield strength of 250 MPa.

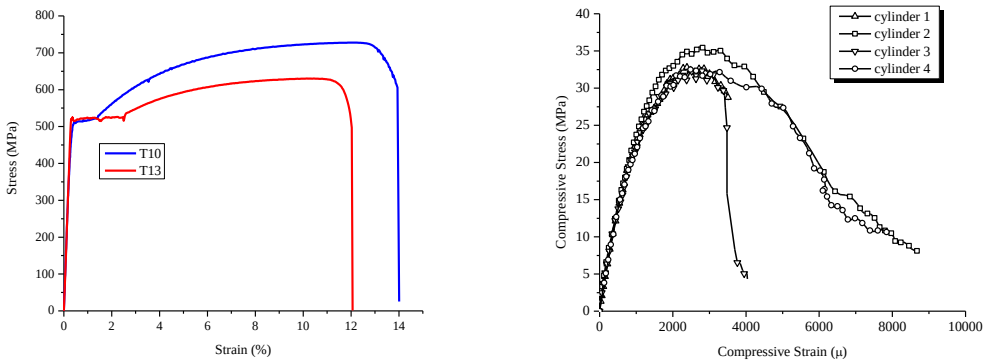

(a) Reinforcement (b) Concrete

Fig. 4.1: Stress-strain relationships of bars and concrete for S1 and S2

4.2.2 Test results at structural level

Figs. 4.2(a) and **(b)** show the deflection curves of S1 and S2 at specified load steps, respectively. It can be observed that the deflections at both sides of the middle joint for each specimen were basically symmetrical except for the regions near the middle joint at large displacements. The beams at both sides of the middle joint failed to keep straight since large cracks occurred at the curtailment points of top bars.

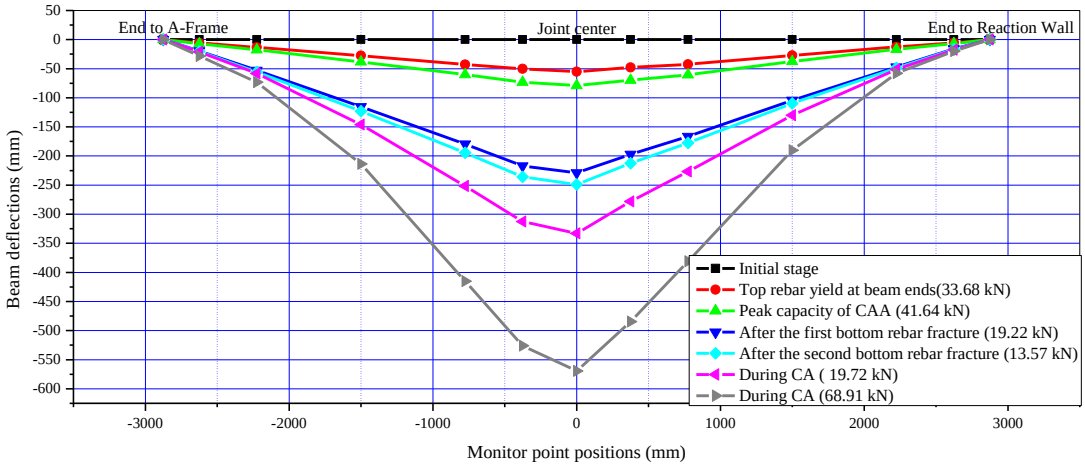

(a) Specimen S1-0.90/0.49/23S

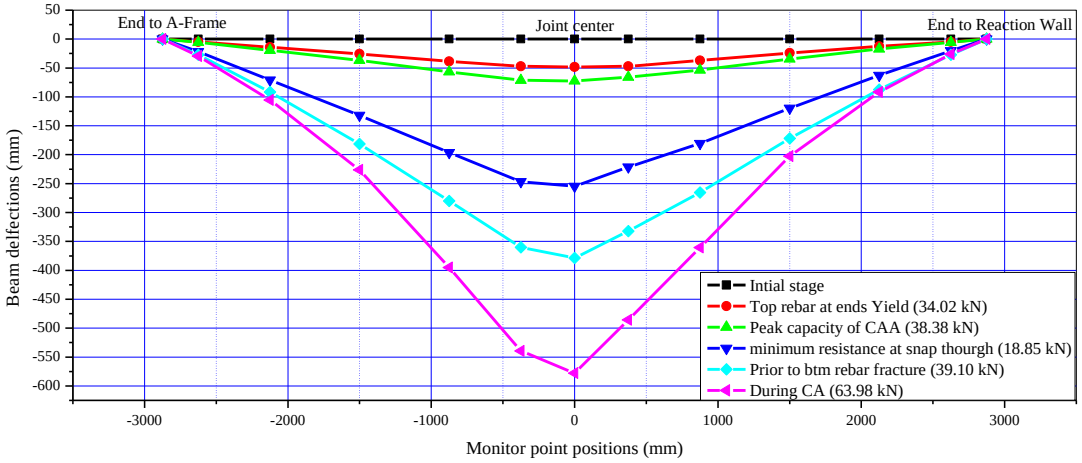

(b) Specimen S2-0.73/0.49/23

Fig. 4.2: Deflection curves of specimens S1 and S2

Figs. 4.3 and **4.4** show the applied load and the horizontal reaction force vs. MJD relationships, respectively. The forces and the corresponding displacements at critical states of the load-MJD history are listed in **Table 4.2**, including compressive arch action capacity and catenary action capacity, etc. The sudden reductions of

applied loads in **Fig. 4.3** were caused by bottom bar fracture near one middle joint interface, and the final descent was caused by top bar fracture at one end-column-stub interface. The fist yielding of top reinforcement at the beam ends and the peak capacity due to compressive arch action are also indicated in **Figs. 4.3** and **4.4**. Note that the variations of axial forces throughout the beams are the same as horizontal reaction forces, which will be explained later. Therefore, **Fig. 4.4** can also represent the axial force vs. MJD relationship. The negative and positive values denote axial compression and tension, respectively.

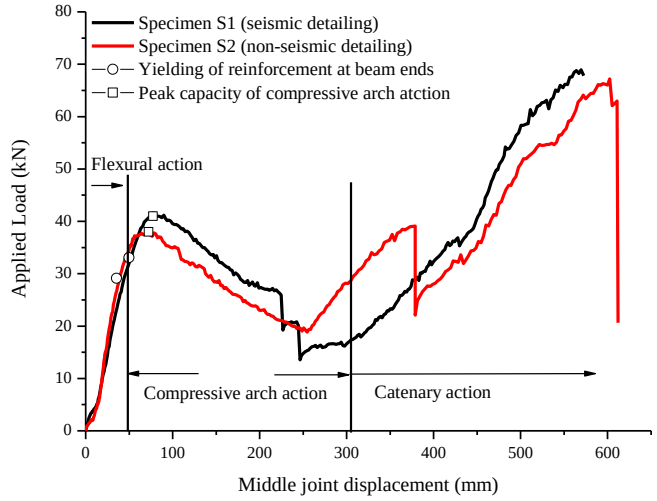

Fig. 4.3: Relationship of applied load to MJD

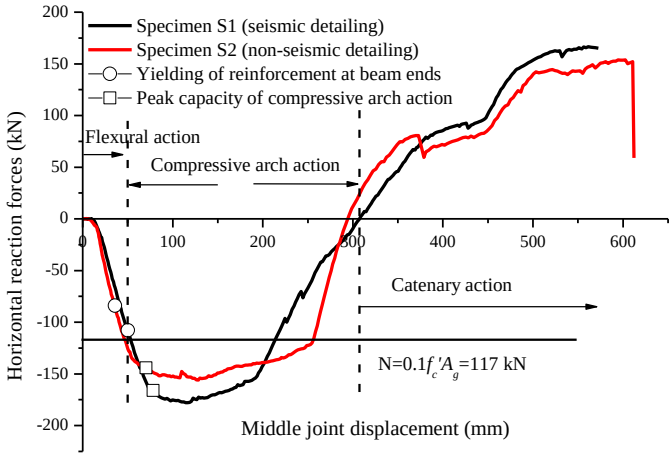

Fig. 4.4: Relationship of horizontal reaction force to MJD

Table 4.2 Force and displacement at critical points of load-MJD curves

Specimen	Critical displacement (mm)					Critical capacity (kN)		
	At the capacity of CAA*	Resistance reversing to rise	1st bar fracture near middle joint†	2nd bar fracture near middle joint†	Top bar fracture at beam end	Calculated capacity of FA‡	Capacity of CAA	Capacity of Catenary action
S1-0.90/0.49/23S	78	246	227	246	573	33.08	41.64	68.91
S2-0.73/0.49/23	73	255	379	N.A.	612	29.02	38.38	67.63

* CAA means compressive arch action;
† The rebars mentioned are located at the bottom layer of the middle joint; N.A. denotes not available.
‡ FA denotes flexural action.

The classification of three different structural mechanisms for S1, viz. flexural action, compressive arch action (CAA) and catenary action, is shown in **Figs. 4.3** and **4.4** as well. Flexural action developed until all plastic hinges occurred at the middle joint interfaces and the beam ends. Catenary action kicked in when the beam axial force changed from compression to tension since the nature of catenary action is a tensile mechanism, as shown in **Fig. 4.4**. The similar classification can also apply to S2.

For each specimen, the middle joint region and the beam ends were initially subjected to positive and negative bending moments, respectively. The bottom reinforcement at the middle joint interfaces yielded rapidly. Thereafter, the yielding of top reinforcement at both beam ends indicated that the plastic hinges have formed at all the critical sections and flexural action has attained its capacity. Based on the conventional plastic hinge mechanism and the nominal ultimate moments of resistance at the critical sections, the capacity of flexural action without considering the presence of beam axial compression was calculated (Yu and Tan 2010b), as listed in **Table 4.2**. However, the experimental flexural capacities, as indicated in **Fig. 4.3** (37.01 kN for S1 and 34.02 kN for S2), were larger than the calculated values. This is because beam axial compression was developed even when the MJD was small, as shown in **Fig. 4.4**.

Fig. 4.3 suggests that CAA enhanced structural resistance on top of flexural action. However, after CAA has attained its capacity, the applied load decreased with increasing MJD, due to geometrical and material nonlinearity. This phenomenon will be explained in detail under cross-sectional analysis.

Catenary action fully utilizes the reserve strength of steel reinforcement. Since the bottom reinforcement near the joint interfaces fractured during the process of developing catenary action, the ultimate capacity of catenary action was determined solely by the top reinforcement for a given deflection limit. Similar to the hardening of steel reinforcement shown in **Fig. 4.1(a)**, the increase of beam axial tensile force was gradually slowing down, as shown in **Fig. 4.4**. However, the vertical component of axial tension force increased with increasing MJD. As a result, the overall structural resistance increased, and the specimens were able to sustain higher applied loads.

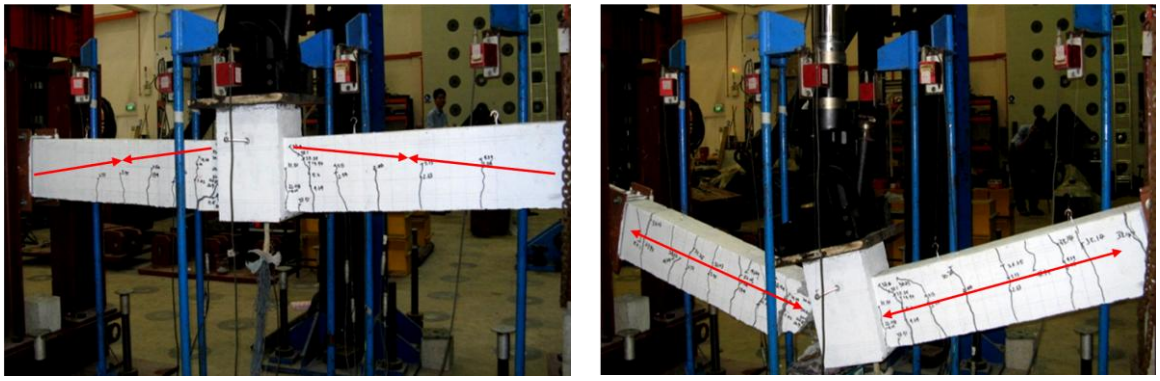

(a) At peak capacity of compressive arch action (b) At peak capacity of catenary action

Fig. 4.5: Beam crack patterns at different structural mechanisms

Fig. 4.5 compares the crack patterns of a two-bay beam at CAA and catenary action stages. The transfer paths of axial forces throughout the beam are also indicated in **Fig. 4.5**. It can be observed that the cracks at CAA stage were mainly caused by bending moments since the cracks ran perpendicular to the beam axis and stopped at neutral axes of sections. During catenary action, cracks were approximately uniformly distributed throughout the beam length and penetrated the whole beam sections, indicating that large tensile forces developed along the beam. The transfer paths of beam axial compression shown in **Fig. 4.5(a)** became leveled off with increasing MJD. When the MJD reached one beam depth, the transfer paths were

roughly along the horizontal direction (corresponding to an unstable state), and then catenary action kicked in to stabilize the beam, as shown in **Fig. 4.5(b)**. Therefore, the MJD of one beam depth is indicative of the mobilization of catenary action in the tests.

Fig. 4.6 shows the failure modes of S1 and S2. The beam crack patterns at both sides of the middle joint were symmetrical except at the local regions near the joint. Due to a lack of a rotational restraint at the middle joint, the middle joint finally rotated to one side, with a wide crack opened and bottom bars fractured at or near the joint interface at that side as well. Cracks were more severe and extensive at three regions throughout the entire beam length, i.e. near the joint interface, at the beam ends and between the curtailment points of a top bar. The cracks at the first two regions were mainly caused by large bending moments and subsequent tensile forces; however, the cracks at the last region primarily resulted from substantial tensile forces with less continuous top reinforcement during catenary action.

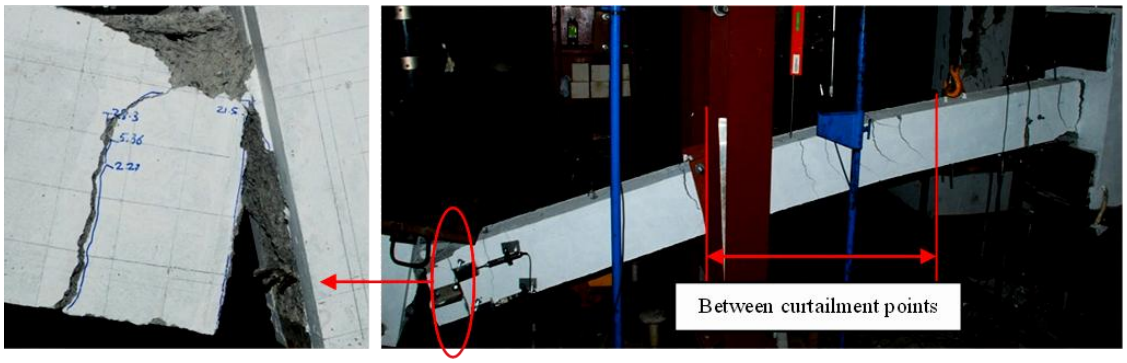

(a) Specimen S1-0.90/0.49/23S

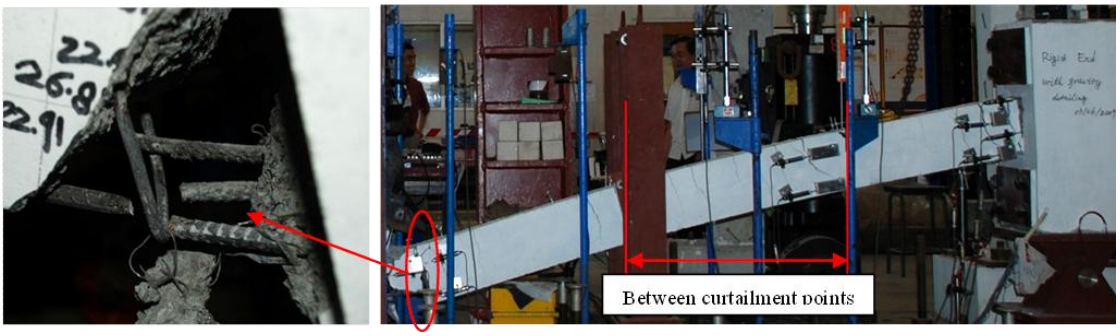

(b) Specimen S2-0.73/0.49/23

Fig. 4.6: Failure modes of specimens S1 and S2

Figs. 4.3, **4.4** and **4.6** demonstrate that the overall structural behavior was not significantly affected by different detailing rules except for the local cracks near the

middle joint. The specimens were very slender, and the arrangement of stirrups insured that the structural resistance governed by shear failure was greater than that governed by flexural failure. Therefore, shear failure was avoided and the advantages of seismic detailing were not apparent. Although the bottom reinforcement for two specimens was lap spliced, no splice failure occurred, suggesting that even the lap splice length of Class A specified in ACI 318-05 can meet the continuity requirements.

4.2.3 Test results at cross-sectional level

As shown in **Fig. 4.2**, the deformed beam configuration can be recorded at each load step. Then the measured reaction forces were used to calculate the cross-sectional forces (including bending moment, axial force and shear force) at specified beam sections according to static equilibrium. The formulae to compute the cross-sectional forces are illustrated in **Fig. 4.7**. Since the positions of the neutral axis varied at different sections, all cross-sectional forces were calculated with reference to the geometrical center of each section.

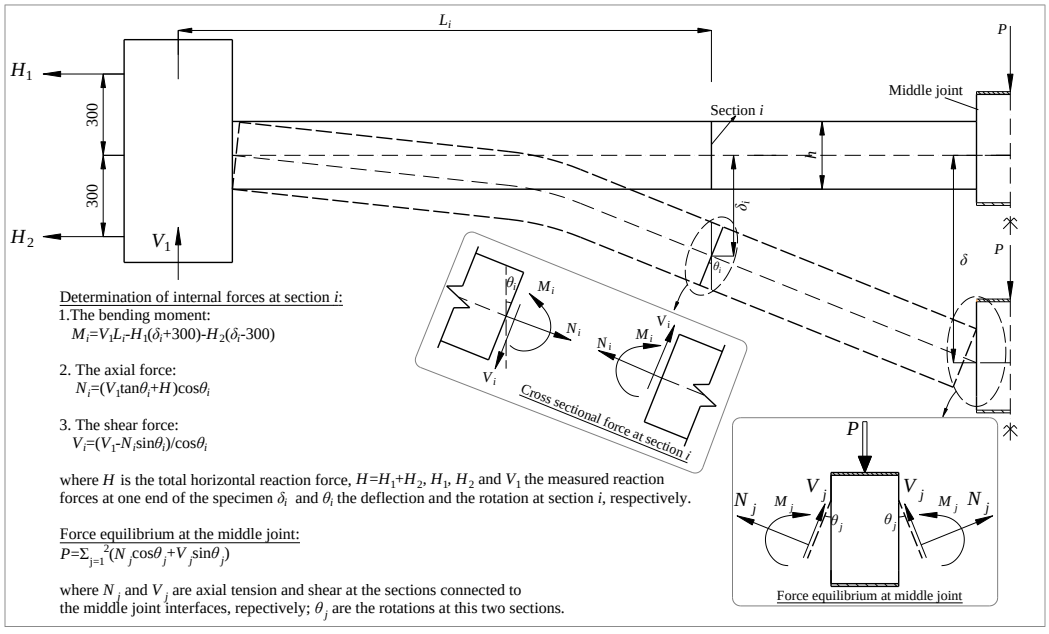

Fig. 4.7: Determination of internal forces at cross-sections

At a beam section, the axial force is calculated by $N_i = \left(V_1 \tan\theta + H\right)\cos\theta$, where V_1 and H are the vertical and the horizontal reactions at the end column stub,

respectively, as shown in **Fig. 4.7**; θ is the rotation at the section. When θ is small, the axial force N_i is roughly equal to H. As a result, although local rotation varied throughout the beam length, the axial forces at different beam cross-sections were almost equal for a given MJD.

Fig. 4.8 shows the comparisons of experimental and theoretical interaction diagrams of axial force and bending moment at the joint interfaces with wide cracks and bottom bar fracture (Yu and Tan 2010b). The sign convention of internal forces is also indicated in **Fig. 4.8**. Negative values of N denote axial compression.

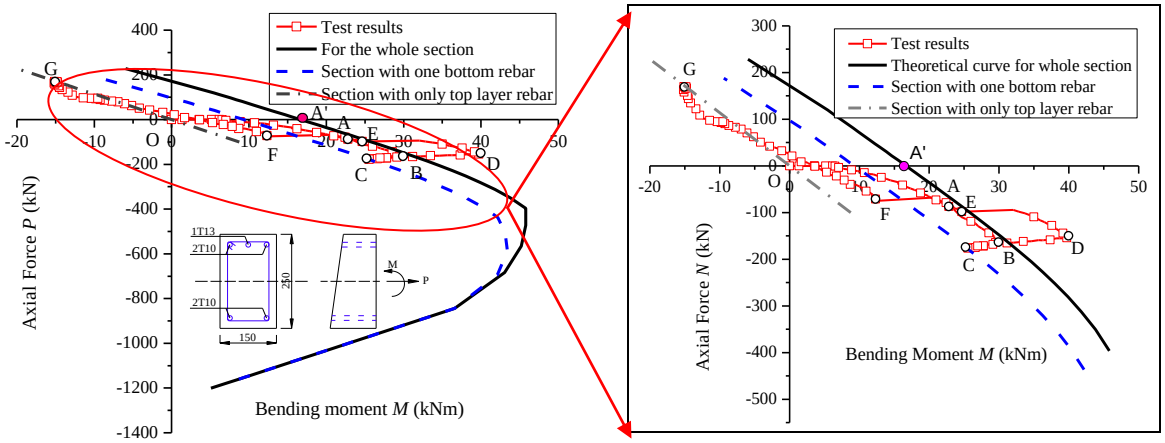

(a) Specimen S1-0.90/0.49/23S

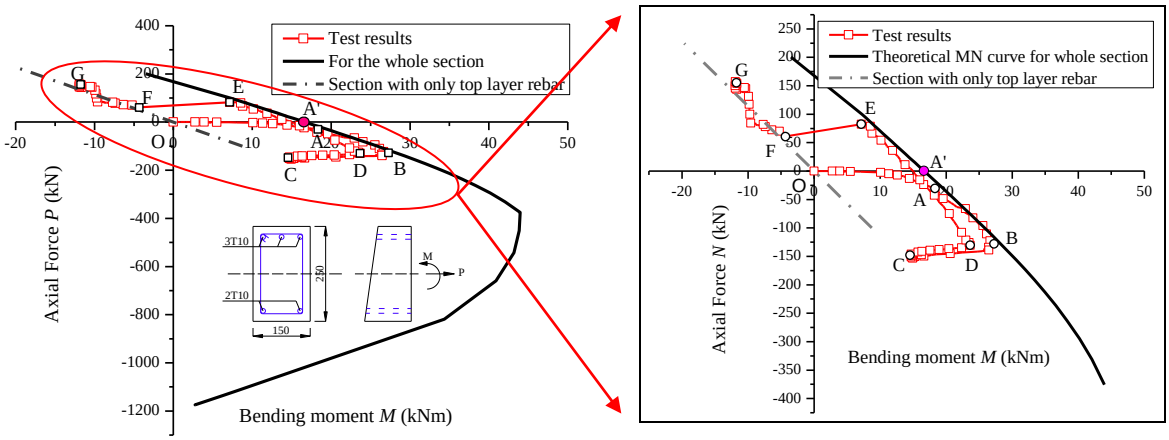

(b) Specimen S2-0.73/0.49/23

Fig. 4.8: Interaction diagrams of axial force and bending moment at joint interfaces

The experimental interaction curves in **Figs. 4.8(a)** and **(b)** follow the path O-A-B-C-D-E-F-G, where O is the origin of coordinates. At point A, the *M*-*N* path has

reached the theoretical *M-N* interaction curve, suggesting that the ultimate moments of resistance have been achieved at the joint interfaces. The part of *M-N* curve where point A is located corresponds to tension steel reaching the yield strength prior to the extreme compression concrete fiber attaining the ultimate strain (say, 0.003 in ACI 318-05). Due to the presence of axial compression force, the ultimate bending moment of resistance increased from A to B, in which B corresponds to the capacity of CAA (41.64 kN for S1 and 38.38 kN for S2). If there was no compression, the ultimate bending moment of resistance at joint interfaces should be located at A', which can be used to calculate the capacity of pure flexural action.

The movement from B to C mainly resulted from the crushing of concrete cover. The change from C to D was primarily attributed to the confinement effect of beam stirrups and the hardening of the bottom reinforcement. Clearly, seismic detailing resulted in a higher confinement effect and whereby the section could sustain a greater bending moment. However, at point D, the larger bending moment still could not insure a lager structural resistance *P* of S1 due to severe *N*-Δ effect (i.e. second-order effect). From the path D to E for S1, one bottom reinforcing bar fractured and the *M-N* curve regressed towards the theoretical interaction diagram of the section with one bottom bar. Nevertheless, before the *M-N* path approached the theoretical curve, another bottom bar fractured, as shown from E to F in **Fig. 4.8(a)**. Eventually, the section contained only top reinforcement. For S2, the unloading of both bending moment and axial compression from D to E, agreed well with theoretical *M-N* curve. At point E, one bottom bar fractured, followed by the jump to point F in **Fig. 4.8(b)**, but another bottom bar failed without fracture. Along the path FG, the bending moment was merely caused by the tension centroid not coincident with the reference point. More detailed interpretation of interaction diagrams can be seen in paper by Yu and Tan (2010b) .

As shown in **Fig. 4.9**, since the structural resistance *P* of a specimen based on shear failure is higher than that based on flexural failure, from consideration of deformed geometry, *P* is given by

$$P = \frac{2\left(M_p + M_n - N\Delta\right)}{l_n} \tag{4-1}$$

Where M_p and M_n are the bending moments acting at the middle joint interfaces and the beam ends, respectively; N is the beam axial compression; Δ is the MJD; and l_n is the net span length of a one-bay beam.

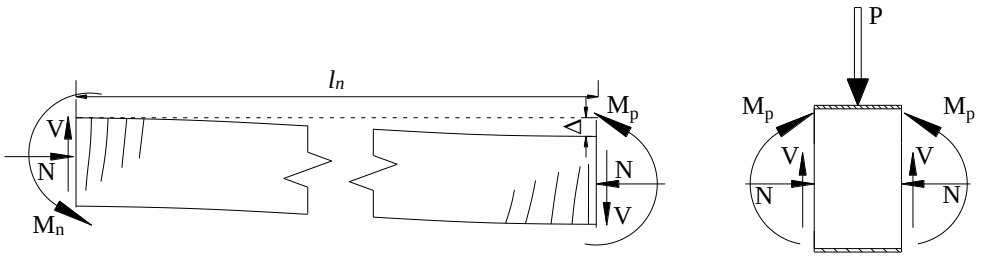

(a)One-bay beam (b) Middle joint

Fig. 4.9: Rigid body diagram of sub-assemblages at compressive arch action

Eq. (4-1) illustrates that the effect of axial compression on the sub-assemblage resistance is two-fold: 1) Due to the presence of beam axial compression, M_p and M_n increase (e.g., from point A' to point B in **Fig. 4.8**), resulting in a larger P; and 2) With increasing Δ, the N-Δ effect increases as well, leading to a smaller P. Therefore, the capacity of CAA can be attained at a relatively smaller MJD than the one corresponding to the maximum axial compression. For example, the displacements corresponding to the CAA capacities are 78 mm and 73 mm for S1 and S2, respectively. However, the displacements corresponding to the maximum axial compression are 114 mm and 128 mm for S1 and S2, respectively.

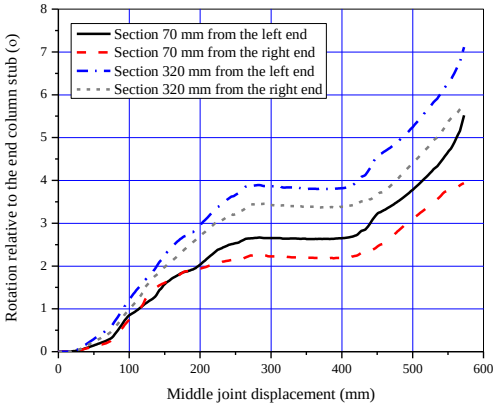

Fig. 4.10: Rotations at both beam ends of specimen S1

Fig. 4.10 shows the flexural rotations at beam sections 70 mm and 320 mm away from the end-column-stub interfaces. The rotations was computed from the readings of LVDTs. As shown in **Fig. 3.6**, the left end of S1 was connected to an A-frame and the right end to a reaction wall. It can be seen that the rotation capacity at the beam ends (i.e. 70 mm to the end) could attain 5.5°. Initially, there was no flexural rotation at the beam ends due to the presence of gaps in connections to the horizontal restraints. Thereafter, the beam-end rotations increased due to negative bending moments. With more cracks occurring, the rotations increased more quickly. Nevertheless, after the MJD had reached around 250 mm, the rotations at both ends became leveled off due to the beam rotation concentrated in the parts between the curtailment points of top reinforcing bars. **Fig. 4.6** shows that many wide cracks penetrated the whole beam sections between the curtailment points at catenary action stage, indicating that the stresses of two continuous top bars in this region were larger than those at the remaning beams. After the redistribtuion of the beam tension, more severe cracks developed at the beam ends, resulting in a further increase of the beam end rotations until the top bars fractured there.

4.2.4 Test results at fiber level

The strain gage readings can shed light on the contributions of top and bottom reinforcing bars to mobilization of different mechanisms. Based on initial bending moments, the whole specimen except the middle joint can be divided into three parts: (1) positive bending moment regions near the middle joint; (2) negative bending moment regions near the beam ends; and (3) transition regions which connect (1) and (2). Moreover, the middle joint is singled out as the fourth part due to different geometric sizes.

Fig. 4.11 shows the strain variations of different reinforcing bars at given sections of S1. The yield strain of reinforcement, around 2800μ, is also indicated in **Fig. 4.11**. Section LB shown in **Fig. 4.11(b)** represents part (1) of S1, where initially the bottom reinforcement was in tension and the top reinforcement in compression due to positive bending moments. However, at around a MJD of 300 mm, the top reinforcement at the joint center and section LB (shown in **Figs. 4.11(a)** and **(b)**) changed from compression to tension. It exactly corresponded to the change of the

beam axial force (or the horizontal reaction) of S1, as shown in **Fig. 4.4**, indicating that the beam tensile force was exclusively provided by the top reinforcement. It is noteworthy that the yielding of top reinforcement could even penetrate to the joint center, as shown in **Fig. 4.11(a)**. **Fig. 4.11(d)** shows the variations of bar strains at section LD, which represents part (2), where the top reinforcement was always in tension and the bottom reinforcement changed from compression to tension at large displacements. Therefore, under catenary action, the tension at part (2) was primarily provided by the top reinforcement with a little contribution from the bottom reinforcement.

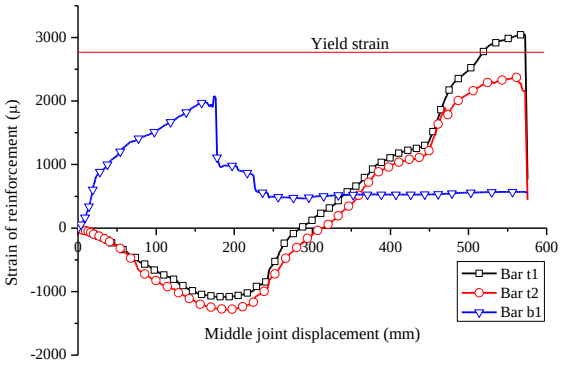

(a) At Middle joint center

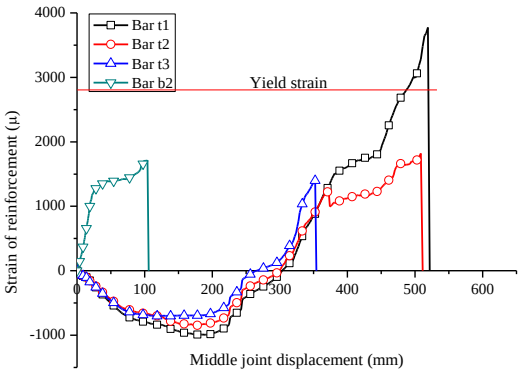

(b) At section LB

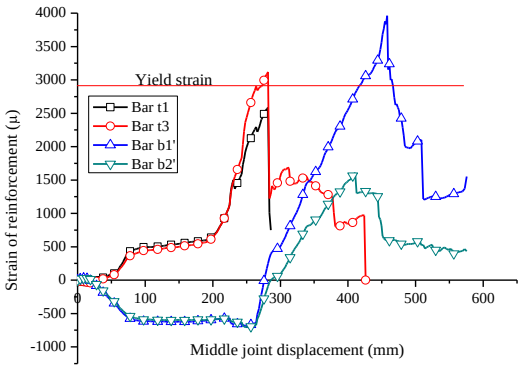

(c) At section LI

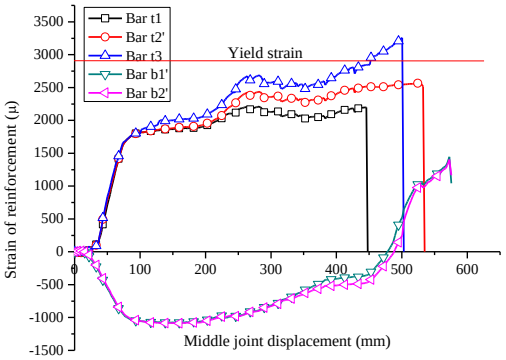

(d) At section LD

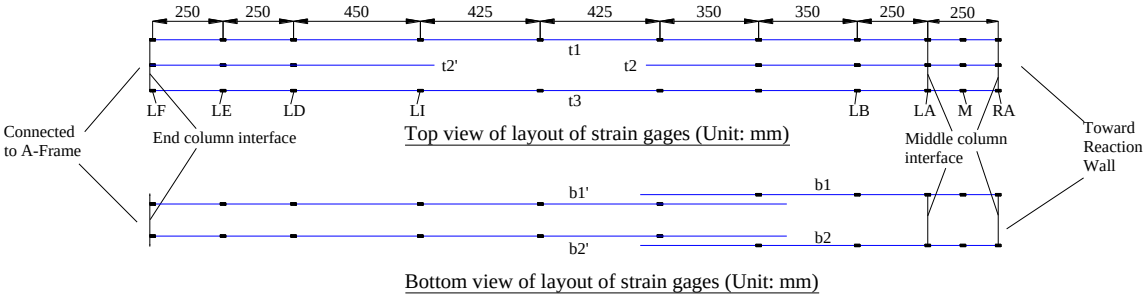

(e) The layout of strain gages

Fig. 4.11: Strains of reinforcing bars at given sections of S1-0.90/0.49/23S

Fig. 4.11(c) shows that both the top and the bottom bars at section LI sustained tension at catenary action stage. This indicates that the sections at the transition regions were subjected to more pure axial tension than other sections. With little effect from bending moment, the distribution of tension at each bar was more uniform. Note that the reduction of strain gage readings in **Fig. 4.11(c)** was caused by debonding of strain gages. The actual strains of the top bars should be in large tension, which is confirmed by the strain gage readings at the counterpart of section LI in S2. The strain variations in **Fig. 4.11(c)** indicate that after fracture at section LA, the bottom bars at Section LI were still able to sustain large tension. Possible load paths to transfer tensile forces to the fractured bottom bars were (a) through beam stirrups and (b) through the bond of concrete. However, load path (a) should be more dominant since concrete is weak in transferring tension force, let alone causing yielding of bottom bars.

In fact, a sudden ascent or descent of strain gage readings was caused by 1) the stress redistribution due to other bar fracture; 2) the interaction from surrounding concrete under severe cracking or crushing regions; and 3) the debonding of strain gages per se under large tension strain of reinforcement. In addition, under very large displacements, fracture of gage wires due to improper arrangement could result in readings directly drop to zero.

The analyses on S2 led to similar findings of S1. To supplement the information on transition part (3) as shown in **Fig. 4.11(c)** and to investigate the strain of reinforcement within the middle joint with lap splice, the strains of reinforcement at two sections of specimen S2 are shown in **Fig. 4.12**.

The position of section LG in specimen S2 is the same as section LI in specimen S1. **Fig. 4.12(a)** shows that at section LG the strains of the bottom reinforcement changed into tension under catenary action and kept increasing until the specimen failed. Unfortunately, the strain readings of the top reinforcement were lost due to strain gage damage. Initially, at the middle joint center of S2 the strains of the lap-spliced bars were very close. After the MJD had achieved around 20 mm, the strains of bars b1 and b2 increased much faster until bar fracture. Note that the sudden strain reduction of bars b1 and b2 probably resulted from the interaction between

bars and surrounding concrete during pullout. Under catenary action, the strains of bars b1' and b2' were quite small, so these two bars were unable to contribute to beam tension forces considerably although they were not fractured. **Fig. 4.12(b)** confirms that the yield penetration of top reinforcement could reach the joint center.

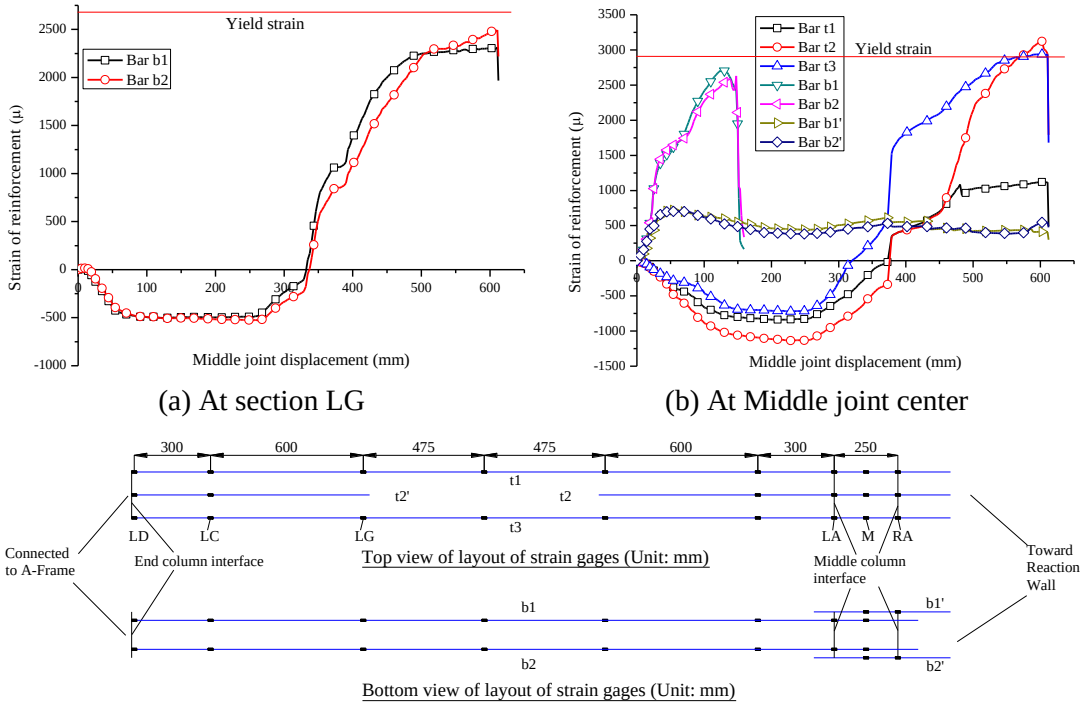

(a) At section LG (b) At Middle joint center

(c) The layout of strain gages

Fig. 4.12: Strains of reinforcing bars at given sections of S2-0.73/0.49/23

Assuming that a plane section remains plane, based on the average strains at the top and the bottom reinforcement of S1, the strain distribution at different sections could be obtained, as shown in **Fig. 4.13**. The strain marked on the left and the right side of a section denotes tensile and compressive strain, respectively. Thus the variation of the compressive zone of S1 under CAA can be visualized. **Fig. 4.13** demonstrates that with increasing MJD, the compressive zone gradually moved from the beam end to the region near the middle joint. However, it can be found that there was no significant variation of the compression zone from the MJD of 80 mm to 100 mm. This resulted from a small change of the beam axial compression between the two above MJDs, as shown in **Fig. 4.4**.

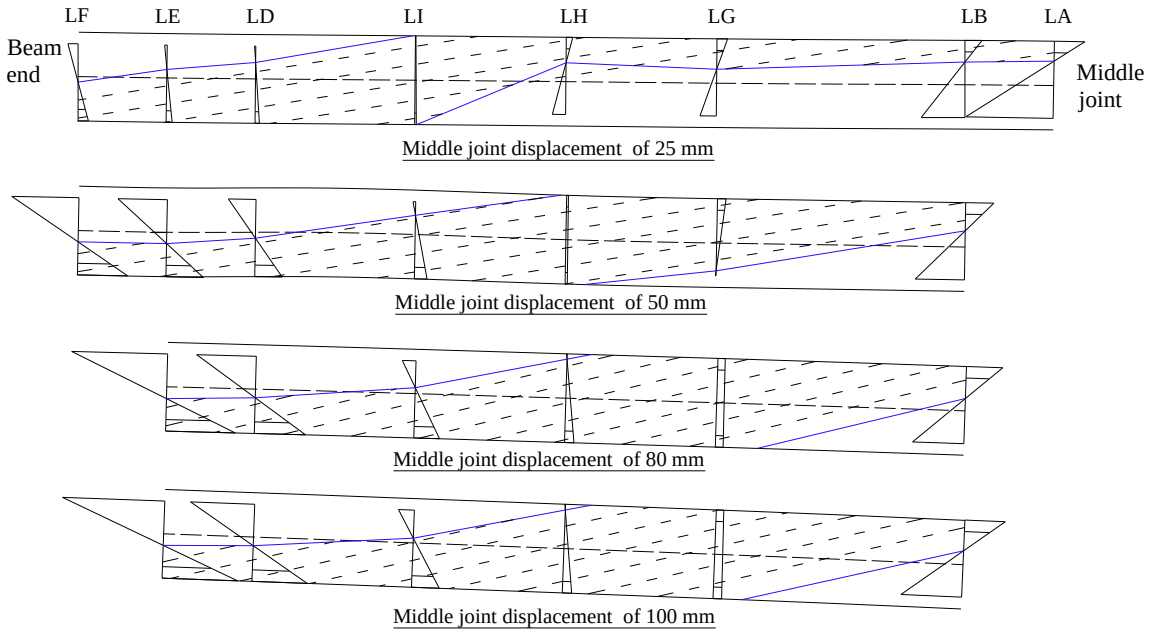

Fig. 4.13: Variations of compression zone over S1 at compressive arch action

4.2.5 Discussions on size effect

Although S1 and S2 are one-half scaled specimens, deformed bars and concrete with smaller aggregates were used in fabrication. Therefore, size effects due to model fabrication and material property distortions were avoided. By virtue of this, the global response of prototype frames can be simulated at model scales (Krawinkler 1988). Additionally, due to the limitation of scaling down materials, Abrams (1987) recommended that the minimum usable factor for testing of isolated RC components in flexure should be one-quarter. Most importantly, the structural behavior of specimens S1 and S2 was ductile, dominated by catenary action rather than shear. As a result, the size effect in the tests can be ignored, and the test results of S1 and S2 can reasonably reflect the structural behavior of the prototype frames.

4.2.6 Progressive collapse resistance of S1 and S2

The testing on S1 and S2 corresponds to nonlinear-static procedure in the design guideline of UFC 4-023-03 (DoD 2010). Therefore, the static test results R_s should be converted to progressive collapse resistance R_d with consideration of dynamic effects. There are two approaches to consider dynamic effects: (1) R_s divided by a dynamic increase factor to obtain R_d, as suggested in UFC 4-023-03; and (2) quasi-

static responses converted to pseudo-static responses by assuming work done by gravity loads equal to energy absorbed by structures (Izzuddin et al. 2008). As discussed in section 2.2.4, the dynamic increase factor (DIF) model in UFC 4-023-03 only applies to the nonlinear static responses with perfect elastic-plastic forms or bilinear models with strength hardening. As a result, the DIF model cannot be used for the structural responses shown in **Fig. 4.3**, and the approach proposed by Izzuddin et al. is employed.

Fig. 4.14 shows the conversion of quasi-static structural responses to pseudo-static structural responses of specimens S1 and S2. It can be found that the first peak pseudo-static structural capacity occurs at the MJD larger than that corresponding to the CAA capacity in quasi-static tests. Moreover, the horizontal grey dash dot lines indicate that if the external load exceeds the first peak pseudo-static capacity of each specimen, the kinetic energy of the sub-assemblage will be reduced to zero only when the sub-assemblage can provide a larger pseudo-static resistance; otherwise, the external load will lead to collapse of the sub-assemblage. **Table 4.3** listed the progressive collapse resistance at CAA and catenary action stages with associated MJDs in accordance with the pseudo-static structural responses. It can be seen that catenary action provided larger progressive collapse resistance than CAA did for both specimens S1 and S2.

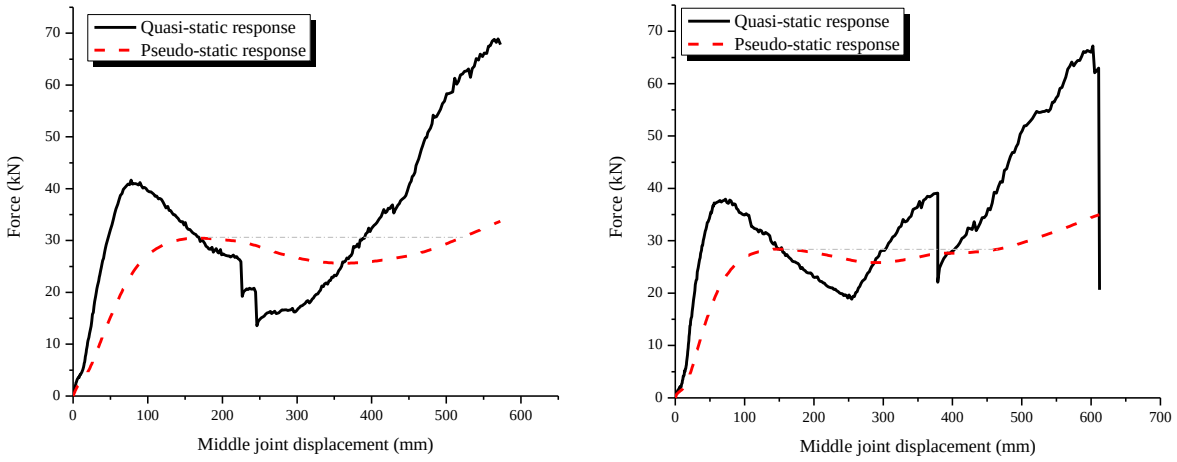

(a) Specimen S1 (b) Specimen S2

Fig. 4.14: Conversion of quasi-static structural responses to pseudo-static structural responses

Table 4.3 Progressive collapse resistance of S1 and S2

Specimen	At CAA stage		At catenary action stage	
	Maximum progressive collapse resistance P_{PC_CAA} (kN)	MJD at P_{PC_CAA} (mm)	Maximum progressive collapse resistance P_{PC_CA} (kN)	MJD at P_{PC_CA} (mm)
S1-0.90/0.49/23S	30.45	168	33.73	572
S2-0.90/0.49/23	28.41	153	34.95	612

In accordance with UFC 4-023-03 (DoD 2010), under a column removal scenario, the gravity load is controlled by the load combination $0.9D+ 0.5L$, where D and L are dead load and live load, respectively. The design loads acting on specimens S1 and S2 are D = 11.65 kN/m and L = 7.2 kN/m, which are equal to one-half of the design loads of the prototype frame (dead load of 23.3 kN/m and live load of 14.4 kN/m). Therefore, the total action acting at the middle column is 38.73 kN, exceeding the progressive collapse resistance provided by catenary action for both specimens, as shown in **Table 4.3**. Thus, due to concentrated loading arrangement, both S1 and S2 tend to collapse.

4.3 Experimental results of specimens S3 to S8

The design and detailing of specimens S3 to S8 are referred to in section 3.3.1. The notation for S3 to S8 is similar to that for S1 and S2. For example, "S3-1.24/0.49/23" indicates specimen S3 designed with a top reinforcement ratio of 1.24% and a bottom reinforcement ratio of 0.49% at the middle joint regions and the beam ends, and with a beam span-to-depth ratio of 23. The test set-up S3 to S8 is shown in **Fig. 3.8**. The corresponding instrumentation is shown in **Figs. 3.10** and **3.11**. Testing was stopped when the top bars at either beam ends of the specimens completely severed.

In this section, the material properties of concrete and steel reinforcement used in specimens S3 to S8 are introduced first, followed by experimental results of structural tests on S3 to S8. Similar to the analyses on specimens S1 and S2, the experimental results of S3 to S8 are also demonstrated at structural, sectional and fiber levels based on detailed instrumentation.

At structural levels, the relationships of applied loads and horizontal reactions vs. middle joint displacement (MJD) are used to represent the overall behavior. In addition, global and local failure modes of specimens are demonstrated. Finally, the overall deflection curves of specimens are presented. At sectional level, the variations of cross-sectional forces, including bending moment, axial force and shear force, are demonstrated. The variations of cross-sectional forces can be used to illustrate the force transfer mechanism at catenary action stage. At fiber level, the strain variations of longitudinal reinforcing bars and stirrups are used to elucidate the force transfer in reinforcement for different structural mechanisms.

4.3.1 Material properties for specimens S3 to S8

Material tests included tensile tests for steel reinforcement, compressive cylinder and split-cylinder tests for concrete. The material properties of reinforcement in S3 and S8 are listed in **Table 4.4**. The ultimate strain corresponds to the tensile strength of reinforcement. For concrete, the compressive cylinder strength is 38.2 MPa, the tensile strength is 3.5 MPa, and the initial modulus of elasticity is 29.6 GPa.

Table 4.4 Material properties of reinforcement for specimens S3 to S8

Rebar type*	Nominal diameter (mm)	Yield strength f_y (MPa)	Elastic Modulus E_s (MPa)	Strain at the start of hardening ε_{sh} (%)	Tensile strength f_u (MPa)	Ultimate strain ε_u (%)
R6	6	349	199177	--	459	--
T10	10	511	211020	2.51	622	11.00
T13	13	494	185873	2.66	593	10.92
T16	16	513	184423	2.87	612	13.43

*:"R" and "T" denote low-yield and high-yield strength reinforcement, with a nominal yield strength of 250 MPa and 460 MPa, respectively.

4.3.2 Applied load and horizontal reaction vs. MJD relationships

Figs. 4.15(a) to **4.17(a)** show the load-MJD relationships of S3 to S8. The sudden reductions in loads marked by crosses resulted from bottom bar fracture at the middle joint interfaces. Subsequent to this, the other sudden reductions were caused by fracture of top bars at either of beam ends.

Figs. 4.15(b) to **4.17(b)** show the horizontal reaction force-MJD relationships of S3 to S8. The horizontal reaction at each end of a specimen is the sum of reactions of two horizontal restraints, as shown in **Fig. 3.8**. Between the sequential fractures of bottom bars at the middle joint interfaces, the horizontal reactions at both ends of the specimens were not equal due to the horizontal force couple provided by the rotational restraint at the middle joint. Therefore, the average values of the horizontal reactions are used in **Figs. 4.15(b)** to **4.17(b)**. It will be shown later that the beam axial force-MJD relationship is almost the same as the horizontal reaction-MJD relationship. Therefore, **Figs. 4.15(b)** to **4.17(b)** can also represent the variations of beam axial forces. The positive and negative values denote beam axial tension and compression, respectively.

Figs. 4.15(b) to **4.17(b)** indicate that the beam axial compression was induced at very small MJDs. As a result, there is no pure flexural action and no distinct demarcation between flexural action and CAA. However, pure flexural capacity, namely P_f, is widely used in design codes to evaluate the ultimate capacity of RC members. Therefore, P_f can be used as a baseline of structural resistance and is set as a hypothetical demarcation of flexural action and CAA. P_f was calculated from the mechanism that assumes the formation of plastic hinges at the middle joint interfaces and the end-column-stub interfaces. It should be noted that the ultimate moment at each plastic hinge was determined without considering the presence of beam axial force. **Table 4.5** summarizes P_f, the first peak load P_{caa}, i.e. CAA capacity, and the maximum axial compression N_{max} for all specimens. It can be seen that P_{caa} exceeds P_f for all specimens. The enhancement of structural resistance at CAA stage is mainly ascribed to the presence of beam axial compression, which enhances the corresponding moment resistance of a section. After P_{caa}, due to second-order effect, the applied load decreased with increasing MJD (Yu and Tan 2012a). This decrease in load was associated with concrete crushing near the joint interfaces and the end-column-stub interfaces.

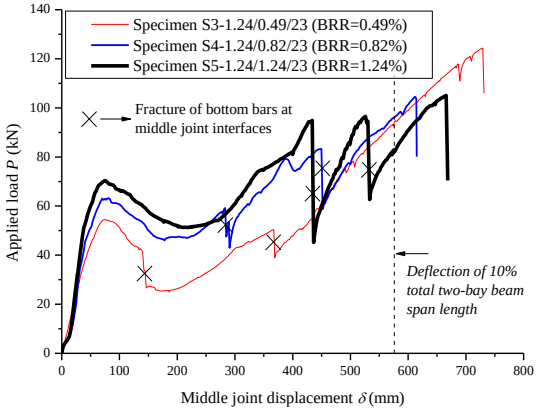

(a) Load-MJD relationship

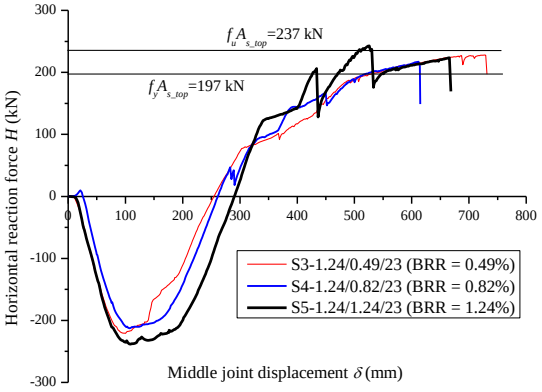

(b) Horizontal reaction force-MJD relationship (A_{s_top}: area of top reinforcement at joint interfaces)

Fig. 4.15: Effect of bottom reinforcement ratio at middle joint region on structural behavior of sub-assemblages

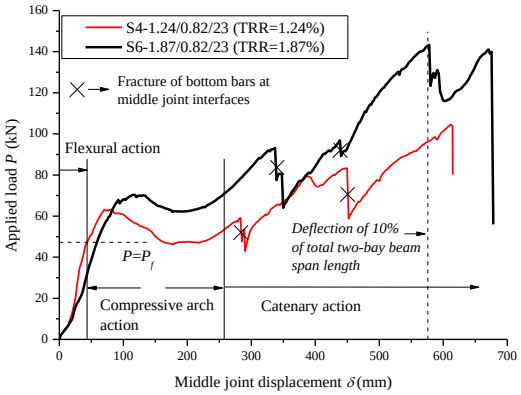

(a) Load-MJD relationship

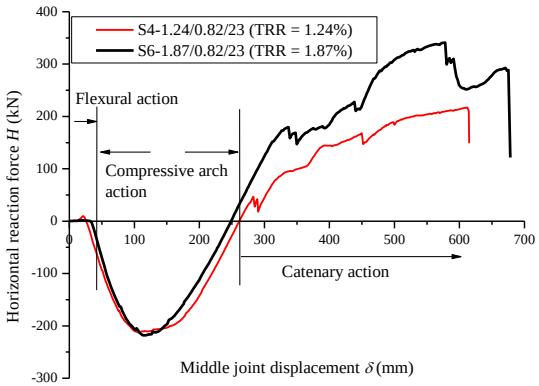

(b) Horizontal reaction force-MJD relationship

Fig. 4.16: Effect of top reinforcement ratio at middle joint region on structural behavior of sub-assemblages

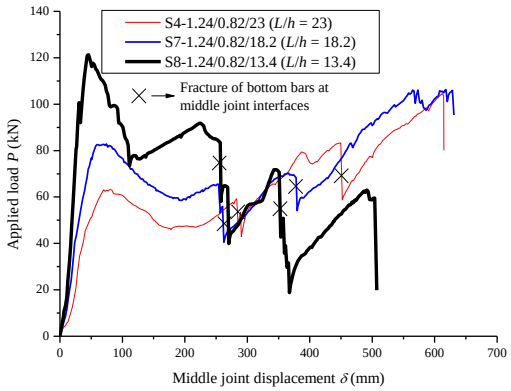

(a) Load-MJD relationship

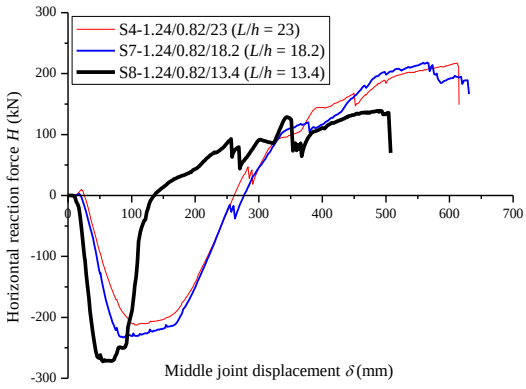

(b) Horizontal reaction force-MJD relationship

Fig. 4.17: Effect of beam span-to-depth ratio on structural behavior of sub-assemblages

With further increasing MJD, when the beam axial force changed from compression to tension, catenary action kicked in. This is because the essence of catenary action is a tensile mechanism. After this transition point, applied loads increased again until top bar fracture. For simplicity, three different structural mechanisms of S4 are denoted in **Fig. 4.16(b)**, and the categorization of structural mechanisms for other specimens is broadly similar.

Table 4.6 lists the detailed information at catenary action stage, including the MJD at the onset of catenary action, the load and the corresponding MJD at each bar fracture. Except for S8, catenary action capacities of all the other specimens are greater than their CAA capacities. This is because the increase of structural resistance of S8 due to catenary action cannot compensate the loss of structural resistance due to shear failure. The details will be explained later.

Table 4.5 Experimental results of S3 to S8 at flexural and CAA stages

Specimens	Flexural action	Compressive arch action (CAA)					
	Calculated capacity P_f [*] (kN)	Peak load P_{caa} [†] (kN)	MJD at P_{caa} (mm)	Horizontal reaction at P_{caa} (kN)	Max. compressive horizontal reaction N_{max} (kN)	MJD at N_{max} (mm)	Enhancement factor α (%)[‡]
S1-0.90/0.49/23S	33.08	41.64	78	-165.3	177.90	114.3	25.9
S2-0.73/0.49/23	29.02	38.38	73	-145.7	155.90	128.3	32.2
S3-1.24/0.49/23	40.89	54.47	74.4	-196.40	221.00	100.1	33.2
S4-1.24/0.82/23	47.76	63.22	81.0	-183.10	212.65	107.2	32.4
S5-1.24/1.24/23	56.61	70.33	74.5	-207.00	238.35	108.7	24.2
S6-1.87/0.82/23	61.97	70.33	114.4	-218.10	218.10	114.4	13.5
S7-1.24/0.82/18.2	61.09	82.82	74.4	-220.00	233.10	87.0	35.6
S8-1.24/0.82/13.4	84.74	121.34	45.9	-264.50	272.50	55.0	43.2

*: P_f is calculated based on conventional plastic hinge mechanism;
†: P_{caa} corresponds to the first peak load in a load-MJD curve, named as CAA capacity.
‡: Enhancement factor $\alpha = \left(P_{caa} - P_f\right) / P_f$.

Table 4.6 Experimental results of S3 to S8 at catenary action stage

Specimens	MJD at the start of catenary action (mm)	Load at 1st fracture of bottom bars P_{t1} (kN)	MJD at P_{t1} (mm)	Load at 2nd fracture of bottom bars P_{t2} (kN)	MJD at P_{t2} (mm)	Load at fracture of top bars P_{t3}^{*} (kN)	MJD at P_{t3} (mm)	$\frac{P_{t3}}{P_{caa}}$ †
S1-0.90/0.49/23S	307.1	25.91	227.0	--	--	68.91	573.0	1.65
S2-0.73/0.49/23	294.4	39.1	378.7	--	--	67.63	612.0	1.76
S3-1.24/0.49/23	254.1	41.26	140.1	50.35	367.2	124.37	729.3	2.28
S4-1.24/0.82/23	261.6	59.18	283.0	83.24	449.6	103.68	614.3	1.64
S5-1.24/1.24/23	290.3	94.86	433.9	94.58	530.3	105.07	665.9	1.49
S6-1.87/0.82/23	248.7	93.03	337.1	96.82	438.4	139.90	675.3	1.99
S7-1.24/0.82/18.2	276.7	65.43	254.1	68.43	378.2	105.99	628.5	1.28
S8-1.24/0.82/13.4	136.0	83.53	256.6	70.62	351.0	59.58	504.1	0.49

*: Except for S6 and S8, P_{t3} of the other specimens represents the capacity of catenary action; catenary action capacities of S6 and S8 are 143.28 kN and 91.83 kN, respectively;

†: P_{caa} denotes structural capacity of compressive arch action

4.3.3 Effect of bottom reinforcement ratio (BRR) at joints on structural behavior

Fig. 4.15 shows the effect of BRR at the joint regions on the overall structural behavior of sub-assemblages. The top reinforcement ratio (TRR) for all the three specimens is the same, i.e. at 1.24%. Within CAA and the initial stage of catenary action prior to bottom bar fracture, a higher BRR gives rise to higher structural resistance for the same deflection. In other words, if a structure is expected to provide large resistance against progressive collapse at a relatively small displacement, more bottom reinforcement is required. In this sense, seismic detailing is beneficial to increase progressive collapse resistance, as the bottom reinforcement should not be less than half of the top reinforcement in a joint (American Concrete Institute 2005). For S5 with BRR equal to TRR, prior to the first fracture of bottom bars, catenary action has attained the resistance of 94.86 kN, around 35% larger than the CAA capacity P_{caa} (equal to 70.33 kN). However, for S3 and S4, at the first fracture of bottom bars, the structural resistance due to catenary action did not exceed CAA capacity. **Fig. 4.15** also shows that a greater

BRR can delay the first fracture of bottom bars. **Table 4.5** shows that for S4, S5 and S6, a higher BRR results in a lower enhancement factor due to CAA.

After a MJD of 530 mm, all the bottom bars of S3, S4 and S5 fractured, and the vertical load was sustained by top bars only. As a result, beams with the same top reinforcement ratio provided similar axial tension and structural resistance under the same MJD, as shown in **Figs. 4.15(a)** and **(b)**, respectively. S3 achieved the largest capacity of catenary action at the expense of the largest MJD. This is because a larger MJD increases the vertical component of beam axial tension in resisting the vertical load. Therefore, TRR determines the capacity of catenary action for a given limit of MJD.

4.3.4 Effect of top reinforcement ratio (TRR) at joints on structural behavior

Fig. 4.16 shows the effect of TRR at the middle joint regions on overall structural behavior of sub-assemblages. The BRRs for S4 and S6 are the same, i.e. at 0.82%. Due to the lap splice of bottom bars within the middle joint in S6, two wide cracks were initiated at the free ends of the splice bars when the MJD was small. Consequently, the stiffness of S6 was smaller than that of S4 before the capacity of CAA was attained, although TRR of S6 was larger than that of S4. The comparison of S4 and S6 in **Fig. 4.16** indicates that the TRR is very beneficial to the overall structural behavior, since a greater TRR can provide a higher capacity of CAA, higher resistance at the first fracture of bottom bars, and a much higher capacity of catenary action. The capacity of catenary action for S6 is 143.28 kN, around 38% higher than that of S4. On the other hand, **Table 4.5** shows that for S4 and S6, a higher TRR results in a lower enhancement factor due to CAA.

4.3.5 Effect of beam span-to-depth ratio on structural behavior

Fig. 4.17 shows that beam span-to-depth ratio affects structural behavior fundamentally since catenary action of S8 with the lowest l/h failed to increase structural resistance beyond CAA capacity. The observed crack patterns of S8 indicate that shear behavior in S8 was dominant, whereas S4 and S7 were

dominated by flexural and axial behavior. Despite 1.2 m shorter than the total span length of S4, S7 behaved similarly to S4. However, a further reduction of 1.2 m in the total span length (e.g. from S7 to S8) resulted in a completely different structural mechanism, suggesting that there is a threshold value of span-to-depth ratio that determines the dominant structural behavior, such as shear and catenary action. **Fig. 4.17(b)** demonstrates that the beam axial compression of S8 was mobilized much more rapidly than S4 and S7 in the initial stage, and the beam axial force of S8 changed from compression to tension at a MJD of 136 mm, significantly smaller than that of S4 and S7, as shown in **Fig. 4.17(b)**. Moreover, the CAA capacity and the enhancement factor due to CAA of S8 were the largest amongst the six specimens. Therefore, RC beams with small span-to-depth ratios are more likely to mitigate progressive collapse via CAA rather than catenary action.

The threshold value of the span-to-depth ratio can be roughly estimated through the comparison of CAA capacity and structural resistance governed by shear. If the former is smaller than the latter, shear failure can be avoided and the structural performance will be more ductile. For the given specimen detailing and the material properties as listed in **Tables 3.2** and **4.4**, respectively, the nominal sectional shear capacity V_n is 75.69 kN in accordance with ACI 318-05. If a strength reduction factor of 0.75 is considered, the shear design strength ϕV_n is 56.77kN. Therefore, structural resistance governed by shear is approximately between 113.54 kN and 151.38 kN. In this batch of specimens, only the CAA capacity of S8 exceeds 113.54 kN. As a result, shear failure occurred for S8, which can be also confirmed by the crack pattern and the failure mode of S8.

4.3.6 Failure modes and crack patterns of specimens S3 to S7

Due to similar failure modes of sub-assemblage specimens S3 to S7, for simplicity, only S5 and S6 are singled out to demonstrate the crack patterns and the failure modes. S5 represents the specimens with continuous bottom reinforcing bars at the middle joint, whereas S6 represents the specimens with lap-spliced bottom reinforcing bars at the middle joint. The load-MJD relationship of S8 indicates that

the structural mechanism of S8 differs from the other specimens. Therefore, the failure modes and the crack patterns of S8 are demonstrated separately.

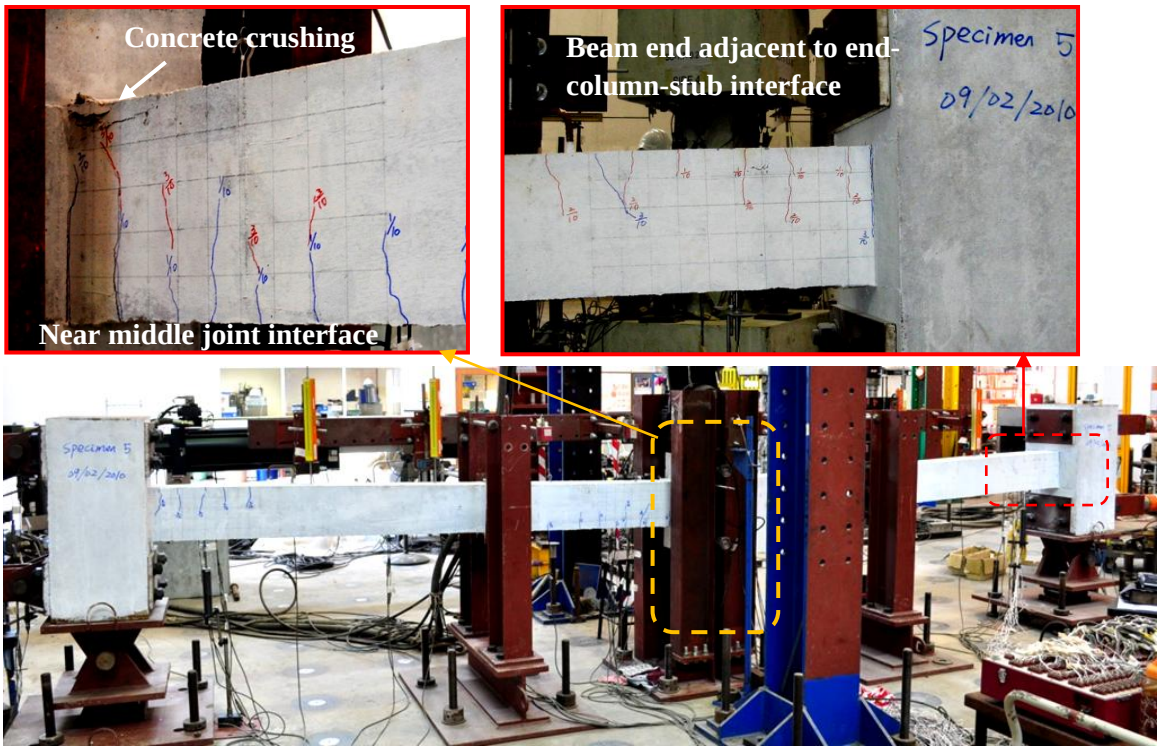

(a) At the capacity of CAA (δ=75 mm)

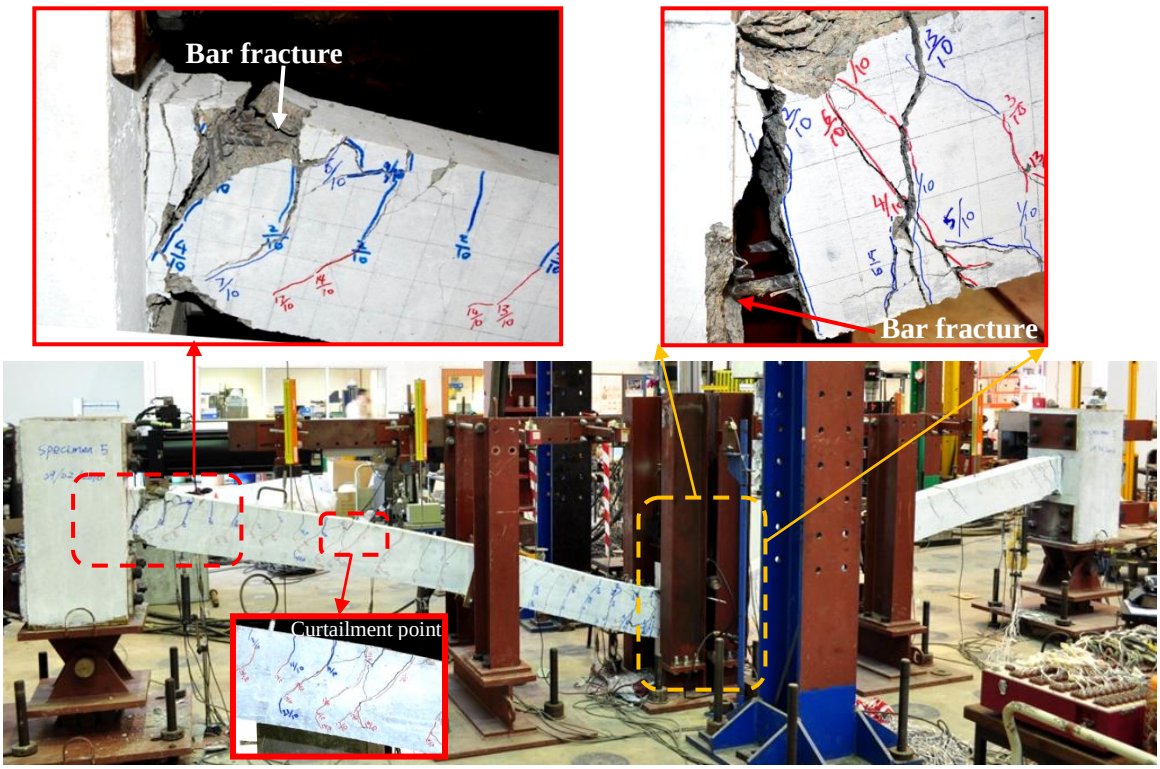

(b) At the capacity of catenary action (δ=665 mm)

Fig. 4.18: Failure modes and crack patterns of S5-1.24/1.24/23

Initially, S5 and S6 were mainly subjected to bending moment, followed by the coupled action of bending moment and beam axial compression. **Figs. 4.18(a)** and **4.19(a)** show that at the CAA capacity, flexural cracks were formed at the middle joint region and the beam ends, and top concrete was crushed near the middle joint interfaces, indicating the effect of bending moment. However, **Fig. 4.19(a)** shows that a major crack was concentrated at the free end of the lap-spliced bottom bars of S6. The numbers indicated at the tip of cracks corresponded to the value of MJD. For example, 1/10 corresponds to the MJD of 0.1 beam depth, i.e. 25 mm and 2/10 to 50 mm.

When increasing MJD to greater than one beam depth, catenary action replaced CAA to sustain the vertical load. Since axial tension was mobilized throughout the beam, extensive tensile cracks were developed throughout the whole length. The cracks ran normal to the beam axis, and some cracks even penetrated the entire beam cross section, such as the crack patterns of S5 as shown in **Fig. 4.18(b)**. Two wide flexural cracks were concentrated at both joint interfaces of S5, resulting in localization of bottom bar strain and the eventual fracture of bottom bars, as shown in the close-up of **Fig. 4.18(b)**. Due to the presence of the rotational restraint in the test set-up, the bottom bars at the other side of the middle joint were either fractured or yanked out. Thereafter, the tensile force could only be transferred via top bars going through the middle joint. When the top bars at either beam ends were completely fractured, as highlighted in **Fig. 4.18(b)**, the whole sub-assemblage failed. In summary, at the end of the test on S5, severe failure was mainly concentrated at the middle joint region and the beam ends.

The overall distribution of cracks of S6 at the ultimate state of catenary action was similar to those of S5. However, severe splitting cracks occurred along the top reinforcement near the beam ends and the middle joint, as shown in **Fig. 4.19(b)**. This is because at catenary action stage large tension force was developed along the top reinforcement with diameter 16 mm and net concrete cover was 20 mm only.

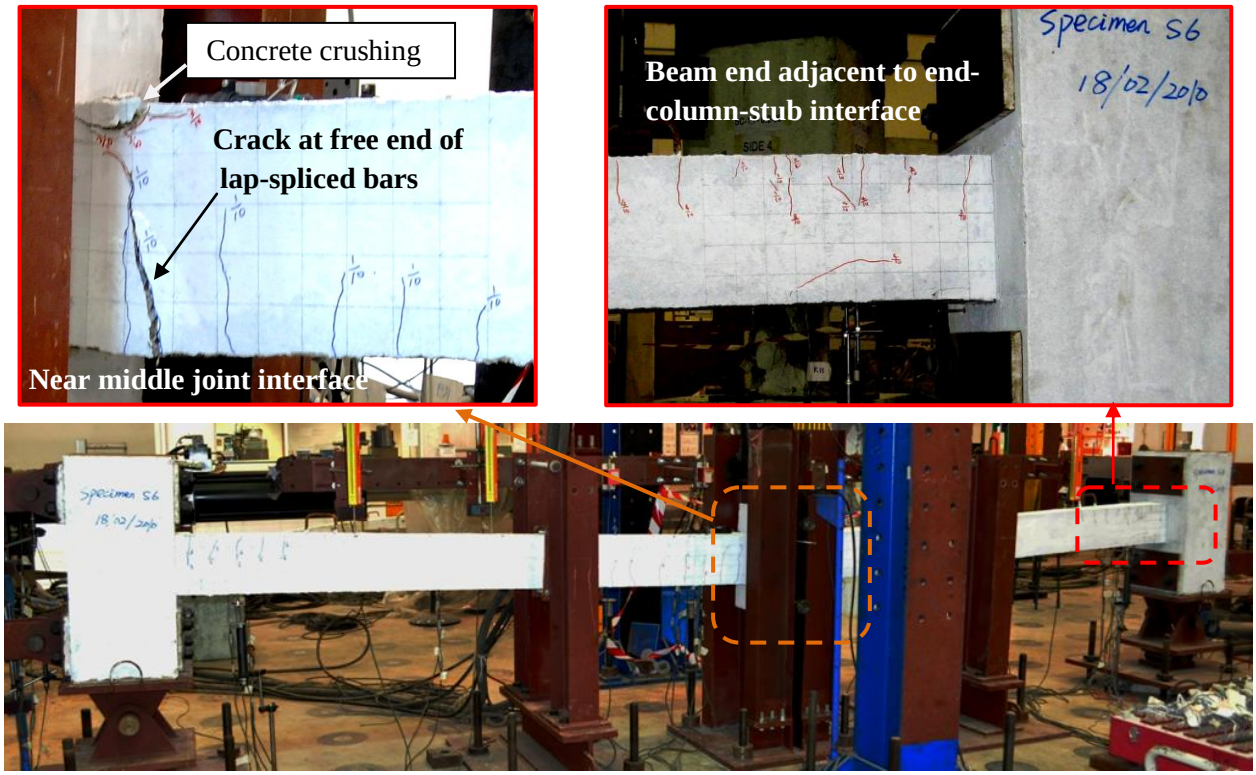

(a) At CAA (δ=100 mm)

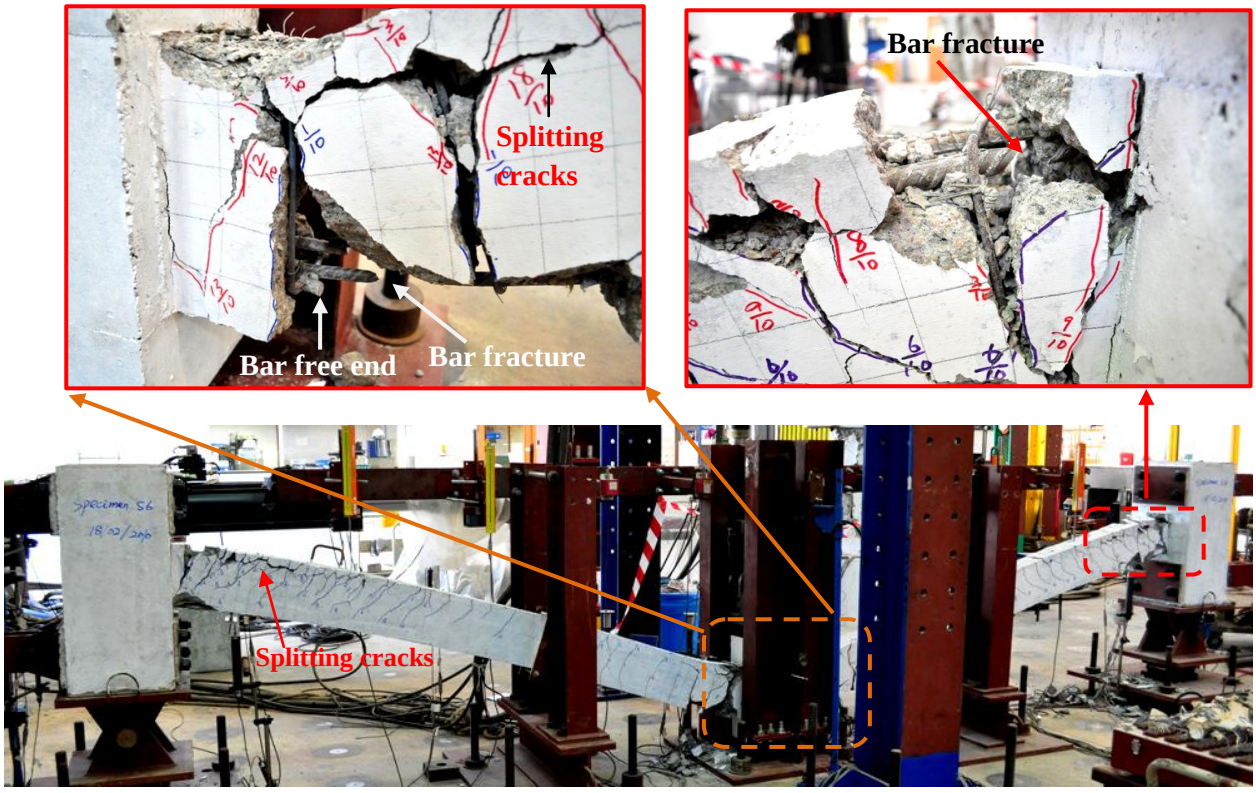

(b) At the capacity of catenary action (δ=675 mm)

Fig. 4.19: Failure modes and crack patterns of S6-1.87/0.82/23

4.3.7 Failure modes and crack patterns of specimen S8

Similar to S5, severe failure of S8 was also concentrated at the middle joint region and the beam ends. Therefore, the crack patterns and the failure modes at these regions are demonstrated. **Fig. 4.20(a)** shows that when S8 was at CAA stage with a MJD of 75 mm, wide cracks occurred near the middle joint interface and inclined cracks appeared at both beam ends. The wide cracks indicated large bending moments and the inclined cracks suggested the presence of large shear forces. In fact, the large shear force caused the fracture of two stirrups located near the middle joint, as shown in **Fig. 4.20(b)**. At catenary action stage, the shear cracks and the flexural cracks intersected with each other, causing severe debonding of concrete. The shear failure inhibited a further large increase in structural resistance even though catenary action was mobilized.

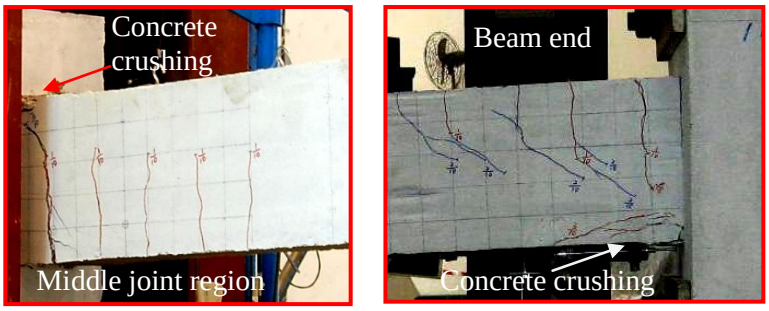

(a) At CAA stage (δ=75 mm)

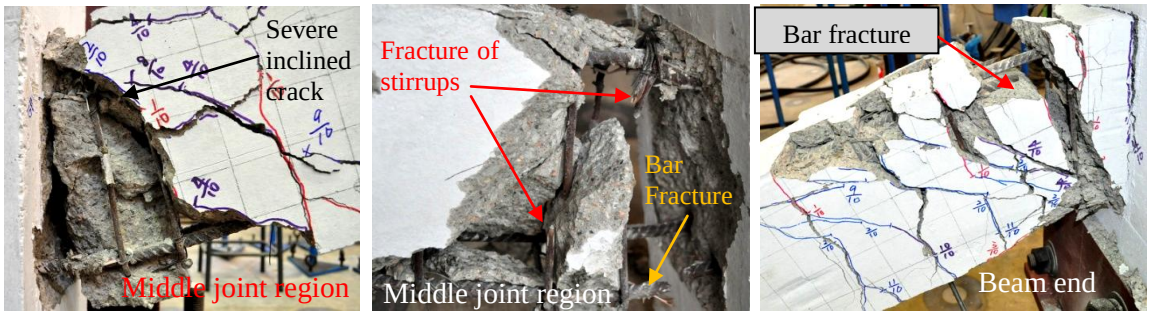

(b) At catenary action capacity (δ=504 mm)

Fig. 4.20: Failure modes and crack patterns of S8-1.24/0.82/13.4

4.3.8 Summary of local failure modes at middle joints and beam ends

Fig. 4.21 demonstrates the local failure modes of regions near the middle joints. There is no appreciable shear distortion at the middle joint panels. All the failures

were concentrated in regions near the joint interfaces. For the specimens with continuous bottom bars (S4, S5, S7 and S8), two wide cracks just occurred at both joint interfaces, whereas for the specimens with lap-spliced bottom bars (S3 and S6), two wide cracks formed at the free ends of spliced bars. It can be observed that for S3, S6 and S7, the longitudinal bond cracks along the top reinforcement ran perpendicular to and intersected with the flexural cracks, causing a loss of bond strength so that the stress along the top bars distributed more uniformly.

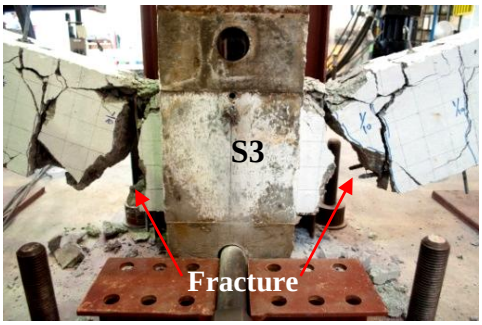

(a) S3-1.24/0.49/23
(lap-spliced bars at bottom)

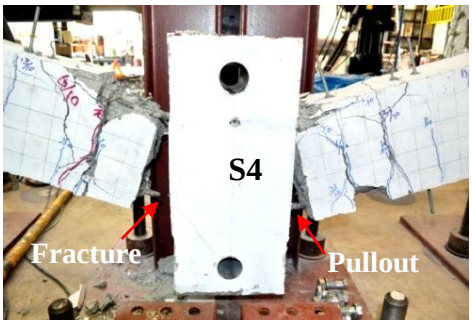

(b) S4-1.24/0.82/23
(continuous bottom bars)

(c) S5-1.24/1.24/23
(continuous bottom bars)

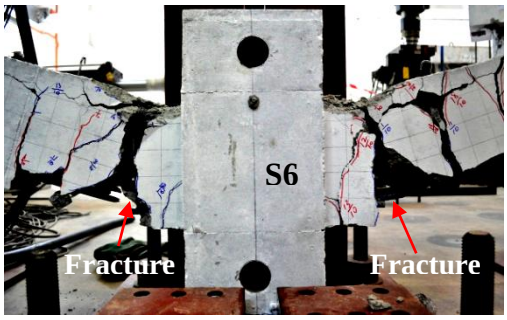

(d) S6-1.87/0.82/23
(lap-spliced bars at bottom)

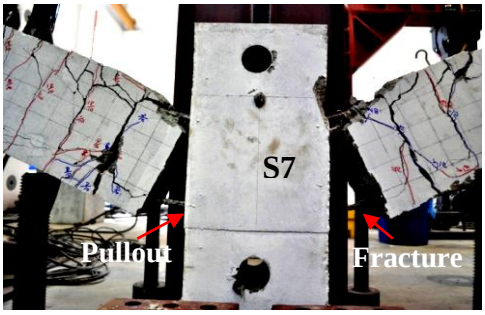

(e) S7-1.24/0.82/18.2
(continuous bottom bars)

(f) S8-1.24/0.82/13.4
(continuous bottom bars)

Fig. 4.21: Local failure modes at middle joint regions

Fig. 4.22 shows that both flexural and shear cracks were extensively developed at the beam ends. Concrete at the compression side was crushed. The crack pattern reflects the coupled action of bending moment (or tension) and shear force. For specimens S6, S7 and S8, severe bond cracks are observed due to large tension. **Figs. 4.14(b)** to **4.16(b)** show that the beam axial tension of specimen S6 was much larger than that of the other specimens at catenary action stage. Accordingly, more severe bond cracks occurred in S6. Severe cracks release the bond between concrete and reinforcing bars and facilitate the rotation of the beam ends.

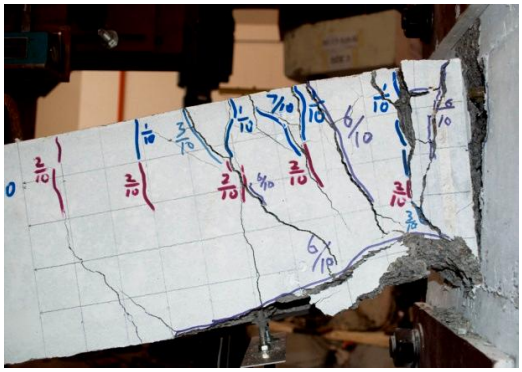

(a) S3-1.24/0.49/23

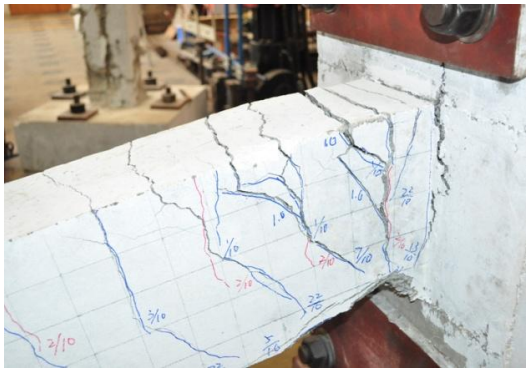

(b) S4-1.24/0.82/23

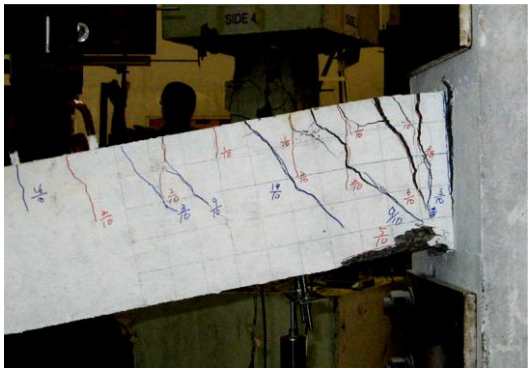

(c) S5-1.24/1.24/23

(d) S6-1.87/0.82/23

(e) S7-1.24/0.82/18.2

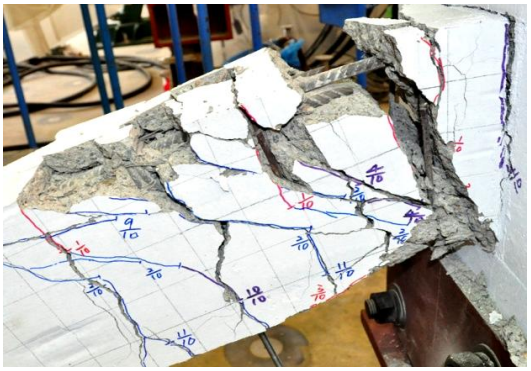

(f) S8-1.24/0.82/13.4

Fig. 4.22: Local failure modes at beam ends

4.3.9 Overall deflections and local rotations of sub-assemblages

Out of brevity, S5 and S8 are selected to show overall deflections at different load steps, as shown in **Figs. 4.23(a)** and **(b)**, respectively. The deflection curves shown in **Fig. 4.23** at both sides of the middle joint are quite symmetrical until the first fracture of bottom bars. The position of bottom bar fracture was random, at either side of the middle joint. **Fig. 4.23** shows that at catenary action stage, the slope of the deflection curves beyond the curtailment point from the end is larger than that of the beam end, since at the free end of the curtailed bars, cracks were more extensively developed due to large tension, as highlighted in **Fig. 4.18(b)**.

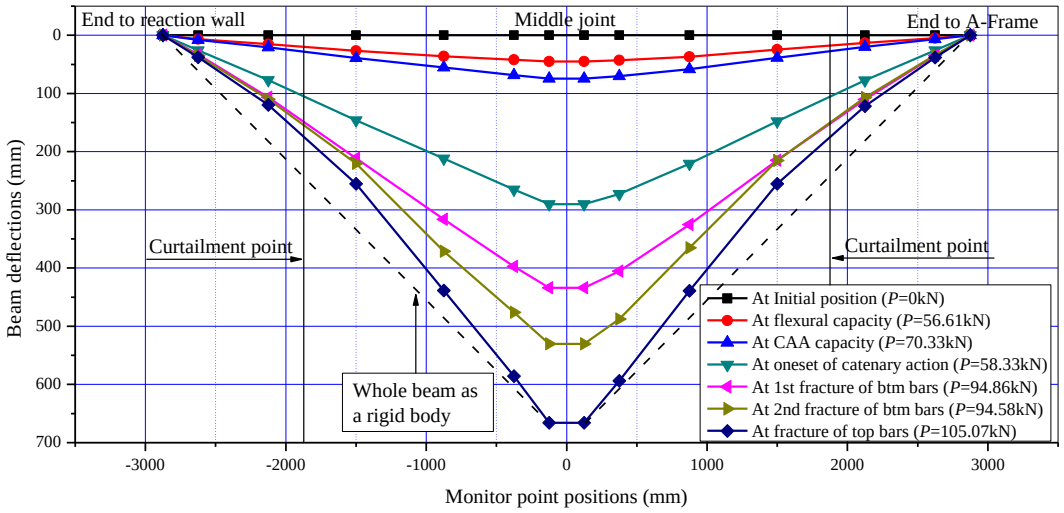

(a) Overall deflection curves of S5-1.24/1.24/23

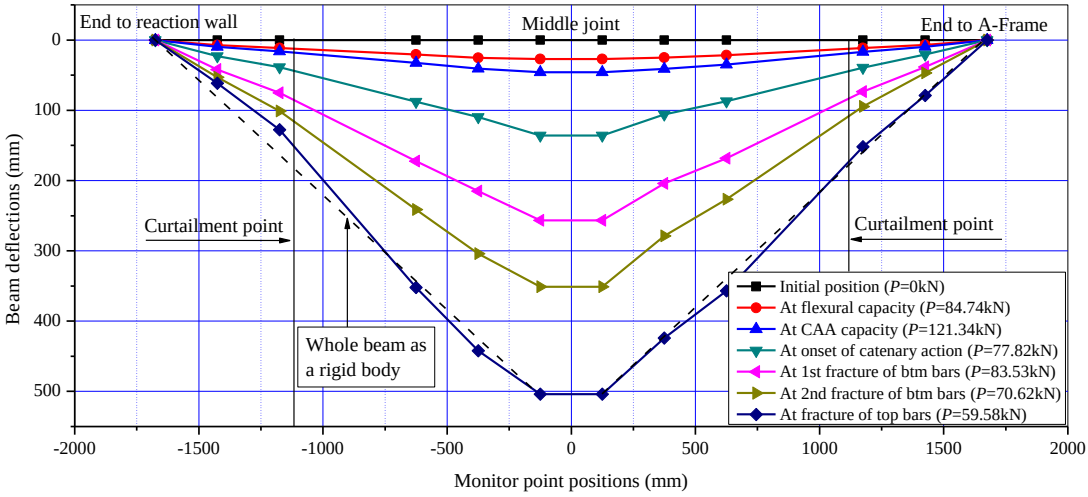

(b) Overall deflection curves of S8-1.24/0.82/13.4

Fig. 4.23: Overall beam deflection curves

The slope of the deflection curves in **Fig. 4.23** represents the local rigid rotation θ_r of beam segments, which are divided by the locations of the instrumentation shown in **Fig. 3.11(a)**. **Fig. 4.23(a)** indicates that the distribution of θ_r is not uniform over the beam length. θ_r near the middle joint interface is larger than the one near the beam ends. On the other hand, in UFC 4-023-03 (DoD 2010), the rotation capacity of an RC framed member, namely, global rotations θ_{gr}, is evaluated by chord rotation, indicated as a dash line in **Fig. 4.23**. It implies that the entire single-bay beam rotates like a rigid body, and the local rotation at each section are equal to θ_{gr} over the entire beam length. Therefore, the rotation capacity can be calculated directly with the ultimate MJD. However, θ_{gr} underestimates the local rotations near the joint interfaces but overestimates those at beam ends. The ultimate rotations at the end of tests are listed in **Table 4.7**. It can be seen that the *local rotation capacities* at the joint interfaces and the beam ends are greater than 13.9° and 6.6°, respectively. In UFC 4-023-03 (DoD 2010), it is required that the *global rotation capacity* of RC members should exceed 11.3° if catenary action is considered. **Table 4.7** shows that the global rotations of all six specimens satisfied this requirement. Additionally, the global rotation capacities were achieved after the fracture of bottom bars and just before the complete fracture of top bars at one beam end.

Table 4.7 Ultimate rotations at joint interfaces and beam ends of sub-assemblages

Specimens	Local rigid rotation θ_r at joint interfaces (deg)*		Local rigid rotation θ_r at beam ends (deg)		Global rotation θ_{gr} (deg)
	A-Frame side	Reaction Wall side	A-Frame side	Reaction Wall side	
S3-1.24/0.49/23	20.9	23.1	9.8	8.4	14.9
S4-1.24/0.82/23	15.0	15.7	7.4	6.6	12.6
S5-1.24/1.24/23	16.0	17.8	8.7	8.6	13.6
S6-1.87/0.82/23	22.0	19.2	10.6	8.4	13.8
S7-1.24/0.82/18.2	17.7	21.7	11.6	9.3	16.3
S8-1.24/0.82/13.4	17.7	13.9	17.5	13.9	18.0

*: The wide crack occurred at 50 mm and 100 mm away from joint interfaces for specimen S3 and S6, respectively, based on Figs. 4.20(a) and 4.20(d). Therefore, for S3 and S6, the local rigid rotation is specified at the position of the cracks rather than real joint interfaces.

4.3.10 Variations of cross-sectional internal forces

Fig. 4.7 shows the determination of cross-sectional forces at section *i* based on detailed instrumentation. All the cross-sectional forces are calculated with reference to the geometric center of the section. The sign conventions of cross-sectional forces are indicated in **Fig. 4.7** as well. With the exception of bending moment, both the axial force and the shear force at section *i* depend on its rotation θ_i. To evaluate the cross-sectional forces accurately, local rotation θ_r should be used, as it accounts for the actual deformed configurations of beams. To simplify the evaluation of cross-sectional forces, global rotation θ_{gr} can be used because θ_{gr} is equal at each section throughout the entire beam length. However, the difference between θ_r and θ_{gr} may cause discrepancies in predicting the axial and the shear forces.

The left one-bay beam of S5 as shown in **Fig. 4.18** is selected to demonstrate the relationships of cross-sectional forces to MJD. **Fig. 4.24(a)** shows the variations of bending moments at the joint interface and the beam end. Both attain the respective maximum values when the beam axial compression reaches the peak capacity, as shown **Fig. 4.24(b)**. This is because axial compression increases the moment capacity via *M-N* interaction (Yu and Tan 2011a; 2012a). After the commencement of catenary action, bending moments throughout the beam keep decreasing. This suggests that at catenary action stage, the distribution of tension over reinforcing bars at the middle joint interface and the beam end critical sections is not uniform (although the net axial force is tension). In other words, some bars are under larger tension and others are under smaller tension or even under compression. However, with the further development of catenary action, the distribution of tension over different bars at one beam section tends to be uniform. After the fracture of bottom bars, the joint interface is under pure tension of top bars without any bending moment. Nevertheless, when the tension is shifted to the geometric center of beam sections, the non-coincidence of the top reinforcement layer and the beam section center induces negative bending moment at the joint interfaces.

Both local rotation θ_r and global rotation θ_{gr} were used to determine the axial force at the joint interface of S5. Regardless of the type of rotations, **Fig. 4.24(b)** illustrates that the beam axial force is not sensitive to rotations. Even though θ_r attains around 18^o at the end of catenary action stage, there are no appreciable discrepancies between beam axial forces and horizontal reaction forces. Therefore, the variations of horizontal reaction forces shown in **Figs. 4.14(b)** to **4.16(b)** can represent the variations of beam axial forces for all specimens.

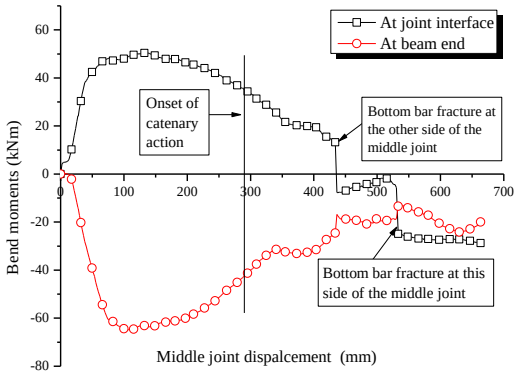

(a) Variation of bending moment

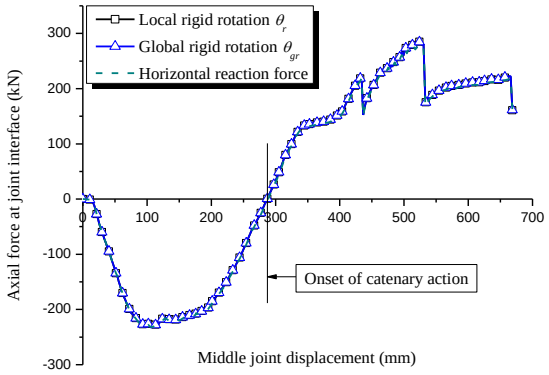

(b) Axial force at the beam section connected to the joint interface

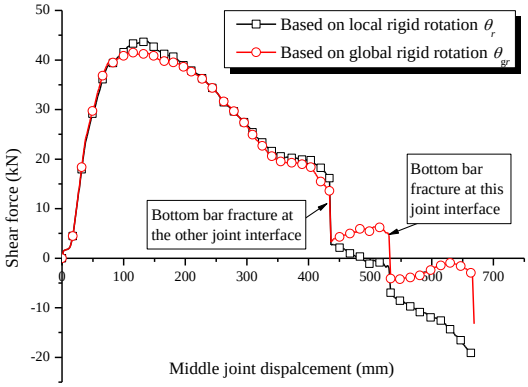

(c) Shear force at the beam section connected to the joint interface

Fig. 4.24: Variations of cross-sectional forces of S5-1.24/1.24/23

Similar to the bending moment acting at the joint interface, shear force increases first and then keeps decreasing after attaining its peak value, as shown in **Fig. 4.24(c)**. Unlike the axial force, after bottom bar fracture, the shear force is significantly affected by the type of rotations. At catenary action stage, the sectional shear force is solely contributed by dowel action of longitudinal bars. Therefore, a sudden reduction of shear force follows each fracture of bottom bars. After the

fracture of two bottom bars, the vertical component of shear force based on *local rigid rotation* changes from positive (i.e. up) to negative (i.e. down). This indicates that the shear force does not help to sustain the applied load. At that stage, the negative shear force is mainly induced by the large axial tension at the section near the joint interface not coinciding with that at the beam end. However, if the shear force is evaluated based on the *global rotation*, the shear force at the joint interface is nearly zero. This is because the axial tension throughout the beam is acting at the same beam axis, and no shear force will be induced by axial tension.

4.3.11 Force transfer mechanisms at the middle joint regions

For a deformed beam shown in **Fig. 4.7**, the force equilibrium at the middle joint gives

$$P = \sum_{j=1}^{2} \left(N_j \sin\theta_j + V_j \cos\theta_j \right) \tag{4-2}$$

where P is the applied load acting onto the middle joint (or the structural resistance), N_j and V_j are the beam axial force and the shear force transferred from beams to both joint interfaces, respectively, and θ_j is the rotation at the beam sections connected to the joint interfaces. θ_j should be evaluated by local rotation to more accurately study the force transfer mechanism near the middle joint, but θ_j can also be estimated by global rotation for simplicity.

Eq. (4-2) indicates that vertical resistance can be divided into two components, i.e. vertical components of the axial force and shear force throughout the beams. Since the shear force can be determined from the bending moments acting at the beams, the second term on the right hand side of Eq. (4-2) equivalently represents the contribution from bending moments as well. **Fig. 4.25** shows the variations of each component of vertical resistance vs. MJD. The components are determined based on local rigid rotation θ_r to illustrate the force transfer mechanisms near the middle joint. For simplicity, specimens S5, S7 and S8 are selected to show the decomposition of the vertical resistance.

A second increase of structural resistance after CAA capacities, as shown in **Figs. 4.24(a)** and **(b)**, is mainly caused by the vertical component of axial force changing from compression to tension. Further development of catenary action with axial tension leads to a significant increase of structural resistance. After the onset of catenary action, the contribution from axial tension increases while that from shear force decreases with increasing MJD. However, prior to bottom bar fracture, the shear force still substantially contributes to structural resistance. This indicates that although catenary action is a tensile mechanism, structural resistance at *catenary action stage* is not solely contributed by tension. Therefore, the vertical components of axial tension cannot be simply summed as structural resistance. After the fracture of bottom bars at both middle joint interfaces, the vertical component of shear force provided by dowel action of top bars changes direction and fails to help balance the applied load.

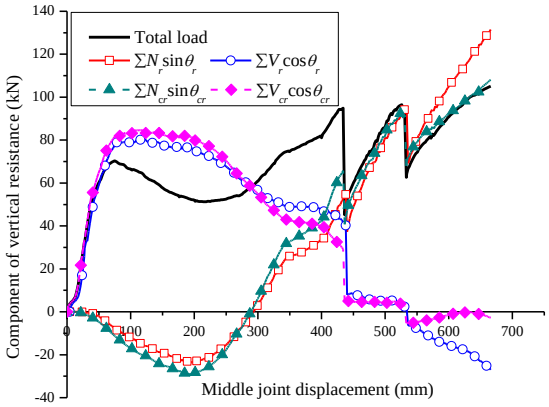

(a) Specimen S5-1.24/1.24/23

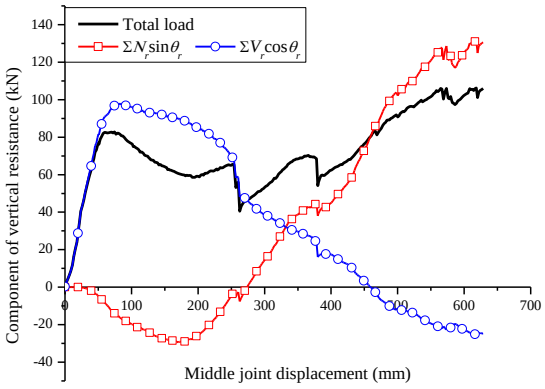

(b) Specimen S7-1.24/0.82/18.2

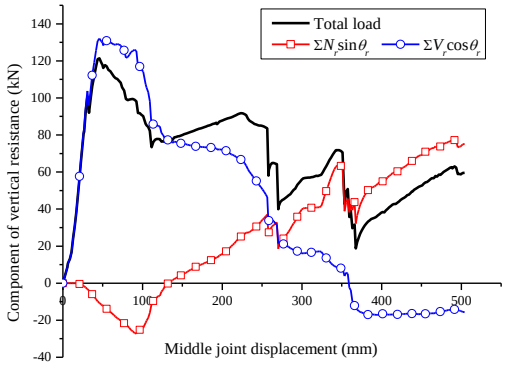

(c) Specimen S8-1.24/0.82/13.4

Fig. 4.25: Decomposition of vertical structural resistance

Catenary action of S8 was mobilized when the beam axial force changed from compression to tension at the MJD of 136 mm, but the axial tension failed to increase structural resistance significantly due to consecutive bar fracture, as shown in **Fig. 4.25(c)**. The shear failure shown in **Fig. 4.20(b)**, comprising the occurrence of a large inclined crack and the fracture of two stirrups, caused a sudden reduction of shear force at a MJD of around 100 mm, as shown in **Fig. 4.25(c)**. Shear failure in S8 rendered it unable to sustain large vertical loads, and shear cracks also damaged the compression zone near the joint interfaces. As a result, the beam axial compression decreased rapidly, and catenary action had to be mobilized at a relatively smaller displacement. This suggests that shear failure can cause early mobilization of catenary action, but catenary action might not increase the structural resistance beyond CAA capacity.

In practice, it is convenient to use the sum of vertical components of axial tension (i.e. $\sum_{j=1}^{2} N_j \sin\theta_j$) to estimate structural resistance P at catenary action stage by assuming the beams to rotate as rigid bodies. That is, θ_j equals to global chord rotation θ_{gr}. **Fig. 4.25(a)** indicates that this assumption can satisfy the equilibrium $P = 2N_{gr}\sin\theta_{gr}$ after the fracture of the bottom bars.

4.3.12 Variations of strains over reinforcing bars

Fig. 4.26 shows the strain profiles over longitudinal reinforcing bars under different MJDs, in which the solid lines with hollow dots denote bar strains at catenary action stage. Specimen S4 is a typical example to represent the strain variations of top and bottom continuous reinforcing bars for specimens S4, S5, S7 and S8, as shown in **Figs. 4.26(a)** and **(b)**. A bottom bar of S6 in **Fig. 4.26(c)** shows the strain variations of lap-spliced reinforcing bars used in S3 and S6.

Based on a bending moment diagram over a beam, a beam can be divided into a positive moment (PM) region, a negative moment (NM) region, and a transition region which connects these two regions. The bottom bars in the PM region (i.e. near the middle joint) and the top bars in the NM region (i.e. near the end-column-stub interface) were in tension throughout the whole loading process, as shown in

Fig. 4.26. In the PM region, the bottom bars yielded in tension at a small MJD of 29.6 mm for S4 as shown in **Fig. 4.26(b)**, followed by severe strain concentration at both joint interfaces. Similarly, **Fig. 4.26(c)** shows that the gradient of lap-spliced bar strains at the joint interfaces suddenly became steep when approaching CAA capacity at a MJD of 81 mm, indicating the occurrence of local strain concentration. In the NM region, beyond a MJD of 200.6 mm, the concentration of top bar strains occurred at the end-column-stub interfaces, as shown in **Fig. 4.26(a)**.

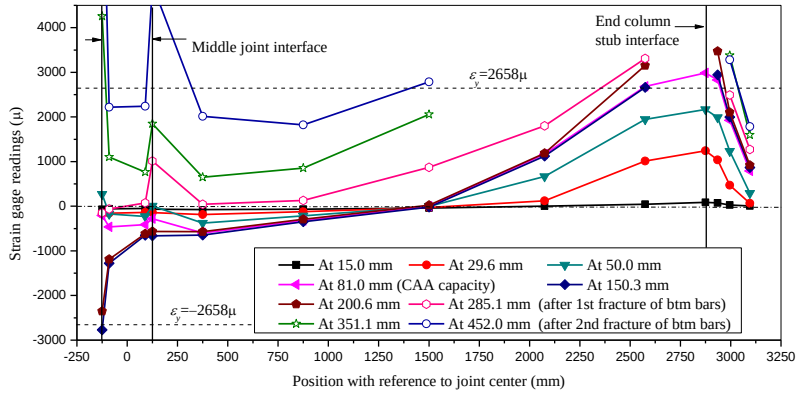

(a) Top reinforcement along S4-1.24/0.82/23

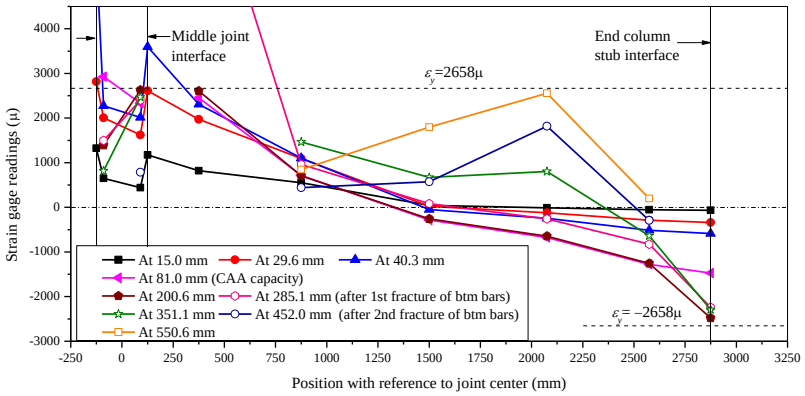

(b) Bottom reinforcement along S4-1.24/0.82/23

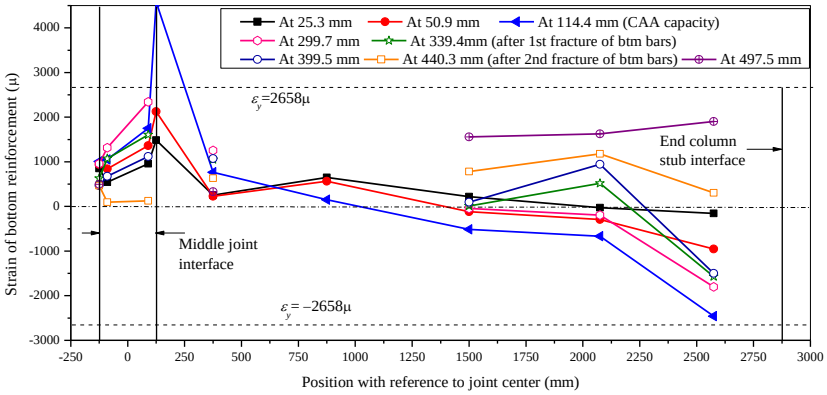

(c) Bottom reinforcement along S6-1.87/0.82/23

Fig. 4.26: Variations of longitudinal reinforcement strains

In the PM region, the top bars were initially in compression and then changed to tension at catenary action stage. The strain concentration at the joint interfaces of S4 started at a MJD of 452 mm, as shown in **Fig. 4.26(a)**, indicating that the top bars were the main component to transmit the vertical force after bottom bars had fractured. In the NM region, the bottom bars near the beam end changed from large compression to small tension at catenary action stage, as shown in **Figs. 4.26(b)** and **(c)**.

Due to large tensile strains at the joint interfaces and the end column stub interfaces, the yielding strain penetration occurred inside the middle joint and the end column stubs, as shown in **Figs. 4.26(a)** and **(b)**, resulting in a severe loss of bond stress and large increment of bar slip at the interfaces. These can increase the rotation capacity of RC beams.

The strains of reinforcing bars in the transition region did not vary significantly, but finally both the top and bottom bars sustained tension at catenary action stage even if the bottom bars had fractured at the joint interfaces. **Figs. 4.26(b)** and **(c)** show that the bottom bars away from the joint interfaces for a certain distance could still contribute to axial tension force in the beam. The tension force in the bottom bars was transmitted via stirrups to the top bars, since the strain gage readings of stirrups indicate that the stirrups kept sustaining the tensile force even after bottom bars had fractured, as shown in **Fig. 4.27**.

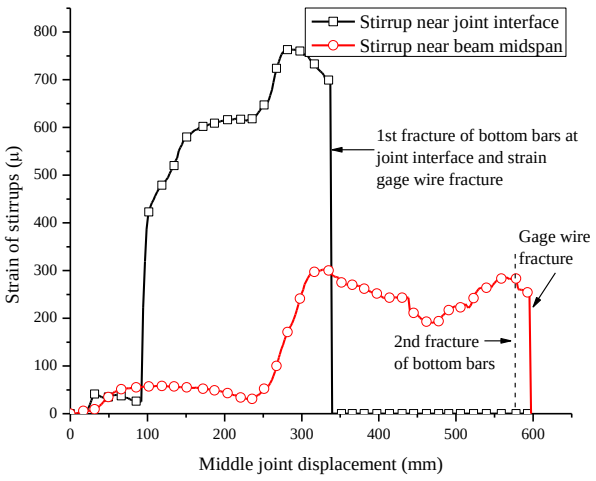

Fig. 4.27: Strains of stirrups in specimen S6

4.3.13 Discussions on criterion of catenary action capacity

So far there is no criterion to define the capacity of catenary action. **Fig. 4.25(a)** shows that catenary action capacity of a sub-assemblage can be estimated by $P = 2N_{gr}\sin\theta_{gr}$ after the fracture of bottom bars, in which N_{gr} and θ_{gr} are the axial tension and the global chord rotation of the "single-bay" beams in the sub-assemblage, respectively. N_{gr} is affected by bar stress and fracture. Unlike a reinforcing bar in a uniaxial tensile test, the longitudinal bars in beams are under a combined action of shear and tension. Therefore, reinforcing bars may not fully attain the tensile strength. As shown in **Fig. 4.15(b)**, the top bars fractured with the stress between the yield strength and the ultimate tensile strength. The strain profiles in **Fig. 4.26(a)** indicate the severe strain concentration of the top bars at the middle joint interfaces and the end-column-stub interfaces. The strain concentration may cause premature fracture of bars. θ_{gr} depends on the MJD and the net span of a "single-bay" beam in a sub-assemblage. Nevertheless, it is difficult and impractical to precisely predict the MJD corresponding to the fracture of reinforcing bars. Except specimens S5 and S8, all the other specimens attained catenary action capacity at the fracture of top bars. Note that the bottom bar fracture at joint interfaces preceded the fracture of top bars at beam ends. Due to symmetrical reinforcement, S5 attained the capacity of catenary action when bottom bars fractured. However, for typical RC frames, the bottom reinforcement at the joint regions is less than the top reinforcement. If the allowable MJD is restricted to the value corresponding to the fracture of bottom bars, the structural resistance from catenary action will be too conservative.

Table 4.6 shows that ultimate MJDs of specimens S3-S7 exceeded 10% of total beam span length, and the corresponding structural resistances P_{t3} are much higher than CAA capacities P_{caa}. Therefore, a simple analytical approach to predict the capacity of catenary action P_t is proposed as follows:

$$P_t = 2 f_y A_{s\_top} \sin\theta_{\max} \tag{4-3}$$

where f_y and A_{s_top} are the yield strength and the area of top reinforcing bars at the middle joint interfaces or the beam ends, respectively; $\theta_{\max}$ is the global rotation of beams corresponding to the MJD equal to 10% of total two-bay beam span length, i.e. 11.3°, which is also recommended in UFC 4-023-03.

It is conservative to limit the steel strength to yield strength and ignore the contribution from bottom bars, in particular, for beams with symmetrical longitudinal reinforcement, such as S5. Additionally, before taking account of catenary action, CAA capacity and maximum shear resistance should be compared to insure that no premature shear failure will occur. Otherwise, even if catenary action is mobilized, the structural resistance may not be increased further, as evidenced by the behavior of S8.

4.4 Summaries and conclusions

Totally, eight simplified beam-column sub-assemblages were tested under a point load and adequate axial and rotational restraints to simulate the structural behavior of RC beams and joints under a middle column removal scenario. Based on the observations and the analyses of experimental results, the following conclusions can be arrived:

(1) With *adequate axial and rotational restraints*, the RC sub-assemblages developed compressive arch action (CAA) and catenary action on top of flexural action. CAA capacity was 13.5%~43.2% larger than flexural capacity calculated via the mechanism that plastic hinges occurred near the middle joint interfaces and the end-column-stub interfaces. The capacity of catenary action was 28%~128% greater than CAA capacity for specimens S1 to S7.

(2) After the occurrence of shear failure in specimen S8, catenary action had to be mobilized at a relatively smaller MJD of around 136 mm, whereas catenary action commenced at around one beam depth (250 mm) for specimens S1 to S7. In other words, provided that shear failure of RC

beams can be prevented, *one beam depth* can be regarded as the deflection corresponding to the *onset of catenary action*. Moreover, the MJD of all sub-assemblage specimens could slightly exceed 10% of total net span length of the two-bay beams prior to complete failure.

(3) CAA is a favorable ALP in terms of small beam deflections as catenary action requires much larger deformations. In the sub-assemblage tests, CAA attained its capacity at a MJD of 0.18~0.46*h*, whereas catenary action achieved its capacity at a MJD greater than 2*h*.

(4) The axial force-MJD relationship is almost the same as the horizontal reaction force-MJD relationship. After the onset of catenary action, both bending moment and shear force continue to resist the applied load even at catenary action stage. Therefore, it is necessary to differentiate *catenary action* and *catenary action stage*. Catenary action is a tensile mechanism associated with the development of beam axial tension. However, at catenary action stage, catenary action is not the sole contributor to structural resistance because the vertical component of shear force also helps to sustain the vertical load. The shear force is induced by the bending moment along the beam and is sustained by dowel action of longitudinal bars. Therefore, each fracture of longitudinal bars causes a reduction of axial tension and shear force. At catenary action stage, the contribution from beam axial tension keeps increasing whereas that from shear keeps decreasing. Whether catenary action can increase the structural resistance depends on whether the contribution of beam axial tension can exceed the loss in shear.

(5) The failure modes and the bar strain gage readings indicate that all specimens failed at the middle joint interfaces and the end column stub interfaces with occurrences of wide cracks and fracture of reinforcement. Prior to bar fracture, severe strain localization occurred at these interfaces. Therefore, if high catenary action capacity is expected at a relatively smaller deflection during structure design, measures should be taken to reduce local strain concentration.

(6) Specimen S1 with seismic detailing has no obvious advantage over specimen S2 with non-seismic detailing in terms of developing catenary action. This is because the structural mechanisms were dominated by flexural and axial action, and the advantage of seismic detailing in shear resistance cannot be fully realized. Moreover, even Class A lap-splice specified in ACI 318-05 can meet the requirements of continuity of reinforcing bars.

(7) Parametric study suggests that CAA can significantly increase the structural resistance of the sub-assemblages with small span-to-depth ratio and low longitudinal reinforcement ratio, and catenary action can significantly increase the structural resistance of the sub-assemblages with large span-to-depth ratio and high longitudinal reinforcement ratio, particularly with high top reinforcement ratio. The detailing with symmetrical longitudinal reinforcement seems more favorable to catenary action, e.g. S5, since catenary action capacity can be attained at a smaller MJD. However, before taking account of catenary action, it is necessary to compare CAA capacity and shear capacity, in particular for the case with short span, e.g. S8. If shear failure occurs first, catenary action can be mobilized early, but the latter may not be able to compensate for the loss of structural resistance due to shear failure. Consequently, the structural resistance cannot be increased significantly.

CHAPTER 5 EXPERIMENTAL RESULTS OF REINFORCED CONCRETE BEAM-COLUMN FRAMES

5.1 Introduction

According to the frame specimen design, test set-up and instrumentation introduced in Chapter 3, experimental results of the RC beam-column frames under a middle column removal scenario will be presented in this chapter. Different from the sub-assemblage tests, the effects of detailing and boundary conditions on overall structural behavior and side joint behavior are the main concerns in the frame tests. Specimens F1 to F4 were designed with conventional detailing in accordance with ACI 318-05, whereas specimens F5 to F7 were designed with special detailing, aiming to improve the rotation capacities of RC beams so as to improve the capacity of catenary action. As for boundary conditions, apart from specimens F3 and F4, all the other specimens included the beam extensions, which represent continuity and axial restraints from adjacent bays to a two-bay beam above a removed column. The detailed information of the frame specimens can be referred to section 3.3.2.

The experimental results of the frame specimens will be illustrated and discussed at structural and fiber levels. At structural level, the results include the following parts: (1) Load-deflection history, i.e., relationships of applied load vs. middle joint displacement (MJD) and total horizontal reaction force vs. MJD; (2) Contribution of horizontal reactions from each horizontal restraint; (3) Crack patterns and failure modes of each specimen; (4) lateral deflections of side columns; and (5) side joint distortions. The results at fiber level are the strain variations of reinforcing bars near the joint interfaces and within the joint panels.

For each specimen, load-deflection history shows the overall picture of structural mechanisms, and crack patterns explain structural mechanisms at different stages in detail. Furthermore, variations of the horizontal reaction force of each restraint and column deflection profiles supplement a more thorough understanding to structural mechanisms and crack patterns. Investigation on strains of reinforcement sheds light on the contributions of reinforcement to different structural mechanisms.

Finally, comparisons of load-deflection history of the specimens with special detailing (F5-SD-MR, F6-SD-PD and F7-SD-PH) and with conventional detailing (F1-CD-NS)) illustrate the advantages of special detailing over conventional detailing in mitigation against progressive collapse. Comparisons of load-deflection history of specimens F1-CD-NS and F3-CD-NS-EX, as well as F2-CD-WS and F4-CD-WS-EX, elucidate the effects of boundary conditions on structural mechanisms. "CD" and "SD" in the specimen notation indicate conventional detailing and special detailing, respectively. "WS" and "NS" stand for with seismic detailing and with non-seismic detailing, respectively. "EX" represents specimens with exterior joints. "MR", "PD" and "PH" respectively denote special detailing with additional *middle reinforcement* layer throughout the entire beam length, *partial debonding* of bottom bars at the joint regions and *partial hinges* near the joint interfaces.

5.2 Material properties

Material tests were conducted according to ASTM specifications to obtain the representative strengths of concrete and steel reinforcement. The tests included tensile tests for steel reinforcement, compressive cylinder and split-cylinder tests for concrete. Concrete cylinders were tested after 28 days and during the period of frame tests. The material properties of steel reinforcement and concrete are listed in **Tables 5.1** and **5.2**, respectively. The fracture strain corresponds to the tensile strength of reinforcement. Specimens F1, F3, F5 and F7 were cast with the same batch of concrete, and the remaining specimens in another batch.

Table 5.1 Material properties of reinforcement in RC frame specimens

Rebar type*	Nominal diameter (mm)	Yield strength f_y (MPa)	Elastic Modulus E_s (MPa)	Strain at the start of hardening ε_{sh} (%)	Tensile strength f_u (MPa)	Ultimate strain ε_u (%)
R6	6	442	209397	--	513	--
T10	10	520	187090	4.12	595	13.70
T13	13	488	170125	2.86	586	11.00

*:"R" and "T" denote low-yield and high-yield strength reinforcement, with a nominal yield strength of 250 MPa and 460 MPa, respectively.

Table 5.2 Material properties of concrete in RC frame spcimens

Concrete	Compressive strength f_c'(MPa)	Elastic modulus E_c (MPa)	Strain ε_c (μ) at f_c'	Tensile strength f_t (MPa)
Specimens F1, F3, F5 & F7	29.69	25473	2436	3.34
Specimens F2, F4 & F6	27.54	22859	2302	2.15

5.3 Experimental results and discussions

Fig. 5.1 provides the specifications of a specimen, including the joint names and the notations of the reaction force at each restraint (i.e., H_1 to H_6, V_1 and V_2) and the constant axial force at each side column (i.e., P_1 and P_2). These notations help to elucidate the test results in the ensuing sections. Note that specimens F3-CD-EX-NS and F4-CD-EX-WS are the only two specimens that do not include any beam extensions. During the testing, fracture of reinforcing bars occurred near the middle joint and side joint interfaces. The beam-column connections are defined in the shaded regions in **Fig. 5.1** according to UFC 4-023-03, consisting of the joint interfaces and the beam ends. Therefore, it can also say that bar fracture occurred within the beam-column connections.

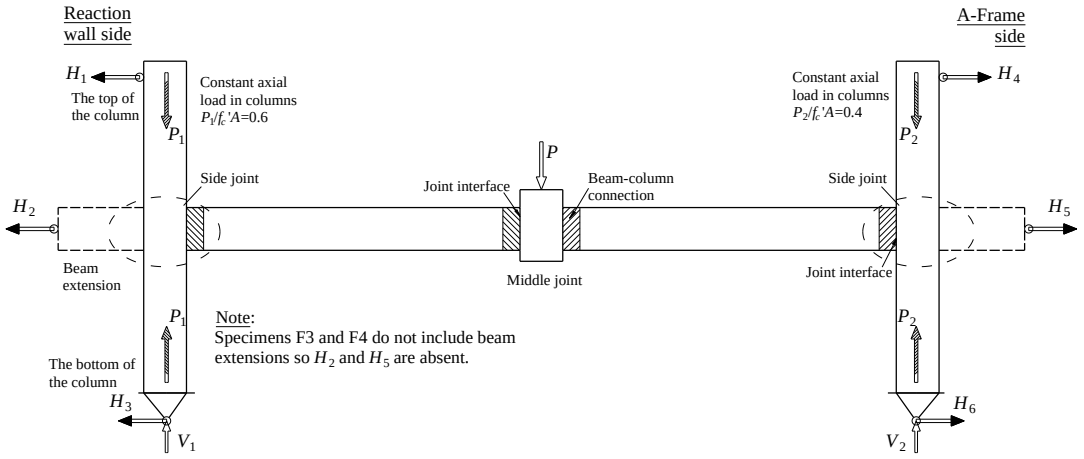

Fig. 5.1: Specifications of an RC frame specimen

With increasing middle joint displacement (MJD), all frame specimens developed structural mechanisms sequentially, i.e. flexural action, compressive arch action (CAA) and catenary action (CTA). **Table 5.3** summarizes critical structural

resistance and corresponding displacements. The MJDs corresponding to CAA capacity ranged from 0.25 to 0.38 beam depth, and the MJDs at the onset of catenary action ranged from 0.95 to 1.29 beam depth. For specimens F1 to F4, structural resistance due to catenary action was not improved significantly. As indicated by the shaded area in **Table 5.3**, the maximum resistance due to catenary action is less than that due to CAA. This was caused by premature fracture of top bars near the side beam-column joint interfaces. For specimens F5 to F7, the structural capacities due to catenary action exceeded the values from CAA by 56% to 120%.

Table 5.3 Summary of frame test results

Specimen	Capacity of Compressive arch action P_{CAA} (kN)	MJD at P_{CAA} (mm)	Max. axial compression $N_{c,max}$ (kN)	MJD at onset of catenary action (mm)	Max. resistance of catenary action P_{CTA} (kN)	MJD at P_{CTA} (mm)	Max. axial tension $N_{t,max}$ (kN)
F1-CD-NS	51.10	61.4	-88.87	306.5	46.27	462.8	163.42
F2-CD-WS	50.75	84.8	-89.74	321.8	43.46	528.0	159.60
F3-CD-NS-EX	45.90	84.4	-48.90	310.7	35.87	524.6	145.32
F4-CD-WS-EX	50.13	83.4	-48.00	320.8	33.37	597.6	155.24
F5-SD-MR	62.84	87.0	-69.71	274.5	98.04	552.4	246.25
F6-SD-PD	45.78	77.4	-43.93	236.4	82.91	527.6	238.15
F7-SD-PH	47.77	94.8	-55.97	274.8	105.04	562.1	256.43

5.3.1 Load-deflection history of RC frames

5.3.1.1 Load-deflection history of specimens F1 and F2

Specimens F1 and F2 were designed with conventional detailing. Except for the arrangement of stirrups in the beams and the columns and horizontal hoops in the joints, all the other detailing for the two specimens was identical. The stirrups in F1 and F2 were designed with non-seismic and seismic detailing, respectively.

Fig. 5.2(a) shows the applied load vs. MJD relationships of F1 and F2. It can be found that their overall trends were quite similar and the capacities of CAA were close to each other. However, due to sequential fracture of beam reinforcing bars, in particular the fracture of top bars near the side joint interfaces, catenary action did not increase structural resistance significantly, not even exceeding CAA capacity. The slight differences in the structural resistance of F1 and F2 at catenary action stage resulted from the sequence of bar fracture. Prior to complete fracture of bottom bars near the middle joint interfaces, structural resistance was contributed by both axial tension and vertical shear (or bending moment). Thereafter, vertical shear diminished rapidly, and structural resistance was solely contributed by axial tension. Thus, the structural resistance of F1 was much greater than that of F2 at the MJDs between 400 mm and 470 mm.

Fig. 5.2(b) demonstrates that the variations of horizontal reaction forces vs. MJD of F1 and F2 were very similar and the commencement of catenary action was around a MJD of 300 mm for both F1 and F2. The similar ultimate axial tension resulted in the close ultimate structural resistance, as shown in **Fig. 5.2(a)**.

The aforementioned comparisons of F1 an F2 suggest that seismic detailing in terms of the arrangement of stirrups in structural members and the provision of hoops in beam-column joints do not significantly affect the structural behavior of RC frames under a middle column removal scenario.

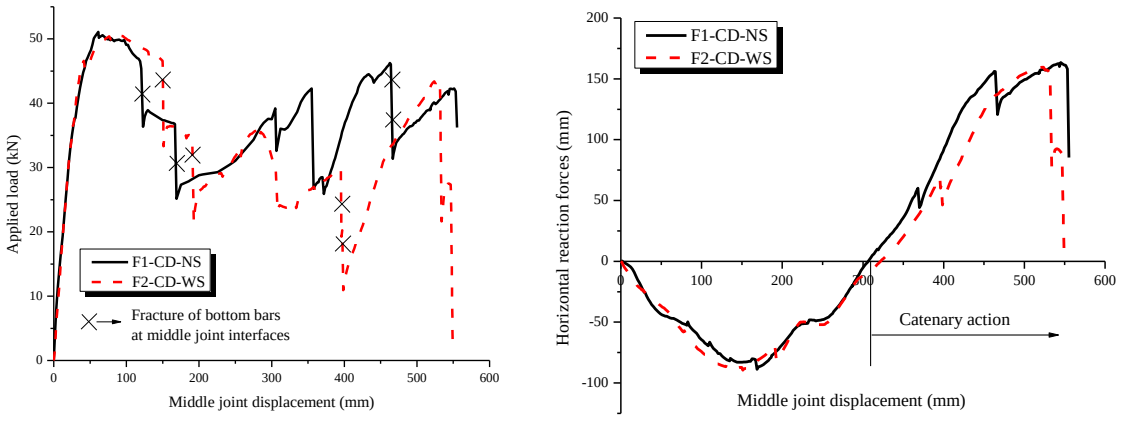

(a) Applied loads (b) Horizontal reaction forces

Fig. 5.2: Applied load and horizontal reaction force vs. MJD of F1 and F2

5.3.1.2 Load-deflection history of specimens F3 and F4

Fig. 5.3(a) shows similar applied load vs. MJD relationships for both F3 and F4. The CAA capacity of F4 was greater than that of F3, although the compressive strength of concrete in F4 was weaker than that in F3. This indicates that the confinement effect due to closer stirrups could slightly contribute to the structural resistance of F4. It can be seen that after fracture of two bottom bars near one middle joint interface, structural resistance was reduced significantly for both F3 and F4. Although catenary action was mobilized, it did not increase structural resistance beyond CAA capacity due to the fracture of top bars at the side joint interfaces.

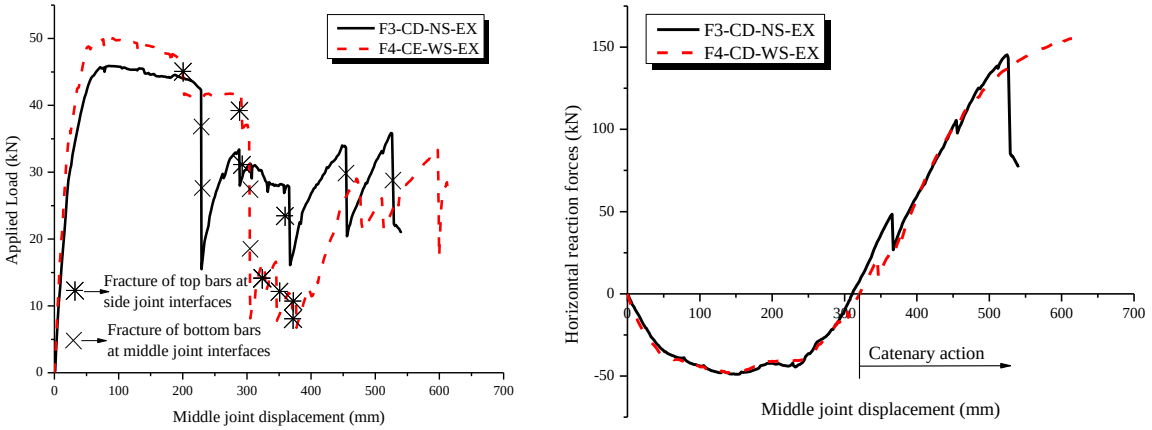

(a) Applied loads (b) Horizontal reaction forces

Fig. 5.3: Applied load and horizontal reaction vs. MJD of F3 and F4

Fig. 5.3(b) shows that the variations of horizontal reaction forces were quite similar for both F3 and F4. The axial forces changed from compression to tension at around a MJD of 310 mm, indicating the commencement of catenary action. It is noted that a similar axial force in **Fig. 5.3(b)** resulted in different structural resistance in **Fig. 5.3(a)**. This phenomenon resulted from the fracture of bars at different locations. As illustrated in the left part of **Fig. 5.4**, when only the bottom bars are fractured at the middle joint interface, the axial force along the beam is determined as

$$N = V_1 \sin\theta + \sum H_i \cos\theta \qquad (5\text{-}1)$$

where V_1 is the vertical reaction beneath a side column; ΣH_i is the total horizontal reactions acting at a side column; and θ is the global chord rotation of a single-bay

beam, equal to $\tan^{-1}(\delta / l_n)$. δ is the MJD (or deflection) and l_n is the net span length of a single-bay beam. Since θ is small and V_1 is much smaller than ΣH_i, the axial force can be estimated as

$$N = \sum H_i \cos\theta \tag{5-2}$$

Therefore, the vertical resistance contributed by catenary action is

$$P_1 = \sum H_i \cos\theta \cdot \sin\theta = \sum H_i \tan\theta \tag{5-3}$$

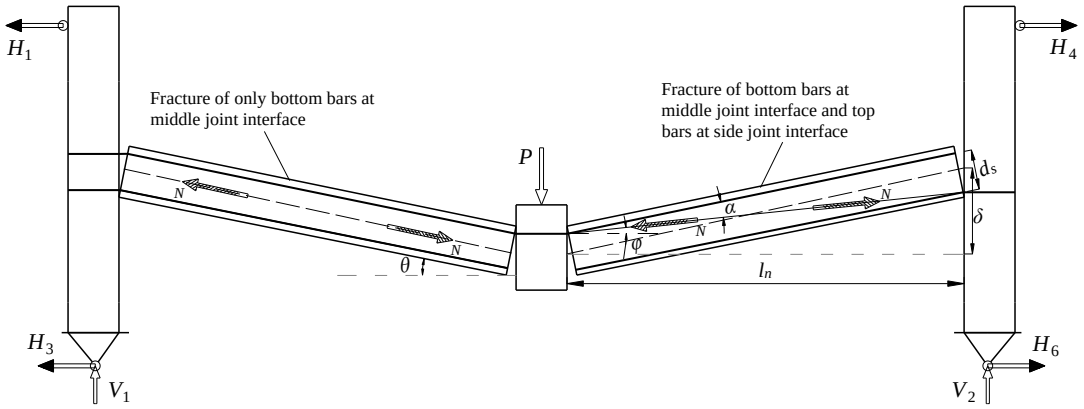

Fig. 5.4: Effect of beam rotation on contribution of axial tension to vertical resistance

Similarly, when the fracture occurs at the bottom bars of a middle joint interface and at the top bars of a side joint interface, as indicated in the right part of **Fig. 5.4**, the vertical resistance contributed by catenary action is

$$P_2 = \sum H_i \tan(\theta - \alpha) \tag{5-4}$$

where α is the angle between the transfer path of axial force and the beam axis. Eq. (5-4) indicates that the fracture of top bars at the side joint interfaces reduces the vertical components of the beam axial forces. Based on geometric relationships, α is determined from the following equation.

$$d_s\left(\tan\theta + \frac{1}{\tan\alpha}\right) = \sqrt{l_n^2 + \delta^2} \tag{5-5}$$

Therefore, α is determined by solving Eq. (5-5).

$$\alpha = \tan^{-1}\left(\frac{l_n d_s}{l_n\sqrt{l_n^2+\delta^2}-\delta d_s}\right) \tag{5-6}$$

where d_s is the distance of the top and bottom reinforcement layers.

For specimen F4, one top bar fractured near the side joint interfaces even earlier than the bottom bars did near the middle joint interfaces. Following the fracture of two bottom bars, all the remaining top bars were severed near the side joint interfaces. Therefore, the structural resistance of F4 is given by Eq. (5-4), which is always much smaller than that of F3 for the same MJDs at catenary action stage.

5.3.1.3 Load-deflection history of specimen F5

Additional reinforcement layer (2T10) was placed at the middle height of beam sections of F5, which was continuous throughout the whole two-bay beam. Under normal conditions, this reinforcement layer does not contribute to structural resistance significantly because it is located near the neutral axis of sections. However, under a middle column removal scenario in the test, severe cracks and fracture of bottom bars occurred near the middle joint interfaces, effective beam depths of beam sections decreased significantly and the additional reinforcement not only facilitated the rotations of shallower beam sections but also offered a higher axial tension capacity.

Fig. 5.5(a) shows the load-deflection history of F5. Catenary action was able to increase structural resistance significantly. At a MJD of 552.4 mm, the structural resistance was 98.04 kN, around 56% larger than CAA capacity. During the development of catenary action, middle reinforcing bars snapped near the middle joint interfaces. **Fig. 5.5(b)** shows the variations of horizontal reaction forces vs. MJD of F5. Axial compression was mobilized initially, followed by axial tension. Catenary action commenced at around a MJD of 275 mm.

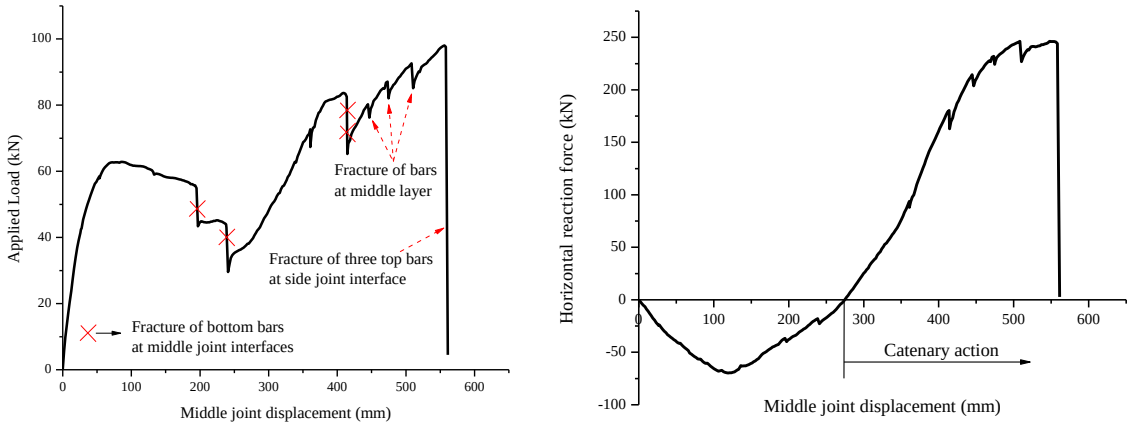

(a) Applied load (b) Horizontal reaction force

Fig. 5.5: Applied load and horizontal reaction force vs. MJD of F5

5.3.1.4 Load-deflection history of specimen F6

High bond strength reduces the slippages of reinforcing bars at cracks and the deflections of beams. Therefore, under normal conditions, a high bond strength offers a high flexural stiffness. However, under a middle column removal scenario, a high bond strength restrains the rotations of beams and causes local strain concentration at cracks, resulting in fracture of reinforcing bars. To eliminate these restraints at large deformations of beams, plastic sleeves were used to wrap the bottom reinforcing bars to separate them from surrounding concrete at the joint regions. The detailing is of F6 shown in **Fig. 3.5(f)**.

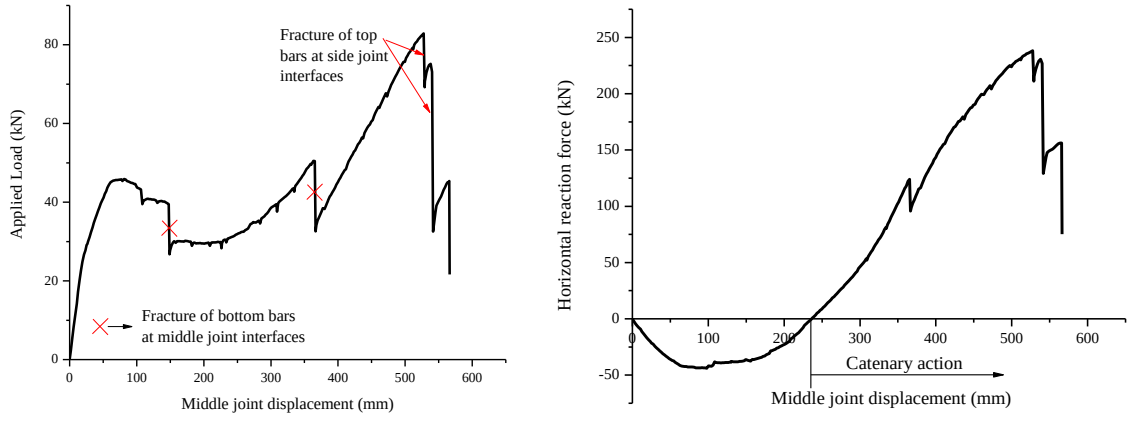

(a) Applied Load (b) Horizontal reaction force

Fig. 5.6: Applied load and horizontal reaction force vs. MJD of F6

Fig. 5.6(a) shows the load-deflection history of F6. After the CAA capacity, catenary action further increased the structural resistance significantly. At a MJD of 527.6 mm, the structural resistance due to catenary action was 82.91 kN, around 81% greater than the CAA capacity. **Fig. 5.6(a)** demonstrates that the partial debonding technique delayed the fracture of one bottom reinforcing bar. The first bottom bar fractured at the debond region of the middle joint at a MJD of 150 mm. The second bar helped to increase the structural resistance to 50.4 kN prior to its fracture at a MJD of 365 mm. The premature fracture of the first bottom bar was probably because cross-sections of the bar were weakened when the bar surface was grinded for mounting strain gages. To confirm the effect of this technique, more tests are required. **Fig. 5.6(b)** demonstrates the variations of the horizontal reaction vs. MJD are similar to those of other specimens. Beam axial force changed from compression to tension at a MJD of 236 mm.

5.3.1.5 Load-deflection history of specimen F7

To improve the rotation capacity of an RC beam, partial hinges were introduced by bending up and down a reinforcing bar to purposely reduce the flexural strength of the beam sections at one beam depth (i.e. 250 mm) away from the joint interfaces. The detailing is shown in **Fig. 3.5(g)**.

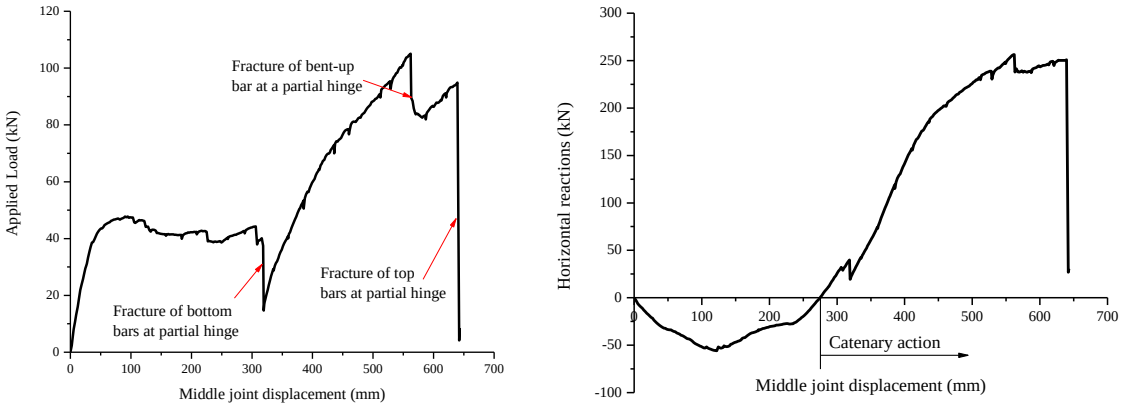

(a) Applied load (b) Horizontal reaction force

Fig. 5.7: Applied load and horizontal reaction force vs. MJD of F7

Fig. 5.7(a) shows the load-deflection history of F7. Similar to other specimens, both CAA and catenary action were mobilized. However, the load-deflection history of

F7 indicates that with the partial hinges, the RC frame specimen could stably provide considerable structural resistance at relatively small MJDs and rapidly increase structural resistance at large MJDs. The large resistance due to CAA was maintained for a wide range of MJDs, from 95 mm to 316 mm. Thereafter, the bottom bars within a partial hinge fractured, followed by a rapid increase of structural resistance due to catenary action. At a MJD of 562.1 mm, catenary action reached its capacity of 105.04 kN, around 2.2 times the CAA capacity. The subsequent fracture of bars at a partial hinge, in particular the snap of top bars, resulted in the complete failure of F7.

Fig. 5.7(b) shows the variations of horizontal reaction forces vs. MJD. Axial forces changed from compression to tension at a MJD of 275 mm. The development of axial tension was much larger than compression. The maximum axial tension was 256.43 kN and the maximum axial compression was only 55.97 kN.

5.3.2 Distributions of horizontal reaction forces

At each side of specimens F1, F2, F5, F6 and F7, the horizontal reactions arise from three restraints, namely, column top, beam extension and column bottom, as indicated in **Fig. 5.1**. For F3 and F4, the horizontal reactions are provided by restraints at the top and the bottom ends of the side columns only.

Figs. 5.8 and **5.9** demonstrate the contribution from each restraint to horizontal reaction forces of F1 and F2, respectively. Several similar observations can be obtained from **Figs. 5.8** and **5.9**:

(1) At CAA stage, in which horizontal reactions are denoted as negative values, horizontal forces were primarily contributed by the restraints at the column bottom (i.e., H_3 and H_6) and secondly by the ends of beam extensions (i.e., H_2 and H_5);
(2) H_2 and H_5 were most sensitive to the fracture of reinforcing bars. Any spike and sudden reduction of the total horizontal reaction were mainly caused by H_2 and H_5 corresponding to bar fracture;
(3) At catenary action stage, in which horizontal reactions are denoted as positive values, the contributions from H_2 and H_5 were the greatest among

all the restraints. The contribution from the restraints at the top of columns (i.e. H_1 and H_4) depended on fracture of top bars near the side joint interfaces. The fracture significantly reduced H_1 and H_4, even less than H_3 and H_6, as indicated in **Figs. 5.8(b)** and **5.9(a)**.

(4) Connection gaps existed at the restraints of the beam extensions because during the initiation of H_2 and H_5 and their transition from negative to positive values, zero values of H_2 and H_5 appeared for a wide range of MJDs.

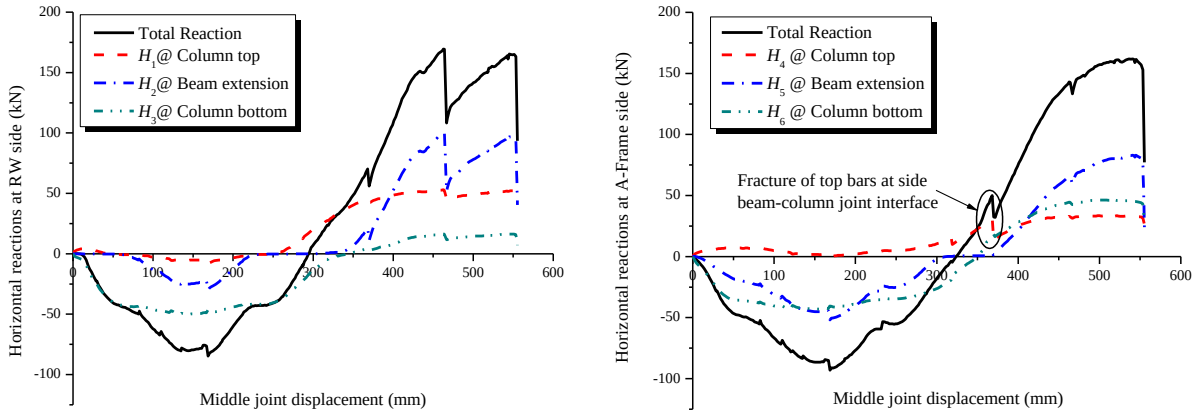

(a) At reaction wall (RW) side (b) At A-Frame side

Fig. 5.8: Contribution of each restraint to horizontal reaction of F1-CD-NS

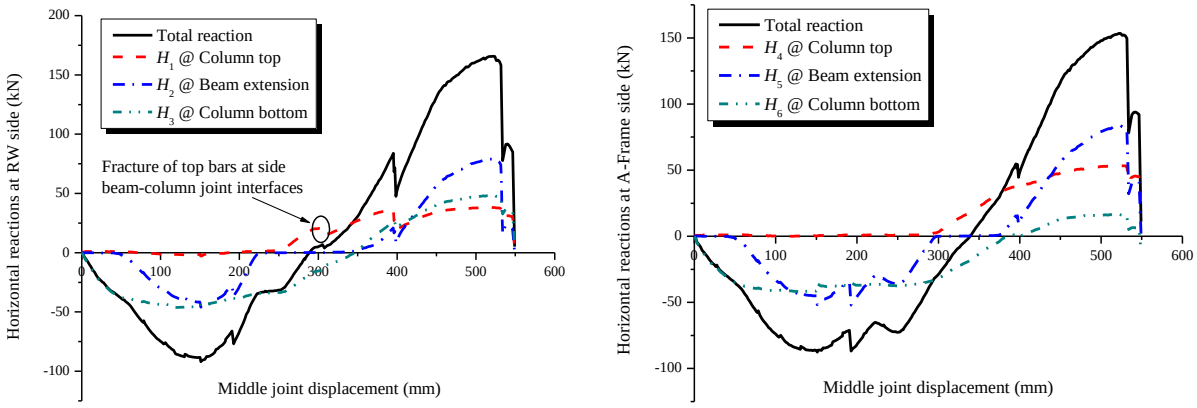

(a) At reaction wall (RW) side (b) At A-Frame side

Fig. 5.9: Contribution of each restraint to horizontal reactions of F2-CD-WS

The top bars near the side joint interfaces of specimens F5, F6 and F7 did not fracture prematurely. As a result, the distributions of horizontal reactions to each restraint at *catenary action stage* are quite similar. For simplicity, only the results of

F6 are presented, as shown in **Fig. 5.10**. It can be found that at the full development of catenary action, the restraints at the beam extensions (i.e., H_2 and H_5) contributed the most to the total horizontal reactions, and the restraints at the top of the side columns were less effective than those at the beam extensions but more effective than those at the bottom of the side columns.

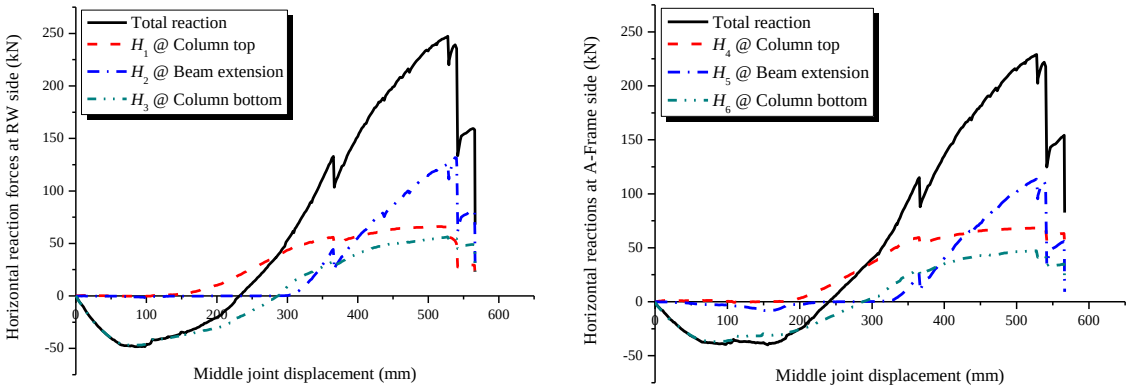

(a) At reaction wall side (b) At A-Frame side

Fig. 5.10: Contribution of each restraint to horizontal reactions of F6-SD-PD

It should also be pointed out that at CAA stage, the negative horizontal reactions of F6-SD-PD and F7-SD-PH were approximately provided by the restraints at the bottom of the columns solely (i.e. H_3 and H_6), as shown in **Fig. 5.10**. This was because connection gaps existed at the ends of the beam extensions. It suggests at CAA stage F6 and F7 sustained applied loads like portal frames.

Due to similarities between the test results of F3 and F4, F3 was selected to represent the distributions of horizontal reactions, as shown in **Fig. 5.11**. The observations are obtained as: (1) the negative horizontal reaction was almost provided by the restraints at the column bottoms solely (i.e. H_3 and H_6) so that F3 and F4 worked as portal frames at CAA stage, similar to F6 and F7; and (2) the premature fracture of top bars at the side joint interfaces reduced the horizontal reactions at the column tops.

In summary, the distribution of horizontal reactions to each restraint at the minimum negative values and the maximum positive values of horizontal reactions are listed in **Table 5.4**. At CAA stage, for specimens with special detailing (F5 to F7) and specimens without beam extensions (F3 and F4), the restraints at the

column bottoms contributed the most reactions. At catenary action, the restraints at the beam extensions provided the most reactions.

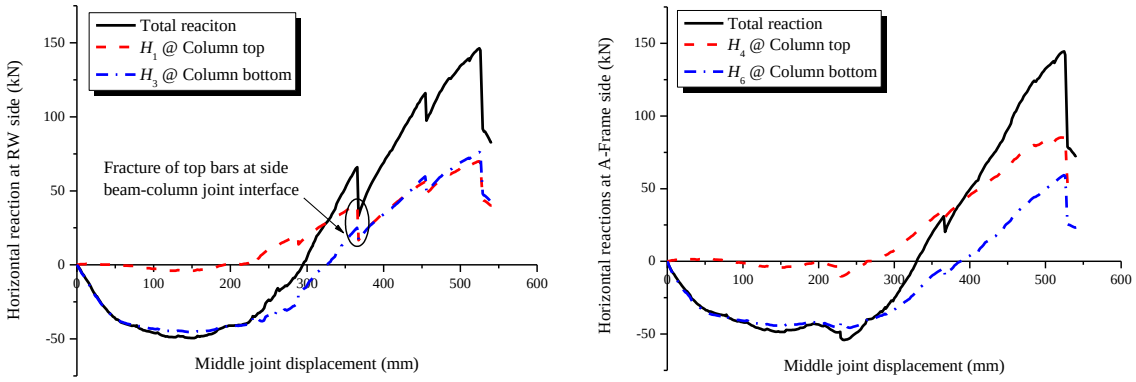

(a) At reaction wall side (b) At A-Frame side

Fig. 5.11: Contribution of each restraint to horizontal reactions of F3-CD-NS-EX

Table 5.4 Distribution of horizontal reactions to each restraint*

No.	H=H_{min} at CAA stage						H=H_{max} at catenary action stage					
	Reaction wall side			A-Frame side			Reaction wall side			A-Frame side		
	$\frac{H_1}{H_{min}}$ (%)	$\frac{H_2}{H_{min}}$ (%)	$\frac{H_3}{H_{min}}$ (%)	$\frac{H_4}{H_{min}}$ (%)	$\frac{H_5}{H_{min}}$ (%)	$\frac{H_6}{H_{min}}$ (%)	$\frac{H_1}{H_{max}}$ (%)	$\frac{H_2}{H_{max}}$ (%)	$\frac{H_3}{H_{max}}$ (%)	$\frac{H_4}{H_{max}}$ (%)	$\frac{H_5}{H_{max}}$ (%)	$\frac{H_6}{H_{max}}$ (%)
F1	10.0	35.4	54.6	0.8	55.9	43.3	31.3	59.1	9.6	20.5	51.3	28.2
F2	3.3	50.3	46.5	0.0	59.4	40.8	23.0	47.8	29.2	34.9	54.5	10.6
F5†	N.A.	45.3	65.7	7.8	18.7	73.5	30.2	54.2	15.6	24.9	59.3	15.0
F6	1.0	3.1	95.9	0.0	7.6	92.4	26.5	50.8	22.8	29.8	49.6	20.6
F7	13.6	4.2	82.2	9.7	13.9	76.4	22.1	59.2	18.7	27.7	56.3	16.0
F3	8.1	N.A.	91.9	8.7	N.A.	91.3	47.9	N.A.	52.1	58.9	N.A.	41.1
F4	7.3	N.A.	92.7	8.3	N.A.	91.7	53.4	N.A.	46.6	47.7	N.A.	52.3

*H_1 to H_6 are indicated in **Fig. 5.1**. H_1 and H_4 are restraints at the top of the columns; H_2 and H_5 are the restraints at the beam extensions; H_3 and H_6 are the restraints at the bottom of the columns.

†when H=H_{min} at CAA stage, H_1 has already changed to tension.

5.3.3 Lateral deflection profiles of side columns of F3 and F4

During the testing of frame specimens F3 and F4, due to adequate continuity of reinforcing bars, large axial forces throughout the two-bay beams were sustained by two side columns and, in turn, the two side columns deformed. However, large lateral deflections (or drifts) of the columns are not expected; otherwise, under large

axial forces along the columns, *P*-delta effect (or second-order effect) will be significant, causing side column failure. In this section, the lateral deflection profiles of the side columns of F3 and F4 will be demonstrated.

Figs. 5.12(a) and **(b)** show the lateral deflection profiles of the side columns of F3 at reaction wall (RW) side and at A-frame (AF) side, respectively. **Figs. 5.13(a)** and **(b)** demonstrate the lateral deflection profiles of the side columns of F4 at RW side and AF side, respectively. The curves with hollow symbols stand for the specimens at CAA stage, and the curves with solid symbols represent the specimens at catenary action stage. The dash dot lines indicate the centroidal axis of each side column. Due to initial imperfections from construction, before loading was applied onto the middle joint and after constant axial loads were applied on the side columns, the side columns had already deflected slightly.

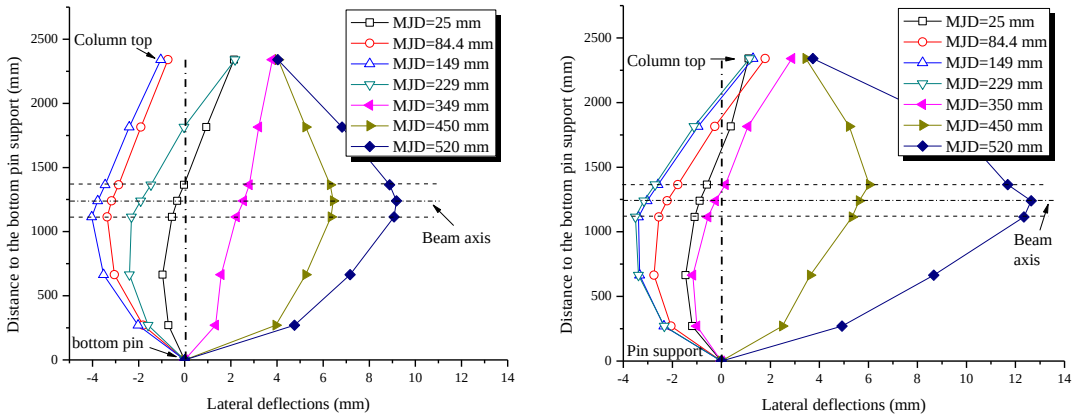

(a) RW side (b) A-Frame side

Fig. 5.12: Lateral deflection profiles of side columns of F3-CD-NS-EX

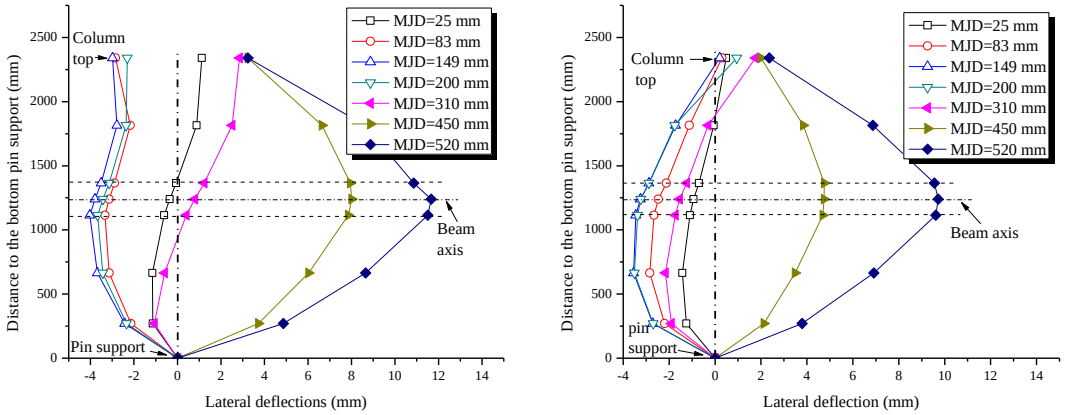

(a) RW side (b) A-Frame side

Fig. 5.13: Lateral deflection profiles of side columns of F4-CD-NS-EX

Overall trends of the lateral deflection profiles of all the side columns of F3 and F4 were similar, and experimental observations are as follows:

(1) The side columns moved outwards at CAA stage and then moved inwards at catenary action stage. At CAA stage, the bottom-half columns deformed more significantly than the top-half columns, arising from large reaction forces at the bottom pin supports, as shown in **Fig. 5.11**.
(2) Furthermore, the lateral column deflection at positions of the exterior joints at catenary action stage was much larger than the one at CAA stage. Therefore, with existing axial loads on the columns, it was very likely that the columns fail due to *P*-delta effect. The test on F3 was terminated due to the side column at the AF side approaching flexural failure. Likewise, although the top bars were severed near both joint interfaces of specimen F4, the columns were still pulled inward through a single layer of bottom bars until they approached flexural failure.

It should be pointed out that the non-zero lateral displacement at the column top resulted from the connection gaps at the column top. Consequently, at CAA stage, both F3 and F4 functioned as portal frames. Prior to a MJD of 250 mm, the top restraints did not provide any reactions. The connection gaps and corresponding restraint stiffness are introduced in Appendix A.

In summary, the side columns moved outwards and then inwards at CAA and catenary action stages, respectively. However, for frame specimens without beam extensions, such as F3 and F4, the large lateral column deflection could result in flexural failure of side columns due to *P*-delta effect. Therefore, catenary action should not be relied upon in practice as it is the precursor to progressive collapse.

5.3.4 Crack patterns and failure modes of RC frames

The overall crack patterns throughout the beams of frames are quite similar to those observed in sub-assemblages. That is, cracks were rather uniformly distributed throughout the whole two-bay beams. Typical failure occurred within the beam-column connections (i.e. near the interfaces of the middle joints and the side joints) rather than within the joint panels. Since the failure near the middle joints consisting

of large cracking, concrete crushing and bar fracture was extensively introduced in Chapter 4, only the failure near the side joints will be highlighted in this chapter.

5.3.4.1 Crack patterns and failure modes of specimens F1 and F2

For simplicity, only F1 is used to demonstrate crack patterns and failure modes, as shown in **Fig. 5.14**. At crack tips, numbers were written down to denote the ratio of a MJD and the beam depth (250 mm in the tests). For example, the number 1/10 represents a MJD of 25 mm, and 6/10 is equal to 150 mm, etc, as shown in **Figs. 5.14(b)** and **(c)**. At the end of the test, catenary action was the dominant structural mechanism. Accordingly, cracks spread throughout the whole two-bay beam. However, there were nearly no cracks at the two side columns, except a few hairline flexural cracks at the joint-column interfaces due to bending moments and hairline inclined cracks at the joint panels due to shear, as shown in **Figs. 5.14(b)** and **(c)**. This indicates that the shear stress at the side joint panels was under a very low level. Cracks at the joint panels initiated at the MJDs of 50 mm and 100 mm for F1 and F2, respectively. The corresponding structural mechanism was CAA.

(a) Overall failure mode

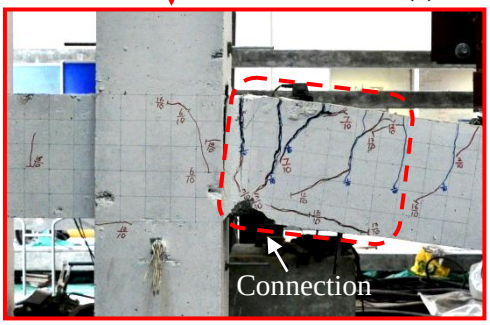

(b) Failure at the side joint towards reaction wall (RW)

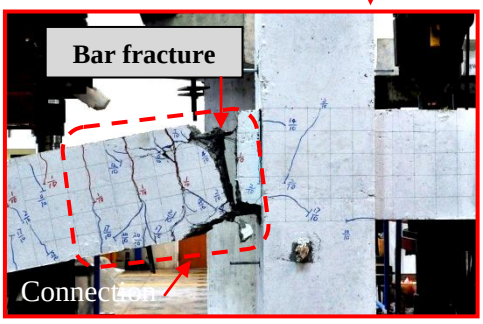

(c) Failure at the side joint towards A-Frame (AF)

Fig. 5.14: Failure modes of specimen F1-CD-NS

F1 eventually failed by fracture of the top bars near a side joint interface, as indicated in **Fig. 5.14(c)**. Also, large cracks and concrete spalling occurred at the beam-column connections, as shown in **Figs. 5.14(b)** and **(c)**, and the bottom bars were completely severed near the middle joint interfaces. Local failures were concentrated at the connections so as to achieve large rotations of beams.

5.3.4.2 Crack patterns and failure modes of specimens F3 and F4

Due to absence of beam extensions, more cracks occurred at the side joints and columns, in particular for F3. **Fig. 5.15(c)** shows that extensive inclined cracks occurred with the side joint panel at AF side, indicating that high shear stress had been mobilized between the MJD of 425 mm and 525 mm, in which the structural mechanism was catenary action. However, due to fracture of top bars at the side joint interface in RW side, as indicated in **Fig. 5.15(b)**, shear stress was not considerably developed at the joint panel. A comparison between the crack patterns within the joint panels shown in **Figs. 5.15(b)** and **(c)** suggests that tension transferred into a joint panel along the top bars was critical to the mobilization of high panel shear stress. On the other hand, axial tension, transferred from the two-bay beam to a side column, caused bending of the side column. As a result, large cracks formed in the column and concrete spalling occurred at one column face, as shown in **Fig. 5.15(c)**.

Due to premature fracture of top bars at both the side joint interfaces of F4, no severe shear cracks can be observed at the two side joint panels, as shown in **Fig. 5.16**. Therefore, the beneficial effect of horizontal hoops at the joint panels on reducing the development of shear cracks was not apparent in the test. At catenary action stage, after fracture of top bars at the side joint interfaces, only the bottom bars transferred tension from the two-bay beam to the two side columns, resulting in a few hairline flexural cracks at the side columns, as shown in **Fig. 5.16**.

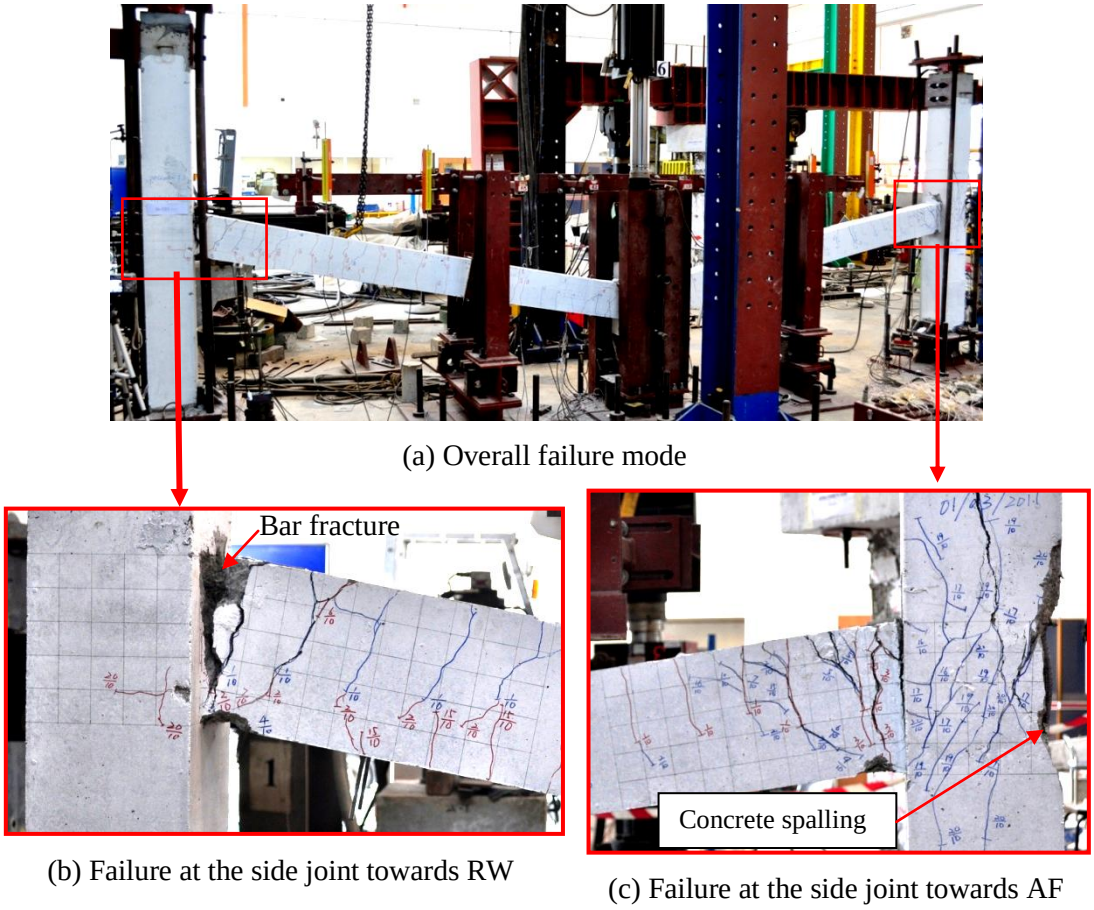

(a) Overall failure mode

(b) Failure at the side joint towards RW

(c) Failure at the side joint towards AF

Fig. 5.15: Failure modes of specimen F3-CD-NS-EX

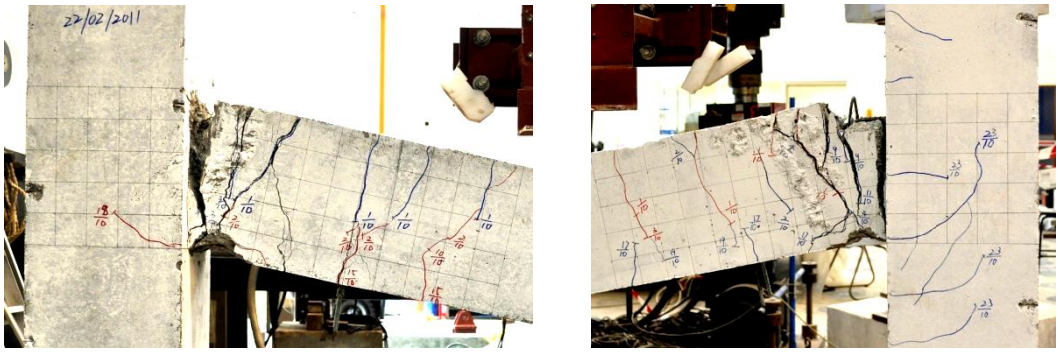

(a) Failure at the side joint towards RW

(b) Failure at the side joint towards AF

Fig. 5.16: Failure modes of specimen F4-CD-WS-EX

5.3.4.3 Crack patterns and failure modes of specimen F5

The development of crack patterns and failure modes of F5 was quite similar to those of F1 and F2. Severe cracks were concentrated within the beam-column connections, and there were a few shear cracks at the joint panels, as shown in **Fig. 5.17**.

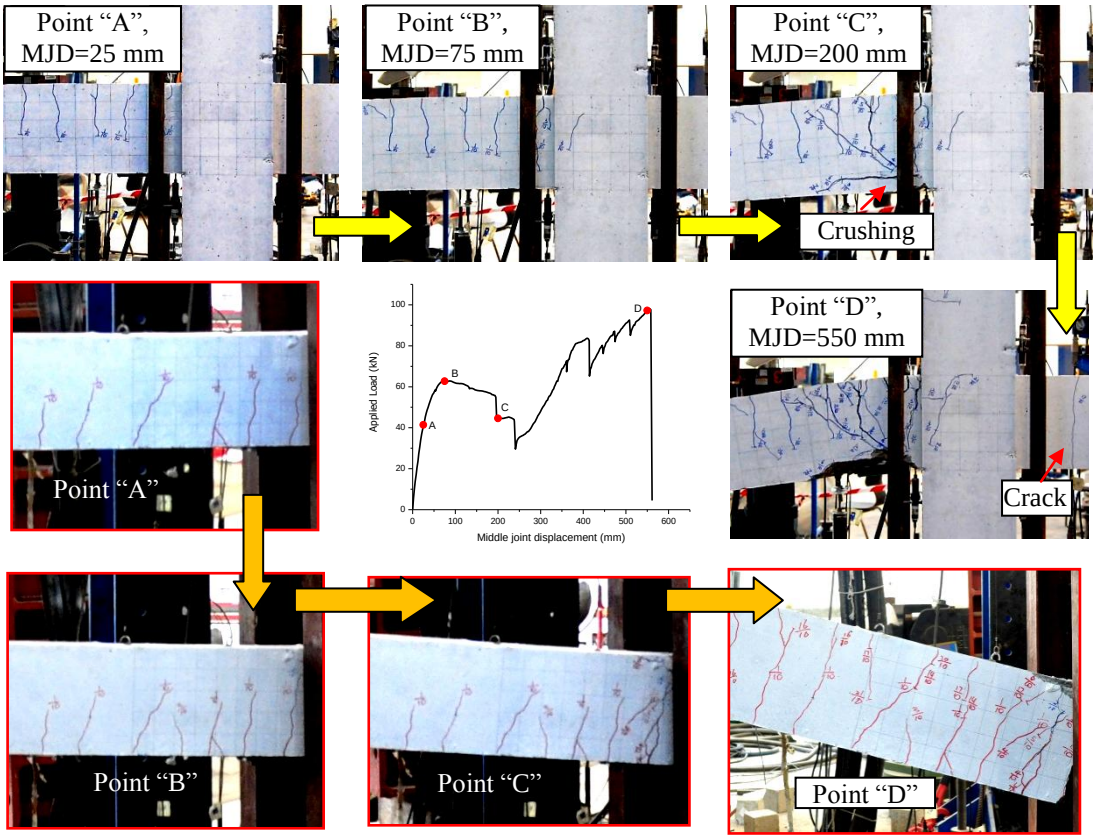

Fig. 5.17: Evolution of crack patterns of specimen F5-SD-MR

The set of figures with red outlines represents the crack patterns of a beam segment adjacent to the middle joint. The other set of figures demonstrates the development of crack patterns of the side joint at AF side. After the capacity of CAA, the decline in structural resistance was associated with crushing of concrete near the middle and side joint interfaces, as indicated in **Fig. 5.17**. The flexural cracks at CAA stage further penetrated the whole beam sections due to axial tension when the structural mechanism "transitioned to" catenary action. A tensile crack at the beam extension initiated at a MJD of 425 mm, indicating that large axial tension transferred through the beam extension. F5 eventually failed by the fracture of all three top bars at one interface of the middle joint.

5.3.4.4 Crack patterns and failure modes of specimen F6

The partial debonding of bottom bars at the joint regions resulted in several new observations which are different from the specimens with conventional detailing:

(1) In the loading process, no flexural cracks were initiated at the debonded zones near the middle joint, as illustrated in **Fig. 5.18(a)**;

(2) Cracks were concentrated at the boundaries of discontinuity, including the boundary of bonded and debonded zones and the beam-column interfaces, as indicated in **Fig. 5.18(a)**;

(3) Severe spalling of concrete occurred within beam-column connections near the side joints where the compressive bars were debonded, as indicated in **Figs. 5.18(b)** and **(c)**.

Moreover, due to large axial tension, wide splitting cracks occurred near one middle joint interface, as shown in **Fig. 5.18(a)**. Specimen F6 failed by the fracture of the top bars at the side joint interface toward RW, as shown in **Fig. 5.18(b)**.

(a) Middle joint

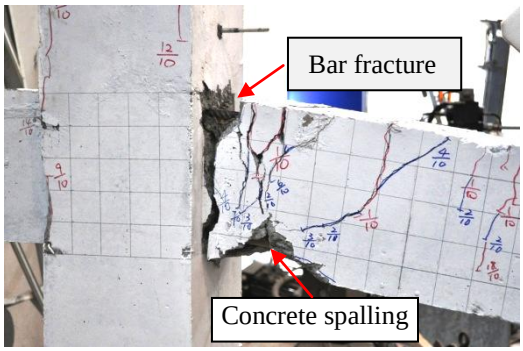

(b) side joint toward RW

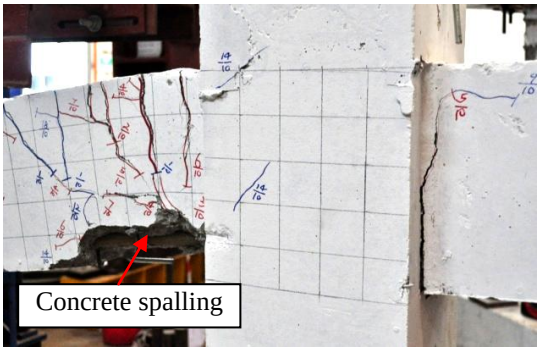

(c) side joint toward AF

Fig. 5.18: Crack patterns and failure modes of specimen F6-SD-PD

5.3.4.5 Crack patterns and failure modes of specimen F7

The development of cracks and failure modes of F7 are shown in **Fig. 5.19**. Due to the presence of partial hinges, the severe local failure including concrete crushing and wide cracks shifted from the joint interfaces to the *locations of partial hinges*,

as highlighted by red dash lines. This suggests that the effective length (or rigid segment) of beams participating in rotating becomes shorter, as illustrated in **Fig. 5.20**. Therefore, for a given MJD, the rotation of the beams of F7 becomes greater.

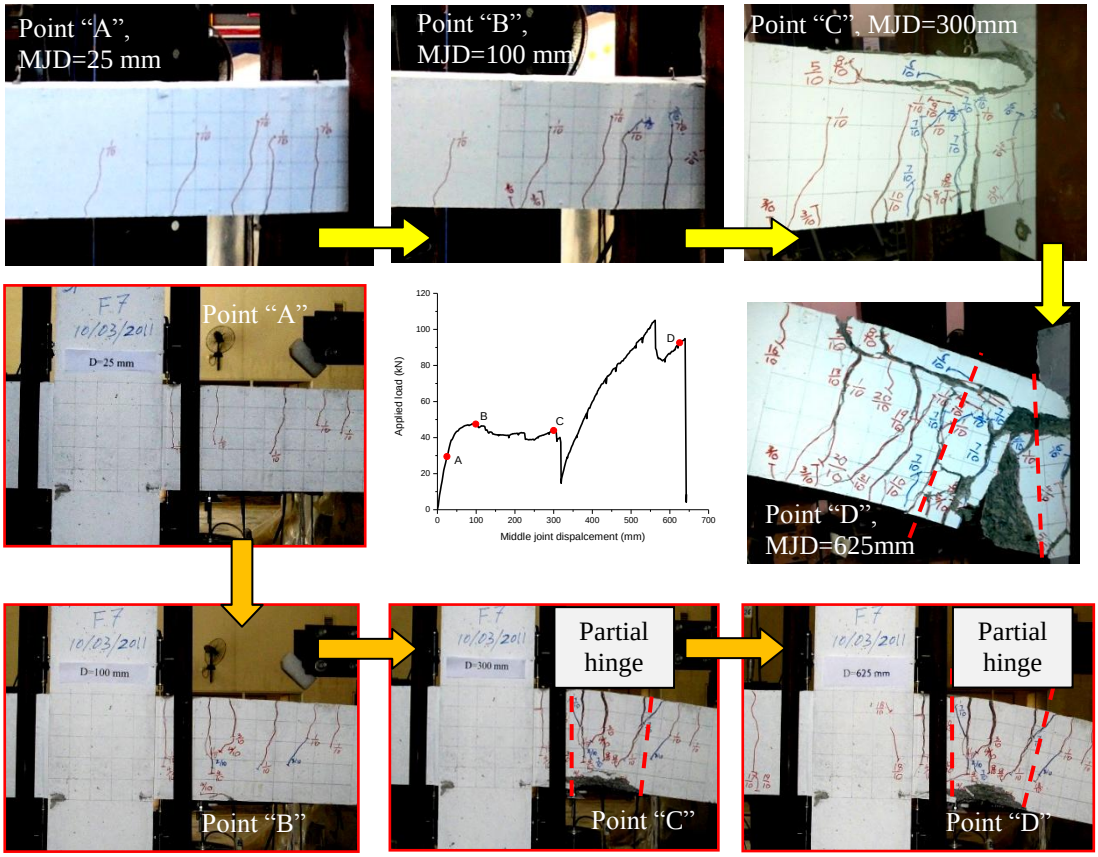

Fig. 5.19: Evolution of crack patterns of specimen F7-SD-PH

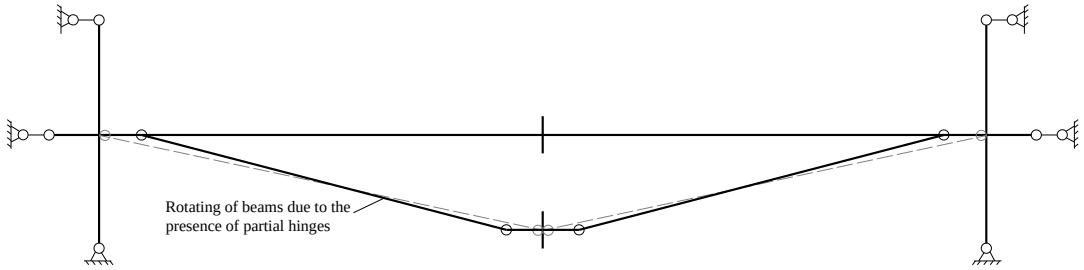

Fig. 5.20: Effect of partial hinges on beam rotating

5.3.5 Strain variations of reinforcing bars of RC frames

Prior to casting of specimens, strain gages had been attached to the surfaces of reinforcing bars. At or near cracks, such as at joint interfaces, reinforcing bars sustained combined action of axial force and bending moment. To track the non-

uniformity of strain distributions along bar cross-sections, strain gages were attached at both the top and the bottom surfaces of some bar cross-sections. To track the distribution of strains along a bar, strain gages were attached over a certain length. The readings of strain gages shed light on the force transfer mechanisms inside the specimens. In this section, the strains of reinforcing bars in F1, F2, F6, F7 and F4 are demonstrated.

5.3.5.1 Strains of reinforcing bars in specimens F1-CD-NS and F2-CD-WS

During the sub-assemblage tests, strain distributions along the bars in the two-bay beams and the middle joints are comprehensively demonstrated. Therefore, in the frame tests on specimens F1 and F2, the main interest was the force transfer mechanisms in local side joint regions. Accordingly, a great many strain gages were attached on bars in the beam-column side joint regions.

Fig. 5.21(a) shows the layout of strain gages attached onto a top and a bottom bar in the side joint connected to A-Frame (AF). "St" and "Sb" indicates the top and the bottom bar in a side joint, respectively. To investigate the effect of shear force on the strain measurements of a longitudinal bar near the side joint interface, strain gages were attached at both the top and the bottom surfaces of the bar. The label with "A" indicates the strain gage mounted on the bottom surface. For the bottom bar, all the strain gages were attached onto the side surface of the bar. Due to high strain gradient near the joint interface, the spacing of strain gages there was much shorter the one within the joint panel. It was found that shear force slightly affected the strains of bars under tension. Therefore, the strain gages at the same layer near the joint interface were selected to demonstrate the strain distribution of bars. However, some strain gages were spoiled during casting, such as St2 and St3A in **Fig. 5.21(a)**, so their data are not shown.

Hogging moment and axial force were transferred from the two-bay beam to the side joint, resulting in top bars in tension and bottom bars in compression. **Fig. 5.21(b)** shows the strain distribution of a top bar in the side joint under different MJDs. It can be seen that the bar tension was significantly reduced only within the joint due to bond stress. However, with increasing MJD, yielding penetration

developed quickly. At a MJD of 100 mm, it has advanced around 100 mm from the joint interface to the joint center. The eventual length of bar yielding was around 125 mm (i.e. half joint depth) prior to bar fracture. **Fig. 5.21(c)** demonstrates the strain distribution of a bottom bar under different MJDs. Due to bond stress within the joint, the large compressive strain at the joint interface was nearly reduced to zero.

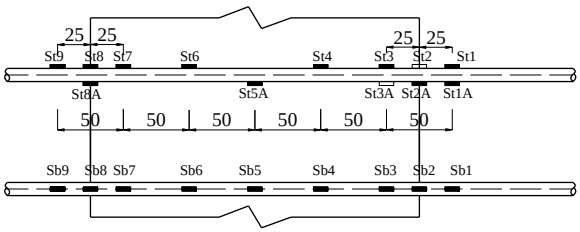

(a) Layout of strain gages (units: mm)

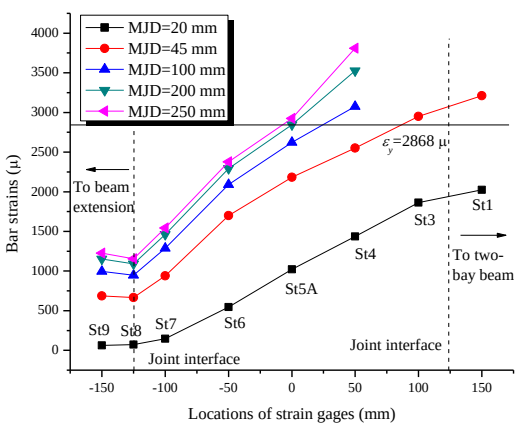

(b) Strain distribution along top bar

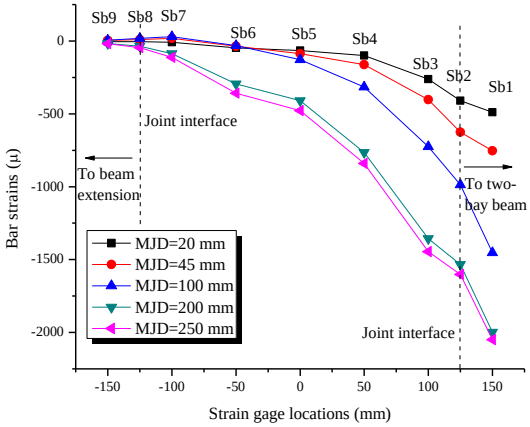

(c) Strain distribution along bottom bar

Fig. 5.21: Strain distribution over bars in AF side joint of F1-CD-NS

The layout and the notations of strain gages in the side joint of F2 connected to the reaction wall was identical to those in F1, as shown in **Fig. 5.22(a)**. **Fig. 5.22(b)** shows that shear force slightly affected the bar strains at the cross-sections near the joint interface (such as pairs of St1 and St1A, St3 and St3A) prior to yielding, but it induced a relatively larger difference of strains at the joint interface, such as the pair of St2 and St2A. Therefore, the average values of strain gages near the joint interface were used to indicate the bar strains.

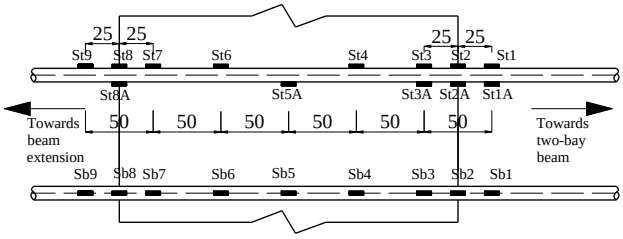

(a) Layout of strain gages (units: mm)

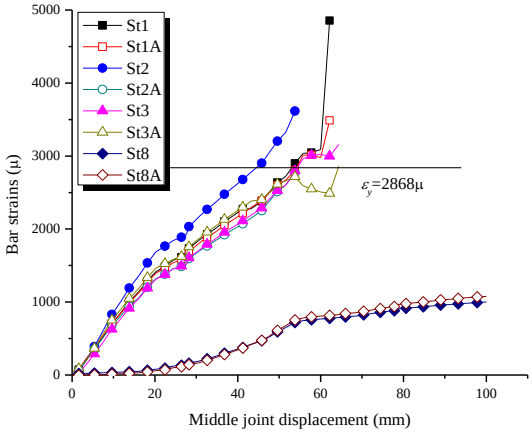

(b) Strains at different surfaces of the top bar

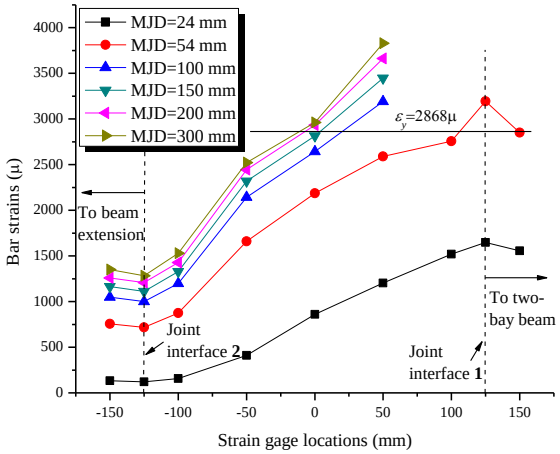

(c) Strain distribution along a top bar

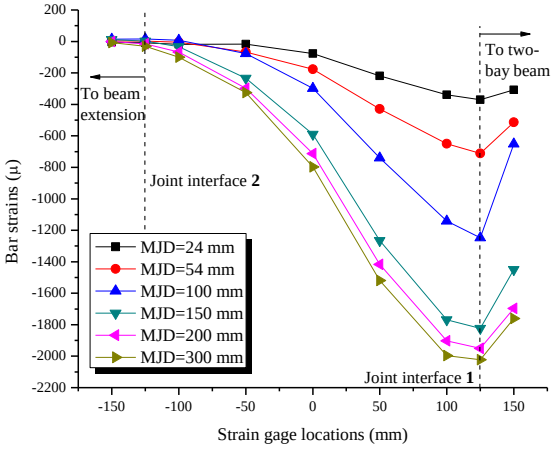

(d) Strain distribution along a bottom bar

Fig. 5.22: Strain distribution of bars in RW side joint of specimen F2-CD-WS

Fig. 5.22(c) shows the strain distribution of a top bar in the side joint under different MJDs. It can be seen that the bar tension was significantly reduced only within the joint due to bond stress. Moreover, at a MJD of 150 mm, yielding penetration has advanced around 125 mm from the joint interface to the joint center, and further developed up to around 136 mm prior to bar fracture. **Fig. 5.22(d)** demonstrates the strain distribution of a bottom bar under different MJDs. Due to bond stress within the joint, the large compressive strain at the joint interface was nearly reduced to zero. The spikes in **Figs. 5.22(c)** and **(d)** indicate that strain concentration occurred at the joint interface.

Fig. 5.21(b) and **Fig. 5.22(c)** show that the bar strain in the beam extension was larger than that at the interface towards the beam extension. That is, the stress at

that interface was smaller than those at both sides. Accordingly, the directions of bond stresses at both sides of the interface were opposite, and the zero-bond stress point (i.e. the first derivative of bar stress distribution) was located at the joint interface. Moreover, within the joint panel, the bond stress was distributed in the same direction through the entire loading history. Therefore, the slip at a wide crack near the joint interface towards the two-bay beam was mainly contributed by the elongation of a bar over the embedment length equal to *one column width*.

5.3.5.2 Strains of reinforcing bars in specimen F6-SD-PD

Fig. 5.23 shows the arrangement of strain gages along the longitudinal reinforcing bars in F6. Since the main interests are on the strain distributions over bars within the middle and the side joints, most strain gages were mounted there, as highlighted in **Fig. 5.23**. Within the middle joint region, one bottom bar was mounted with a series of strain gages, denoted as **Mb**. **Mt** and **St** are used to indicate the strain gages along a top bar in the middle joint region and in the side joint region, respectively. In the notation of strain gages, letter "A" indicates that strain gages were mounted at the bottom layer of bar cross-sections whereas the notation without "A" represents strain gages at the top layer of bar cross-sections.

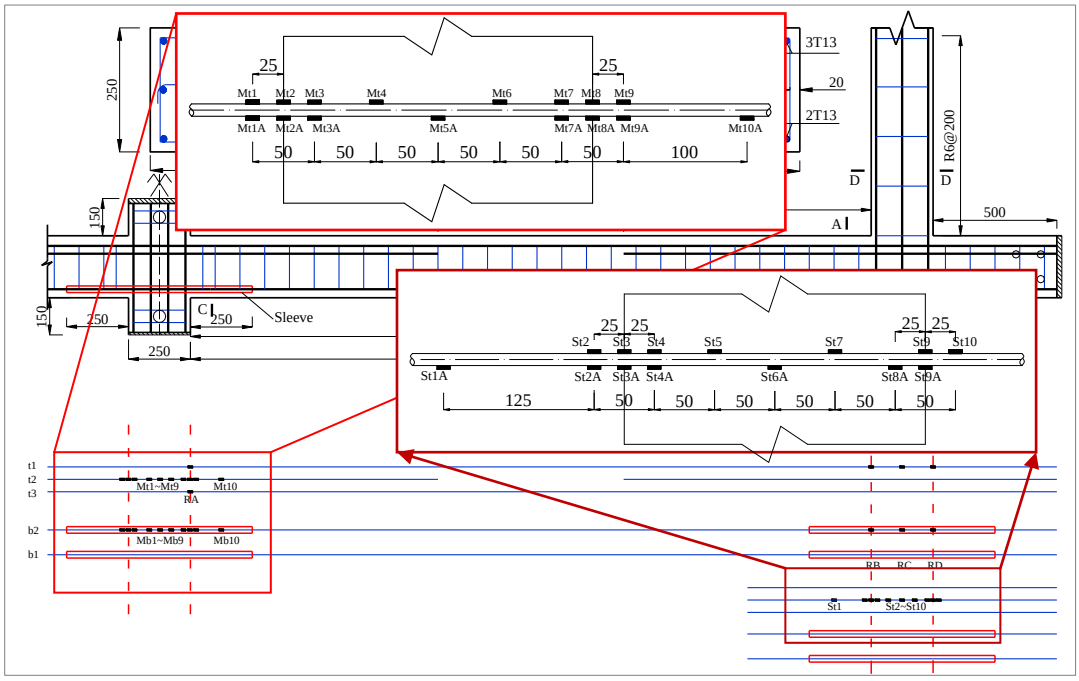

Fig. 5.23: Arrangement of strain gages in specimen F6-SD-PD (unit: mm)

Fig. 5.24 shows the development of strains at the top and bottom layers of bar cross-sections vs. MJD. For debonded bottom bars, the strains across the bar sections were quite uniform prior to reaching the yield strain, as shown in **Fig. 5.24(a)**. However, for top bars, the strains at different layers diverged even though the bar was still at elastic stage, as seen in **Fig. 5.24(b)**. This is because the top bar was under combined action of axial force and shear force locally whereas the bottom bar did not sustain large shear force, as illustrated in **Fig. 5.25**.

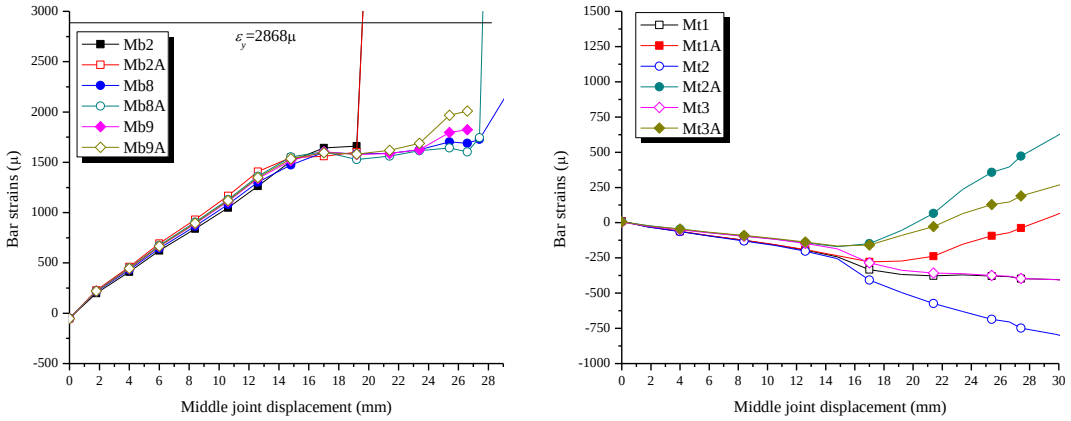

(a) Debonded bottom bar (b) Top bar

Fig. 5.24: Distribution of strains at the cross-sections of bars in the middle joint region

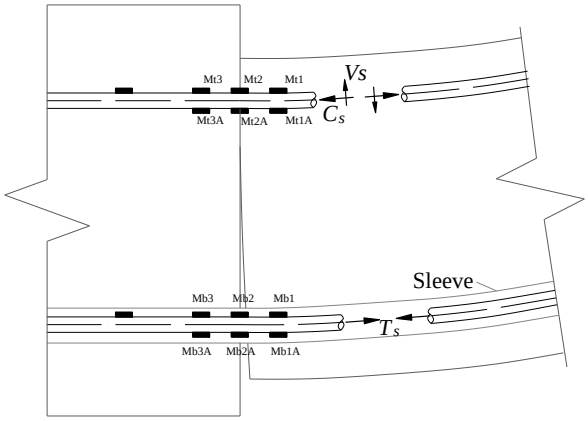

Fig. 5.25: Forces transferred by different layers of reinforcing bars

Local shear force induced bending moments at the bar cross-sections, resulting in discrepancy of strains at the top and the bottom layers at the same bar section, as illustrated in **Fig. 5.24(b)**. Similarly, for a top bar at side joints mainly under tension,

the strain distribution of the bar was also affected by local shear due to dowel action, as shown in **Fig. 5.26**. The effect of local shear on strain distribution across bar cross-sections was significant near the cracks. For the locations far from the cracks, local shear effect could be ignored. The non-uniformity in strains possibly prohibited a bar section from achieving the tensile strength that is typically obtained by tensile tests. A comparison between **Figs. 5.24(a)** and **5.26** suggest that partial debonding technique can eliminate the effect of local shear on the distribution of bar strains.

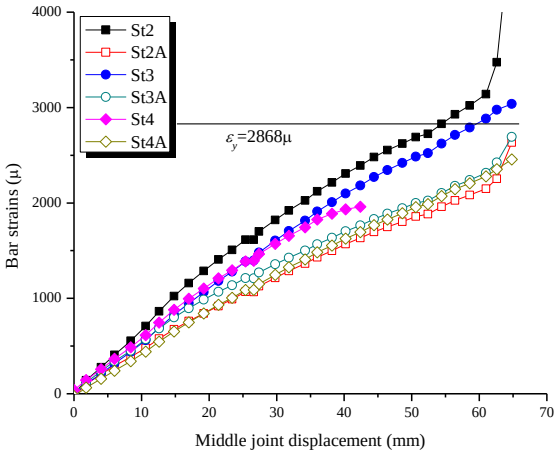

Fig. 5.26: Distribution of strains at bar sections near the side joint interface

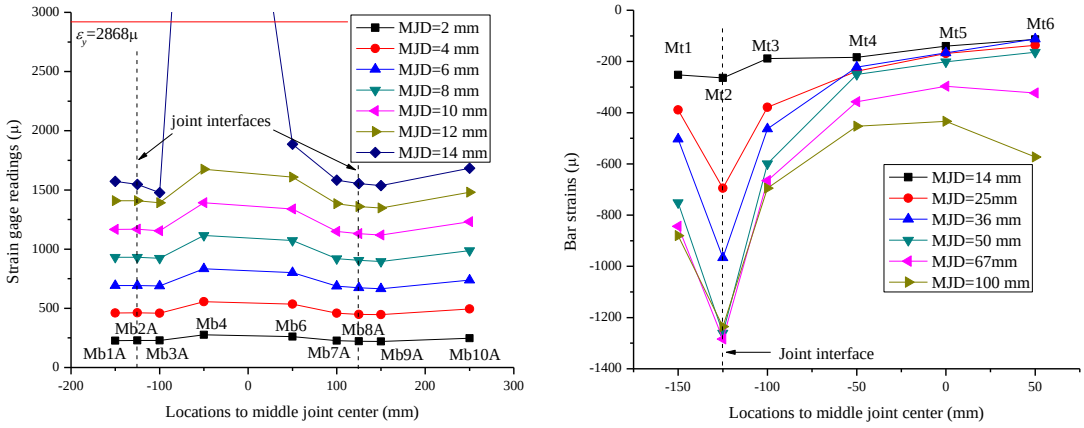

(a) Debonded bottom bar (b) Top bar

Fig. 5.27: Strain distribution along bars at middle joint region

Fig. 5.27(a) shows the strain distribution along a debonded bottom bar in the middle joint region. As expected, the strain distribution along the debonded bar was very uniform without any strain concentration. It is noted that yielding of the

bottom bar initiated within the middle joint instead of at the joint interfaces. For the top bar which was embedded in concrete, strain concentration occurred at a joint interface, as shown in **Fig. 5.27(b)**.

Fig. 5.28 shows the strain distribution of a top bar within a side joint region. Near the joint interface, the strains are determined by the average values of the top and the bottom strain gage readings. Since after bar yielding many strain gages were spoiled, the strain distriburions at large MJDs were not shown herein. At early stage of CAA (say, MJD $\leq$ 65 mm), the strain distribution of a top bar within the side joint was shown in **Fig. 5.28(a)**. The large bar stress at the joint interface towards the two-bay beam was monotonically reduced by bond stress within the joint panel, indicating that the bond stresses were in the same direction. At a MJD of 65 mm, yielding of the top bar occurred near the joint interface towards the two-bay beam.

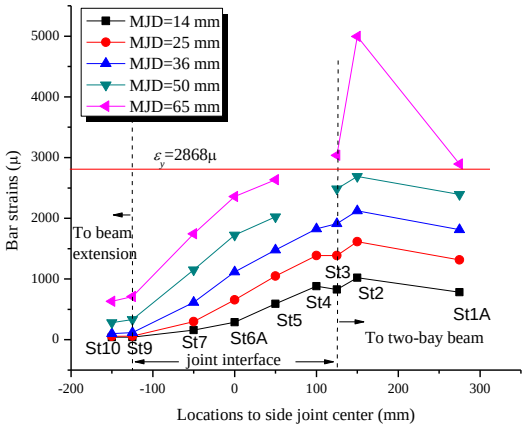

(a) Strain distribution along a top bar at CAA stage

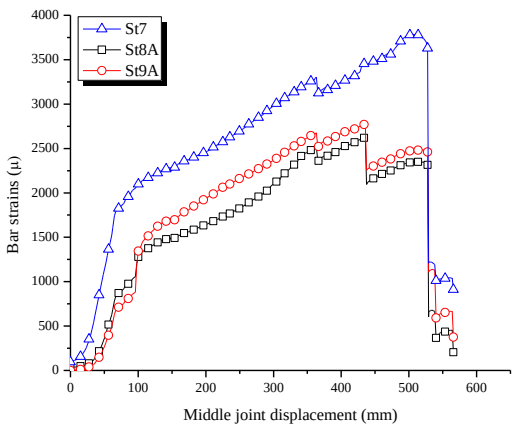

(b) Development of strains near joint interface

Fig. 5.28: Strain distribution and development in side joint region

The strain gages denoted as St8A and St9A were located near and at the joint interface towards the beam extension, respectively, and the gage St7 was located in the joint panel, as indicated in **Fig. 5.23**. **Fig. 5.28(b)** shows that after around a MJD of 100 mm, the strain at St8A became consistently smaller than those at St7 and St9A. That is, the stress at St8A was at the saddle point of the local stress distribution. Therefore, the directions of the bond stresses at both sides of St8A were opposite, and the zero-bond-stress (i.e. the gradient of bar stress) was located at St8A. Similar to specimens F1 and F2, the bond stresses within the side joint panel of F6 remained the same direction throughout the entire loading history. The

slip at the cracked joint interface towards the two-bay beam was mainly contributed by the elongation of the bar over the embedement length from St2 to St8A, i.e. around one column width.

5.3.5.3 Strains of reinforcing bars in specimen F7-SD-PH

Fig. 5.29 shows the arrangement of strain gages in F7. The main interests are the strains of the bent-up and bent-down bars inside the partial hinges. Therefore, a series of strain gages were attached onto these bars. Similar to F6, the labels **Mt** and **Mb** denote the strain gages at the top and the bottom bar in the middle joint region, respectively. Likewise, the labels **St** and **Sb** denote the strain gages at the top and the bottom bar in the side joint region, respectively.

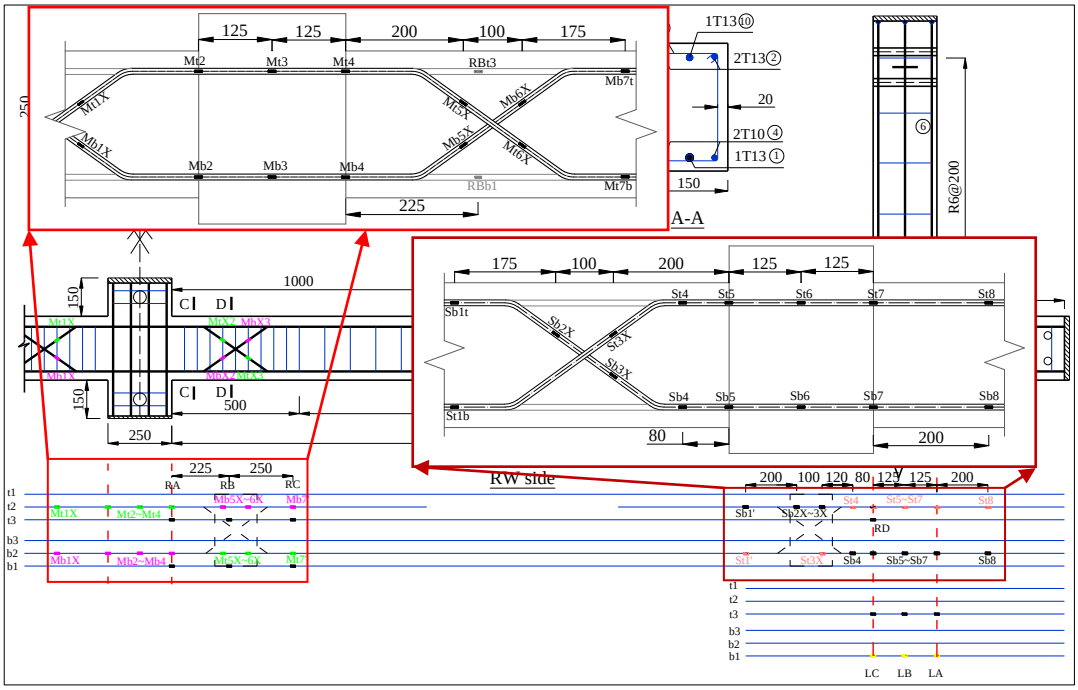

Fig. 5.29: Arrangement of strain gages of specimen F7-SD-PH (unit: mm)

Fig. 5.30 and **Fig. 5.31** show the development of strains at bent-bars in the middle and the side joint regions, respectively. Several observations on F7 can be summarized:

(1) Bent-bars were always in tension associated with large tensile strains, as indicated by the strain gages labeled "X" in **Figs. 5.30** and **5.31**;

(2) Near the joint interfaces, the compressive strains of bars were very small, such as Mt4 in **Fig. 5.30(a)** and Sb4 and Sb5 in **Fig. 5.31(b)**;

(3) Near the joint interfaces, the strains at the straight part of bars which were adjacent to the bent part of bars increased quickly in tension together with the bent part, such as Mt4 and Mt5X in **Fig. 5.30(a)**, Mb2 and Mb1X in **Fig. 5.30(b)**, as well as St5 and St3X in **Fig. 5.31(a)**.

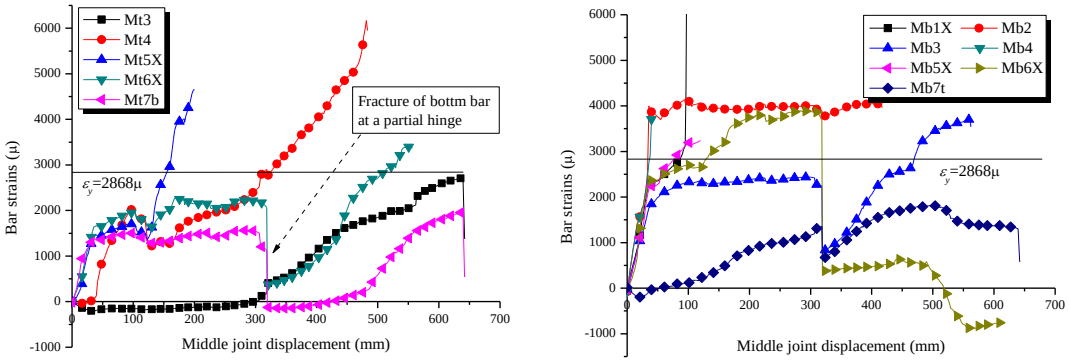

(a) Bent-down bar (b) Bent-up bar

Fig. 5.30: Strains of bent bars in the middle joint region

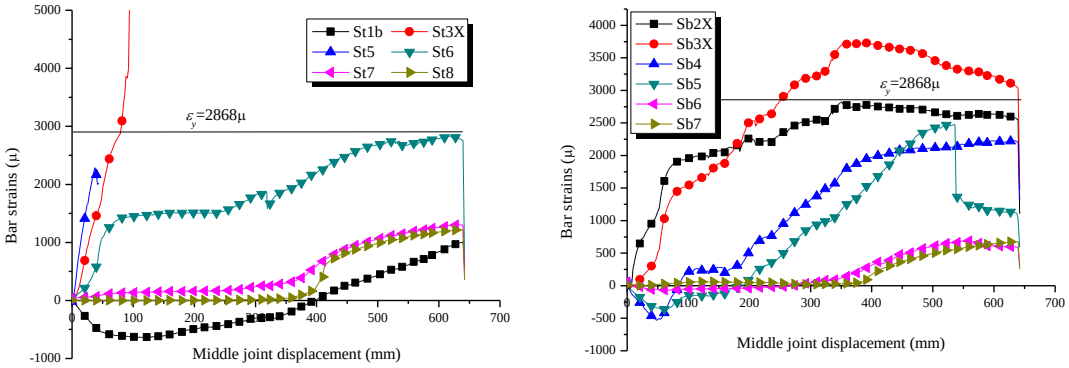

(a) Bent down bar (b) Bent-up bar

Fig. 5.31: Strains of bent bars in the side joint region

Fig. 5.32 illustrates the force transfer mechanism within a partial hinge by a "truss analogy". The dash lines in the truss, representing the top and the bottom chords, were analogous to the straight bars. Subjected to the combined action of bending moment and axial force, both the bottom and the inclined bars were elongated due to tension whereas the top member was contracted due to compression. This is why the bent parts of the bars were always in tension during the test. The compression of the top bars in the partial hinge can be confirmed by severe crushing of concrete

shown in **Fig. 5.19** and the readings of the strain gage named as RBt3 near the middle joint in **Fig. 5.29**. At a MJD of 205 mm, the strain at RBt3 approached around 5000μ.

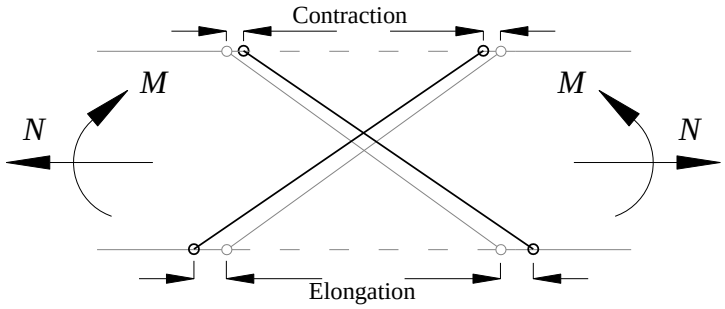

Fig. 5.32: Force transfer mechanism in partial hinge by truss analogy

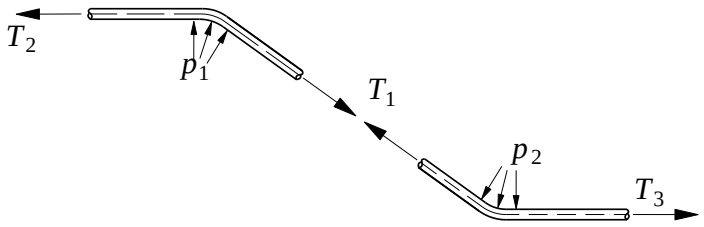

Fig. 5.33: Force transfer in bent bars

Fig. 5.33 visualizes the force transfer in a single bent bar. Assuming this bar is located in a sagging moment region, then the bottom part should be in tension and the top part should be in compression. However, due to the mobilization of large tension T_1 in the bent part of the bar, the tension T_3 in the bottom part increases further and the force acting in the top bar part becomes tension (T_2) as well. Therefore, the tensile strains at Mb2 and Mb4 increased faster than the ones at Mb1X and Mb5X, respectively, as shown in **Fig. 5.30(b)**, and the tensile strain at Mt4 developed more slowly than the one at Mt5X, as shown in **Fig. 5.30(a)**. The forces p_1 and p_2 acting at the kinks of the bar are resisted by surrounding concrete.

5.3.5.4 Strains of reinforcing bars in specimen F4-CD-WS-EX

The strain distribution of bars in the side joints of F4 is the main interest. The corresponding arrangement of strain gages is shown in **Fig. 5.34**. The top bars are definitely in tension. Therefore, a 90^o hook was used to increase the anchorage lengths. However, the bottom bars are initially in compression and subsequently

change to tension at catenary action stage. Consequently, the bottom bars were bent up with a 90^{o} hook as well. Besides the strain gages denoted with "St" at a top bar and the ones denoted with "Sb" at a bottom bar, the strain gages denoted as HP1, HP2 and HP3 were mounted to the horizontal hoops in the joint panel.

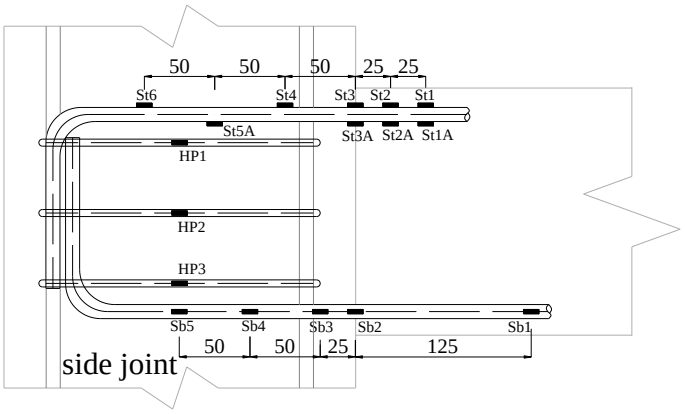

Fig. 5.34: Arrangement of strain gages in a side joint of F4-CD-WS-EX (unit: mm)

Fig. 5.35(a) demonstrates the strain distribution along a top bar in the side joint region. The strain profiles in this region were similar to a bar subjected to a pullout force at relatively small MJDs. At a MJD of 50 mm, the yielding in tension had already initiated near the side joint interface, as indicated by the blue line in **Fig. 5.35(a)**. With increasing MJD, the yield penetration spread quickly into the joint panel. At a MJD of 100 mm, yielding had spread to 80 mm from the joint interface.

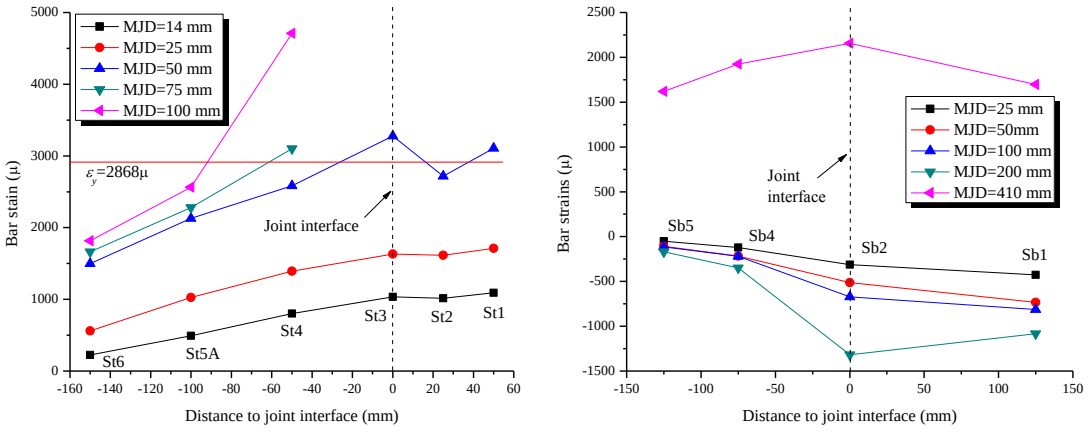

(a) Top bar (b) bottom bar

Fig. 5.35: Distribution of bar strains in side joint region of F4-CD-WS-EX

Fig. 5.35(b) demonstrates the strain profiles of a bottom bar in the side joint region. It can be seen that the strain concentration of the bar occurred locally at the joint interface no matter the bar was subjected to compression or tension.

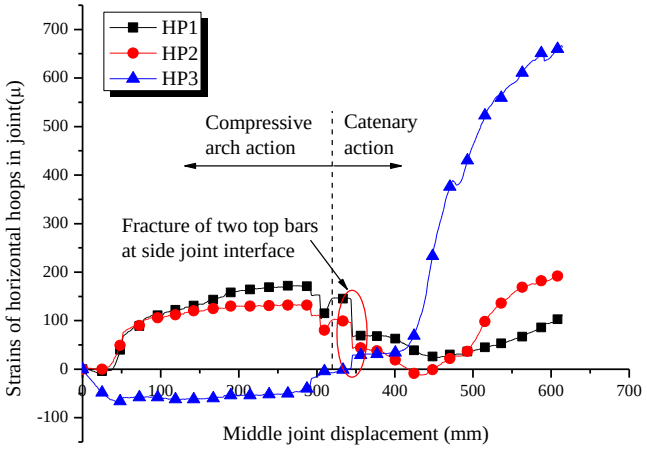

Fig. 5.36: Strains of horizontal hoops in side joint of F4-CD-WS-EX

Fig. 5.36 shows the strain development of the horizontal hoops after F4 was loaded at the middle joint. It can be seen that the hoop strains were very small, less than 700μ. This indicates that the shear stress in the joint panel was not large.

5.3.6 Shear distortion at joint panels of side joints

Two potential meters were diagonally installed at the side joints to record possible shear distortion of joint panels, as shown in **Fig. 3.13(a)**. Based on the geometric relationships shown in **Fig. 5.37**, shear distortion γ can be converted from the readings of two potential meters.

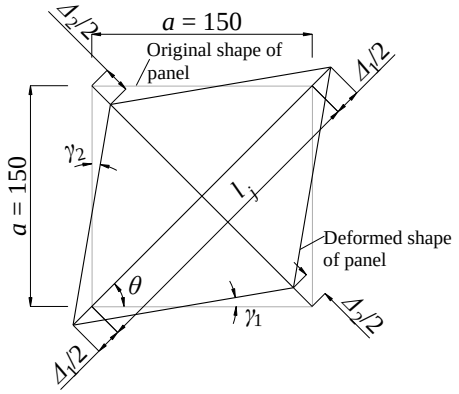

Fig. 5.37: Determination of shear distortion at joint panels (unit: mm)

Shear distortion γ is given by

$$\gamma = \gamma_1 + \gamma_2 = \frac{\Delta_1 - \Delta_2}{\sqrt{2}a} \tag{5-7}$$

where Δ_1 and Δ_2 are the deformations of two potential meters, positive for lengthening and negative for shortening; and a = 150 mm as indicated in **Fig. 5.37**.

Note that shear distortion of joint panels is a meaningful parameter only prior to the fracture of top bars at the side joint interfaces. After the fracture of all the top bars, the joint panel simply became one part of a column because the beam-column connection was through a single layer of reinforcement. **Table 5.5** summarizes the maximum shear distortions at the joint panels. It can be found that except for the side joint towards A-Frame side of F3, the joint shear distortions of the other joints were less than 30×10^{-4} rad. Additionally, there is no general rule to specify under what structural mechanism, the maximum shear distortion will occur.

In section 5.3.4, it is found that for RC frames with beam extensions, i.e. specimens F1, F2, F5 to F7, very few shear cracks occurred at the side joint panels, indicating low shear stress was induced in the joint panels. Accordingly, the shear distortions of the joint panels could be ignored. However, extensive shear cracks were found in a side joint panel of specimen F3. Therefore, F3 and F4 that do not have beam extensions are selected to demonstrate the development of shear distortions vs. MJD.

Table 5.5 Maximum shear distortions at joint panels

Specimen	Maximum shear distortion γ_{max} at joint panels (10^{-4} rad)*		Structural mechanisms corresponding to γ_{max}	
	RW side	A-Frame side	RW side	A-Frame side
F1-CD-NS	9.8	22.4	CTA†	CAA
F2-CD-WS	4.4	9.1	CTA	CAA
F3-CD-NS-EX	11.4	89.8	CAA	CTA
F4-CD-WS-EX	8.1	7.4	CAA	CAA
F5-SD-MR	23.1	28.1	CTA	CTA
F6-SD-PD	27.6	11.9	CTA	CTA
F7-SD-PH	12.3	10.6	CAA	CTA

*: γ_{max} represents the maximum magnitude of the shear distortion;
†: CTA stands for catenary action

Figs. 5.38(a) and **(b)** show the development of shear distortions at the side joint panels of F3 and F4, respectively. Due to fracture of top bars near the side joint interfaces, shear distortions were significant. For the side joint at the reaction wall (RW) side of F3, the shear distortion varied within 11.4×10^{-4} rad, as shown in **Fig. 5.38(a)**. The shear distortions of the two side joints of F4 ranged from -8×10^{-4} rad to $+8\times10^{-4}$ rad, as presented in **Fig. 5.38(b)**. Thus, there was nearly no shear cracks at these joint panels. However, between the MJD of 425 mm and 500 mm, the shear distortion at the side joint toward the A-frame side of F3 increased rapidly, up to 90×10^{-4} rad. Accordingly, the shear cracks at this side joint panel formed extensively within this range of MJDs, as shown in **Fig. 5.15(c)**. Even so, the failure of F3 was governed by the side column rather than the joint panel.

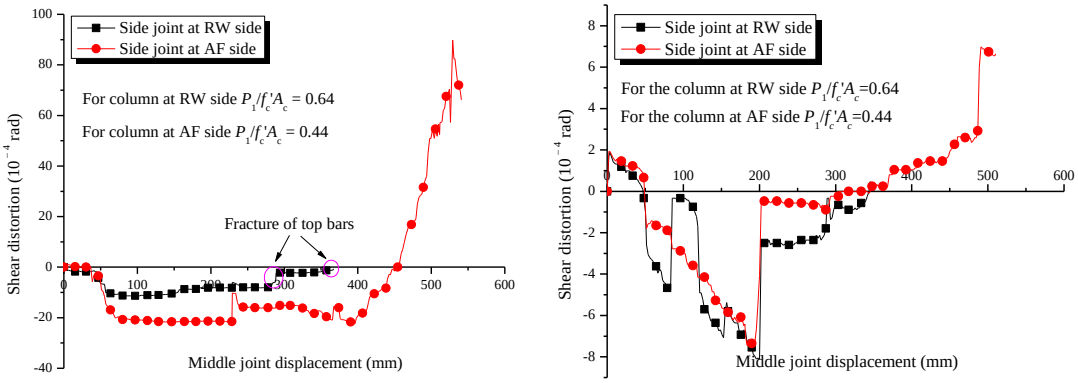

(a) Specimen F3 (b) Specimen F4

Fig. 5.38: Development of shear distortion of frames without beam extensions

For the side joints without horizontal hoops in F3, as shown in **Fig. 5.38(a)**, it can be seen that prior to a MJD of 360 mm, the shear distortion at the side joint toward RW side was much smaller than the one facing A-frame side. This indicates that high column axial stress could inhibit the development of joint distortion at a joint panel. However, the effect of column axial stress on shear distortion becomes less significant for the side joint panels with horizontal hoops, as indicated by a comparison of the shear distortions at the two joint panels of F4, as shown in **Fig. 5.38(b)**.

Furthermore, a comparison between the shear distortion measurements of F3 and F4 suggests that under the same column axial stress, horizontal hoops in joint panels

could effectively reduce shear distortion. Similar observations could be found when the results of F1 and F2 are compared.

In summary, based on the results of shear distortions and crack patterns at the joint panels, it can be concluded that beam-column *joint panels* are not critical components for RC frames subjected to a middle column removal scenario.

5.3.7 Effect of detailing on structural behavior of RC frames

With identical longitudinal reinforcement, the comparisons of load-deflection history between F1 and F2 as well as F3 and F4 suggest that seismic detailing in terms of arrangement of stirrups in structural members and horizontal hoops in joints does not significantly affect structural behavior of RC frames subjected to a middle column removal scenario. This is ascribed to the following facts:

(1) Structural behavior of RC frames subjected a middle column removal scenario is dominated by bending moment and axial force throughout beams rather than shear. Provided that the structural resistance due to shear is greater than that due to flexure, failure modes are governed by catenary action of beams rather than the shear capacity of joints.

(2) At the beam-column connections, severe cracks occur with very limited compressive zones at the beam sections, significantly reducing confinement effect in spite of a high reinforcement ratio of stirrups in the beams;

(3) Failure mainly occurs at the beam-column connections rather than within the joint panels so that the function of the horizontal hoops in the joints is not mobilized.

On the other hand, three different detailing schemes were adopted for RC frames to improve the rotation capacities of RC beams under large axial tension. For specimens F1, F5, F6 and F7, their top reinforcement was 3T13, at a reinforcement ratio of 1.24%. Additionally, with the exception of the bottom reinforcement ratio of F7 (1T13+2T10) at 0.90%, the bottom reinforcement ratios of the other three frame specimens were identical at 0.82% (2T13). Therefore, the longitudinal reinforcement ratios for these four specimens can be regarded as approximately the same. Moreover, the arrangement of stirrups in these four specimens was the same.

Fig. 5.39 shows the effects of different detailing rules on the load-deflection history of RC frames and the variations of beam axial forces.

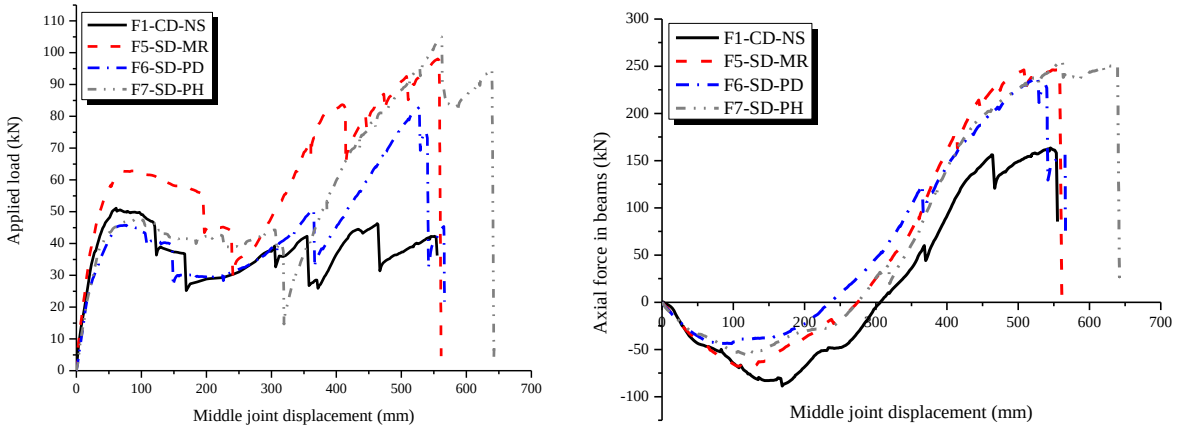

(a) Load-deflection history (b) Variation of axial force

Fig. 5.39: Effects of special detailing on structural behavior of RC frames

With an additional middle reinforcement layer, the capacity of CAA was increased considerably. As illustrated in **Fig. 5.39(a)**, the CAA capacity of F5 was 20% greater than those of F1, F6 and F7. Cracks developed and propagated rapidly along the beams of F5. At a MJD of 75 mm, crack tips had already crossed the middle reinforcement layer. As a result, the middle reinforcement layer functioned as purely tensile reinforcement. Accordingly, the bending moment resistance of beam sections at the joint interfaces increased, resulting in a larger CAA capacity. Due to late fracture of bottom bars at the middle joint interfaces, between the MJD of 300 mm and 400 mm, dowel action in F5 was much larger than other specimens, leading to higher structural resistance.

Fig. 5.39(b) shows the effects of different detailing rules on the variations of axial force vs. MJD. It can be seen that the maximum axial compression of F6 was lowest. Due to partial debonding of bottom bars at the beam-column joints, the bottom bars under compression could bend flexibly so that they did not sustain compression as large as the bars firmly bonded by concrete did. As a result, the maximum axial compression was lowered. On the other hand, since fracture of one bottom bar at the middle joint region was delayed, the axial tension of F6 at the initial stage of catenary action was larger than the other specimens, as indicated in **Fig. 5.39(b)**.

Fig. 5.20 can be used to illustrate the effect of partial hinges in F7 on structural resistance. Due to the presence of partial hinges, the effective lengths of beams that were able to rotate as rigid bodies became shorter. Therefore, under a given axial tension and MJD, the structural resistance contributed by the vertical projection of axial tension increased.

Table 5.6 summarizes the contribution of different special detailing rules to the structural resistance at both CAA and catenary action stages based on comparisons with F1.

Table 5.6 Contribution of special detailing techniques to structural resistance

Specimen	Special detailing	Contribution to structural resistance	
		At CAA stage	At catenary action stage
F5-SD-MR	Additional middle layer of reinforcement	Increase structural resistance by increasing the moment resistance at joint interfaces	Increase structural resistance by larger axial tension and dowel action
F6-SD-PD	Partial debonding of bottom reinforcement at joint regions	No significant effect	Increase structural resistance by delaying the fracture of bottom bar and larger axial tension
F7-SD-PH	Partial hinges at one beam depth away joint interfaces	No significant effect	Increase structural resistance by larger axial tension and shortening the effective beam length for rigid rotating

5.3.8 Effect of boundary conditions on structural behavior of RC frames

Since CAA and catenary action of RC frames were mainly mobilized along the two-bay beams, the remaining structures including the side columns and the side joints could be regarded as generalized restraints at the ends of the beams. All these generalized restraints can be converted to equivalent axial, rotational and vertical restraints, as illustrated in **Fig. 5.40**. Since the vertical settlements at the supports are not considered, only the axial and rotational restraints are indicated, namely, K_a and K_r in **Fig. 5.40**, respectively. During the tests, the characteristic values of K_a

and K_r depend on the stiffnesses of the side columns and joints, and the elastic restraints at the top and the bottom ends of the side columns and at the beam extensions. The values of K_a and K_r for RC frames F1, F2, F3 and F4 as well as simplified sub-assemblage S4 are shown in **Table 5.7**. The reason to include S4 is that the longitudinal reinforcement ratios and the arrangement of stirrups of S4 was the same as the aforementioned RC frames. **Table 5.7** suggests that the presence of the restraints connected to beam extensions increased K_a and K_r. **Table 5.7** also indicates that the equivalent axial restraints in the sub-assemblage tests were much stronger than those in the frame tests. Stronger restraints resulted in larger beneficial effect from CAA on increasing structural resistance. It can be seen that the enhancement factor of S4 was the largest among all specimens. The ways to determine equivalent stiffness are introduced in Appendix A.

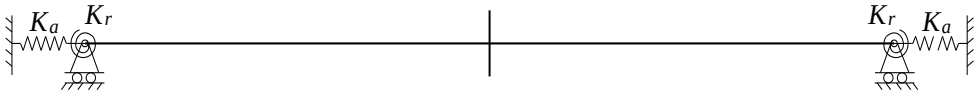

Fig. 5.40: Equivalent boundary conditions for a two-bay beam

Table 5.7 Effect of boundary restraints on enhancement factor due to CAA

Specimen	K_a (kN/m)	K_r (kNm/rad)	CAA capacity P_{CAA} (kN)	Flexural capacity P_f (kN)*	Enhancement factor α (%)†
F1-CD-NS	23500	32900	51.10	45.78	11.6
F2-CD-WS			50.75	45.55	11.4
F3-CD-NS-EX	13950	20000	45.90	45.78	0.2
F4-CD-NS-EX			50.13	45.54	10.0
S4	429217	30000	63.22	47.76	32.37

*: P_f is determined based on conventional plastic hinge mechanism without considering the presence of beam axial force;

†: $\alpha = (P_{CAA} - P_f) / P_f$.

Except the boundary conditions, all the other geometric properties were identical for F1 and F3. F1 included the restraints at the ends of beam extensions while F3 did not have any beam extensions. Therefore, a comparison between F1 and F3 could show the effect of boundary conditions on structural behavior of RC frames with

conventional non-seismic detailing, as shown in **Fig. 5.41**. Likewise, **Fig. 5.42** shows the effect of restraints on structural behavior of RC frames with conventional seismic detailing based on a comparison between F2 and F4.

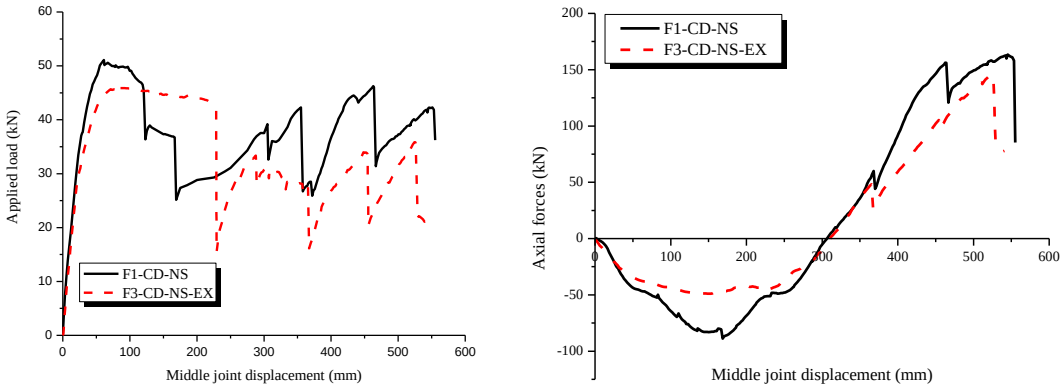

(a) Load-deflection histories (b) Variations of axial forces

Fig. 5.41: Effect of restraints at beam extensions on structural behavior of RC frames with non-seismic detailing

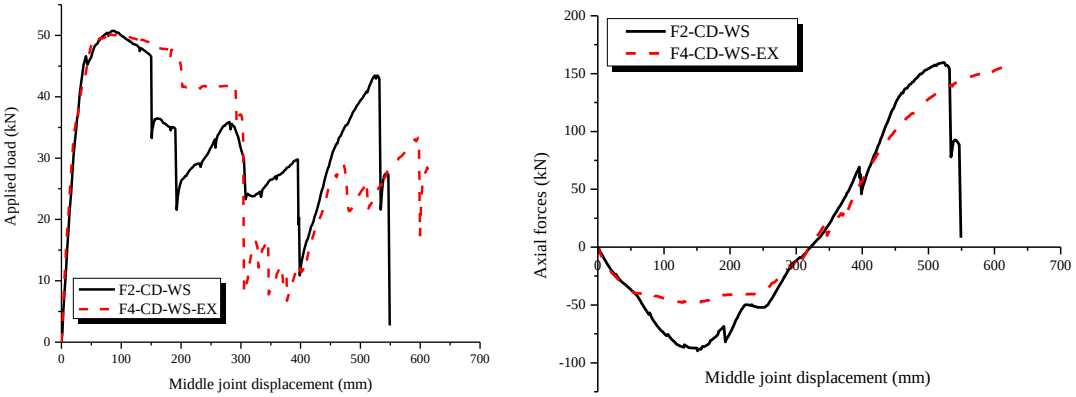

(a) Load-deflection histories (b) Variations of axial forces

Fig. 5.42: Effect of restraints at beam extensions on structural behavior of RC frames with seismic detailing

Similar findings for comparisons between F1 and F3, as well as between F2 and F4, are summarized as follows:

(1) At small MJDs, there were no appreciable differences between the specimens with and without restraints at the ends of beam extensions. This is because the connection gaps existed at the restraints at the column tops and the beam extension ends so that all specimens worked as portal frames.

(2) The CAA capacity of F1 was slightly higher than that of F3 due to a larger K_a. This benefit due to stronger restraints was not evident for F2 over F4. However, the maximum axial compression of F1 and F2 due to a larger K_a significantly exceeded those of F3 and F4, respectively.

(3) Due to stronger boundary restraints, the rotation of the two-bay beam was achieved at the expense of severe concrete crushing and fracture of bottom bars at the middle joint interfaces. As a result, after the CAA capacity, the respective structural resistance of F1 and F2 decreased more rapidly than those of F3 and F4, respectively.

(4) At catenary action stage, due to premature fracture of top bars at the side joint interfaces, the comparisons of structural resistance at this stage are not so meaningful. However, it is noteworthy that with the restraints provided at the beam extensions, the side columns did not fail prematurely.

(5) Due to detailing of top bars at the side joints, fracture of top bars in F3 and F4 (which were bent down into the columns) occurred at a relatively smaller MJD than those in F1 and F2 (which were extended through joint cores into beam extensions), respectively.

5.4 Comparisons of test results between RC frames and sub-assemblages

The tests on sub-assemblages were directly concerned with the structural mechanisms throughout the two-bay beams which were above missing columns. The tests on frames were to more realistically demonstrate the structural behavior of whole frames, including beams, columns and joints, in spite of some imperfect connections at the boundaries. Both series of tests show that *the failure of RC structures was mainly concentrated on the beam-column connections rather than the joint panels under a middle column removal scenario.*

Due to different test set-ups, the restraints of the sub-assemblage tests were stiffer than those of the frame tests. As a result, *at CAA stage, an increase of structural resistance due to CAA in the sub-assemblage tests was more evident than that in the frame tests*, as was evident by the comparison between F1 and S4 in **Table 5.7**.

However, at catenary action stage, the effect of boundary conditions on structural behavior also depends on the continuity of reinforcing bars. The bar continuity could be weakened by either bar pullout or bar fracture. To sustain further applied loads via catenary action, large rotations have to be achieved, perhaps at the expense of fracture of bottom bars at the middle joint interfaces. This phenomenon could be found in both the sub-assemblage tests and the frame tests. Thereafter, *the top layer of reinforcing bars could still provide large structural resistance to the RC frames, like catenary action of the sub-assemblages.* Nevertheless, *early fracture of top bars at the side joint interfaces significantly weakened the development of catenary action of RC frames with conventional detailing*. The early fracture of top bars near the side joint interfaces was attributed to the following facts:

(1) Embedment lengths of top bars in the side joints were much shorter than those in the enlarged end-column stubs of sub-assemblages;
(2) Axial loads in the side columns provided higher confining stress to the top bars so that the bond stress was increased even after bar yielding had occurred.

The early fracture of top bars near the side joint interfaces indicates that it is reasonable to place the internal ties on either side of a beam, rather than within the beam cross-section or the floor area directly above the beam, as advocated by the tie force approach in UFC 4-023-03.

On the other hand, the special detailing, including additional middle layer reinforcement, partial debonding of bottom bars at joints and partial hinges at a beam depth away from joint interfaces, can increase the rotation capacity of beam-column connections and subsequently attain large structural resistance via catenary action without early fracture of top bars. At the end of the tests, the global chord rations of F5, F6 and F7 exceeded 0.20 rad.

5.5 Summary and conclusions

In this chapter, the test results on RC frames subjected to a middle column removal scenario are demonstrated comprehensively. Following conclusions are obtained:

(1) With increasing MJD, CAA and catenary action were mobilized sequentially along the two-bay beams. CAA capacities were attained at the MJD from 0.25*h* to 0.38*h*, where *h* was the beam depth, and catenary action was mobilized at the MJD from 0.95*h* to 1.29*h*.

(2) Failure was mainly concentrated at the beam-column connections rather than the joint panels. For interior side joints (i.e. the side joints with beam extensions), only a few cracks occurred at the joint panels, and for exterior side joints (i.e. the side joints without beam extensions), such as joints in F3, extensive shear cracks formed at one joint panel, but the final failure was controlled by side column failure instead of joint failure.

(3) Stronger boundary restraints at the ends of two-bay beams could result in more rapid declining of structural resistance after CAA capacity because severe concrete crushing and bar fracture occurred to accommodate large deformations and to achieve large rotations at beam-column connections.

(4) Compared with the sub-assemblages, the top bars of RC frames with conventional detailing fractured at the side joint interfaces when the MJDs were relatively small, significantly wrecking the development of catenary action. This was because in the side joints of RC frames, the development lengths of top bars were shorter at cateanry action stage and axial loads in the side columns resulted in higher bond stress, leading to smaller slips at the joint interfaces.

(5) Test results suggest that the frame specimens with special detailing, including additional middle layer reinforcement, partial debonding of bottom bars at joints and partial hinges at a beam depth away from joint interfaces, were able to effectively achieve higher rotation capacities and yet without premature bar fracture. Subsequently, catenary action could be fully utilized.

(6) Catenary action is a double-edged sword. It is the last line defense of structural resistance against progressive collapse, but on the other hand, it may seriously jeopardize the stability of columns. Therefore, for interior bays, beams could be designed with catenary action to safeguard against collapse due to adequate lateral

restraints to related columns. However, for exterior bays, catenary action is not encouraged.

CHAPTER 6 ANALYTICAL MODEL FOR COMPRESSIVE ARCH ACTION OF REINFORCED CONCRETE BEAM-COLUMN SUB-ASSEMBLAGES

6.1 Introduction

Alternate load path method is one of the direct design approaches to evaluate structural resistance against progressive collapse of buildings. Typically, this approach is conducted by introducing column removal scenarios (DoD 2010; GSA 2003). Accordingly, several research groups (Sasani and Kropelnicki 2008; Su et al. 2009; Yu and Tan 2011a; 2012b) have experimentally studied the structural behavior of reinforced concrete (RC) sub-assemblages under a middle column removal scenario. The test results (Su et al. 2009; Yu and Tan 2011a; 2012b) indicate that compressive arch action (CAA) can substantially increase the progressive collapse resistance of RC frames beyond mere flexural capacity, based on the mechanism that plastic hinges have formed at critical sections of a sub-assemblage and the ultimate moment of resistance at each hinge is determined ignoring the presence of axial compression in beams. However, to attain CAA capacity, sub-assemblages have to undergo larger deflections, say, around 0.16~0.34 of beam depth in Su et al's tests (2009) and around 0.18~0.46 of beam depth in Yu and Tan's tests (2012b).

The test results (Su et al. 2009; Yu and Tan 2011a; 2012b) also demonstrated that catenary action can replace CAA to provide resistance when beam axial forces change from compression to tension. However, mobilization of catenary action requires much larger deflections, normally in the order of one beam depth or more. Thus, catenary action raises higher requirements on the continuity of longitudinal reinforcement and the rotation capacity of RC beams. Compared with catenary action, CAA is a favorable alternate load path as it requires much smaller deflections.

CAA is a structural mechanism in RC beams associated with axial compression (thrust), analogous to compressive membrane action (CMA) in RC slabs. Therefore,

the research on CMA is beneficial to provide a deeper understanding of CAA. Park proposed a model to calculate the CMA capacity and peak thrust of lateral-edge-restrained RC slabs, based on the assumptions at a plastic stage (Park and Gamble 2000). Similarly, Park's model can be used to estimate the CAA capacity of RC beams and sub-assemblages. Typically, RC beams are doubly-reinforced, and the compression reinforcement ratio can range from a small value to one as large as the tension reinforcement ratio. However, Park's model cannot consider the actual stress state of compression reinforcement at the critical sections along a beam. This would lead to inaccurate predictions of CAA capacity, as Yu and Tan's test results (2010b) demonstrated that at the capacity of CAA, compression reinforcement at the middle joint regions could either be in yield or in elastic state. Therefore, the compression reinforcement stress cannot be simply specified as attaining either yield strength or zero stress state, as advocated in Park's model. In addition, Park's model has only taken account of the effect of partial axial restraints (i.e. finite axial restraint stiffness) at beam ends without considering other imperfect boundary conditions. Therefore, Park's model is unable to consider the effects of partial rotational restraints (i.e. finite rotational restraint stiffness) and axial connection gaps at the beam ends on CAA. The ends of a beam are beam-column joints in framed structures, and rotation of joints is very common in a deformed RC frame. Therefore, the effect of partial rotational restraints on CAA of beams should be considered. Connection gaps may occur in laboratory tests, or in sub-assemblages with expansion joints.

To predict CAA capacity of RC beams and to incorporate the actual stress state of compression reinforcement, rotational restraints and axial connection gaps, a new analytical model is proposed in this chapter, starting from first principle rather than simply modifying Park's existing model. The proposed model is able to predict the CAA capacity, maximum axial compression and load-deflection trend of RC sub-assemblages at CAA stage. The proposed model is validated by available test results (Su et al. 2009; Yu and Tan 2011a; 2012b) and then used to conduct parametric studies, including the effects of imperfect boundary conditions, beam reinforcement ratio, and beam span-to-depth ratio on CAA.

6.2 Mechanism of compressive arch action

In the test results on RC sub-assemblages demonstrated in Chapter 4, the structural mechanisms of sub-assemblages are categorized into flexural action, CAA and catenary action. However, there is *no distinct demarcation* between flexural action and CAA in the load-deflection relationships of RC sub-assemblages. The test results (Yu and Tan 2011a) show that with adequate axial and rotational restraints, beams are able to develop axial forces throughout the entire loading history, even prior to achieving ultimate moments of resistance at critical sections.

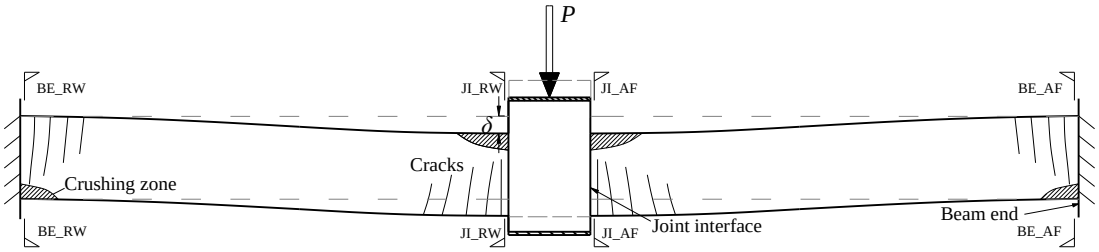

(a) A beam-column sub-assemblage subjected to a concentrated load

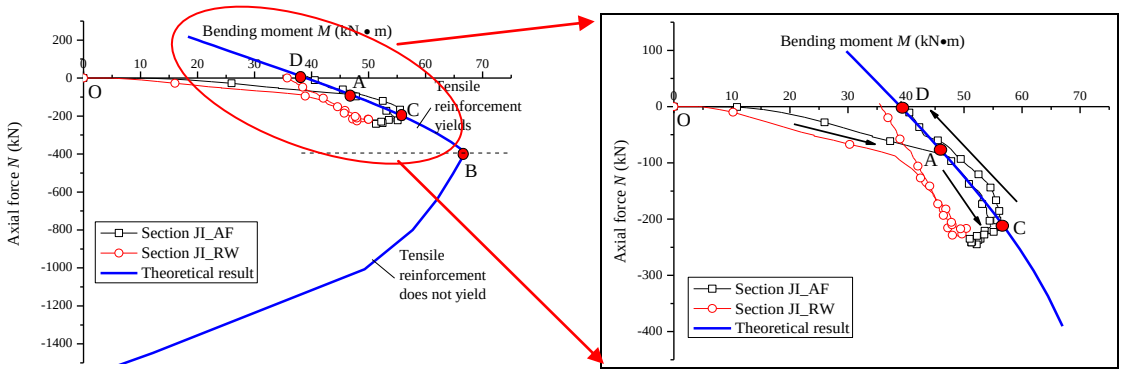

(b) At middle joint interfaces

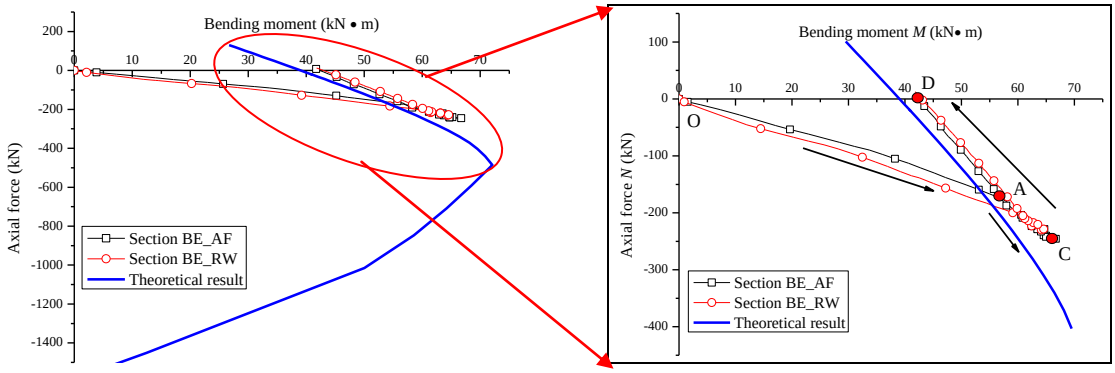

(c) At beam ends

Fig. 6.1: *M-N* interaction diagram of critical beam sections

As illustrated in **Fig. 6.1(a)**, a beam-column sub-assemblage is subjected to a concentrated load with both ends fixed (Yu and Tan 2012b). For a typical example, the experimental and theoretical *M*-*N* interaction diagrams at the middle joint interfaces and the beam ends of sub-assemblage specimen S5 are shown in **Figs. 6.1(b)** and **(c)**, respectively. Negative axial force denotes compression. The theoretical *M*-*N* interaction diagrams are computed based on the assumptions that (1) a plane section remains plane and (2) maximum strain in the extreme compression fiber of concrete is 0.003 (MacGregor and Wight 2005), and no strength reduction factor is considered. Curve BD indicated in **Fig. 6.1(b)** corresponds to "tension failure" of a beam section, that is, the tension steel has already reached the yield strength when the extreme concrete fiber reaches ultimate compressive strain of 0.003.

For joint interface JI_AF, with increasing sub-assemblage deflection, the state of *M*-*N* interaction moves from origin O to point A, as shown in **Fig. 6.1(b)**. Thereafter, the point traverses along the path AC due to the presence of axial compression increasing the ultimate moment of resistance, and reverses along the path CD after crushing of concrete occurs. The experimental *M*-*N* path ACD agrees well with the part BD of the theoretical *M*-*N* diagram. At point A, the ultimate moment of resistance at section JI_AF is attained. However, axial compression has already been mobilized at point A, resulting in an enhanced ultimate moment of resistance compared to the pure flexure at point D. Similar observations can be obtained for the other critical sections (i.e. Section JI_RW, BE_AF, BE_RW) from **Figs. 6.1(b)** and **(c)**. Therefore, when plastic hinges have formed at all critical sections, the ultimate moment of resistance at each hinge has already exceeded the pure flexural strength.

Although there was no pure flexural action in the sub-assemblage tests, flexural action capacity is still used to evaluate structural resistance based on conventional design philosophy and to assess enhancement of structural resistance due to CAA.

6.3 Development of the proposed model

Fig. 6.1(a) shows that plastic hinges have occurred at the joint interfaces and the beam ends of an RC beam-column sub-assemblage with a concentrated load applied at the middle joint. Due to symmetry, the free body diagrams of a one-bay beam and the middle joint at CAA stage are shown in **Figs. 6.2(a)** and **(b)**, respectively.

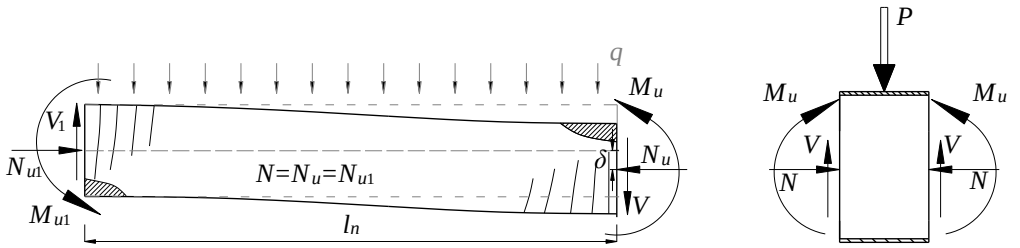

(a)One-bay beam (b) Middle joint

Fig. 6.2: Free body diagrams of RC specimens under compressive arch action

Due to axial restraints at both ends of the beam, considerable axial compression is mobilized throughout the beam length. Provided that the resistance of the sub-assemblage based on shear failure is greater than that based on flexural failure, with consideration of N-δ effect, vertical resistance P is determined based on force equilibrium in the vertical direction at the middle joint as shown in **Fig. 6.2(b)** and moment equilibrium in the one-bay beam as shown in **Fig. 6.2(a)**.

$$P = 2V = \frac{2\left(M_{u1} + M_u - N\delta - ql_n^2/2\right)}{l_n} \tag{6-1}$$

where V is the shear force acting at the joint interfaces; M_{u1} and M_u are ultimate bending moments acting on the beam ends and the joint interfaces, respectively; N is the beam axial compression; δ is the beam deflection at the middle joint; q is the self-weight or applied uniform loads on the beam; and l_n is the net span length of a one-bay beam.

At CAA stage, the effect of axial force N is two-fold, as illustrated in Eq. (6-1): (1) N increases ultimate moments of resistance M_{u1} and M_u, as the M-N path AC shown in **Figs.6.1(b)** and **(c)**, so that structural resistance P is increased; and (2) N also causes detrimental N-δ effect to structural resistance P. On the other hand, Eq.

(6-1) suggests that to obtain the relationship of vertical resistance P and deflection δ of a sub-assemblage, the relationships of bending moment M and axial force N to δ should be determined first. Test results in **Fig. 6.1** show that the interactions of M and N at critical sections during the test agree well with theoretical M-N interaction diagrams. Therefore, based on theoretical M-N interaction diagrams, both M_u and M_{u1} can be estimated once N is known. Then the kernel of the proposed model is to obtain the relationship between N and δ. In the following subsections, N-δ relationship will be constructed through compatibility conditions and force equilibrium of sub-assemblages based on the following assumptions.

6.3.1 Assumptions of the proposed model

The proposed model applies only after plastic hinges have occurred at several critical sections, as shown in **Fig. 6.1(a)**. To compute cross-sectional forces, including M and N, the conventional assumptions used in ACI 318-05 (American Concrete Institute 2005) are adopted, namely: 1) a plane section remains plane; 2) at each critical section, compression concrete has attained its strength with an idealized equivalent rectangular stress block and an ultimate strain of 0.003 in the extreme compression fiber of concrete, tension reinforcement has yielded and concrete tensile strength is ignored. Based on assumption (1), the proposed model may not be applicable for deep beams.

Based on test observations, it is assumed that 3) plastic hinges occur at the beam ends and at the middle joint interfaces, symmetrically located at both sides of the middle joint, as indicated in **Fig. 6.1(a)** Depending on the supports from surrounding structures, the restraints of sub-assemblages may rotate and translate slightly at the beam ends. Therefore, it is further assumed that 4) the stiffness values of imperfect axial and rotational restraints are linear elastic and symmetrical at both the beam ends, and beams are fully restrained against vertical translation at the ends. According to test results (Yu and Tan 2010b), at CAA stage, the strain of compression reinforcement increased first and subsequently decreased. The maximum compressive strain could either reach yield or remain elastic. Thus, it is assumed that 5) material property of compressive steel reinforcement is elastic-

perfectly plastic, and the unloading slope after yielding is equal to the initial elastic modulus, as seen in **Fig. 6.3**.

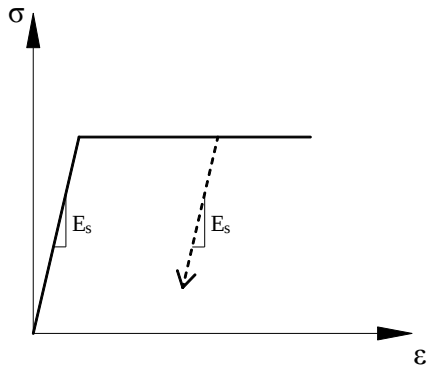

Fig. 6.3: Constitutive relationship of compression reinforcement

Following the above assumptions, neutral axis depths at the beam ends and the middle joint interfaces, which are used to determine internal forces, will be linked to vertical deflection δ via compatibility conditions and force equilibrium.

6.3.2 Compatibility conditions

After the ultimate moments of resistance have been obtained at the beam ends and at the joint interfaces, due to symmetry, the deformation and the rotation of one-half sub-assemblage are exaggeratedly drawn in **Fig. 6.4**. Due to mobilization of axial compression throughout the beam, the deformed beam causes horizontal expansion by an amount of $(t+t_0)$ and $0.5\varepsilon b_j$ at the lateral support and the middle joint interface, respectively. The term t is the small lateral deformation of the support and t_0 is the gap between the support and the beam end. The existence of t_0, caused by connection gaps, is found in the laboratory tests, so it is considered in this chapter. The term $0.5\varepsilon b_j$ represents small axial deformation of the middle joint, in which ε is axial strain throughout the middle joint and b_j is the middle joint width.

On the other hand, as shown in **Fig. 6.4**, a large crack with a width of l_1 occurs at the beam end, and crushing of concrete with a length of $c\tan(\theta+\varphi)$ happens at the middle joint interface, in which φ is the beam end rotation with respect to the rotated support and θ is the rotation of the lateral support at the beam end. Axial

compression in the beam results in a contraction of εl_n along the axis of the deformed beam. Axial strain ε along the beam is assumed equal to the one in the middle joint, since the axial compression is constant throughout the whole sub-assemblage. As shown in **Fig. 6.4**, the projection of the displaced beam segment onto the original beam configuration yields the *compatibility equation*.

$$\left[l_n + 0.5\varepsilon b_j + (t+t_0)\right]\sec(\varphi+\theta) = l_1 + (1-\varepsilon)l_n - c\tan(\varphi+\theta) \tag{6-2a}$$

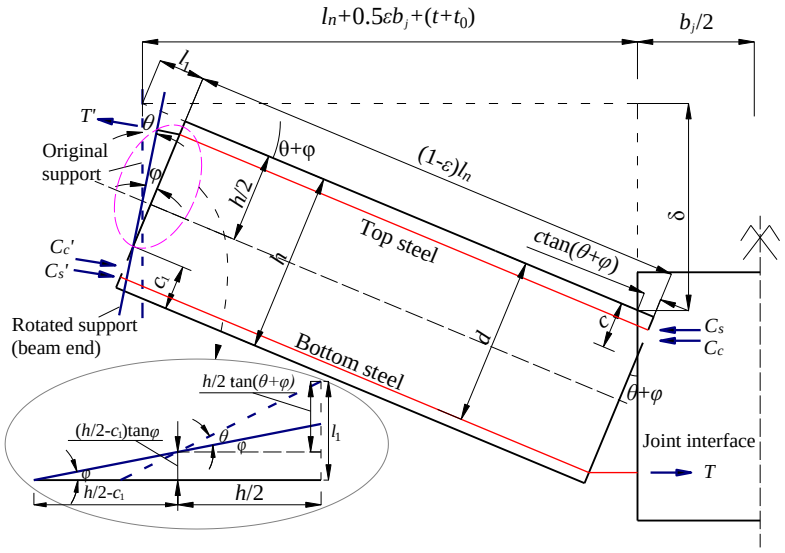

Fig. 6.4: Compatibility conditions of beam-column sub-assemblage

Since the net span length of the single-bay beam is l_n and the middle joint width is b_j, the total net span length of the sub-assemblage is $l = 2l_n + b_j$. If the ratio l_n / l is denoted as β, the joint width b_j can be expressed as $(1-2\beta)l$ and Eq. (6-2a) can be converted into

$$\left[\beta l + 0.5\varepsilon(1-2\beta)l + (t+t_0)\right]\sec(\varphi+\theta) = l_1 + (1-\varepsilon)\beta l - c\tan(\varphi+\theta) \tag{6-2b}$$

According to geometric relationships at the beam end restrained by the external support, as illustrated in the close-up insert in **Fig. 6.4**, crack width l_1 at the beam end (i.e. the distance of the top fiber at the beam end to the original support) is given by

$$l_1 = \frac{h}{2}\tan(\varphi+\theta) + \left(\frac{h}{2} - c_1\right)\tan\varphi \tag{6-3}$$

where h is the beam depth and c_1 is the neutral axis depth at the beam end.

Substituting Eq. (6-3) into Eq. (6-2b) and rearranging the equation to obtain the expression for the neutral axis depth c at the middle joint interface, the following equation is obtained.

$$c = \frac{h}{2} - \frac{0.5\varepsilon l + (t + t_0)}{\sin(\varphi + \theta)} - (1 - \varepsilon)\beta l \frac{2\sin^2[(\varphi + \theta)/2]}{\sin(\varphi + \theta)} + \left(\frac{h}{2} - c_1\right)\frac{\tan\varphi}{\tan(\varphi + \theta)} \tag{6-4}$$

Detailed derivation process from Eqs. (6-2) and (6-3) to Eq. (6-4) is given in Appendix I.

Since the partial rotational restraint at the beam ends is assumed as a linear elastic spring with a stiffness K_r, when the bending moment M_{u1} acts at the beam end, the corresponding rotation of the lateral support θ can be obtained.

$$\theta = M_{u1} / K_r \tag{6-5}$$

Moreover, axial strain ε of the beam segment and outward lateral displacement t of the linear elastic axial restraint at the beam end are determined by the induced beam axial compression N throughout the beam. Since all plastic deformations are concentrated at the middle joint interface and the beam end, the beam segment is assumed to deform elastically and uniformly. Therefore,

$$\varepsilon = \frac{N}{bhE_c} \tag{6-6}$$

$$t = \frac{N}{K_a} \tag{6-7}$$

where b is the beam width; E_c is the elastic modulus of concrete and K_a is the stiffness of axial restraints.

Since φ and θ are small, the trigonometric functions in Eq. (6-4) can be replaced by equivalent infinitesimal mathematical terms. Also, the beam axial strain ε and the movements of the axial restraints (t+t_0) are extremely small compared with l_n. Therefore,

$$\sin\theta \approx \theta = \frac{M_{u1}}{K_r};$$

$$\sin(\varphi+\theta) \approx 2\sin\left(\frac{\varphi+\theta}{2}\right) \approx \varphi+\theta = \frac{\delta}{l_n + 0.5\varepsilon b_j + (t+t_0)} \approx \frac{\delta}{l_n} = \frac{\delta}{\beta l}, \text{ and } \varphi = \frac{\delta}{\beta l} - \frac{M_{u1}}{K_r}$$

$$\tan(\varphi+\theta) \approx \varphi+\theta;\ \tan\varphi \approx \varphi$$

Substituting Eqs. (6-6), (6-7) and the equivalent values of the trigonometric functions into Eq. (6-4) gives the following equation:

$$c = \frac{h}{2} - \frac{\delta}{2} - \frac{\beta l^2}{2\delta}\left(\frac{1}{bhE_c} + \frac{2}{lK_a}\right)N - \frac{\beta l t_0}{\delta} + \left(\frac{h}{2} - c_1\right)\left(1 - \frac{M_{u1}\beta l}{K_r\delta}\right) \tag{6-8}$$

where c and c_1 are the neutral axis depths at the middle joint interface and the beam end, respectively. Detailed derivation process to obtain Eq. (6-8) is given by Appendix I.

Eq. (6-8) suggests that c can be expressed as a function of two variables c_1 and δ as both N and M_{u1} can also be determined by c_1, which will be explained later. Thus, for a given middle joint vertical displacement δ, c becomes a function of a single variable c_1. To solve two unknowns c and c_1, another equation correlating them can be obtained via equilibrium condition.

6.3.3 Equilibrium condition

When a beam is under CAA, rotations of beam sections are very small, so that there is no appreciable discrepancy between horizontal reaction forces and axial forces throughout the beam (Yu and Tan 2012b). Therefore, the axial forces acting at the beam ends (N_{u1}) and the joint interfaces (N_u) are equal. The magnitudes of N_{u1} and N_u are denoted as N.

$$N = N_{u1} = N_u \tag{6-9}$$

Based on assumptions 1) and 2), the stress and strain distributions as well as internal force components at a beam section are shown in **Fig. 6.5**. Both M and N are calculated with respect to the middle-depth axis of a beam section.

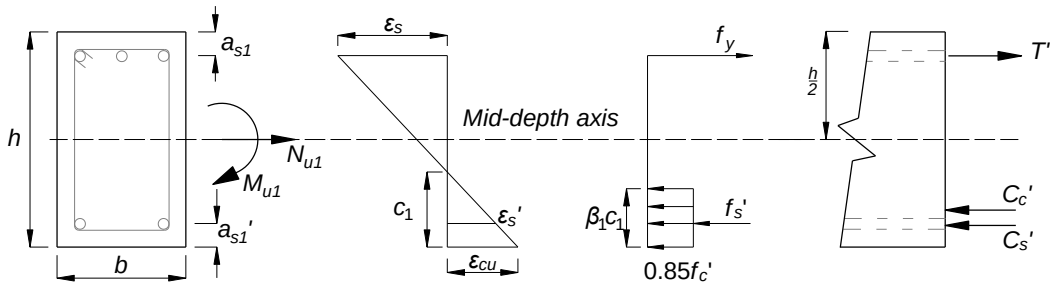

(a) Section and forces (b)Strain distribution (c)Stress distribution (d)Internal forces

Fig. 6.5: Strain and stress distribution at a beam section

Fig. 6.5(d) shows that the beam axial force of a section is contributed by compression concrete, compression and tension reinforcement. Therefore,

$$N_{u1} = C_c' + C_s' - T' \tag{6-10}$$

$$N_u = C_c + C_s - T \tag{6-11}$$

where C_c' and C_c are the concrete compressive forces, C_s' and C_s the steel compressive forces, and T' and T the steel tensile forces, acting on the beam ends and the middle joint interfaces, respectively. Based on **Fig. 6.5(c)**, C_c' and C_c can be calculated as

$$C_c' = 0.85 f_c' b \beta_1 c_1 \tag{6-12}$$

$$C_c = 0.85 f_c' b \beta_1 c \tag{6-13}$$

where f_c' is the compressive strength of concrete based on cylinder tests, and β_1 is the ratio of the depth of the equivalent rectangular stress block to the neutral-axis depth, as defined in ACI 318-05 (American Concrete Institute 2005).

According to **Fig. 6.5(b)**, the strains of compression and tension reinforcement at the beam ends are given by

$$\varepsilon_s' = \left(1 - \frac{a_{s1}'}{c_1}\right)\varepsilon_{cu} \tag{6-14a}$$

$$\varepsilon_s = \left(\frac{h - a_{s1}}{c_1} - 1\right)\varepsilon_{cu} \tag{6-14b}$$

where a'_{s1} and a_{s1} are the distances from the extreme compression fiber of concrete to the centroid of compression and tension reinforcement at the beam ends, respectively, and ε_{cu} is the ultimate compressive strain of concrete, assumed as 0.003.

After obtaining ε'_s via Eq. (6-14a), the compression reinforcement stress can be determined according to perfectly-elastic plastic constitutive model, as shown in **Fig. 6.3**. Except the first load step, the strain at each load step should be compared with the one at the last step to check whether compression reinforcement has started to unload. Accordingly, the steel compressive force is given by

$$\begin{aligned} C'_s &= \varepsilon'_s E_s A'_s \ (\text{if } \varepsilon'_s < \varepsilon_y) \\ C'_s &= f_y A'_s \ (\text{if } \varepsilon'_s \geq \varepsilon_y \ \& \ \varepsilon'_s \geq \varepsilon'_{sp}) \\ C'_s &= \left[f_y - E_s \left(\varepsilon'_{sp} - \varepsilon'_s \right) \right] A'_s \ (\text{if } \varepsilon_s' \geq \varepsilon_y \ \& \ \varepsilon_s' < \varepsilon_{sp}') \end{aligned} \tag{6-15}$$

where ε_y is the yield strain of steel reinforcement, ε'_{sp} is the strain of compression reinforcement at the last load step, and A'_s is the area of compression reinforcement.

According to **Fig. 6.5(c)**, the force of tension reinforcement at the beam end is calculated as

$$T' = f_y A_s \tag{6-16}$$

Since the tension reinforcement is at yield, ε_s is greater than ε_y. According to Eq. (6-14b), c_1 at the beam end should be less than $c_{yt1} = (h - a_{s1}) / (1 + \varepsilon_y / \varepsilon_{cu})$.

Furthermore, the compressive and the tensile forces of reinforcement at the joint interfaces can be determined in a similar way as Eqs. (6-14) to (6-16), but they are expressed as functions of neutral axis depth *c* at the middle joint interface. Finally, according to **Fig. 6.5(d)**, the bending moments M_{u1} and M_u at the beam ends and the joint interfaces can be determined with respect to mid-depth axis, respectively.

$$M_{u1} = C_c'\left(\frac{h}{2} - \frac{\beta_1 c_1}{2}\right) + C_s'\left(\frac{h}{2} - a_{s1}'\right) + T'\left(\frac{h}{2} - a_{s1}\right) \quad (6\text{-}17)$$

$$M_u = C_c\left(\frac{h}{2} - \frac{\beta_1 c}{2}\right) + C_s\left(\frac{h}{2} - a_s'\right) + T\left(\frac{h}{2} - a_s\right) \quad (6\text{-}18)$$

where a_{s1}' and a_s' are the distances from the extreme compression fiber of concrete to the centroid of compression reinforcement, a_{s1} and a_s the distance from the utmost tension fiber of concrete to the centroid of tension reinforcement, at the beam ends and the joint interfaces, respectively.

In summary, Eqs. (6-10) to (6-18) show that N_u and M_u are functions of c, and N_{u1} and M_{u1} are functions of c_1. Moreover, the force equilibrium in Eq. (6-9) correlates c with c_1. In other words, c is a function of c_1.

6.3.4 Procedure to implement the model

Force equilibrium gives one equation in terms of two unknowns c and c_1 independent of δ, and compatibility condition produces the second equation (i.e., Eq. (6-8)) in terms of c, c_1 and δ. Consequently, for a given δ, by solving these two non-linear equations simultaneously, the values of c and c_1 can be obtained. Subsequently, by substituting c and c_1 into Eqs. (6-9) to (6-18), one can obtain axial force N and bending moments M_{u1} and M_u. Substituting N, M_{u1} and M_u into Eq. (6-1) can determine vertical resistance P. Note that it is rather tedious to express these two non-linear equations explicitly. However, by following the procedure shown in **Fig. 6.6** and gradually increasing δ, the relationships of P, N, M_{u1} and M_u in terms of δ can be easily calculated. Then CAA capacity and maximum beam compression force can be obtained as well. The implementation of this model can be achieved by using Matlab program or Excel spreadsheets.

In the implementation of the model, as outlined in **Fig. 6.6**, two points should be noted:

(1) Determine the upper bound value (denoted as c_{1_upp}) of neutral axis depth c_1 at the beam end to ensure that the neutral axis depth c at the middle joint

interface is greater than zero via Eq. (6-8) and tension reinforcement is at yield stage.

(2) Substitute Eq. (6-8) into the nonlinear equation provided by force equilibrium (combining Eqs. (6-9) to (6-16)) to solve c_1 in an interval between $0.01c_{yt1}$ and c_{1_upp}. If there is no solution in this interval, calculation should be stopped and P_{max} and N_{max} can be selected from the previous load steps.

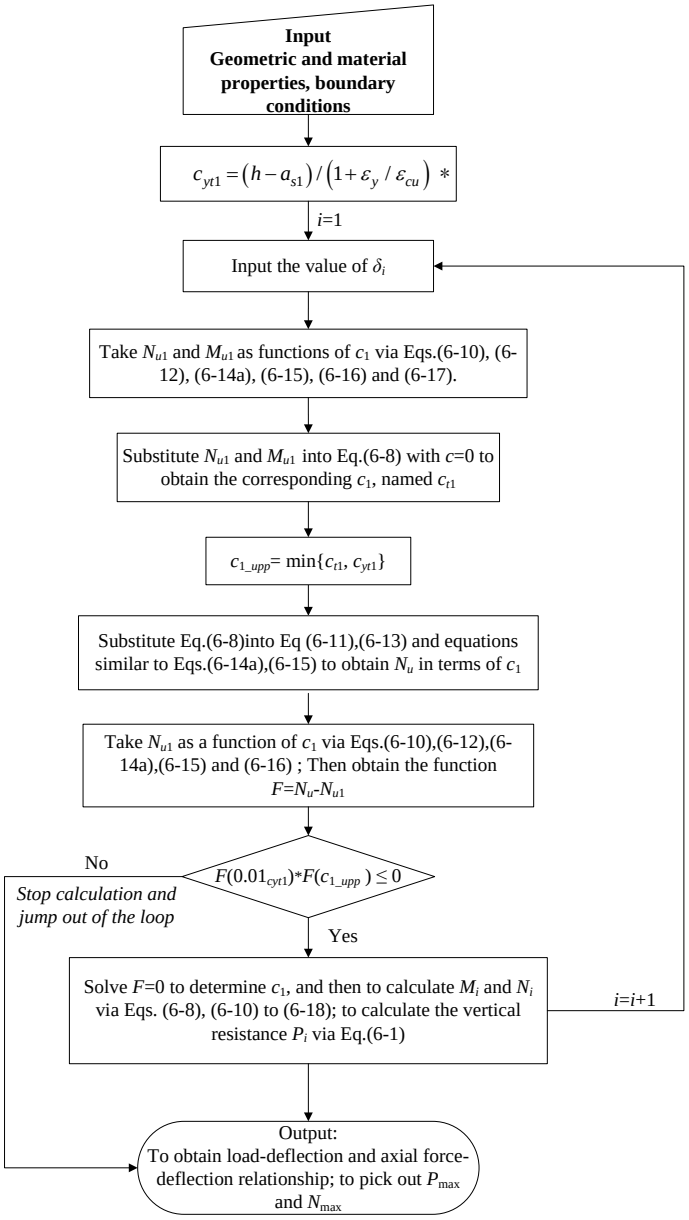

*: c_{yt1} is the neutral axis depth corresponding to the simultaneous occurrence of tensile rebar yielding and concrete crushing at beam ends.

Fig. 6.6: Procedure to calculate the vertical resistance and internal forces

Based on geometrical parameters of specimen S4, as shown in **Table 6.1**, **Fig. 6.7** illustrates the determination of neutral axis depths at a given middle joint displacement δ from $0.1h$ to h, where h is the beam depth of S4. Two curved surfaces are determined by compatibility condition and force equilibrium, respectively. At each δ, with increasing c_1, compatibility equation (Eq. (6-8)) causes c to decrease, even to negative values. Therefore, it is necessary to set an upper limit of c_1 to preclude this situation. The intersections of the two surfaces are the system solutions. **Figs. 6.7(a)** and **(b)** indicate that with increasing δ, both c and c_1 increase first and then decrease. Note that in this case, the compression reinforcement is at elastic stage.

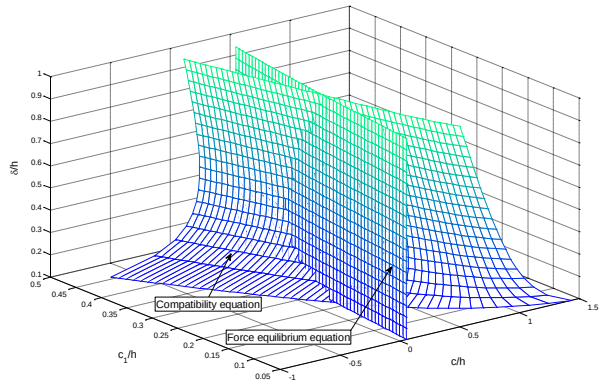

(a) Variations of c_1 at beam ends

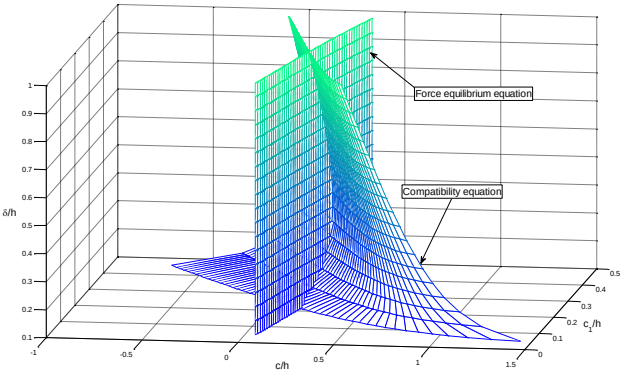

(b) Variations of c at middle joint interfaces

Fig. 6.7: Variations of neutral axis depths at critical sections

6.3.5 Equivalent stiffness of restraints

All restraints from the surrounding structure to a beam-column sub-assemblage can be converted to axial (or horizontal), vertical and rotational restraints. Assuming the surrounding structure to be in elastic state, each restraint stiffness can be evaluated

by applying a unit displacement at one end of the sub-assemblage corresponding to that degree of freedom and then back calculating the resistance provided by the surrounding structure via linear elastic finite element analysis. It is most likely that the restraint stiffnesses at the two ends of a sub-assemblage are not equal. To satisfy assumption 4) in section 6.3.1, it is necessary to obtain the equivalent stiffness of axial and rotational restraints.

With increasing central deflection, at each load step, the reaction forces at the sub-assemblage ends are in equilibrium along the axial restraint direction. The equivalent axial restraints must satisfy force equilibrium and deformation compatibility caused by the actual axial restraints at both ends of a sub-assemblage. Therefore,

$$k_1 \Delta_1 = k_2 \Delta_2 = k_{eq} \Delta \tag{6-19}$$

$$2\Delta = \Delta_1 + \Delta_2 \tag{6-20}$$

Combining Eq. (6-19) with Eq. (6-20) gives

$$k_{eq} = \frac{2k_1 k_2}{k_1 + k_2} \tag{6-21}$$

where k_1 and k_2 are the axial stiffnesses, Δ_1 and Δ_2 the displacements of axial restraints at each end of the sub-assemblage, respectively; k_{eq} and Δ are the axial stiffness and the displacement of equivalent axial restraints, respectively.

For example, if a sub-assemblage simply supported at both ends, either k_1 or k_2 is equal to zero. As a result, k_{eq} is zero according to Eq. (6-21). As shown in Eq. (6-8), the value of neutral axis depth *c* at the joint interfaces will tend to negative infinity, i.e. no compression zone at middle joint interfaces. In other words, *CAA cannot be mobilized*.

The equivalent rotational stiffness is simply selected as the smaller stiffness of both ends because the weaker rotational restraint dominates the structural mechanism of a sub-assemblage. For example, if one end is a pin, the existence of compression zone and tension reinforcement will produce a couple, which violates the pin

boundary condition. Therefore, it is impossible for a compression zone to develop at the sub-assemblage end, and thus CAA cannot be mobilized. That is, weak rotational restraints will inhibit the development of CAA. However, the structural behavior under extreme weak rotational restraints is outside the scope of this study.

When CAA cannot be mobilized, beam axial compression N equals to zero. Accordingly, Eq. (6-1) is simplified to calculate the capacity of pure flexural action. To obtain flexural capacity via the proposed model, a small axial restraint stiffness (e.g. K_a=10^{-2} kN/m) should be set in Eq. (6-8).

6.4 Discussions on the proposed model

The limitations of the proposed model are caused by assumption 2), in which the ultimate compressive strain of concrete ε_{cu} is assumed constant. **Fig. 6.8(a)** shows the actual variations of strains of concrete and reinforcement throughout CAA. With increasing sub-assemblage deflection, the strain profile at a critical section sequentially experiences profiles 1 to 3. It can be seen that the strain of tension reinforcement ε_s keeps increasing, and the strains of both concrete (ε_{cu}) and compression reinforcement (ε_s') increase first and then start decreasing after attaining the peak values. Accordingly, the neutral axis depth c_1 increases first and then decreases. If ε_{cu} is assumed fixed, as illustrated in **Fig. 6.8(b)**, the variations of both ε_s' and c_1 are similar to the ones in the actual CAA process. However, at CAA stage, the assumption of constant ε_{cu} leads to an artificial unloading in tension reinforcement, as illustrated by the transition of strain profile 1 to 2 shown in **Fig. 6.8(b)**. To conform with reality and to avoid possible errors caused by this "unloading" process, the tension reinforcement is assumed to remain at yield, and the corresponding stress is taken as the yield strength in analysis.

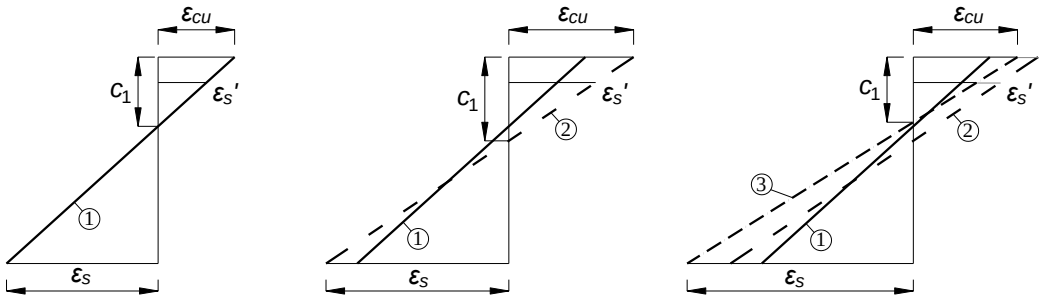

At Start of CAA | Around CAA Capacity | At decline of CAA

(a) Actual strain variations at CAA stage

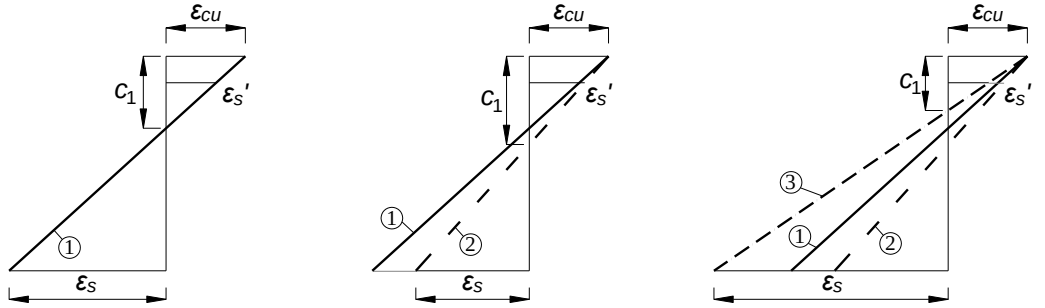

At Start of CAA | Around CAA Capacity | At decline of CAA

(b) Strain variations based on assumed constant ultimate concrete strain

Fig. 6.8: Comparisons of strain variations in actual CAA and the proposed model

Another issue is the distribution of compressive forces at concrete and compression reinforcement. As shown in **Fig. 6.8(a)**, ε_{cu} may increase beyond 0.003. Accordingly, the actual variation range of ε_s' is larger than the one in the proposed model, as illustrated in **Fig. 6.8(b)**. Therefore, compression reinforcement may sustain larger compressive force. Additionally, after concrete has attained a larger ε_{cu}, even beyond the crushing strain, the compression reinforcement has to sustain more compressive force. However, in the proposed model, as shown in **Fig. 6.8(b)**, the contributions of concrete and compression reinforcement to compressive forces are overestimated and underestimated, respectively. Therefore, the shortcoming caused by constant ε_{cu} will become more obvious if severe concrete crushing occurs at some critical sections. However, RC beams are usually under-reinforced so that they can fail in a ductile mode, i.e. reinforcement yielding prior to concrete crushing. As a result, *M-N* interaction of beam sections is similar to the one shown

in **Figs. 6.1(b)** and **(c)**, and compression failure with severe concrete crushing can be avoided.

In summary, assumption 2) is a trade-off between the simplicity to obtain cross-sectional forces and the complexity to determine them via numerical analysis. The agreement of the experimental *M-N* path and analytical *M-N* interaction diagram at each section in **Figs. 6.1(b)** and **(c)** indicates that assumption 2) is acceptable in terms of accuracy to determine cross-sectional forces. Moreover, the validity and accuracy of the proposed model to predict CAA capacity and maximum beam compression will be evaluated by test results (Su et al. 2009; Yu and Tan 2011a; 2012b).

6.5 Validation of the proposed model

Comparisons of experimental and analytical results are listed in **Table 6.1**. Similar to test results, the proposed model does not consider the effect of self-weight of specimens. The pertinent parameters for the proposed model are included in **Table 6.1** as well. More detailed information about those tests, such as test set-ups, beam section dimensions, etc, can be found in papers (Su et al. 2009; Yu and Tan 2011a; 2012b). With the exception of the axial force of A6, comparisons in **Table 6.1** indicate that the proposed analytical model is able to predict the capacity of CAA and maximum beam axial compression with satisfactory accuracy and reliability. For predicting CAA capacity, the mean value is 0.955, and the coefficient of variation is less than 10%.

Table 6.1 Comparisons of experimental and analytical results

Test*	Boundary conditions			l/h†	Longitudinal reinforcement at middle joints‡		Material properties		Capacity of compressive arch action (kN)			Maximum axial compression (kN)		
	Axial stiffness (kN/m)	Axial gap (mm)	Rotational stiffness (kN·m/rad)		Top	Bottom	f_c' (MPa)	f_y (MPa)	Experimental results P_{caa}	Analytical results P_a	P_a/P_{caa}	Experimental results N_{max}	Analytical results N_a	N_a/N_{max}
S1	$1.06x10^5$	0.5	$1.0x10^4$	23	2T10 +1T13	2T10	31.24	511	41.64	43.57	1.046	177.9	156.70	0.881
S2		1.2		23	3T10	2T10			38.38	38.39	1.000	155.9	141.86	0.910
S3	$4.29x10^5$	1.0	$3.0x10^4$	23	3T13	2T10	38.15	511 (T10); 494 (T13); 513 (T16)	54.47	56.15	1.031	221.0	227.85	1.031
S4		0.8		23	3T13	2T13			63.22	63.90	1.011	212.7	231.50	1.088
S5		0.8		23	3T13	3T13			70.33	72.16	1.026	238.4	224.03	0.940
S6		0.8		23	3T16	2T13			70.33	74.08	1.053	218.1	196.49	0.901
S7		1.2		18.2	3T13	2T13			82.82	83.15	1.004	233.1	244.61	1.049
S8		0.8		13.4	3T13	2T13			121.34	126.31	1.041	272.5	300.15	1.101
A1	$1.0x10^6$	0	$1.75x10^4$	9	2ϕ12	2ϕ12	24.55	350 (ϕ12); 340 (ϕ14)	168	152.53	0.908	388	338.71	0.873
A2					3ϕ12	3ϕ12	26.83		221	190.04	0.860	324	367.68	1.135
A3					3ϕ14	3ϕ14	29.64		246	228.34	0.928	305	403.08	1.322
A4					2ϕ12	1ϕ14	21.89		147	133.09	0.905	344	305.08	0.887
A5					3ϕ12	2ϕ12	25.16		198	169.14	0.854	393	348.02	0.886
A6					3ϕ14	2ϕ14	27.21		226	200.00	0.885	191§	380.37	--
B1				14	3ϕ14	3ϕ14	17.63		125	111.93	0.895	225	230.45	1.024
B2				19		3ϕ14	18.32		82.9	79.71	0.962	210	222.67	1.060
B3				19		2ϕ14	20.06		74.7	72.57	0.971	210	244.85	1.166
C1				13.5	2ϕ12	2ϕ12	15.12		60.9	49.62	0.815	108	90.949	0.842
Mean for all specimens											0.955			1.006
COV for all specimens											0.075			0.132

*: Tests S1~S8 are from Yu and Tan (2011a; 2012b) and Tests A1~C1 are from Su et al. (2009), and the concrete strength by the latter are converted from cubic strength to cylinder strength by multiplying 0.76;

†: l is total length of the whole two-bay beam, equal to the summation of two times net span length of a single-bay beam and a joint width;

‡:"T" denotes high strength reinforcement and the following number is bar diameter;

§: This axial force deviates largely from other test results within the same batch, so it is not used for comparison.

Fig. 6.9 shows that the proposed model can also predict the reasonable trend of load-deflection (*P*-*δ*) and beam axial force-deflection (*N*-*δ*) relationships of the sub-assemblages, from the deflection of *one-tenth* to *one* beam depth. However, compared with experimental results, the proposed model tends to predict smaller displacements corresponding to the capacity of CAA and the maximum beam axial force, respectively. Based on the assumption 2), the model can only be applied when sufficient vertical deflection has occurred to allow plastic hinges to develop at all critical sections. Additionally, when the middle joint of a sub-assemblage reaches a displacement of one beam depth, it is likely that catenary action takes over CAA to sustain applied loads. Therefore, the *P*-*δ* and *N*-*δ* relationships are discussed within the deflection range of *one-tenth* to *one* beam depth, so that the plastic hinges at critical sections have already formed, and catenary action of sub-assemblages has not yet commenced.

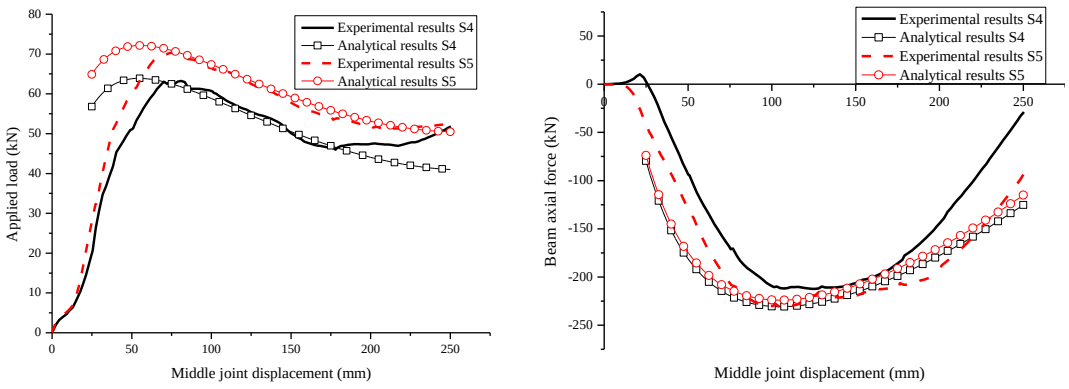

(a) Load-displacement relationship

(b) Beam axial force-displacement relationship

Fig. 6.9: Comparisons of applied load and axial force vs. displacement relationships

Based on accuracy and reliability, the proposed model is an efficient tool to investigate the effects of pertinent parameters on CAA. In the following sections, after the comparisons with Park's model, parametric studies are conducted with the proposed model.

6.6 Comparisons with Park's model

The proposed model is initially compared with Park's model under the same partial axial restraints without considering the effects of axial connection gaps and partial rotational restraints. Thereafter, the actual boundary conditions are introduced into the proposed model to highlight the necessity of considering the effects of imperfect boundary conditions on CAA.

Fig. 6.10(a) shows the comparisons of two models based on the parameters of specimen S4, as listed in **Table 6.1**. Initially, S4 is regarded as axially restrained with a stiffness of 4.29×10^5 kN/m. The rotational restraint stiffness is assumed infinitely large, and there are no axial connection gaps. Under this controlled boundary condition, Park's model with assumed yielding compression reinforcement overestimates the CAA capacity. If the compression reinforcement stress is taken as zero, the CAA capacity is underestimated compared to the test result. The close-up in **Fig. 6.10(a)** demonstrates that at CAA stage, the stress state of compression reinforcement is actually elastic, which is predicted by the proposed model. The maximum compressive stress is around 260 MPa, much lower than the yield strength of steel reinforcement at 494 MPa. Consequently, the capacity predicted by the proposed model is in between two limits estimated by Park's model. Finally, the actual boundary conditions are introduced into the proposed model. Due to the gaps and the partial rotational restraints, the CAA capacity reduces from 69.32 kN to 63.55 kN, but the corresponding middle joint displacement increases. It indicates that boundary conditions are crucial for an accurate prediction of CAA capacity.

Fig. 6.10(b) shows the comparisons based on the parameters of specimen A5, as listed in **Table 6.1**. Besides the axial stiffness of $1.0\text{x}10^6$ kN/m, the rotational restraint stiffness $1.75\text{x}10^4$ kN m/rad is also introduced into the proposed model because this rotational stiffness is adequately large so that there is no appreciable effect on CAA capacity. The proposed model indicates that the compression reinforcement has yielded when CAA attains its capacity, as shown in **Fig. 6.10(b)**. Thus, CAA capacity predicted by the proposed model is very close to the one predicted by Park's model which assumed yielding compression reinforcement.

Unlike S4, the yield strength of compression reinforcement in A5 is much lower, at 350 MPa. At CAA stage, the stress level of compression reinforcement of A5 did not deviate significantly from the yield strength, so the overall trend of the load-middle joint displacement relationship calculated by both models agree well with each other, as shown in **Fig. 6.10(b)**. Clearly, assuming zero stress for compression reinforcement is too conservative, which will downplay the contribution due to CAA.

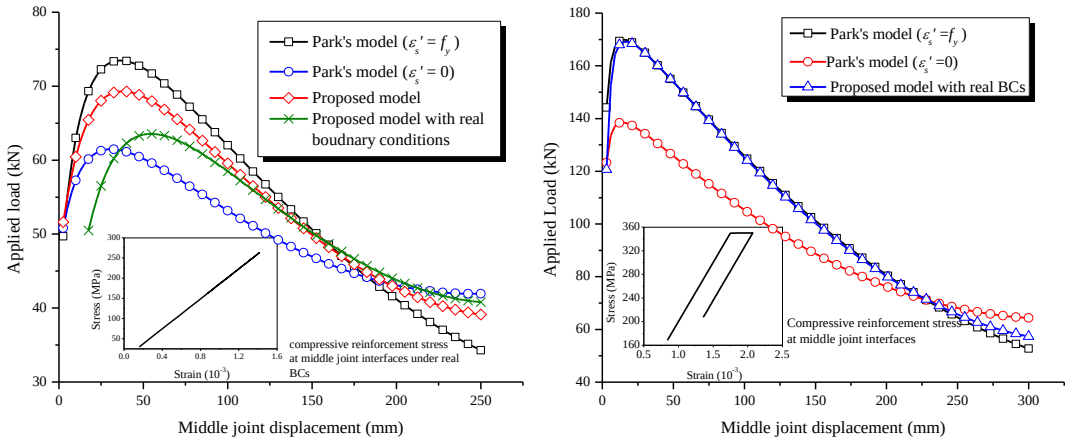

(a) Based on S4 (w/ high-strength bars) (b) Based on A5 (w/ moderate-strength bars)

Fig. 6.10: Comparisons of the proposed model and Park's model

The above comparisons illustrate that the variations of compression reinforcement stress should be considered in determining CAA capacity and maximum axial compression. This can be achieved by the proposed model. When the compression reinforcement is in elastic stress state, say much lower than the yield stress, the prediction based on yield strength will overestimate CAA capacity. Meanwhile, assuming zero stress for compression reinforcement in doubly-reinforced beams is far too conservative. Therefore, the accuracy of CAA capacity predicted by the proposed model is dependent on the stress state of compression reinforcement.

6.7 Effects of imperfect boundary conditions on compressive arch action

The boundary conditions discussed herein include axial and rotational restraints and axial connection gaps at the beam ends. For RC structures, beams above a missing

column are supported by adjacent frames. External loads acting on sub-assemblages are transferred to adjacent frames or the remaining structure due to continuity. The stiffness of axial and rotational restraints depends on the structural stiffness of adjacent frames or the remaining structure. It can be assumed that the initial damage is confined to a local region, for instance, just within the frame which has lost a column, but the remaining structure is still at elastic stage. Then the stiffnesses of both axial and rotational restraints can be obtained via linear elastic analysis on the remaining structure. Finally, the equivalent restraint stiffness can be evaluated by the method suggested in section 6.3.5.

As for structural testing in a laboratory, the connections at the boundaries of specimens may not be perfect. To some extent, connection gaps are inevitable. However, axial connection gaps have a detrimental effect on CAA, especially on the development of beam axial compression. Similarly, Park and Gamble (2000) pointed out that the behavior of one-way slab strips is much less sensitive to imperfect restraint against rotation and vertical translation than to small horizontal displacement.

For typical RC framed structures, the ratio of beam span to depth is around 8~12. Due to the removal of a middle column, this ratio is approximately doubled, i.e. 16~24. Therefore, specimen S4 (l/h=23) and S7 (l/h=18.2) listed in **Table 6.1** represent typical RC beams. Moreover, the restraints in sub-assemblage tests, including two horizontal pin-pin connections and pin supports seated onto rollers, can be converted into equivalent axial and rotational restraints as well as rigid vertical supports at two ends of the two-bay beam. It is found that the effects of connection gaps, partial axial and rotational restraints on S4 and S7 are quite similar. Thus, for simplicity, the effects of imperfect boundary conditions on CAA will be illustrated based on the material and geometrical properties of S4. In cast in-situ concrete structures, there are no axial connection gaps for continuous RC beams. Hence, the capacity of CAA (P_0 = 69.10 kN) and the magnitude of maximum axial compression (N_0 = 275.90 kN) of S4 with *zero gap*, calculated by the proposed model, are used to normalize the applied load P and the beam axial force N in all cases, respectively. On the other hand, to obtain more general conclusions on the

effects of partial axial and rotational restraints on *CAA capacity*, specimens A5 and S7 are compared as well. The corresponding material and geometric properties as equivalent restraint stiffness of S4, S7 and A5 are included in **Table 6.1**.

6.7.1 The effect of axial connection gaps

Except the values of gaps, all the other parameters of S4 are the same as those listed in **Table 6.1**. **Fig. 6.11** shows that the overall trends of load-deflection and beam axial force-deflection relationships are similar under different connection gaps and indicates that CAA capacity and maximum axial compression are very sensitive to the magnitude of axial connection gaps. Compared with a beam span length of 5750 mm, a gap of 0.8 mm is negligible. However, when the gap increases by 0.8 mm, the CAA capacity P_a and the maximum axial compression N_{max} of the sub-assemblage decrease by around 8% and 19%, respectively. Therefore, it is necessary to measure the gaps between axial restraints and a specimen during testing. Otherwise, the structural capacity of the specimen due to CAA will be underestimated compared to its prototype in RC structures. However, this analytical model can be used to re-evaluate P_a of tested specimens with zero gaps to make specimens more representative to continuous beams in RC structures.

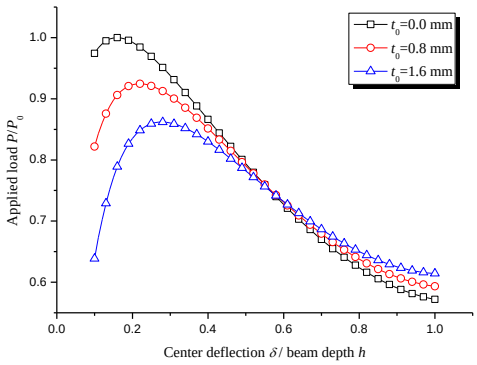

(a) Load-deflection relationship (P_0 = 69.10 kN)

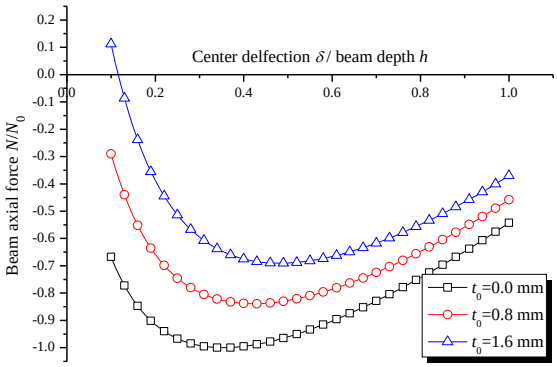

(b) Beam axial force-deflection relationship (N_0 = 275.90kN)

Fig. 6.11: Effect of axial connection gaps on CAA

6.7.2 The effect of axial restraint stiffness

To illustrate the effect of axial restraint stiffness K_a on CAA, the stiffness term is normalized by the beam axial stiffness, as follows:

$$\gamma_a = \frac{K_a}{E_c bh / l} \tag{6.22}$$

where l is the net span length of the two-bay beam, i.e. $2l_n$ plus the middle column width of 250 mm. For specimen S4, the two-bay beam uncracked axial stiffness $E_c bh / l$ is equal to 1.93×10^5 kN/m. This value is used to calculate the relative axial stiffness γ_a of restraints for all cases. As shown in **Table 6.1**, K_a for specimen S4 is 4.29×10^5 kN/m, so γ_a of specimen S4 during the test is 2.22.

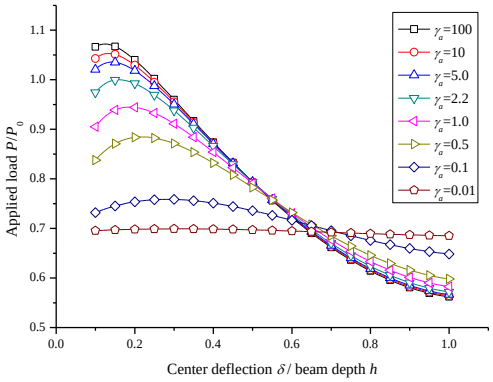

(a) Load-deflection relationship

(P_0 = 69.10 kN)

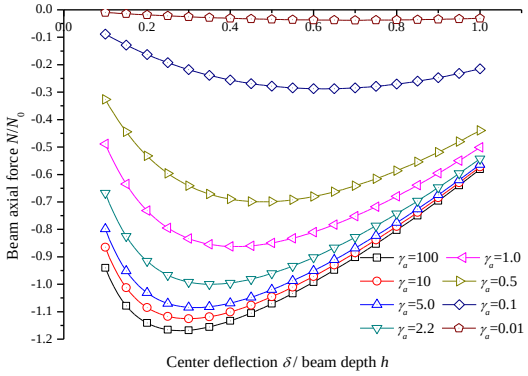

(b)Beam axial force-deflection relationship

(N_0 = 275.90 kN)

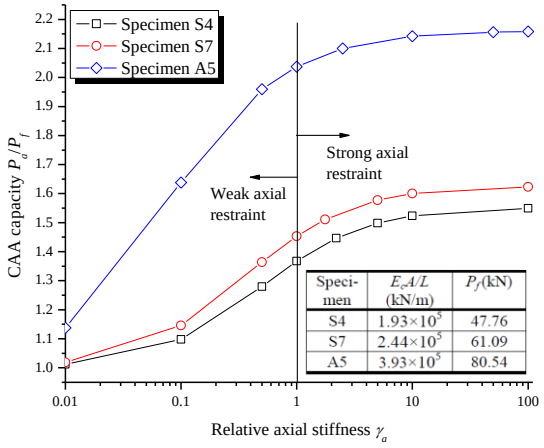

(c) Variation of CAA capacity

Fig. 6.12: Effect of axial restraint stiffness on CAA

Figs. 6.12(a) and **(b)** show that the effect of axial restraint stiffness K_a on the load-deflection and the axial force-deflection relationships becomes apparent only when the axial restraint is *weak*, defined as γ_a < 1.0. With further increasing deflection of the sub-assemblage which has attained CAA capacity, a larger axial restraint

stiffness corresponds to a steeper decrease of structural resistance and axial compression, as shown in **Figs. 6.12(a)** and **(b)**, respectively. Moreover, a small axial restraint stiffness inhibits the mobilization of large axial force, as shown in **Fig. 6.12(b)**. For example, when γ_a = 0.01 (i.e. axial restraint is too weak), structural resistance P is nearly constant with increasing deflection δ, and beam axial force N is so small that it can be ignored. Therefore, the structural mechanism of the sub-assemblage with γ_a = 0.01 is almost identical to pure flexural action.

A comparison between **Figs. 6.12(a)** and **(b)** suggests that compared to CAA capacity P_a, the maximum beam axial force N_{max} is more sensitive to the variation of K_a. It should be noted that an increase of axial restraint stiffness K_a is always beneficial to both P_a and N_{max}. However, when axial restraint is *weak*, i.e. $\gamma_a < 1.0$, a larger K_a can more effectively increase P_a and N_{max}; when axial restraint is *strong*, defined as $\gamma_a \geq 1.0$, K_a does not significantly affect both P_a and N_{max}, and the marginal effect of a greater K_a on increasing both of them decreases quickly. For example, from γ_a = 0.1 to 1.0, P_a and N_{max} of S4 increase by around 24% and 197%, respectively. However, from γ_a = 1.0 to 10, P_a and N_{max} only increase by around 12% and 30%, respectively. When $\gamma_a > 5.0$, the effect of K_a on CAA can be neglected, since from γ_a = 5 to 100, the enhancement of CAA capacity is only 3.6%.

Similar conclusions about the effect of axial restraint stiffness K_a on *CAA capacity* can also be found in specimens S7 and A5, as illustrated in **Fig. 6.12(c)**. Flexural capacity P_f is based on a mechanism that plastic hinges have formed at the middle joint interfaces and the beam ends, as shown in **Fig. 6.1(a)**, without considering the presence of beam axial force. The ratio of P_a/P_f represents the enhancement of structural resistance due to CAA. The uncracked axial stiffness of sub-assemblages for each specimen is indicated in **Fig. 6.12(c)** as well. It can be found that CAA capacity is sensitive to K_a only when axial restraint is weak (i.e. $\gamma_a < 1.0$). The effect of a greater K_a on CAA capacity becomes marginalized when axial restraint is strong (i.e. $\gamma_a \geq 1.0$). Therefore, to be conservative in design, the beneficial effect of CAA on structural resistance can be considered only when *strong axial restraints* are provided.

6.7.3 The effect of rotational restraint stiffness

As shown in **Fig. 6.4**, due to rotated beam end supports, neutral axis depth c_1 (or compressive depth) decreases. If the rotational restraint stiffness K_r is too small, the supports can easily rotate, and CAA may not be effectively mobilized. Guice and Rhomberg (1988) concluded that high rotational restraint stiffness does not affect compressive membrane capacity of RC slab strips. In a real building, the supports at the beam ends are not as rigid as idealized; they can be considered as partial rotational restraints. To illustrate the effect of K_r, the term is normalized by the rotational stiffness of beam ends $4E_cI/l$. Then the relative stiffness γ_r is given by

$$\gamma_r = \frac{K_r}{4E_cI/l} \tag{6.23}$$

where I is the second moment inertia of an uncracked beam section.

For specimen S4, the rotational stiffness of beam ends $4E_cI/l$ is equal to 4028 kNm/rad. This value is used to calculate γ_r of restraints for all cases. As shown in **Table 6.1**, K_r of specimen S4 is 30000 kNm/rad, so corresponding γ_r is equal to 7.4.

Figs. 6.13(a) and **(b)** show that the effect of rotational restraint stiffness K_r on load-deflection and axial force-deflection relationships is insignificant when rotational restraint is strong, also defined as $\gamma_r \geq 1.0$. For example, when γ_r equals to 5.0, 7.4 and 100, the load-deflection and axial force-deflection relationships in these three cases are almost identical. A greater K_r results in a steeper decrease of structural resistance after CAA capacity.

Fig. 6.13(a) shows that strong rotational restraint (i.e. $\gamma_r \geq 1$) has no significant effect on CAA capacity. From $\gamma_r = 1$ to 5, the increase of CAA capacity of S4 is less than 5%. Moreover, when $\gamma_r \geq 5$, the effect of rotational restraint stiffness K_r on both CAA capacity P_a and maximum beam axial force N_{max} can be neglected, as shown in **Figs. 6.13(a)** and **(b)**. However, for weak rotational restraint, defined as $\gamma_r < 1$, both P_a and N_{max} decrease significantly with reducing K_r, since large rotations at beam ends will substantially reduce the compressive depth of beam sections. When γ_r is too small, e.g. less than 0.2, CAA cannot be effectively developed.

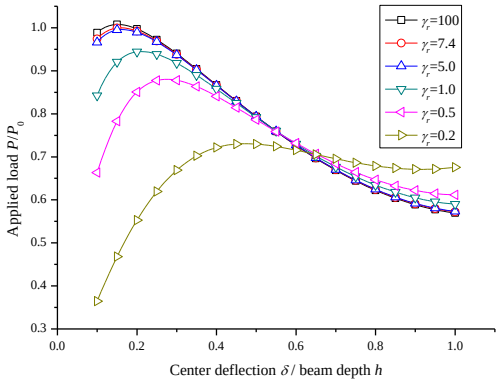

(a) Load-deflection relationship

(P_0 = 69.10 kN)

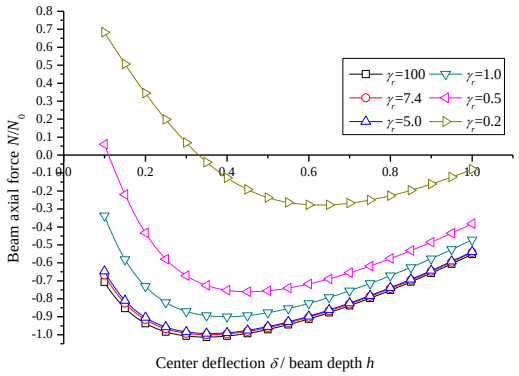

(b) Beam axial force-deflection relationship

(N_0 = 275.90 kN)

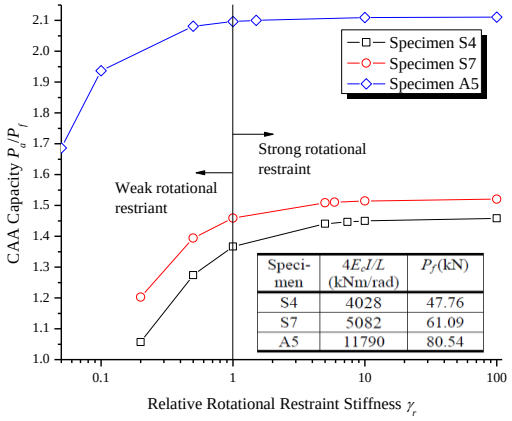

(c) Variation of CAA capacity

Fig. 6.13: Effect of rotational restraint stiffness on CAA

Similar conclusions about the effect of rotational restraint stiffness K_r on *CAA capacity* can also be found in specimens S7 and A5, as illustrated in **Fig. 6.13(c)**. That is, when $\gamma_r < 1$, a larger K_r results in a greater CAA capacity, but when $\gamma_r \geq 1$, the rotational restraint stiffness K_r nearly has no effect on CAA capacity. This conclusion confirms Guice and Rhomberg's finding in their experiments that high rotational restraint stiffness does not affect compressive membrane capacity of RC slabs. However, to mobilize CAA, adequate rotational restraints must be provided. To be conservative in design, the provision of strong *rotational restraints* with $\gamma_r \geq$ 1.0 can be regarded as a prerequisite to include CAA.

6.8 Effect of span-to-depth ratio and mechanical reinforcement ratio on compressive arch action

Su et al.(2009) reported that CAA is a function of flexural reinforcement ratio and the ratio of a single-bay beam span (l_n) to depth (h). Considering various yield strengths of steel reinforcement and compressive strengths of concrete, the mechanical reinforcement ratio $\omega = \rho f_y / f_c$ is a more representative parameter than the reinforcement ratio by area, since ω is frequently used as a measure of the flexural behavior of a beam and incorporates three major variables affecting that behavior (MacGregor and Wight 2005). Therefore, by using the proposed model, the effects of span-to-depth ratio (l_n/h) and mechanical reinforcement ratio (ω) of beams on CAA are investigated. It should be noted that flexural reinforcement is the tension reinforcement at critical sections, such as the middle joint interfaces and the end-column-stub interfaces of RC sub-assemblages. The top and the bottom reinforcement at the middle joint interfaces under sagging moment are in compression and tension, respectively. However, the top compression reinforcement at the middle joint interfaces is the same as the tension reinforcement at the end-column-stub interfaces subjected to hogging moment. As a result, the total reinforcement at the middle joint interfaces can represent all flexural reinforcement at critical sections of a single-bay beam at one side of the middle joint. Consequently, the total reinforcement ratio at middle joint interfaces is used to determine mechanical reinforcement ratio ω.

Based on the investigation of imperfect boundary conditions, both the axial and the rotational restraints in Yu and Tan's tests (Yu and Tan 2012b) can be categorized as strong restraints. Such restraints with zero gaps are used to investigate the effect of beam span-to-depth ratio l_n/h and mechanical reinforcement ratio ω on CAA of RC sub-assemblages. Five groups of case study are listed in **Table 6.2**. It can be seen that a large range of flexural reinforcement ratio is covered, ranging from 0.49% to 1.87%. The single-bay beam span-to-depth ratio l_n/h varies from 6.5 to 11. Note that the plastic hinges occur at the joint interfaces, rather than at the center of the total span. Besides CAA capacity P_a, the flexural action capacity P_f and the enhancement factor α are listed in **Table 6.2** as well.

Table 6.2 Study cases with different beam span-to-depth ratios and mechanical reinforcement ratios*

l_n/h	Longitudinal reinforcement and ratio at middle joint interfaces†		Mechanical reinforcement ratio ω (%)	Flexural action capacity P_f (kN)	CAA capacity P_a (kN)	Enhancement factor α ($=(P_a-P_f)/P_f$)
	Top	Bottom				
11	3T10 (0.73%)	2T10 (0.49%)	16.32	30.25	53.65	0.774
	3T13 (1.23%)	2T10 (0.49%)	22.46	40.47	61.29	0.514
	3T13 (1.23%)	2T13 (0.82%)	26.51	47.27	68.50	0.449
	3T13 (1.23%)	3T13 (1.23%)	31.81	55.94	76.69	0.371
	3T16 (1.87%)	2T13 (0.82%)	35.72	61.56	78.94	0.282
9.5	3T10 (0.73%)	2T10 (0.49%)	16.32	35.03	64.31	0.836
	3T13 (1.23%)	2T10 (0.49%)	22.46	46.86	73.09	0.560
	3T13 (1.23%)	2T13 (0.82%)	26.51	54.74	81.50	0.489
	3T13 (1.23%)	3T13 (1.23%)	31.81	64.78	91.00	0.405
	3T16 (1.87%)	2T13 (0.82%)	35.72	71.29	93.38	0.310
8.5	3T10 (0.73%)	2T10 (0.49%)	16.32	39.15	73.64	0.881
	3T13 (1.23%)	2T10 (0.49%)	22.46	52.37	83.41	0.593
	3T13 (1.23%)	2T13 (0.82%)	26.51	61.18	92.86	0.518
	3T13 (1.23%)	3T13 (1.23%)	31.81	72.40	103.49	0.429
	3T16 (1.87%)	2T13 (0.82%)	35.72	79.67	105.98	0.330
7.5	3T10 (0.73%)	2T10 (0.49%)	16.32	44.37	85.59	0.929
	3T13 (1.23%)	2T10 (0.49%)	22.46	59.36	96.61	0.628
	3T13 (1.23%)	2T13 (0.82%)	26.51	69.34	107.39	0.549
	3T13 (1.23%)	3T13 (1.23%)	31.81	82.05	119.46	0.456
	3T16 (1.87%)	2T13 (0.82%)	35.72	90.29	122.08	0.352
6.5	3T10 (0.73%)	2T10 (0.49%)	16.32	51.20	101.38	0.980
	3T13 (1.23%)	2T10 (0.49%)	22.46	68.49	114.07	0.665
	3T13 (1.23%)	2T13 (0.82%)	26.51	80.00	126.57	0.582
	3T13 (1.23%)	3T13 (1.23%)	31.81	94.67	140.54	0.485
	3T16 (1.87%)	2T13 (0.82%)	35.72	104.19	143.34	0.376

*: The stiffness of the axial and the rotational restraints and the material properties is the same as Yu and Tan's test (2012b): f_c=38.2 MPa, f_y=511 for T10, f_y=494 for T13, f_y=513 for T16, E_s=200 GPa for all reinforcement.

†: $\rho = A_s / bd$, in which b=150 mm and d=215 mm.

Fig. 6.14 shows that the variation range of the enhancement factor α of RC sub-assemblages due to CAA is very large, from around 30% to 100%, under different combinations of beam span-to-depth ratios l_n/h and mechanical reinforcement ratios ω. With increasing ω, enhancement factor α decreases significantly for a given l_n/h. In other words, RC beams with low reinforcement ratios can gain the beneficial effect from CAA. For instance, under l_n/h = 11, when the mechanical reinforcement

ratio ω decreases from 35.72% to 16.32%, the enhancement factor α increases from 28.2% to 77.4%. For a known ω, a smaller l_n/h results in a greater enhancement factor α. That is, the enhancement of structural resistance due to CAA in a stocky RC beam is more evident. For example, under ω=16.32%, when l_n/h decreases from 11 to 6.5, the corresponding α increases from 77.4% to 98.0%. However, when ω=35.72%, such a variation of l_n/h only results in α increasing from 28.2% to 37.6%.

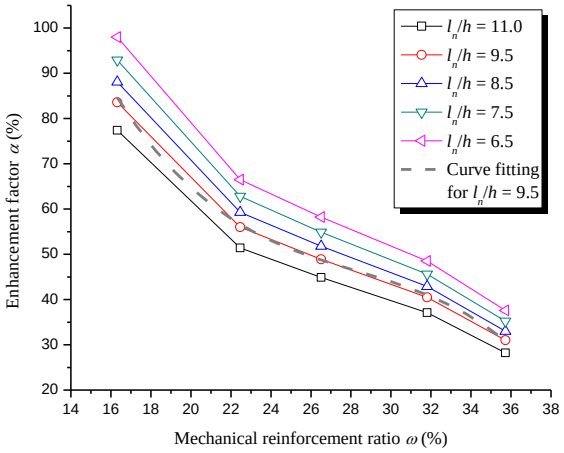

Fig. 6.14: Effect of span-to-depth ratio and mechanical reinforcement ratio on enhancement factor

In summary, for beams under adequate axial and rotational restraints, a lower mechanical reinforcement ratio and a lower span-to-depth ratio will give rise to a significant enhancement of structural resistance contributed by CAA.

6.9 Implementation of CAA into design

Due to the dynamic nature of progressive collapse, the quasi-static structural resistance must be multiplied with a dynamic increase factor (DIF), which depends on structural ductility, to evaluate the ultimate progressive collapse resistance. The DIF model proposed in UFC 4-023-03 implies that structures behave in perfectly elastic-plastic modes or in hardening modes. That is, with increasing structural deflection, structural resistance remains constant or keeps increasing. Prior to attaining CAA capacity, RC structures do perform in hardening modes provided that adequate horizontal restraints are provided at both ends of two-bay beams

above a removed column. Therefore, if the deflection corresponding to CAA capacity is not greater than allowed deflection limits in UFC-4-023-03, the structural mechanism of CAA can be confidently incorporated into the alternate load method in design.

Since the parametric studies are conducted based on an RC sub-assemblage subjected to a concentrated load and RC members in design are typically under uniformly distributed load (UDL), the effect of loading types on CAA is studied first.

6.9.1 Effect of loading types on CAA

With plastic hinges occurring symmetrically at the middle joint interfaces and the beam ends, as shown in **Fig. 6.1(a)**. The corresponding flexural capacity P_f in the absence of beam axial force is given by

$$P_f = 2\left(M_n + M_{n1}\right)/l_n \tag{6-24}$$

where M_n and M_{n1} are the nominal moments of resistance at the middle joint interfaces and the end-column-stub interfaces based on ACI 318-05 (American Concrete Institute 2005); and l_n is a net span length of a single-bay beam.

With consideration of CAA, the structural capacity P_a under a concentrated load is calculated as

$$P_a = 2\left(M_u + M_{u1} - N\delta\right)/l_n \tag{6-25}$$

where M_u and M_{u1} are the ultimate moments of resistance at the middle joint interfaces and the end-column-stub interfaces due to the presence of axial force N; and δ is the middle joint displacement.

Similarly, the flexural capacity P_f and the CAA capacity P_a corresponding to the plastic hinge mechanism of a sub-assemblage under a UDL magnitude of q are computed as

$$P_f = q\cdot\left(2l_n\right) = 4\left(M_n + M_{n1}\right)/l_n \tag{6-26}$$

$$P_a = q\cdot\left(2l_n\right) = 4\left(M_u + M_{u1} - N\delta\right)/l_n \tag{6-27}$$

A comparison between Eqs. (6-24) and (6-26) or Eqs. (6-25) and (6-27) indicates that the total load sustained by a sub-assemblage under a UDL is double that under a concentrated load. Nevertheless, the enhancement of structural resistance due to CAA, defined as $\left(P_a - P_f\right)/P_f$, are given by

$$\alpha = \frac{\left(M_u + M_{u1} - N\delta\right) - \left(M_n + M_{n1}\right)}{M_n + M_{n1}} \tag{6-28}$$

Eq. (6-28) indicates that enhancement of structural resistance is independent of loading types. Therefore, the findings from parametric studies are valid for structures under both loading types.

6.9.2 Enhancement factor of structural resistance due to CAA

The test results and the above analyses have shown that CAA is a ductile structural mechanism. As a result, the enhanced ultimate moments can be categorized as deformation-controlled actions. In UFC 4-023-03 (DoD 2010), localized plastic hinges are introduced into RC framed members to account for material nonlinearity, in which the deformation-controlled bending moment in beams represents nominal moment without considering the presence of axial force. Eq. (6-28) indicates that if nominal moments (i.e. M_n and M_{n1}) at critical sections are multiplied by a coefficient of $(1+\alpha)$, the corresponding ultimate flexural capacity is identical to CAA capacity. Accordingly, the moment-rotation relationship of a plastic hinge with consideration of CAA is shown in **Fig. 6.15**, in which M_y is the yield moment of a section, θ_y and θ_m are rotations corresponding to M_y and $(1+\alpha)M_n$, respectively, and *a*, *b*, *c* are nonlinear modeling parameters of the plastic hinge according to UFC 4-023-03.

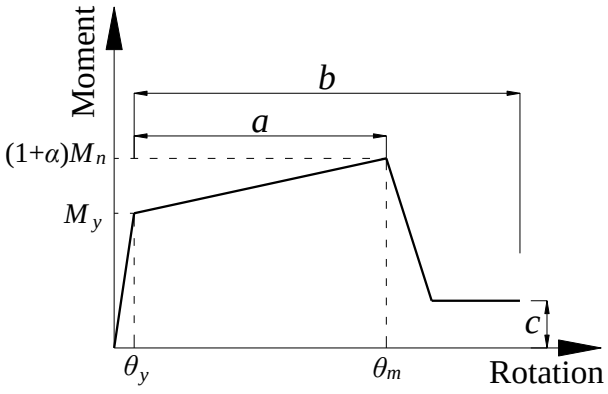

Fig. 6.15: Moment-rotation relationship of a plastic hinge with CAA

With adequate boundary restraints (i.e. $\gamma_a \geq 1.0$ and $\gamma_r \geq 1.0$) and shear strength, CAA can be incorporated into the design against progressive collapse, and the enhancement of structural resistance is a function of mechanical reinforcement ratio ω and beam span-to-depth ratio l_n/h. Based on nonlinear regression of structural resistance enhancement factor curves in **Fig. 6.14**, the enhancement factor function is given by

$$\alpha = 1.89e^{-0.058\left(\frac{l_n}{h}\right)}\left(3.50 - 30.21\omega + 102.64\omega^2 - 121.15\omega^3\right) \quad (6\text{-}29)$$

When l_n/h = 9.5, the predicted curve by Eq. (6-29) is shown in **Fig. 6.14**. It can be seen that Eq. (6-29) can reasonably determine an enhancement factor for a given ω and l_n/h. Therefore, during the design, the enhancement factor of an RC beam can be roughly estimated by Eq. (6-29), or more precisely determined by the proposed analytical model.

6.9.3 Deformation corresponding to CAA capacity

On the other hand, in UFC 4-023-03(DoD 2010), the nonlinear modeling parameters (such as *a*, *b* and *c* in **Fig. 6.15**) and acceptance criteria for RC beams are explicitly provided. If the rotation at a critical section corresponding to $(1+\alpha)M_n$ (i.e CAA capacity of RC beams) is within the acceptance criteria, then CAA can be used to effectively mitigate progressive collapse without excessive deformation. Since the deflection corresponding to CAA by the proposed model is always

relatively smaller than that found in the tests, the experimental results will be used to compare with acceptance criteria.

Table 6.3 shows the plastic rotations at the critical sections corresponding to CAA capacity (i.e. the ultimate moment of $(1+\alpha)M_n$) based on sub-assemblage tests (Sasani and Kropelnicki 2008; Su et al. 2009; Yu and Tan 2011b; 2012b). Total rotations θ_m corresponding to CAA capacity are computed by assuming all the plastic deformations are concentrated at two localized plastic hinges for each single-bay beam, as shown in **Fig. 6.1**. Due to small deflection, total rotation θ_m at the critical sections is given by $\theta_m = \delta_a/l_n$, in which δ_a is the middle joint displacement of a sub-assemblage at CAA capacity. In addition, rotation θ_y corresponding to the yield moment M_y at each critical section is also provided in **Table 6.3**. The way to determine θ_y is illustrated in Appendix II. Then the plastic rotation a_{ext} at each section in the experiments is determined as $(\theta_m - \theta_y)$. According to Table 4-1 in UFC 4-023-03(DoD 2010), for beams controlled by flexure, the nonlinear modeling parameters and acceptance criteria depend on reinforcement ratio indicator $(\rho-\rho')/\rho_{bal}$, provision of transverse reinforcement, and the ratio of applied shear force V to the shear strength provided by concrete only (i.e. $b_w d\sqrt{f_c'}$) at a section. The terms ρ and ρ' are tension and compression reinforcement ratios, respectively, and ρ_{bal} is the balanced steel ratio (MacGregor and Wight 2005). The terms b_w and d are the web width and the effective depth of beam section. In all the tests, the transverse reinforcement is categorized as nonconforming, and $V/b_w d\sqrt{f_c'} \le 3$. A component is conforming if, within the flexural plastic hinge region, hoops are spaced at $\le d/3$, and if, for components of moderate and high ductility demand, the strength provided by the hoops is at least three-fourths of the design shear. Otherwise, the component is considered nonconforming (DoD 2010). As a result, the acceptance criteria for plastic rotations of primary component, denoted as a_1 in **Table 6.3**, is solely determined by $(\rho-\rho')/\rho_{bal}$. In UFC 4-023-03, the value of a_1 is actually identical to the modeling parameter a, as indicated in Fig. 6.15. The ratio of a_{ext} to a_1 shows that except specimens A3 to A6 with an extremely short beam span-to-depth ratio of 4.1, all the other specimens can attain CAA capacity prior to reaching the specified deformation in acceptance criteria. This suggests that for

typical RC beams in practice with a beam span-to-depth ratio greater than 8, CAA can be safely and confidently incorporated into design in accordance with the modeling parameters and acceptance criteria in UFC 4-023-03 (DoD 2010).

Table 6.3: Structural deformation corresponding to CAA capacity

Spec-imen	Beam span to depth ratio l_n/h	Middle joint interface					End-column-stub interface				
		Yield rotation θ_y (rad)	Plastic rotations $a_{ext} = \theta_m - \theta_y$ (rad)	$\frac{\rho-\rho'}{\rho_{bal}}$	Accept. Criteria a_1	$\frac{a_{ext}}{a_1}$	Yield rotation θ_y (rad)	Plastic rotation $a_{ext} = \theta_m - \theta_y$ (rad)	$\frac{\rho-\rho'}{\rho_{bal}}$	Accept. Criteria a_1	$\frac{a_{ext}}{a_1}$
S1	11.0	0.0040	0.0243	-0.175	0.05	0.49	0.0061	0.0222	0.175	0.041	0.54
S2	11.0	0.0040	0.0225	-0.103	0.05	0.45	0.0052	0.0214	0.103	0.045	0.48
S3	11.0	0.0036	0.0234	-0.266	0.05	0.47	0.0076	0.0195	0.266	0.037	0.53
S4	11.0	0.0060	0.0234	-0.146	0.05	0.47	0.0077	0.0217	0.146	0.043	0.51
S5	11.0	0.0079	0.0192	0.000	0.05	0.38	0.0079	0.0192	0.000	0.050	0.38
S6	11.0	0.0060	0.0356	-0.370	0.05	0.71	0.0106	0.0310	0.370	0.032	0.98
S7	8.6	0.0047	0.0299	-0.146	0.05	0.60	0.0060	0.0286	0.146	0.043	0.67
A1	4.1	0.0016	0.0376	0.000	0.05	0.75	0.0016	0.0376	0.000	0.050	0.75
A2	4.1	0.0023	0.0438	0.000	0.05	0.88	0.0023	0.0438	0.000	0.050	0.88
A3	4.1	0.0029	0.0594	0.000	0.05	1.19	0.0029	0.0594	0.000	0.050	1.19
A4	4.1	0.0012	0.0519	-0.061	0.05	1.04	0.0017	0.0514	0.061	0.047	1.09
A5	4.1	0.0016	0.0561	-0.083	0.05	1.12	0.0023	0.0554	0.083	0.046	1.21
A6	4.1	0.0021	0.0544	-0.105	0.05	1.09	0.0030	0.0534	0.105	0.045	1.19
B1	6.6	0.0054	0.0452	0.000	0.05	0.90	0.0054	0.0452	0.000	0.050	0.90
B2	9.1	0.0074	0.0301	0.000	0.05	0.60	0.0074	0.0301	0.000	0.050	0.60
B3	9.1	0.0053	0.0261	-0.142	0.05	0.52	0.0069	0.0245	0.142	0.043	0.57
C1	6.1	0.0050	0.0226	0.000	0.05	0.45	0.0050	0.0226	0.000	0.050	0.45
SS	10.5	0.0033	0.0175	-0.273	0.05	0.35	0.0080	0.0128	0.273	0.036	0.35

6.9.4 Estimation of restraint stiffness

The boundary restraint stiffnesses of a two-bay beam should be determined first either to run the analytical model proposed in the companion paper or to check whether the restraint stiffnesses are adequate (i.e. $\gamma_a \geq 1.0$ and $\gamma_r \geq 1.0$) so that the enhancement factor α by Eq. (6-29) can be directly used. Assuming that the initial damage is confined to the frame which has lost a column, both the stiffnesses of axial and rotational restraints can be obtained via linear elastic analysis on the remaining structure. Both the columns adjacent to the removed column and the in-plane floors can resist axial compression in beams, in which the latter can sustain much more axial compression (Sasani et al. 2011). This is because the in-plane floors can help to transfer beam axial compression to more columns. Therefore, it is

important to properly model the axial stiffness of floor elements to ascertain the restraint stiffnesses.

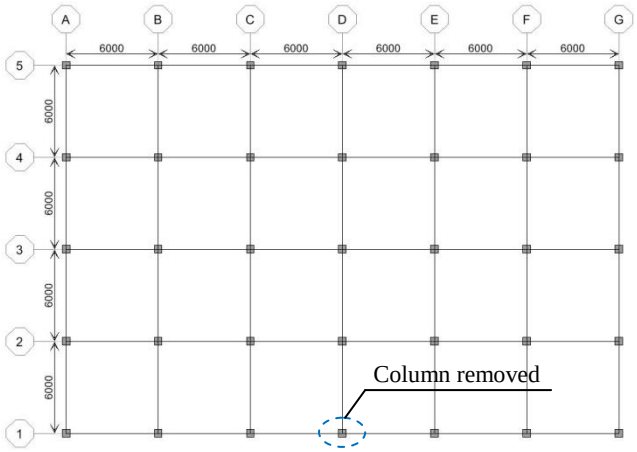

(a) Plan view of the building

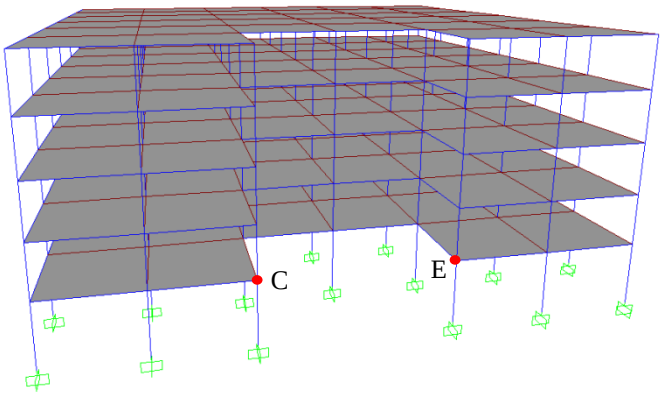

(b) 3D view of the building

Fig. 6.16: Approach to determine restraint stiffness of RC beams

Fig. 6.16 demonstrates that a 5-story commercial building, of which the ground story is 4.0 m high and a typical story is 3.3 m high, is subjected to a middle column removal in the ground story. Two points, denoted as C and E in **Fig. 6.16(b)**, will be applied a unit horizontal force and a unit moment to ascertain the axial and rotational restraint stiffnesses to the two-bay beam CE, respectively. The spans at two orthogonal directions are 6 m, as shown in **Fig. 6.16(a)**. The beam sections are 300 mm wide by 500 mm deep. The column section in the ground story is 600 mm × 600 mm, and that in the other stories is 500 mm × 500 mm. The slab thickness is 200 mm. The compressive strength and the elastic modulus of concrete are 30 MPa and 25,743 MPa, respectively. As a result, the axial and the rotational stiffnesses of

the uncracked two-bay beam are EA/l = 3.35×10^5 kN/m) and $4EI/l$ = 2.80×10^4 kNm/rad, respectively. **Table 6.4** shows the restraint stiffness at both ends of the two-bay beam CE with and without modeling slabs. A similar analysis can also be conducted on the two-bay beam BD. It can be found that incorporating the slab significantly increases the axial restraint stiffness, but not much effect on rotational stiffness. Moreover, compared with the uncracked concrete two-bay beam (i.e. CE and BD) stiffnesses, the analysis incorporating the slab modeling indicates that the axial restraints are adequate to develop CAA. However, when the penultimate column B1 is removed, the slab modeling slightly improves the axial restraint stiffness at the left end of beam AC from 0.217×10^5 kN/m to 0.227×10^5 kN/m. Moreover, the equivalent axial restraint stiffness at the left end of the two-bay beam AC (i.e. 0.432×10^5 kN/m), which is solely provided by column A1, is much weaker than that of two-bay beam AC (i.e. 3.35×10^5 kN/m). As a result, CAA cannot be mobilized and beam AC must rely on its pure flexural resistance to redistribute gravity loads.

Table 6.4: Effect of slabs on restraint stiffnesses to two-bay beams

Modeling schemes	Restraint position	Two-bay beam CE due to removal of column of D1		Two-bay beam BD due to removal of column C1		Two-bay beam AC due to removal of column B1	
		Axial restraint stiffness (10^5 kN/m)	Rotational restraint stiffness (10^5 kNm/rad)	Axial restraint stiffness (10^5 kN/m)	Rotational restraint stiffness (10^5 kNm/rad)	Axial restraint stiffness (10^5 kN/m)	Rotational restraint stiffness (10^5 kNm/rad)
Without modeling slabs	Left end of the two-bay beam k_1	0.875	3.385	0.589	2.966	0.217	1.291
	Right end of the two-bay beam k_2	0.875	3.385	1.107	3.617	1.284	3.754
	Equivalent stiffness	0.875	3.385	0.769	2.966	0.371	1.291
With modeling slabs	Left end of the two-bay beam k_1	4.013	4.581	3.008	4.529	0.227	1.359
	Right end of the two-bay beam k_2	4.013	4.581	4.380	4.686	4.464	4.405
	Equivalent stiffness*	4.013	4.581	3.567	4.529	0.432	1.359

* Equivalent axial stiffness $K_a = 2k_1k_2/(k_1+k_2)$, and equivalent rotational stiffness $K_r = \min(k_1, k_2)$.

6.9.5 Summary and discussions

Both flexural and CAA resistance against progressive collapse requires the continuity of bottom reinforcement at the joint above a removed column; otherwise, no large bending moment can be developed at joint interfaces and no compression zone there as well. Accordingly, neither flexural mechanism nor CAA can be mobilized whichever boundary conditions are provided. The continuity of reinforcement can be achieved by using continuous bars, mechanical spliced bars and lap-spliced bars with adequate splice length, etc. In fact, the indirect approach in design codes and guidelines has already required the continuity of bars (or ties).

Under the continuity of reinforcement, progressive collapse resistance is checked after a building has been designed under combinations of conventional loads. With nonlinear modeling parameters in UFC 4-023-03, it is convenient to conduct nonlinear static analysis under different column loss scenarios. When the pure flexural resistance cannot resist progressive collapse, CAA can be employed by increasing nominal moment capacity at critical beam sections with enhancement factors α if strong boundary conditions (i.e. $\gamma_a \geq 1.0$ and $\gamma_r \geq 1.0$) are provided and shear is not governing behavior.

The proposed procedure to incorporate CAA into structural analysis against progressive collapse does not explicitly consider beam axial force. The effect of axial compression on the beams above the removed column is represented by enhanced moment resistance at joint interfaces, and the capability of transferring axial compression to the surrounding structures without causing failure of adjoining columns can be ensured by the prerequisite strong boundary conditions (i.e. $\gamma_a \geq 1.0$ and $\gamma_r \geq 1.0$). Compared with the proposed procedure, more advanced modeling techniques can be utilized to incorporate CAA into structural analysis, such as by introducing fiber plastic hinges at critical sections (Sasani et al. 2011) and by using fiber-based beam element for an entire two-bay beam (Yu and Tan 2011b). However, both fiber-based hinges and beam elements require detailed characterizations of material properties of concrete and reinforcement identical to those in new buildings, which are not available at design stage. Also, the estimation of plastic hinge length by using fiber-based hinges may introduce additional

inaccuracy in predicting structural deformation. Moreover, the analysis with alternate load path approach is interested in checking whether CAA capacity can be achieved within specified deformation limits (such as acceptance criteria in UFC 4-023-03) rather than the accurate deformation corresponding to maximum structural capacity. Due to the availability of design strength of concrete and reinforcement and the relatively smaller deformation corresponding to CAA capacity compared to acceptance criteria in UFC 4-023-03, as shown in **Table 6.3**, the proposed procedure is suggested for checking progressive collapse resistance in design.

6.10 Conclusions

An analytical model is proposed in this paper to evaluate compressive arch action (CAA) of RC beam-column sub-assemblages under a middle column removal scenario, considering the combined effects of stress state of compression reinforcement and imperfect boundary conditions on CAA. The imperfect boundary conditions include partial axial and rotational restraints, and axial connection gaps at beam ends. The comparisons of experimental and analytical results indicate that this model is able to predict both the CAA capacity and the maximum beam axial compression of RC sub-assemblages with satisfactory accuracy and reliability. A comparison of the proposed model to Park's model suggests that it is necessary to consider the actual stress value of compression reinforcement rather than assuming it as yield strength or zero.

CAA capacity and beam axial compression are much more sensitive to axial connection gaps than to the other imperfect boundary conditions. Due to inevitable connection gaps in actual tests, it is very likely to underestimate the enhancement of structural resistance contributed by CAA. However, in actual RC buildings, connection gaps do not exist due to monolithic casting of continuous beams, so its detrimental effect on CAA may be ignored.

Adequate axial and rotational restraint stiffness must be provided to develop CAA. Provided that the respective axial and the rotational restraint stiffness is greater than the corresponding stiffness of restrained uncracked beams, the variation of each restraint stiffness does not significantly affect the CAA capacity and the maximum

axial compression of beams. However, when reducing the stiffness of weak restraints ($\gamma_a < 1$ or $\gamma_r < 1$), both the CAA capacity and the maximum beam axial compression will decrease substantially. Therefore, from conservatism, it is suggested that only when both relative axial and rotational stiffness are greater than one (i.e. $\gamma_a \geq 1$ and $\gamma_r \geq 1$), CAA can be considered as a beneficial alternate load path to mitigate progressive collapse.

Span-to-depth ratio and mechanical reinforcement ratio of beams are two key parameters affecting the CAA capacity under given boundary conditions. The enhancement of structural resistance due to CAA is highly dependent on different combinations of these two parameters. For beams under adequate axial and rotational restraints, lower mechanical reinforcement ratio and lower span-to-depth ratio will give rise to significant enhancement of structural resistance contributed by CAA.

With nonlinear modeling parameters and acceptance criteria in UFC 4-023-03, CAA can be incorporated into design against progressive collapse via multiplying nominal ultimate moments of resistance at critical sections by an enhancement factor. To check whether restraint stiffness provided by remaining structure is adequate, slab modeling should be included.

Appendix I: Procedure to derive the compatibility equation

Substituting Eq. (6-3) into Eq. (6-2b), the following equation can be obtained.

$$\left[\beta l + 0.5\varepsilon(1-2\beta)l + (t+t_0)\right]\sec(\varphi+\theta) = \left(\frac{h}{2}-c\right)\tan(\varphi+\theta) + \left(\frac{h}{2}-c_1\right)\tan\varphi + (1-\varepsilon)\beta l$$

(a-1)

Multiplying $\cos(\varphi+\theta)$ to both sides of Eq. (a-1) and rearranging it leads to:

$$0.5\varepsilon l + (t+t_0) = \left(\frac{h}{2}-c\right)\sin(\varphi+\theta) + \left(\frac{h}{2}-c_1\right)\tan\varphi\cos(\varphi+\theta) + (1-\varepsilon)\beta l\left[\cos(\varphi+\theta)-1\right]$$

(a-2)

Due to $\cos(\varphi+\theta)-1 = -2\sin^2\left(\frac{\varphi+\theta}{2}\right)$, Eq. (a-2) can be further simplified as

$$0.5\varepsilon l + (t+t_0) = \left(\frac{h}{2}-c\right)\sin(\varphi+\theta) + \left(\frac{h}{2}-c_1\right)\tan\varphi\cos(\varphi+\theta) - 2(1-\varepsilon)\beta l\sin^2\left(\frac{\varphi+\theta}{2}\right)$$

(a-3)

Dividing $\sin(\varphi+\theta)$ at both sides of Eq. (a-3) and moving variable c to the left hand side yields

$$c = \frac{h}{2} - \frac{0.5\varepsilon l + (t+t_0)}{\sin(\varphi+\theta)} + \left(\frac{h}{2}-c_1\right)\frac{\tan\varphi}{\tan(\varphi+\theta)} - \frac{2(1-\varepsilon)\beta l\sin^2\left[(\varphi+\theta)/2\right]}{\sin(\varphi+\theta)}$$

(a-4)

Eq. (a-4) is the same as Eq. (6-4)

Substituting the equivalent values of the trigonometric functions, including $\sin(\varphi+\theta) = \tan(\varphi+\theta) = \varphi+\theta = \frac{\delta}{\beta l}$, $\sin\left(\frac{\varphi+\theta}{2}\right) = \frac{\delta}{2\beta l}$, and $\tan\varphi = \varphi = \frac{\delta}{\beta l} - \frac{M_{u1}}{K_r}$, into Eq. (a-4) gives the following equation.

$$c = \frac{h}{2} - \frac{(0.5\varepsilon l + t)}{\delta}\beta l - \frac{\beta l t_0}{\delta} + \left(\frac{h}{2}-c_1\right)\left(1 - \frac{M_{u1}\beta l}{K_r\delta}\right) - (1-\varepsilon)\frac{\delta}{2} \qquad \text{(a-5)}$$

Substituting Eqs. (6-6) and (6-7) into Eq. (a-5), and

$$c = \frac{h}{2} - (1-\varepsilon)\frac{\delta}{2} - \frac{\beta l^2}{2\delta}\left(\frac{1}{bhE_c} + \frac{2}{lK_a}\right)N - \frac{\beta l t_0}{\delta} + \left(\frac{h}{2} - c_1\right)\left(1 - \frac{M_{u1}\beta l}{K_r \delta}\right) \quad \text{(a-6)}$$

Compared with unity, the compressive strain ε of beams can be neglected. Therefore, Eq. (a-6) can be simplified as

$$c = \frac{h}{2} - \frac{\delta}{2} - \frac{\beta l^2}{2\delta}\left(\frac{1}{bhE_c} + \frac{2}{lK_a}\right)N - \frac{\beta l t_0}{\delta} + \left(\frac{h}{2} - c_1\right)\left(1 - \frac{M_{u1}\beta l}{K_r \delta}\right) \quad \text{(a-7)}$$

Eq. (a-7) is the Eq. (6-8) shown in section 6.3.2.

Appendix II: Approach to determine rotation corresponding to yield moment

Rotation θ_y corresponding to the yield moment M_y at critical sections are determined with the effective stiffness values provided in Table 6-5 in ASCE/SEI 41-6 (ASCE 2007). For RC beams, the effective stiffness is $0.5E_cI_g$, where E_c is the elastic modulus of concrete and I_g the gross cross-sectional moment of inertia. When the middle joint interface reaches yield moment, based on the moment diagram of a two-ends-fixed beam subjected a point load acting at the beam center, the counter-flexural point is roughly at the middle point of the "single-bay" beams. That is, from the counter-flexural point to the middle joint interface (the distance denoted as l_{cf}), the curvature linearly increases from zero to φ_y .As a result, the yield rotation θ_y is given by

$$\theta_y = \varphi_y l_{cf} / 2 = \left(M_y / 0.5E_cI_g\right) l_{cf} / 2 \tag{II-1}$$

where the yield moment M_y is the determined as follows (Park and Paulay 1975):

$$M_y = 0.5 f_c bkd\left(d - \frac{kd}{3}\right) + f_s' A_s' \left(d - d'\right) \tag{II-2}$$

where f_c is the stress of the ultimate compressive concrete fiber; b and d are the width and the effective depth of a beam section, respectively; f_s' and A_s' are the stress and the area of compression steel, respectively; d' is the distance from the ultimate compressive fiber of concrete to the centroid of compression steel; and k is the ratio of neutral axis depth to the effective depth, which is given by

$$k = \left[\left(\rho + \rho'\right)^2 n^2 + 2\left(\rho + \rho' \frac{d'}{d}\right) n\right]^{1/2} - \left(\rho + \rho'\right) n \tag{II-3}$$

where ρ and ρ' are tension and compression reinforcement ratio, respectively; and n is ratio of the elastic modulus of steel reinforcement to concrete.

CHAPTER 7 NUMEIRCAL ANALYSIS WITH COMPONENT-BASED JOINT MODELING AND BAR FRACTURE

7. 1 Introduction

In the tests on RC beam-column sub-assemblages under a middle column removal scenario (Yu and Tan 2011b; 2012b), although no joint panel distortion was observed, severe failure occurred at the middle joint interfaces and the interfaces between the beam ends and the column stubs with occurrences of wide cracking, large slip and bar fracture, as shown in **Fig. 7.1(a)**. For sub-assemblages with lap-spliced bottom bars in the middle joint region, local failure shifted from the middle joint interfaces to the free ends of lap-spliced bars, as shown in **Fig. 7.1(b)**. These failures caused discontinuous zones in the sub-assemblages, allowing the beams to rotate easily so that catenary action of beams could be mobilized, and thereby increasing structural capacity. Therefore, it is necessary to separate the joints from the rest of structural members and to model them as independent elements. Moreover, the joint elements should incorporate the bond-slip behavior at the joint interfaces until bar fracture or pullout occurs.

Running parallel to the joint research, several research works (Bao et al. 2008; Khandelwal et al. 2008; Lee et al. 2010; Yu and Tan 2010a) indicate that macromodel-based finite element method (macro-FEM) is an effective and efficient approach to analyze structural behavior under a middle column removal scenario (MCRS), which involves both material and geometric nonlinearity. In the macromodel-based finite element analysis (macro-FEA), beams and columns are modeled with nonlinear fiber elements, and each fiber is assigned uniaxial material properties. Furthermore, joint behavior can be explicitly incorporated into structural analysis using component-based joint models.

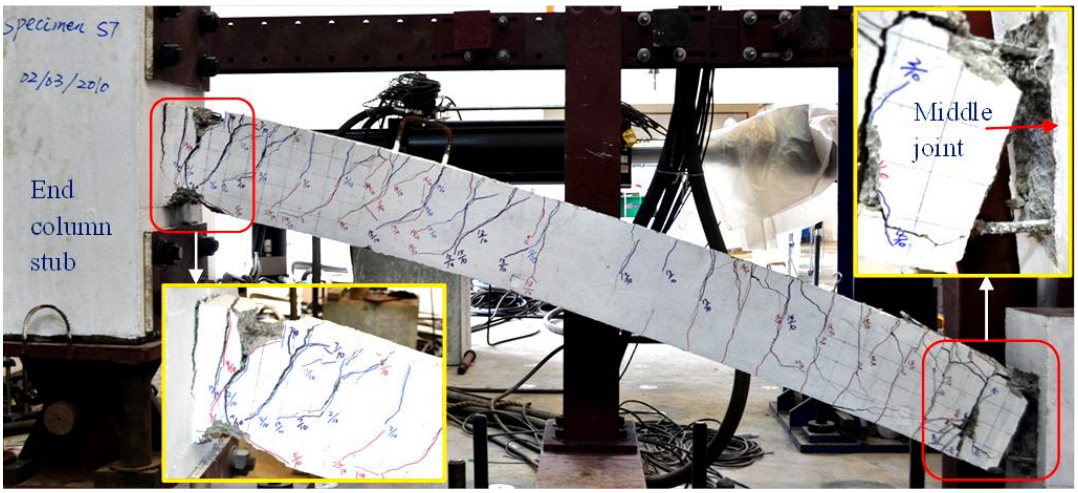

(a) Specimen with continuous bottom bars at the middle joint

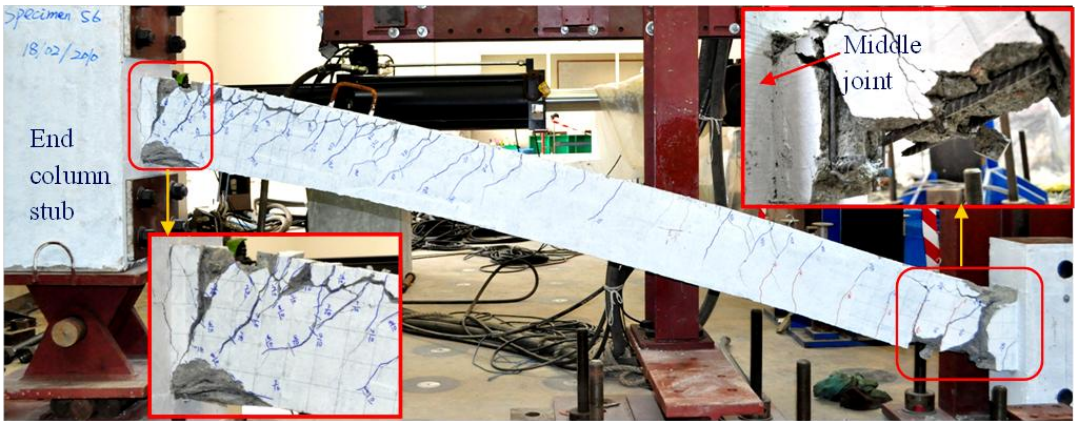

(b) Specimen with lap-spliced bottom bars at the middle joint

Fig. 7.1: Failure modes of RC beam-column sub-assemblages

In this chapter, a component-based joint model is proposed, and the approaches to calibrate the properties of each component (or spring) of the joint model, in particular, bar force-slip springs, are presented. To calibrate the bar force-slip springs with consideration of bar fracture or pullout, a new bar stress-slip model is developed based on the assumption that uniform bond stress is respectively distributed over the elastic and the inelastic development length of a reinforcing bar. A simplified approach is proposed to calibrate compressive springs. Finally, the proposed joint model is incorporated into macro-FEA by using commercial software Engineer's Studio (Forum8 2008) to simulate large-deformation responses of RC beam-column sub-assemblages under a MCRS. The validity of macro-FEA is evaluated by comparing the predicted load-deformation history and variations of

beam axial forces with experimental results. With the proposed joint model, bar fracture mode can be captured in the load-deformation history of RC sub-assemblages, indicating that the simulations are more realistic.

7.2 Development of component-based joint model

Similar to the component method used in steel structure connections (Jaspart 2000), the principle of a component-based joint model is to decompose complex mechanisms of a joint into a series of simple components, each of which represents a unique load transfer path and can be characterized by an equivalent uniaxial nonlinear spring. To consider the contribution of joint panel distortion and bar slip effect at joint interfaces to RC structure deformations, the idea of modeling RC joints as an assembly of springs has been employed on seismic research on joints (Lowes and Altoontash 2003; Mitra 2007; Youssef and Ghobarah 2001) and just recently, on progressive collapse (Bao et al. 2008; Yu and Tan 2010a).

Unlike the diversity of steel connection arrangement, configurations of RC joints are quite regular, and hence, there are only limited load transfer paths from adjoining members to joints. Therefore, the component-based joint models proposed by Youssef and Ghobarah (2001) as well as Lowes and Altoontash (2003) are generic to cast in-situ RC joints. Based on above two models, a component-based joint is proposed to simulate RC joints and structural behavior under a MCRS, as shown in **Fig. 7.2**. Since main variations of load transfer paths and failure occur at the beam-joint interfaces, the corresponding interface springs are represented explicitly, while the connections at the column-joint interfaces are assumed rigid. Three types of springs are used in this proposed model:

(1) Joint panel spring (k_s): The joint panel is characterized by four pins and four rigid members enclosing the joint, as shown in **Fig. 7.2**. Two diagonal springs represent the ability to resist shear distortion in the joint panel. Although shear distortion is not appreciable for interior joints under a MCRS (Yu and Tan 2012b), it can be dominant for exterior joints.

(2) Joint interface spring (k_{bs}): This shear spring k_{bs} represents the shear transferred from the adjoining beams to the joint panel across the cracked joint interfaces.

When interface shear slip and crack width are small, interface shear is mainly resisted by shear strength of flexural compression zones and interlock of aggregates. However, at catenary action stage, interface shear is mainly sustained by dowel action of flexural reinforcement due to a large crack width. However, conventional frame members have adequate shear capacity to preclude shear failure. Moreover, interface shear transfer is not the main mechanism for members under a MCRS. Therefore, k_{bs} is taken as an elastic linear spring with a large stiffness as suggested by Lowes and Altoontash (2003).

(3) Bar force-slip spring (k_{bb} and k_{bt}): The pair of k_{bb} and k_{bt} is able to represent bending moment combined with beam axial compression or tension transferred from adjoining beams into the joint panel. Each spring should include the contribution from both concrete and reinforcement. However, typically, tensile contribution from concrete can be ignored. In the tests conducted by Yu and Tan (2011b; 2012b), it is found that flexural and axial action were most dominant, and the tests were eventually stopped due to complete failure of bar force-slip springs at some joint interfaces, such as bar fracture. Therefore, tensile bar force-slip relationship is the most critical to joints subjected to a MCRS.

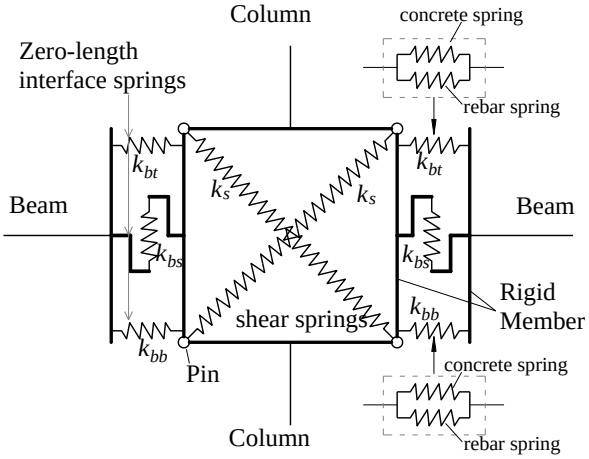

Fig. 7.2: Proposed component-based joint model

The major difference of joint configuration between the proposed model and the models proposed by Youssef and Ghobarah (2001) as well as Mitra and Lowes (2007) is the location of spring k_{bt} and k_{bb}. For RC sub-assemblages under a MCRS, with increasing sub-assemblage deflection, k_{bt} at the middle joint will transit from a

compressive spring to a tensile spring. In the load-deflection history of an RC sub-assemblage, k_{bb} at the middle joint always works as a tensile spring. Therefore, in the proposed joint model, k_{bt} and k_{bb} are specified at the centroid of steel reinforcement at the joint interfaces. However, Yourssef and Ghobarah's model as well as Mitra and Lowes's model determined the distance between k_{bt} and k_{bb} based on that the ultimate moment of the transformed section (consisting of the steel and concrete springs) is the same as that of the actual section without considering beam axial force. Accordingly, at the positive bending moment region, k_{bb} is located at the centroid of tension reinforcement and k_{bt} at the centroid of compression zone, which may not coincide with the centroid of compression reinforcement. In addition, similar to Yourssef and Ghobarah's model, a pair of diagonal springs is used in the proposed model to represent shear panel behavior, rather than a single panel element used in Mitra and Lowes's model.

For RC beam-column sub-assemblages under a MCRS, unlike in a seismic event, the unloading and reloading of springs are not crucial. However, detailed information about unloading and reloading of these springs can be found in the report written by Lowes et al. (2003) and the help document of Engineer's studio (Forum8 2008). Therefore, in this chapter, it is only concerned with the calibration of the envelopes of spring force-deformation relationships. Moreover, the curved envelopes will be converted into simplified multi-linear models so that the stiffness of each spring can be determined, which can then be used as input data for macro-FEA.

7.2.1 Shear panel spring

The monotonic relationship between shear stress τ_p in a joint panel and shear distortion γ can be obtained via modified compression field theory (Vecchio and Collins 1986). Then the relationship τ_p–γ can be converted into the force-deformation relationship of two diagonal springs. The force in each diagonal spring F_s can be calculated through force equilibrium at a pin, as shown in **Fig. 7.3(a)**.

$$F_s = \sqrt{\left(\tau_p b_j d_j / 2\right)^2 + \left(\tau_p h_b d_j / 2\right)^2} = \tau_p d_j l_j / 2 \tag{7-1}$$

where b_j and d_j are the joint width and the out-of-plane depth, respectively; h_b is the beam height, and l_j is the diagonal length of the joint panel.

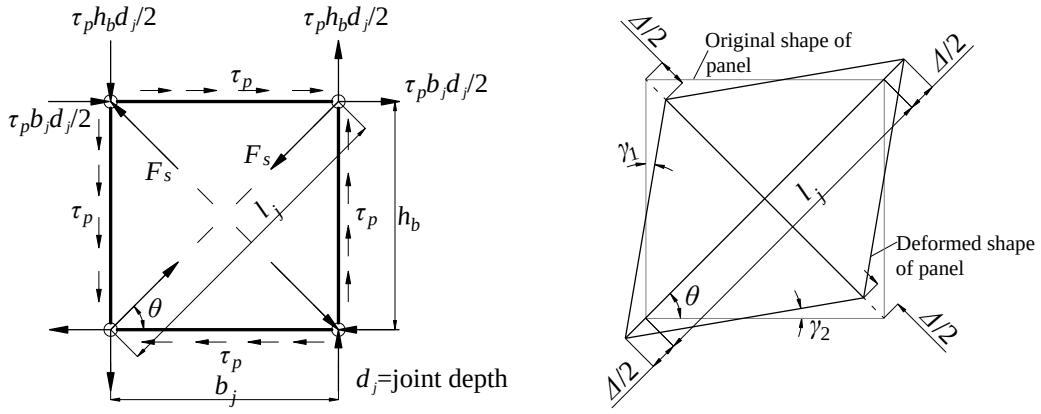

(a) Force equilibrium (b) Shear distortion

Fig. 7.3: Shear panel spring

Since the stiffnesses of the two springs are assumed equal, the elongation of one spring is equal to the contraction of the other spring. According to geometric relationship shown in **Fig. 7.3(b)**, shear distortion is given by Youssef and Ghobarah (2001) as:

$$\gamma = \gamma_1 + \gamma_2 = \frac{2\Delta}{l_j \sin(2\theta)} \tag{7-2}$$

where θ is the angle of the diagonal line of the joint with respect to horizontal direction. The derivation of Eq. (7-2) is also shown in Appendix I.

7.2.2 Tensile Bar force-slip spring

To obtain the relationship of tensile bar force vs. slip at the joint interfaces, bond-slip behavior within joints should be incorporated, in particular, the effects of *finite embedment length* and *high post-yield stress levels* of bars must be considered. Therefore, the bar force-slip relationship at the joint interfaces is different from that based on adequate embedment length.

7.2.2.1 Background of bar force-slip modeling

In essence, the development of bond stress is a three-dimensional phenomenon, and corresponding bond failure, defined as reinforcing bars failing to transfer force prior to bar fracture, is affected by many parameters. Bond failure includes splitting and pullout failure (CEB-FIP 2000). If confinement from surrounding concrete on reinforcement is inadequate, concrete splitting failure may occur, possibly for cases with lap splicing within beams or columns; if embedment length of reinforcement is insufficient, steel pullout failure can occur, probably for cases with column bars anchored into foundations or beam bars extending into exterior joints. If bond failure is avoided, material strength of bars can be fully utilized and reinforcing bars will fail by fracture. During testing (Yu and Tan 2011b; 2012b), whether bars were lap-spliced at the middle joints or anchored into the end column stubs, no splitting failure was observed, indicating that there was adequate confinement to the bars going through the middle joints or anchored into the end column stubs. Therefore, bond response in this chapter will be concentrated on the bond-slip behavior under adequate confinement without considering splitting failure of concrete.

Under good confinement, bond-slip relationship of reinforcing bars in the longitudinal direction is the only concern. To investigate local bond-slip behavior, many systematic pullout tests of reinforcing bars with short embedment lengths had been conducted (Eligehausen et al. 1983; Hawkins et al. 1982). In these tests, large slips of bars occurred when they were subjected to small strains. However, the pullout tests with long embedment lengths (Shima et al. 1987; Viawanthanatepa et al. 1979) indicate that post-yield strains could be developed in the anchored bars. Moreover, yielding of bars can reduce bond strength significantly. Therefore, the local bond-slip models that are based on the pullout tests of reinforcing bars with short embedment lengths, such as the models proposed by Hawkins et al. (1982) and Eligehausen et al. (1983), cannot be directly applied to the bars that experience high inelastic strains. On the other hand, Shima's bond-slip model considers the effect of bar strain on local bond-slip relationship. However, since Shima's model is based on the pullout tests of initial undamaged concrete cylinders, it does not

consider bond deterioration at the loaded ends of bars. The bond strength from Shima's model can be regarded as the upper limit.

Since anchorage slip is one of the major components of inelastic deformations of RC members, various bar stress-slip models have been proposed to evaluate slip of reinforcing bars at the loaded ends. Multiplied with bar cross-sectional area, bar stress-slip relationships can be converted to bar force-slip relationships, so the two types of relationships are essentially the same. Generally, bar stress-slip models fall into two broad categories, namely, macro and micro-models (Sezen and Setzler 2008). Macro-models deal with the average bond-slip behavior and often assume a uniform or stepped bond stress over the development length of reinforcing bars. These include the models proposed by Alsiwat and Saatcioglu (1992), Lowes and Altoonash (2003), Sezen and Setzler (2008), and they are computationally-efficient. On the other hand, micro-models incorporate *local* bond-slip models to consider overall bond-slip behavior of a bar with long embedment length (Ciampi et al. 1982; Filippou 1985; Ueda et al. 1986). Over a given embedment length of a reinforcing bar, the local bond stress and bar slip differs from point to point. Thus, to obtain stress-slip relationship at one point of a bar, micro-models require several nested iteration loops over the embedment length of bars to satisfy force equilibrium, local bond-slip relationship, constitutive model of steel and compatibility conditions between steel and concrete, which are computationally demanding.

An alternative way to model bar force-slip relationships at loaded ends is to directly use experimental results of bar force-slip response under similar bond conditions, such as the model proposed by Zhao and Sritharan (2007) for bars with adequate embedment length. However, available test data are very limited.

7.2.2.2 Development of proposed macro bar stress-slip model

To obtain the envelops of bar force-slip relationship at the joint interfaces rather than to explore detailed information on bond stress within the joint regions of sub-assemblages, a simplified macro-bar-stress-slip model is proposed with the assumptions that (1) the distribution of bond stress within an elastic part or an inelastic part of a reinforcing bar remains uniform; (2) the slip of a reinforcing bar

at the joint interfaces is computed directly from the bar extension over the embedment length within the joints and the slip at the free end; (3) the constitutive model of reinforcement is bilinear. Moreover, the proposed model considers the effects of short embedment length and high post-yield stress on bar stress-slip relationships.

Reinforcing bars are typically continuous or lap-spliced in interior RC joints, and anchored with a hook in exterior RC joints. Under monotonic loading, a continuous bar is subjected to axial tension and slip at the bar center is always zero, while a lap-spliced or anchored bar is subjected to a pulling force at the loaded end and stress at the free end is always zero. The differences in boundary conditions of continuous and anchored (or lap-spliced) bars result in different strain distributions over embedment length, development of slips and failure modes. Therefore, the approach to determine slips of continuous bars at joint interfaces is introduced first, followed by the approach for anchored or lap-spliced bars.

7.2.2.3 Slips of continuous bars at joint interfaces under axial tension

Continuous bars at the middle joints of RC sub-assemblages are under axial tension subjected to a MCRS. Based on assumption (1), the distribution of bond stress τ and bar stress f of a continuous bar under axial tension with applied stress f_s at the joint interfaces is illustrated in **Fig. 7.4**. Due to geometric and loading symmetry, one-half of the joint width is regarded as the physical embedment length l_{embd} of the bar. Because of constant inelastic bond strength τ_{YT}, the bar stress linearly decreases from f_s to the yield strength f_y over the inelastic length l_{yrq}. Similarly, due to constant elastic bond strength τ_{ET}, the bar stress f is linearly distributed over the elastic length l_e. Even if the bar is stressed up to the center, as shown in **Fig. 7.4**, the associated slip is equal to zero due to symmetry. In other words, the boundary conditions of the continuous bar are a *zero-slip* and a *non-zero stress* at the center. As a result, the bar can only fail by fracture, and the slip at each joint interface is solely determined by bar extension s_{ext} according to assumption (2).

$$slip = s_{ext} = \int_0^l \varepsilon(x)dx \tag{7-3}$$

where $\varepsilon(x)$ is the strain at position x; the position x=0 is defined at a point with a zero-slip; and l is the smaller of the embedment length l_{embd} and the stressed length of the bar.

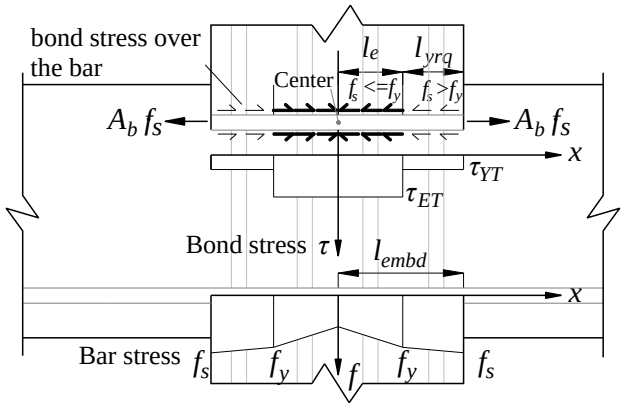

Fig. 7.4: Bond and bar stress distribution for a continuous bar under axial tension

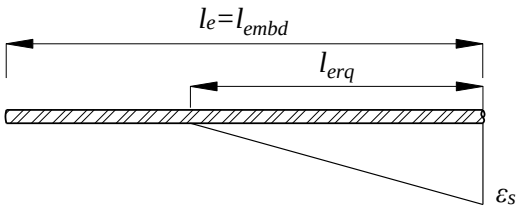

(a) Category 1: $f_s \le f_y$ and $l_{erq} \le l_{embd}$

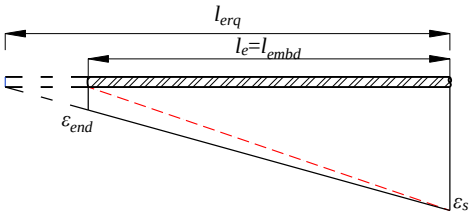

(b)Category 2: $f_s \le f_y$ and $l_{erq} > l_{embd}$

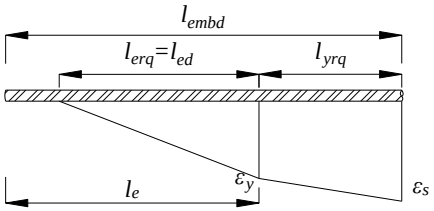

(c) Category 3: $f_s > f_y$ and $l_{ed}+l_{yrq} \le l_{embd}$

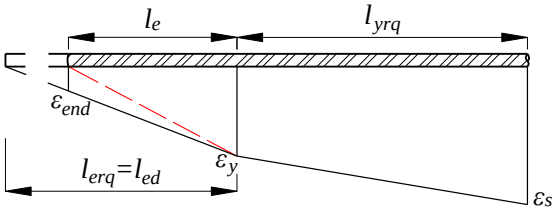

(d) Category 4: $f_s > f_y$ and $l_{ed}+l_{yrq} > l_{embd}$ but $l_{yrq} \le l_{embd}$

l_{embd} = bar embedement length;
l_{erq} = required elastic length, for reducing maximum elastic stress to zero;
l_{ed} = elastic development length, for reducing yield strength to zero ($l_{ed} \ge l_{erq}$);
l_{yrq}=required inelastic length, for reducing maximum inelastic stress to yield strength;
l_e = available elastic length, equal to $l_{embd} - l_{yrq}$.

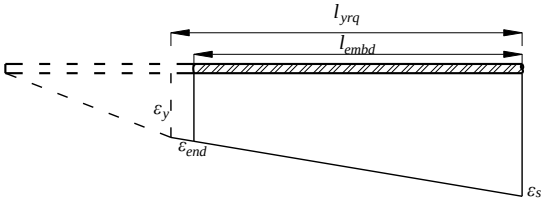

(e) Category 5: $f_s > f_y$ and $l_{yrq} > l_{embd}$

Fig. 7.5: Categories of strain profiles under axial tension

Eq. (7-3) indicates that the extension of a continuous bar is just the area of the strain diagram over length *l*. According to assumption (3), the bar strain is linearly distributed at the elastic and the inelastic parts of the bar as well. Depending on the *stress state* and the *embedment length*, the strain profiles over the embedment length l_{embd} can be divided into five categories, as shown in **Fig. 7.5**. Due to symmetry, only one-half the continuous bar is shown.

1) Category 1 ($f_s \le f_y$ and $l_{erq} \le l_{embd}$)

As shown in **Fig. 7.5(a)**, when a bar is subjected to an elastic stress f_s at the joint interface (or the loaded end), the *available elastic length* l_e, in which the elastic bond strength is allowed to develop, is equal to the physical embedment length l_{embd}. Based on assumption (1), a uniform elastic bond strength τ_{ET} is mobilized over the *required elastic length* l_{erq}, in which the bar stress can increase from zero to the maximum elastic stress f_s. As a result, the strain is linearly distributed from zero to ε_s over l_{erq}. Force equilibrium along the length l_{erq} produces

$$f_s A_b = \tau_{ET} \pi d_b l_{erq} \tag{7-4}$$

where A_b is the nominal area of the bar, and d_b is the bar diameter. By substituting the bar cross-sectional area in terms of the bar diameter, the required elastic length l_{erq} can be determined.

$$l_{erq} = \frac{f_s d_b}{4\tau_{ET}} \tag{7-5}$$

Eq. (7-5) indicates that with increasing stress f_s at the loaded end, the required elastic length l_{erq} increases. In particular, when f_s reaches the yield strength f_y of the bar, the *elastic development length* l_{ed} is attained, the shortest length in which the bar stress can increase from zero to the yield strength. Therefore, $l_{erq} \le l_{ed}$. However, l_{ed} is still shorter than the embedment length l_{embd} in this category. Therefore, the slip due to bar extension s_{ext} is given by

$$s_{ext} = \frac{1}{2}\varepsilon_s l_{erq} = \frac{1}{2}\cdot\frac{f_s}{E_s}\cdot\frac{f_s d_b}{4\tau_{ET}} = \frac{d_b f_s^2}{8E_s\tau_{ET}} \tag{7-6}$$

where ε_s is the strain at the loaded end of the bar and E_s the elastic modulus of the reinforcing bar.

2) Category 2 ($f_s \le f_y$ and $l_{erq} > l_{embd}$)

As shown in **Fig. 7.5(b)**, due to finite dimensions of joints, it is likely that the required elastic length l_{erq} exceeds the physical embedment length l_{embd} even before applied bar stress f_s attains the yield strength f_y. Therefore, the bar center is also stressed. Accordingly, the slip due to bar extension is calculated as

$$s_{ext} = \frac{1}{2}\left(\varepsilon_s + \varepsilon_{end}\right) l_{embd} \tag{7-7}$$

where ε_{end} is the strain at the bar center, as illustrated in **Fig. 7.4**. ε_{end} can be determined by using a similar triangle in **Fig. 7.5(b)**.

$$\varepsilon_{end} = \left(1 - \frac{l_{embd}}{l_{erq}}\right)\varepsilon_s \tag{7-8}$$

By substituting Eqs. (7-8) and (7-5) into Eq. (7-7), the slip due to bar extension can be calculated in terms of f_s.

$$s_{ext} = \frac{\varepsilon_s}{2}\left[l_{erq} - \frac{\left(l_{erq} - l_{embd}\right)^2}{l_{erq}}\right] = \frac{2\tau_{ET} l_{embd}}{d_b E_s}\left(\frac{f_s d_b}{2\tau_{ET}} - l_{embd}\right) \tag{7-9}$$

A comparison between Eqs. (7-6) and (7-9) indicates that a smaller embedment length results in a smaller bar extension provided all the other parameters in Eqs. (7-6) and (7-9) remain the same.

3) Category 3($f_s > f_y$ and $l_{ed} + l_{yrq} \le l_{embd}$)

When the applied stress f_s at the joint interface exceeds the yield strength f_y, i.e. at strain hardening stage, a uniform inelastic bond stress τ_{YT} is mobilized over the

required inelastic length l_{yrq}, in which the bar stress f_s can increase from the yield strength f_y to the maximum inelastic stress. Force equilibrium over the length l_{yrq} requires

$$f_s A_b = \tau_{YT} \pi d_b l_{yrq} + f_y A_b \tag{7-10}$$

By substituting the bar cross-section area, l_{yrq} can be determined as

$$l_{yrq} = \frac{\left(f_s - f_y\right) d_b}{4\tau_{YT}} \tag{7-11}$$

As shown in **Fig. 7.5(c)**, if the embedment length l_{embd} is adequate, the available elastic length l_e, obtained by subtracting the required inelastic length l_{yrq} from the embedment length l_{embd}, is greater than the elastic development length l_{ed}. In other words, l_{embd} exceeds the total length $l_{ed} + l_{yrq}$. Therefore, the slip due to bar extension s_{ext} can be computed by integrating the strains over the length $l_{ed} + l_{yrq}$.

$$s_{ext} = \frac{1}{2}\varepsilon_y l_{ed} + \frac{1}{2}\left(\varepsilon_y + \varepsilon_s\right) l_{yrq} \tag{7-12}$$

where the elastic development length l_{ed} is given by

$$l_{ed} = \frac{f_y d_b}{4\tau_{ET}} \tag{7-13}$$

Based on assumption (3) that the constitutive model of reinforcement is bilinear, ε_s is given by

$$\varepsilon_s = \varepsilon_y + \varepsilon_h = \frac{f_y}{E_s} + \frac{f_s - f_y}{E_h} \tag{7-14}$$

where E_h is the hardening modulus of reinforcement.

By substituting Eqs. (7-11), (7-13) and (7-14) into Eq. (7-12), the slip due to bar extension can be determined in terms of the bar stress f_s.

$$s_{ext} = \frac{f_y^2 d_b}{8\tau_{ET} E_s} + \frac{\left(f_s - f_y\right) f_y d_b}{4\tau_{YT} E_s} + \frac{\left(f_s - f_y\right)^2 d_b}{8\tau_{YT} E_h} \tag{7-15}$$

4). Category 4 ($f_s > f_y$, $l_{ed} + l_{yrq} > l_{embd}$ ***and*** $l_{yrq} \le l_{embd}$ ***)***

As illustrated in **Fig. 7.5(d)**, an applied inelastic stress f_s (i.e. $f_s > f_y$) decreases to the yield strength over the required inelastic length l_{yrq}. However, due to the limited embedment length l_{embd}, the yield stress cannot decrease to zero over the available elastic length l_e. That is, l_{yrq} is smaller than l_{embd} but the total length ($l_{ed} + l_{yrq}$)is greater than l_{embd}. The slip due to bar extension is determined as

$$s_{ext} = \frac{1}{2}\left(\varepsilon_{end} + \varepsilon_y\right) l_e + \frac{1}{2}\left(\varepsilon_y + \varepsilon_s\right) l_{yrq} \tag{7-16}$$

According to **Fig. 7.5(d)**, the available elastic length l_e is given by

$$l_e = l_{embd} - l_{yrq} \tag{7-17}$$

At the center of the continuous bar, ε_{end} is computed by using a similar triangle.

$$\varepsilon_{end} = \frac{\left(l_{ed} - l_e\right)}{l_{ed}} \varepsilon_y \tag{7-18}$$

By substituting Eqs. (7-11), (7-14) and (7-18) into Eq. (7-16), s_{ext} becomes a function of f_s.

$$s_{ext} = \frac{2\tau_{ET}}{E_s d_b}\left[l_{ed}^2 - \left(l_{yrq} + l_{ed} - l_{embd}\right)^2 \right] + \frac{\left(f_s - f_y\right) f_y d_b}{4\tau_{YT} E_s} + \frac{\left(f_s - f_y\right)^2 d_b}{8\tau_{YT} E_h} \tag{7-19}$$

where $l_{ed} = f_y d_b / (4\tau_{ET})$ and $l_{yrq} = \left(f_y - f_s\right) d_b / (4\tau_{YT})$. A comparison between Eqs. (7-19) and (7-15) indicates that a shorter embedment length results in a smaller slip due to bar extension provided all other parameters remain the same.

5) Category 5($f_s > f_y$ ***and*** $l_{yrq} > l_{embd}$ ***)***

If the embedment length l_{embd} is too short, it is possible that the inelastic bond stress τ_{YT} is mobilized over the entire embedment length l_{embd}. Moreover, the required inelastic length l_{yrq} can even exceed l_{embd}, as shown in **Fig. 7.5**(e). Therefore, the slip due to bar extension s_{ext} is calculated as

$$s_{ext} = \frac{1}{2}\left(\varepsilon_{end} + \varepsilon_s\right) l_{embd} \tag{7-20}$$

where ε_{end} is given by

$$\varepsilon_{end} = \varepsilon_y + \frac{\left(l_{yrq} - l_{embd}\right)\left(\varepsilon_s - \varepsilon_y\right)}{l_{yrq}} = \frac{f_y}{E_s} + \frac{\left(l_{yrq} - l_{embd}\right)}{l_{yrq}} \cdot \frac{\left(f_s - f_y\right)}{E_h} \tag{7-21}$$

By substituting Eqs. (7-11), (7-14) and (7-21) into Eq. (7-20), s_{ext} can be expressed as

$$s_{ext} = \frac{f_y l_{embd}}{E_s} + \left(\frac{f_s - f_y}{E_h} - \frac{2\tau_{YT} l_{embd}}{d_b E_h} \right) l_{embd} \tag{7-22}$$

In summary, depending on different *bar stress state* f_s and *physical embedment length* l_{embd}, the determination of bar extension s_{ext} can be divided into five categories. However, for a joint with specific geometric properties and loading conditions, it is not necessary for a reinforcing bar in the joint to go through each category in a sequential manner.

7.2.2.4 Slip of anchored bars at joint interfaces under pulling force

Lap-spliced bars in the middle joint regions and the anchored bars in the end-column-stubs of the sub-assemblages are under pulling force subjected to a MCRS. For an anchored bar, a pullout force is applied at the loaded end, where a wide crack has formed, say, at a joint interface. With increasing pullout force, if the embedment length is adequate, the bar can always exhibit a zero-slip at the point with a zero-stress, as defined in the macro-models proposed by Lowes and Altoonash (2003), as well as Zhao and Sritharan (2007). Accordingly, the strain profile is similar to the one shown in **Fig. 7.5(a)** or **Fig. 7.5(c)**, depending on the bar stress state. However, if the embedment length is limited, the bar can be stressed up to the free end, which is the physical cut-off point of the bar, as indicated in **Fig. 7.6**. In this case (that is, when the physical embedment length l_{embd} is less than the required development length), besides the bar extension, the slip at the loaded end should also include the slip at the free end. That is,

$$s = s_{ext} + s_0 = \int_0^l \varepsilon(x)dx + s_0 \tag{7-23}$$

where s_0 is the free end slip.

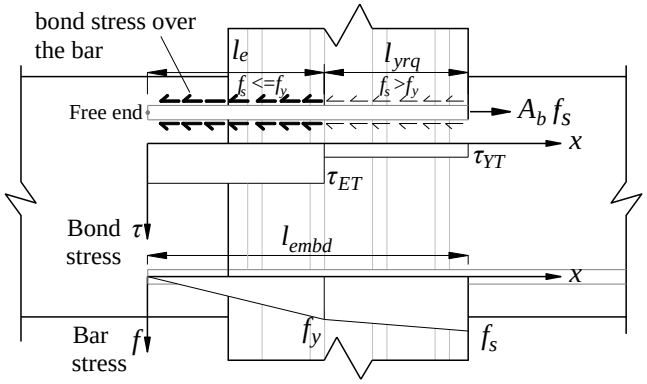

Fig. 7.6: Bond and bar stress distribution for an anchored bar under pullout

To satisfy the conditions of *zero strain at the free end*, the strain profile of categories 2 and 4 over the available elastic length l_e should be modified by red dash dot lines, as shown in **Figs. 7.5(b)** and **(d)**, respectively. Therefore, bar extension s_{ext} in category 2 becomes

$$s_{ext} = \frac{1}{2}\varepsilon_s l_{embd} = \frac{f_s l_{embd}}{2E_s} \tag{7-24}$$

and bar extension s_{ext} in category 4 is modified to

$$s_{ext} = \frac{1}{2}\varepsilon_y l_e + \frac{1}{2}(\varepsilon_y + \varepsilon_s) l_{yrq} \tag{7-25}$$

where l_{yrq} and ε_s are given by Eqs. (7-11) and (7-14), respectively and $l_e = l_{embd} - l_{yrq}$.

In general, the slip at the free end is either zero or very small as compared to bar extension, but it is an indicator to check whether pullout failure occurs. Moreover, The free end slip can mobilize bond strength and satisfy equilibrium (Eligehausen et al. 1983). However, a uniform or stepped bond stress model cannot directly account for slip at the free end because increasing slip does not increase the bond capacity of the bar (Sezen and Setzler 2008). Therefore, an alternative approach must be employed for bars with strain profiles of *category 2* and *4* shown in **Figs. 7.5(b)** and **(d)**, respectively. Alsiwat and Saatcioglu (1992) used the local bond-slip model

proposed by Eligehausen et al. (1983) to obtain the free end slip s_0 of a bar, which is given by

$$s_0 = s_1 \left(\frac{\tau_e}{\tau_u} \right)^{2.5} \tag{7-26}$$

where ultimate bond stress τ_u and corresponding slip s_1 are respectively computed as

$$\tau_u = \left(20 - \frac{d_b}{4} \right) \sqrt{\frac{f_c'}{30}} \tag{7-27}$$

$$s_1 = \sqrt{\frac{30}{f_c'}} \tag{7-28}$$

and the term τ_e is the elastic bond stress at the free end of a bar and is calculated as

$$\tau_e = \begin{cases} 0 & \text{if } l_e > l_{erq} \\ \dfrac{f_{se} d_b}{4 l_e} & \text{if } l_e \le l_{erq} \end{cases} \tag{7-29}$$

where f_{se} is the maximum elastic steel stress generated in the elastic region ($\le f_y$), and l_e is the available elastic length of the bar. For category 2 shown in **Fig. 7.5(b)**, $l_e = l_{embd}$, but for category 4 show in **Fig. 7.5(d)**, $f_{se} = f_y$ and $l_e = l_{embd} - l_{erq}$.

Eq. (7-29) suggests that if the embedment length of bar is adequate, i.e. l_e greater than the required elastic length l_{erq}, bond stress at the free end is not mobilized; otherwise, elastic bond stress will be generated. Therefore, for a bar with a strain profile of either *category 1* or *3* as shown in **Figs. 7.5(a)** and **(c)**, respectively, there is no free end slip and Eqs. (7-6) and (7-15) can be directly used to calculate total slip solely due to bar extension. However, for a bar with a strain profile as shown in **Figs. 7.5(b)** or **(d)**, l_e is smaller than l_{erq}, τ_e is generated. If τ_e reaches the ultimate bond stress τ_u specified in Eq. (7-26) (or if $s_0 \ge s_1$), that bar will fail by pullout. For example, if l_e is equal to zero, as the strain profile of category 5 shown in **Fig. 7.5(e)**, τ_e will become infinitely large, resulting in a pullout failure. Therefore, an anchored bar subjected to a pulling force can never develop a strain profile similar to the one shown in **Fig. 7.5(e)**.

In practice, it is common to use hooks for anchorage of reinforcing bars in exterior beam-column joints. Based on experimental data, Filippou et al. (1983) suggested that a hooked bar can be modeled as a straight bar with an equivalent length of

$$l_{eq} = l_s + 5d_b \tag{7-29}$$

where l_s is the straight embedment length. In the proposed model, this recommendation is adopted.

7.2.2.5 Summary on the procedure to determine bar stress-slip relationship

In summary, the procedure to determine the slip of a reinforcing bar for a given stress at the loaded end is illustrated in **Fig. 7.7**.

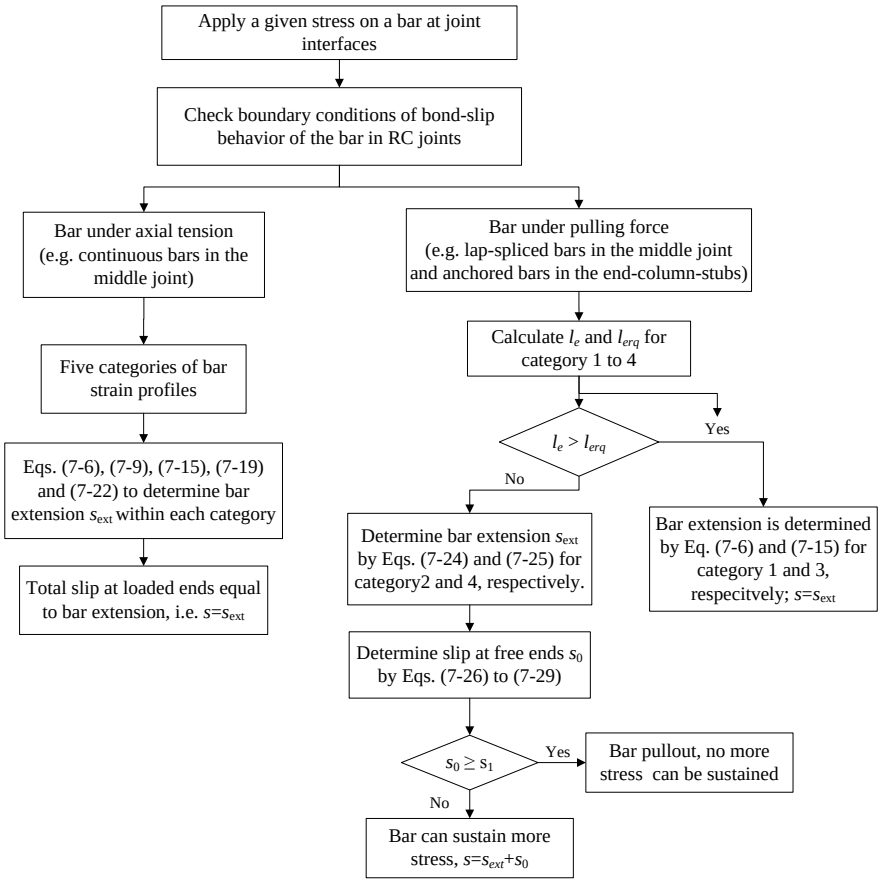

Fig. 7.7: Procedure to determine bar slip for a given load

The bar stress-slip relationship can be determined by gradually increasing the stress from zero to bar tensile strength. If a pullout failure occurs, the loading process would be terminated. Finally, the bar stress-slip relationship can be converted to the

bar force-slip relationship by multiplying cross-sectional areas of bars at the same layer, and the bar force-slip envelop can be used for a component spring in a component-based joint model.

7.2.2.6 Determination of uniform bond strength

Uniform bond strength for bars at both the elastic and inelastic stages was evaluated from published pullout, beam and column tests, as listed in **Table 7.1**. The values of uniform bond strength are empirical in nature but uniform bond strength is a function of steel stress state and concrete compressive strength. Although the bond strength for bars in elastic tension τ_{ET} varies for different bond conditions, it does not significantly affect bar force-slip relationship since elastic slip is very small. Since the database of pullout tests is much larger than that of beams and columns, τ_{ET} is specified as $1.8\sqrt{f_c'}$ for all analyses in this chapter.

Table 7.1 Empirical average bond strength

Bar stress, f_s (f_y = tensile yield strength)	Average bond strength (MPa)	Related tests	Research reference
Tension , $f_s < f_y$	$\tau_{ET} = 1.8\sqrt{f_c'}$	Pullout tests	Lowes and Altoontash (2003)
	$\tau_{ET} = 0.83\sqrt{f_c'}$	beam tests	Sozen and Moehle (1990)
	$\tau_{ET} = 1.0\sqrt{f_c'}$	column tests	Sezen and Setzler (2008)
Tension, $f_s > f_y$	$\tau_{YT} = 0.05\sqrt{f_c'}$ to $0.4\sqrt{f_c'}$	Pullout tests	Lowes and Altoontash (2003)
	$\tau_{YT} = 0.5\sqrt{f_c'}$	column tests	Sezen and Setzler (2008)
Compression, $-f_s < f_y$	$\tau_{EC} = 2.2\sqrt{f_c'}$	Pullout tests	Lowes and Altoontash (2003)
Compression, $-f_s > f_y$	$\tau_{YC} = 3.6\sqrt{f_c'}$	Pullout tests	

After a bar has yielded in tension, the average bond strength decreases significantly, ranging from $\tau_{YT} = 0.05\sqrt{f_c'}$ to $0.4\sqrt{f_c'}$ in pullout-out tests. This calibration was based on very limited test results. The lower bound is determined from a bar in a damaged anchorage zone (Eligehausen et al. 1983). The upper bound is based on

Shima's tests with initial undamaged concrete cylinders, which does not represent the bond conditions that exist for yielded reinforcing bars anchored in the vicinity of beam and column flexural tension zones (Lowes and Altoontash 2003). Due to bond deterioration, τ_{YT} should take on a smaller value, which will be explained later. Moreover, the evaluation of τ_{YT} also depends on the selection of constitutive models of reinforcement. Average bond stress over a bar segment can be determined from the difference of forces at the two segment ends divided by the surface area of the segment. The stress at each end is typically computed from the strain measured by strain gages. When a bar is at inelastic stage, the corresponding stress-strain curve can be characterized or simplified with different constitutive models, leading to different bar stresses and bond stresses for the same inelastic strains.

Due to Poisson effect, the diameter of a bar under compression increases, so that the average bond strength in compression becomes larger compared with the one under tension. In particular, when a bar has yielded, the Poisson effect is more dominant. Therefore, average bond strength at bar yielding in compression τ_{YC} is much greater than the one in elastic compression τ_{EC}.

7.2.2.7 Determination of hardening modulus of reinforcing bars

The constitutive model for a reinforcing bar is simplified into a bilinear model, as shown in **Fig. 7.8**. For a bilinear constitutive model for reinforcing bars, there is no general way to determine the hardening modulus E_h. For a bar that will fail by fracture, the hardening modulus E_h is determined by equating the area enveloped by the original and the idealized bilinear bar stress-strain curves. To capture bar fracture, both curves terminate at the ultimate tensile strength point f_u without considering the necking of bars in tension, suggesting that at bar fracture the bilinear model can absorb the same amount of strain energy as the original stress-strain model. To satisfy this requirement, an *artificial yield strength* f_y' will be introduced, as indicated in **Fig. 7.8**. The post-yield stress-strain relationship in the bilinear model goes through the artificial yield strength point f_y' and the ultimate tensile strength point f_u. Thus, the value of E_h is given by $\left(f_u - f_y'\right)/\left(\varepsilon_u - f_y'/E_s\right)$. Prior to attaining f_y', it is assumed that the reinforcing bar behaves elastically.

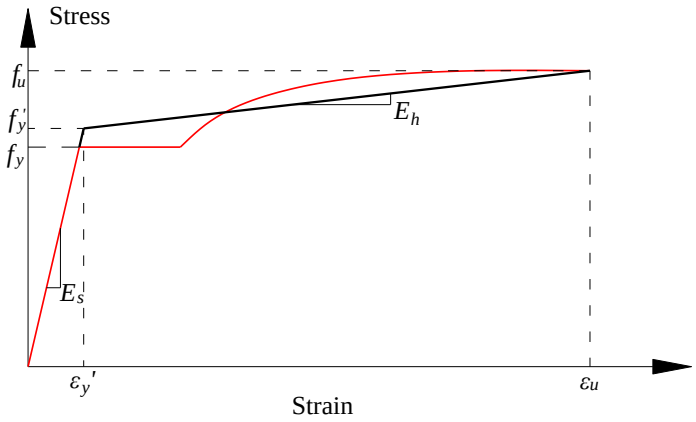

Fig. 7.8: Constitutive model of steel reinforcement

7.2.2.8 Validation of the proposed macro bar force-slip model

(1) Comparison with Shima's micro model

Very limited pullout tests or beam tests were available to validate the proposed bond-slip model because previous tests were more concerned with bond-slip relationships at elastic and early post-yield stages of reinforcing bars, rather than at the stage approaching fracture. To check the versatility of the proposed model for a continuous bar under axial tension and an anchored bar with an adequate embedment length under a pulling force, the bar stress-slip relationships predicted by the *proposed macro-model* are compared with predictions from Shima's *local bond-slip micro-model* (Shima et al. 1987). This is because Shima's model has been validated sufficiently at the elastic and early post-yield stages of bars. Moreover, it has considered the effect of bar strain on bond stress, as indicated in Eq. (7-30). During analysis, both models employ the bilinear constitutive model of reinforcement.

$$\frac{\tau}{f_c'} = \frac{0.73\left[\ln(1+5s)\right]^3}{1+\varepsilon\times 10^5} \tag{7-30}$$

where τ is bond stress; f_c' is compressive strength of concrete; $s = 1000S/d_b$, in which S is slip and d_b is bar diameter; and ε is bar strain.

Two case studies have been conducted to represent different boundary conditions of bond-slip relationships. In case 1, the bar is under axial tension on both sides. In case 2, the bar is under a pure pullout force with an embedment length identical to one of the bars anchored into end column stubs in the sub-assemblage tests (Yu and Tan 2012b). The material properties of reinforcing bars and concrete for the sub-assemblage tests as well as the other parameters for the proposed macro-model are listed in **Table 7.2**.

Table 7.2 Material properties for verification cases

Study cases	f_y (MPa)	E_s (MPa)	f_u (MPa)	E_h (MPa)	τ_{ET} (MPa)	τ_{YT} (MPa)	d_b (mm)	f_c' (MPa)	l_{embd} (mm)
#1: under axial tension	494	185873	593	929	$1.8\sqrt{f_c'}$	$0.2\sqrt{f_c'}$ ~ $0.4\sqrt{f_c'}$	13	38.2	125
#2: under pullout									425

Figs. 7.9(a) and **(c)** show the bar stress-slip relationships in case 1 and case 2, respectively. In both cases, the bar fails by fracture rather than by pullout, and the slip at the loaded end is solely contributed by the bar extension. As aforementioned, post-yield bond strength τ_{YT} varies with a range from $0.05\sqrt{f_c'}$ to $0.4\sqrt{f_c'}$ .Therefore, three different values of τ_{YT} are used in the proposed model. **Figs. 7.9(a)** and **(c)** suggest that the bar stress-slip relationship predicted by the proposed model agrees well with that from Shima's model when τ_{YT} varies between $0.2\sqrt{f_c'}$ and $0.3\sqrt{f_c'}$. The value of τ_{YT} has no evident effect on the bar stress-slip response when the bar is at the early post-yield stage, but it significantly affects the ultimate slip corresponding to bar tensile strength, as shown in **Figs. 7.9(a)** and **(c)**. Furthermore, the distribution of bond stress over the bar at different loaded stresses determined by Shima's model, as shown in **Figs. 7.9(b)** and **(d)**, indicates that τ_{YT} (i.e. average bond strength over the whole inelastic region) decreases slightly as the length of inelastic region increases. When the loaded stress approaches the bar tensile strength, τ_{YT} is around $0.24\sqrt{f_c'}$ for case 1 and around $0.26\sqrt{f_c'}$ for case 2. Note that the

bond stress distribution along one-half of the bar under axial tension is shown in **Fig. 7.9(b)** due to symmetry.

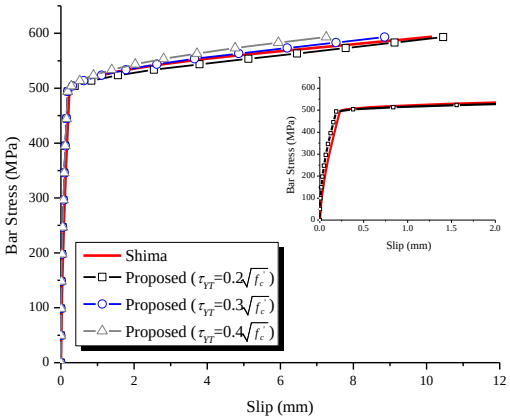

(a) Bar stress-slip relationship of case 1

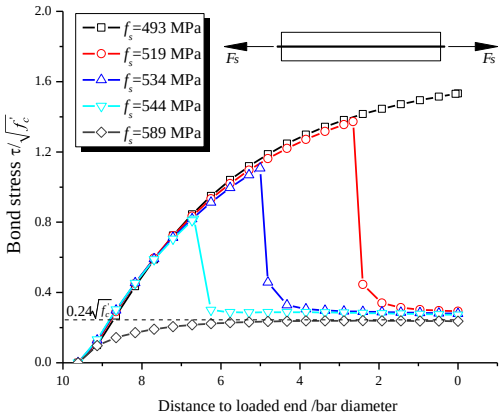

(b) Bond stress distribution under different loaded stress in case 1

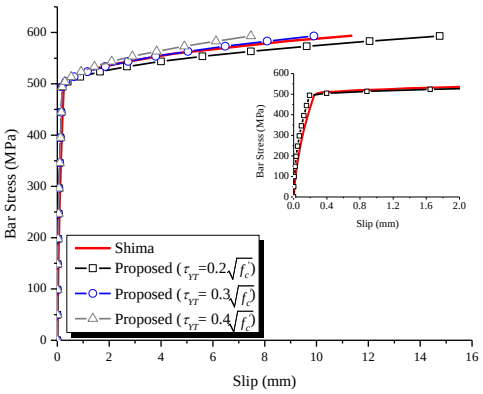

(c) Bar stress-slip relationship of case 2

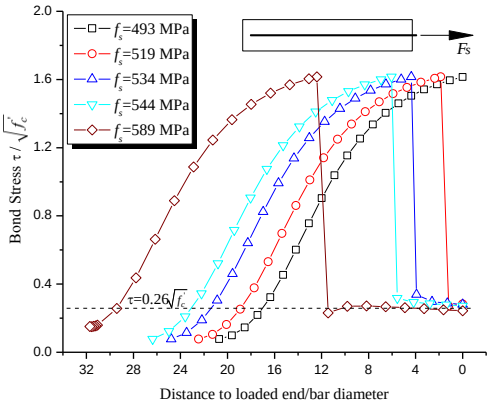

(d) Bond stress distribution under different loaded stress in case 2

Fig. 7.9: Verification of the proposed model

The insets in **Figs. 7.9(a)** and **(c)** indicate that $\tau_{ET} = 1.8\sqrt{f_c'}$ is slightly conservative to simulate the bar stress-slip relationship prior to yielding of bars. However, the slip corresponding to bar yielding is around 0.2 mm, less than 2% of the total slip at bar fracture. Therefore, the accuracy of τ_{ET} is insignificant to bar stress-slip relationship.

(2) Validation via a pullout test with large inelastic strains

A pullout test (Viawanthanatepa et al. 1979) with large inelastic strains is used to validate the proposed model, and the material and geometric properties of the bar

and concrete are indicated in **Fig. 7.10(a)**. To obtain the average bond strength τ_{YT} in the inelastic region, Shima's model is used. To show that τ_{YT} also depends on the selection of steel constitutive models, both bilinear and Maekawa's constitutive models (Maekawa et al. 2003) for reinforcement are employed, in which the latter can characterize the whole bar stress-strain relationship, similar to the curve shown in **Fig. 7.8**.

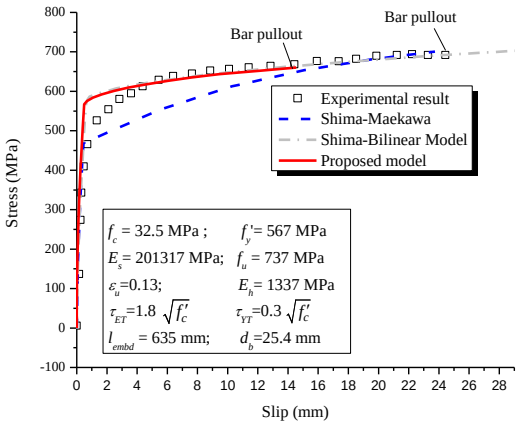

(a) Bar stress vs. slip of specimen No. 3 (Viawanthanatepa et al. 1979)

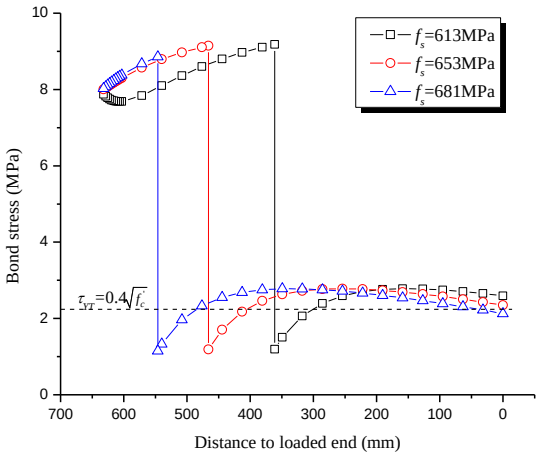

(b) bond stress distribution with Maekawa's model

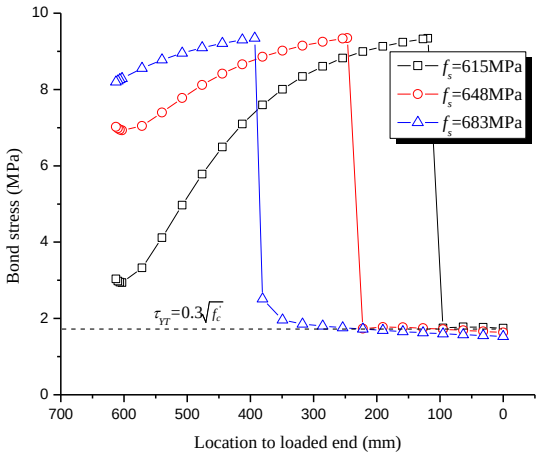

(c) bond stress distribution with Bilinear model

Fig. 7.10: Experimental and analytical bar stress vs. slip response

Fig. 7.10(a) shows that bar-stress vs. slip relationships predicted by the proposed model agree well with the experimental results except at the transition stage, i.e., when a bar changes from elastic to early post-yield stage. This is mainly ascribed to the simplified bilinear constitutive model of reinforcing bars. Moreover, the

proposed model is conservative in predicting a pullout failure compared with the test result. However, Shima's model is unable to predict pullout failure, so it overestimates the ultimate stress and slip until bar fracture. With the bilinear model for reinforcement, Shima's model suggests that average bond strength τ_{YT} is around $0.3\sqrt{f_c'}$, as shown in **Fig. 7.10(b)**. This value is adopted in the proposed macro-model for this case. However, with Maekawa's model for reinforcement, τ_{YT} is around $0.4\sqrt{f_c'}$, as shown in **Fig. 7.10(c)**, indicating the selection of constitutive reinforcement models affects the value of inelastic bond strength τ_{YT}.

In summary, the proposed macro-model is more suitable to predict fracture of continuous bars under axial tension and anchored bars with adequate embedment length, but it is more conservative in predicting bar pullout failure. This is due to the selection of the bilinear constitutive model for reinforcement. Taking predictions from Shima's model as the upper bound, average bond strength at inelastic stage (i.e. τ_{YT}) should be capped to $0.3\sqrt{f_c'}$. However, due to bond deterioration, this value should be further reduced during analysis.

7.2.3 Compressive bar force-slip model

As illustrated in **Fig. 7.2**, compressive force at the joint interfaces is contributed by both concrete and reinforcement. It is not easy to isolate their respective contribution. For a concrete spring, the force depends on the compression zone of joint interfaces and compressive strength of concrete. Furthermore, at compressive arch action (CAA) stage of RC beams, the variation of neutral axis depth depends not only on the geometrical parameters and material properties of beams, but also on the boundary conditions, as discussed in chapter 6. The variation of neutral axis, in turn, affects the stress of compressive reinforcement. Therefore, to determine the compressive spring force-slip relationship prior to structural analysis, the viable approach is to assume constant neutral axis depth.

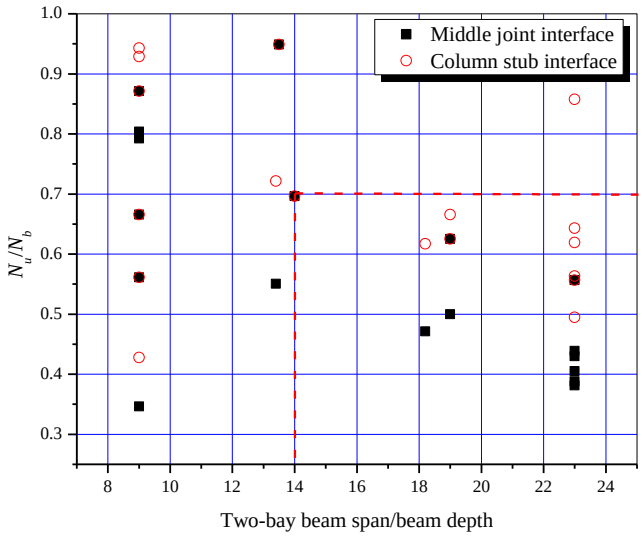

Fig. 7.11: Maximum axial force at compressive arch action of beams

At the middle joint and the column stub interfaces of RC sub-assemblages (Su et al. 2009; Yu and Tan 2012b), the ratio of maximum axial force N_u at CAA stage and the axial force N_b corresponding to balanced failure is shown in **Fig. 7.11**. N_b is obtained from cross-sectional analysis with the extreme compression concrete fiber reaching the limit compressive strain ε_{cu} simultaneously with tensile reinforcement attaining yield strain ε_y. It can be found that N_u ranges from 0.4~1.0N_b. However, span-to-depth ratios of typical beams range from 8 to 12, and become 16 to 24 after a middle column is removed. **Fig. 7.11** indicates that within this range N_u is smaller than 0.7N_b. Out of conservatism, it is assumed that N_u equals to 0.7N_b and the neutral axis depth c_N of a joint interface is calculated based on the condition that both 0.7N_b and the ultimate moment are acting at the joint interface. The strain and stress distribution at this state is shown in **Fig. 7.12**. Then the neutral axis is kept constant as c_N to formulate the stiffness properties of compressive springs. At the ultimate state of N_u=0.7N_b, the compressive force provided by concrete and compression reinforcement is given by

$$F_c = C_s + C_c = f'_{scr} A'_s + 0.85 f'_c b \beta c_N \tag{7-31}$$

where C_s and C_c are the compressive forces contributed by steel reinforcement and concrete, respectively; f'_{scr} is the compressive bar stress at the critical state shown in **Fig. 7.12**; A'_s is the compression bar area; f'_c is the concrete compressive strength; b

is the beam width; β is the ratio of the depth of the equivalent rectangular stress block to the neutral-axis depth, as defined in ACI 318-05 (American Concrete Institute 2005).

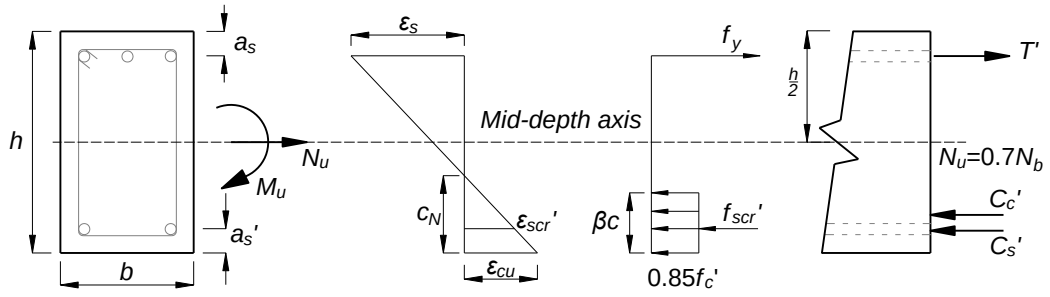

Fig. 7.12: Stress and strain distribution at beam sections

Because the compressive springs at the joint interfaces eventually change to tensile springs, in which tension is provided by reinforcing bars only, it is convenient to shift the compressive resultant C_c provided by concrete to the centroid of compression reinforcement. The shift of C_c will lead to a certain error in calculating the ultimate moment of resistance due to a little change of lever arms. However, the axial force is regarded as the primary variable herein. Similar to Lowes' approach (Lowes et al. 2003), prior to the strain of compression bars reaching ε_{scr}', C_c is linearly linked to compression bar strain ε_s'.

$$F_c = f_s' A_s' + \left(\varepsilon_s' / \varepsilon_{scr}'\right) 0.85 f_c' b \beta c_N \tag{7-32}$$

When ε_s' exceeds ε_{scr}', C_c is assumed constant as $0.85 f_c' b \beta c_N$ because concrete stress has a limit. In other words, the constitutive model of concrete is assumed to be *perfect elastic-plastic*. When a bar is stressed up to the free end with compression, due to concrete excelling at sustaining compression, the slip at the free end could be ignored and the loaded end slip solely depends on the shortening of the bar. Similar to tensile bar stress-slip derivation, compressive bar stress-slip relationship is obtained and is used to determine the relationship of compressive spring force and slip. However, it is impossible for concrete to follow the entire stress-strain curve of compression reinforcement. Moreover, for RC sub-assemblages under a MCRS, compressive springs will transit into tensile springs when catenary action kicks in,

and sub-assemblages typically fail in tension. Therefore, the ultimate force of compressive springs is not a critical parameter, and a strain value of $10\varepsilon_{cu}$ is tentatively used to determine the ultimate force and deformation of compressive springs.

7.3 Validation of component-based joint models

7.3.1 Overall modeling parameters

The proposed model is validated through comparisons of simulated and observed responses for RC beam-column sub-assemblages S4, S5 and S6 under a MCRS. The specimen detailing and test results for these have been introduced in chapters 3 and 4, respectively.

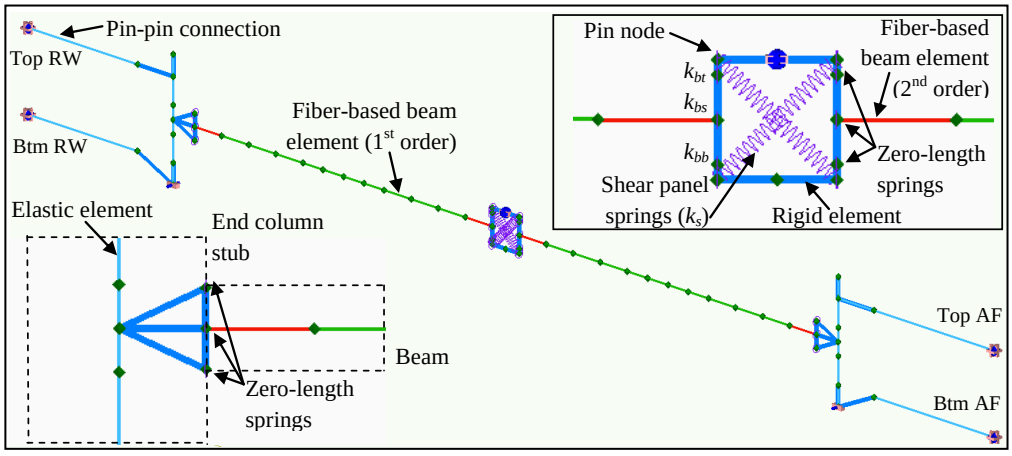

Fig. 7.13: Macro finite element model of sub-assemblages

The proposed joint model is incorporated into macro-FEA with Engineer's Studio (Forum8 2008), as seen in **Fig. 7.13**. To realistically simulate the structural behavior of each specimen, the whole specimen and the boundary connections in the test-up are modeled. Cracks, deformations and failures were mainly developed throughout the beams, so they are modeled with fiber-based elements, in which the beams near the joint and the end-column-stub interfaces are modeled with 2nd-order (three node isoparametric) fiber-based elements and the rest with 1st-order (two node isoparametric) fiber-based elements. The column stubs are modeled with elastic beam elements. Besides the middle joint, the end-column-stub interfaces are also modeled with spring elements to represent discontinuity in large deformations. The

analysis is conducted by applying a displacement-controlled load at the top of the middle joint until the specimen fails.

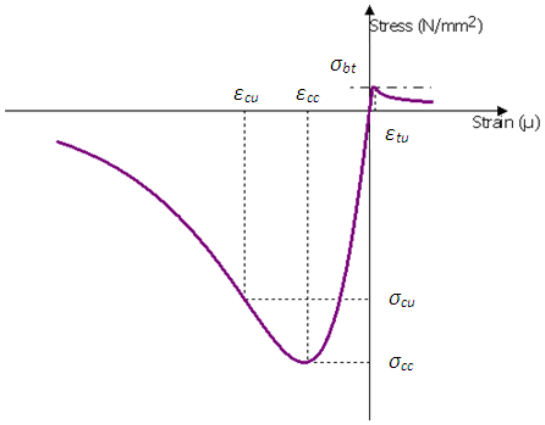

Fig. 7.14: Constitutive model of concrete for beams in Engineer's Studio

The constitutive models of concrete and reinforcement developed by Maekawa's research group (Maekawa et al. 2003), namely COM3, are employed for uniaxial material properties of concrete and steel fibers, respectively. Concrete model of COM3 is an elasto-plastic fracture model of concrete in compression, and its tensile branch has incorporated the contribution of bond-slip into tension-stiffening for concrete in tension, as shown in **Fig. 7.14**. Therefore, it is unnecessary to consider bond-slip relationship explicitly within the beams and "perfect bond" is assumed. Note that although considerable axial compression was mobilized throughout the beams at CAA stage, the beam sections near the beam-column interfaces had large cracks (Yu and Tan 2012b). Consequently, the confinement effect due to stirrups is not considered. The steel model of COM3 has considered the effect of bond-slip implicitly and represents the average stress-strain relationship of bars throughout the cracked concrete.

During the tests (Yu and Tan 2012b), the reaction force and the corresponding displacement of each restraint were recorded. **Fig. 7.15** shows the force-displacement relationships of those restraints, namely, Top-RW, Btm-RW, Top-AF and Btm-AF, which are indicated in **Fig. 7.13**. The corresponding restraint stiffness can be evaluated with linear regression based on the slope of the force-displacement relationship for each branch. From tests, it was found that connection gaps existed

between the restraints and the specimens. To validate the proposed joint model and the approaches to calibrate the spring properties, the restraints in the macro-FEA are modeled with linear spring elements. These elements also include the connection gaps. For simplicity, only the boundary conditions of specimens S4 and S6 are shown in **Figs. 7.15(a)** and **(b)**, respectively. The stiffness and the gaps of compression and tension branches are indicated in **Fig. 7.15** as well. The boundary conditions of other specimens can be obtained from the author's research group website (FERGAN 2011).

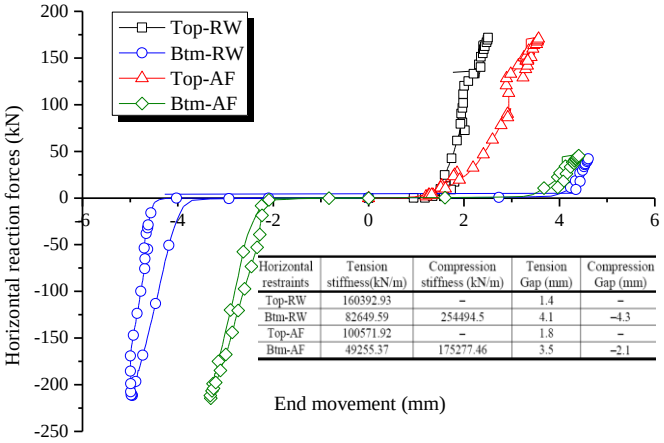

Horizontal restraints	Tension stiffness(kN/m)	Compression stiffness (kN/m)	Tension Gap (mm)	Compression Gap (mm)
Top-RW	160392.93	–	1.4	–
Btm-RW	82649.59	254494.5	4.1	−4.3
Top-AF	100571.92	–	1.8	–
Btm-AF	49255.37	175277.46	3.5	−2.1

(a) Specimen S4

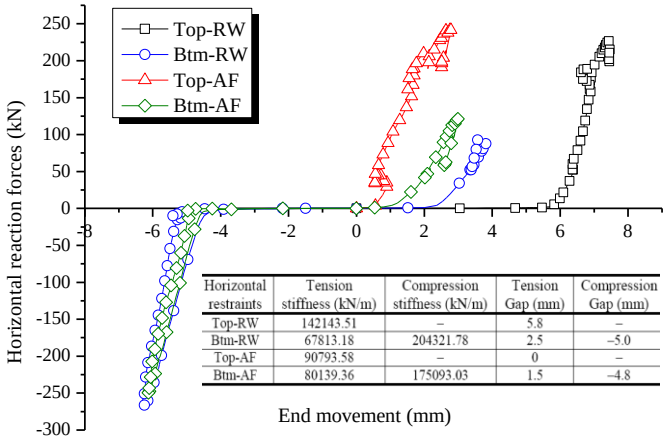

Horizontal restraints	Tension stiffness (kN/m)	Compression stiffness (kN/m)	Tension Gap (mm)	Compression Gap (mm)
Top-RW	142143.51	–	5.8	–
Btm-RW	67813.18	204321.78	2.5	−5.0
Top-AF	90793.58	–	0	–
Btm-AF	80139.36	175093.03	1.5	−4.8

(b) Specimen S6

Fig. 7.15: Stiffness or axial restraints at end column stubs

7.3.2 Spring parameters in component-based joints

The interface springs k_{bt}, k_{bs} and k_{bb} illustrated in **Fig. 7.2** are modeled with zero-length springs, as indicated in **Fig. 7.13**. The spring properties in Engineer's Studio are modeled by using multi-linear envelopes with Takeda hysteresis model. The non-linear force-deformation relationships of shear panel springs (k_s) and bar force-slip springs (k_{bb} & k_{bt}) are then simplified into multi-linear and tri-linear relationships, respectively, as shown in **Fig. 7.16**. The backbone curve of shear panel spring is symmetric for positive and negative branches. The critical points to determine the multi-linear model are indicated in **Fig. 7.16(a)** and are located at the intersections of lines from linear regression at each segment. Because the material and geometric properties of the middle joints in Yu and Tan's tests are nearly the same, the force-deformation relationship of k_s is kept the same for all specimens. The general tri-linear backbones of k_{bb} and k_{bt} are shown in **Fig. 7.16(b)**. The values of critical points as indicated in **Fig. 7.16(b)** depend on the reinforcement detailing at the joint interfaces. F_{yt} corresponds to the bar yielding in tension, and F_{ut} corresponds to the smaller capacity based on bar fracture or pullout. F_{mt} is the average value of F_{yt} and F_{ut}. According to Eqs. (7-31) and (7-32), F_{c1} and F_{c2} denote the smaller and the larger capacities corresponding to concrete attaining crushing strain ε_{cu} and compressive reinforcement reaching yield in compression, respectively. F_{c3} is the spring ultimate capacity.

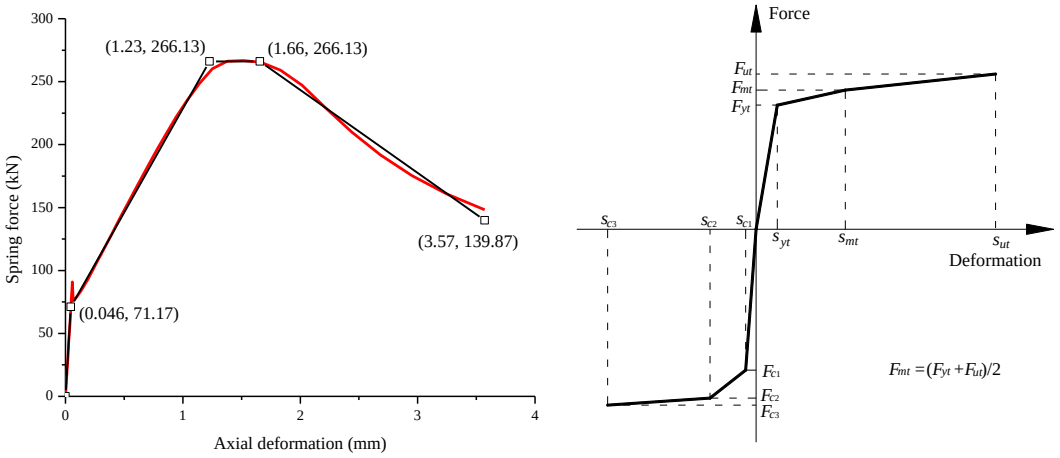

(a) Shear panel spring k_s (symmetric) (b) Bar force-slip spring k_{bb} & k_{bt}

Fig. 7.16: Multi-linear springs for finite element analysis

Based on the case studies in section 7.2.2.8, Shima's model provides an upper limit of inelastic average bond strength τ_{YT} for bars in the sub-assemblage tests. The limit is around $0.24\sqrt{f_c'} \sim 0.26\sqrt{f_c'}$. After bond deterioration is considered, τ_{YT} should be reduced further. Viawanthanatepa et al. (1979) observed that a large portion of the bar embedment length (254 mm out of 635 mm) suffered severe losses of bond strength when a bar with 25 mm diameter was at the pulling-through stage. That is, the bond deterioration zone could reach 10 times the bar diameter. Quereshi and Maekawa (1993) experimentally found that the bond deterioration zone could extend to about 5 times the diameter of reinforcing bars under pure pullout and increase in size when the RC interface is subjected to coupled tension and shear. The impact of bond deterioration on bond-slip response is more evident for bars with short embedment length. As a result, based on embedment length, effect of coupled tension and shear, and large tensile strains, τ_{YT} took on a small value, $0.1\sqrt{f_c'}$ and $0.2\sqrt{f_c'}$ for the continuous bars in the middle joints and the anchored bars in the end column stubs, respectively, and $0.15\sqrt{f_c'}$ for the lap-spliced bars in the middle joints.

The spring properties of k_{bb} and k_{bt} of specimens S4, S5 and S6 are shown in **Table 7.3**. The springs k_{bb} at the middle joint interfaces and k_{bt} at the end-column-stub interfaces transferred tension only. Thus, only the properties of the tensile branch are listed. During the validation process, it is found that the extension of a bar between two adjacent flexural cracks near a joint interface can contribute considerably to the ultimate bar slip at the joint interface, in particular, for bars with short embedment lengths under axial tension. For example, the ultimate slip of the continuous bar embedded in the middle joint of specimen S4 is around 12 mm. However, the spacing of severe flexural cracks is 100 mm for S4, as shown in **Fig. 7.17**, and the extension of around 50 mm of the bar contributes around 5 mm to the slip between the joint interface and the beam end. Therefore, for specimens S4 and S5, total slip at the interfaces includes the contribution of beam bar extension, as indicated in **Table 7.3**. If there is no test result about the average spacing of flexural cracks, they can be estimated as one-half the maximum crack spacing computed in accordance with Eurocode 2 (European Committee for Standardization 2004). Note

that the large cracks at the middle joint interface of S4 as shown in **Fig. 7.17** is caused by flexure rather than interface shear.

Table 7.3 Spring properties of k_{bb} and k_{bt}

At middle joint interfaces*										
Name	k_{bt}						k_{bb}			
	l_{embd} (mm)	E_h (MPa)	Tensile branch		Compressive branch		l_{embd} (mm)	E_h (MPa)	Tensile branch	
			S_t (mm)	F_t (kN)	S_c (mm)	F_c (kN)			S_t (mm)	F_t (kN)
S4	125+ (50)	929	0.30	196.71	0.068	477.52	125+ (50)	929	0.30	131.14
			7.93	216.42	0.157	544.63			7.93	144.28
			17.26	236.13	0.217	554.74			17.26	157.42
S5	125+ (25)	929	0.25	196.71	0.072	497.24	125+ (25)	929	0.25	196.71
			7.42	216.42	0.157	560.36			7.42	216.42
			16.75	236.13	0.217	570.47			16.75	236.13
S6	265	832	0.26	309.43	0.080	531.69	530	929	0.19	131.14
			9.98	339.29	0.210	649.57			5.28	144.28
			25.75	369.15	0.270	661.93			19.61	157.42
At end-column-stub interfaces†										
Name	k_{bb}						k_{bt}			
	l_{embd} (mm)	E_h (MPa)	Tensile branch		Compressive branch		l_{embd} (mm)	E_h (MPa)	Tensile branch	
			S_t (mm)	F_t (kN)	S_c (mm)	F_c (kN)			S_t (mm)	F_t (kN)
S4	425	929	0.19	131.14	0.074	461.35	425	929	0.19	196.71
			4.00	144.28	0.157	502.24			4.00	216.42
			14.75	157.42	0.216	508.98			14.75	236.13
S5	425+ (25)	929	0.25	196.71	0.072	497.25	425+ (25)	929	0.25	196.71
			5.34	216.42	0.157	560.36			5.34	216.42
			17.42	236.13	0.216	570.48			17.42	236.13
S6	425	929	0.19	131.14	0.070	481.49	425	832	0.26	309.43
			4.00	144.28	0.157	524.85			5.47	339.29
			14.75	157.42	0.216	531.59			20.21	369.15

* $\tau_{YT} = 0.1\sqrt{f_c'}$ for continuous bars and $\tau_{YT} = 0.15\sqrt{f_c'}$ for lap-spliced bars due to longer embedment length; For S4 and S5, the tensile slip includes the contribution of beam bar extension near interfaces. The length of beam bars are half the average spacing of severe cracks, as indicated in brackets. However, for compressive slip, the contribution of beam bars is ignored.

† $\tau_{YT} = 0.2\sqrt{f_c'}$ for all cases. Specimen S5 includes the contribution of beam bar extension to total tensile slip.

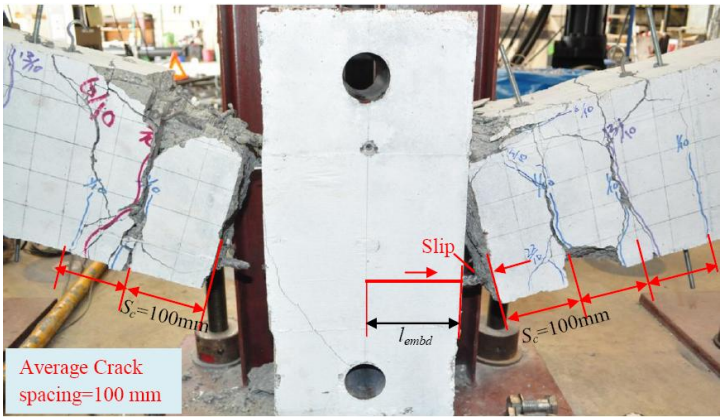

Fig. 7.17: Contribution of beam bars to slip at joint interfaces of S4

7.3.3 Comparisons with experimental results

Fig. 7.18 shows that the simulated structural behavior of RC beam-column sub-assemblages under a MCRS agrees well with the experimental results in terms of (a) applied load vs. MJD relationship and (b) beam axial force vs. MJD relationship. This indicates that the macro-FEA with the proposed component-based joint model and the proposed calibration procedure on spring properties can capture essential structural behavior with satisfactory accuracy, including CAA and catenary action. With the joint model, even bar fracture can be predicted. Otherwise, structural resistance at catenary action stage will be significantly overestimated. Similar to experimental results, the first fracture in numerical analyses occurred at k_{bb} of one middle joint interface and the final fracture occurred at k_{bt} of one end-column-stub interface. Due to non-uniform material properties, imperfect construction and the rotational restraint at the middle column stub, the bottom bars at the middle joint interfaces sequentially fractured during the tests. However, in numerical analyses, the fractures of k_{bb} at both joint interfaces occur almost simultaneously. After the fracture of k_{bb} at the middle joint interfaces, the beam axial force is mainly transferred by k_{bt} at the middle joint interfaces. The good agreement between numerical and experimental results at this range as shown in **Fig. 7.18** suggests that the proposed bar stress-slip model can provide appropriate tensile spring properties.

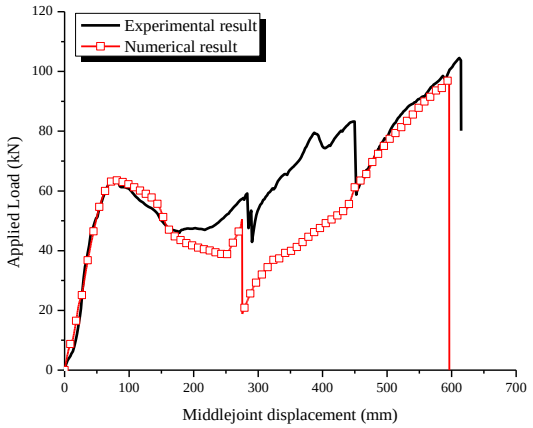

(a) S4-Applied load vs. MJD

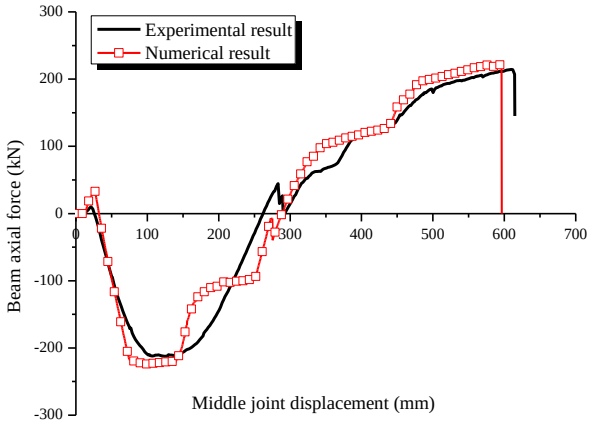

(b) S4-Axial force vs. MJD

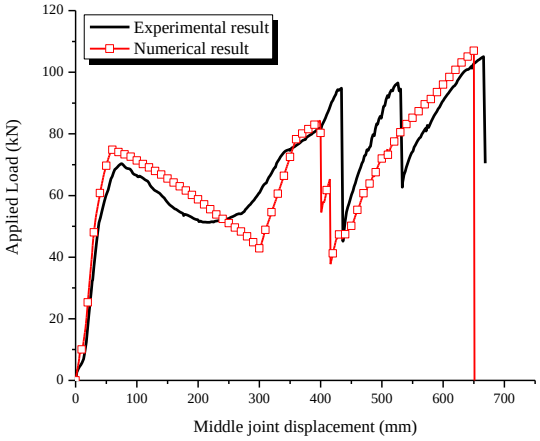

(c) S5-Applied load vs. MJD

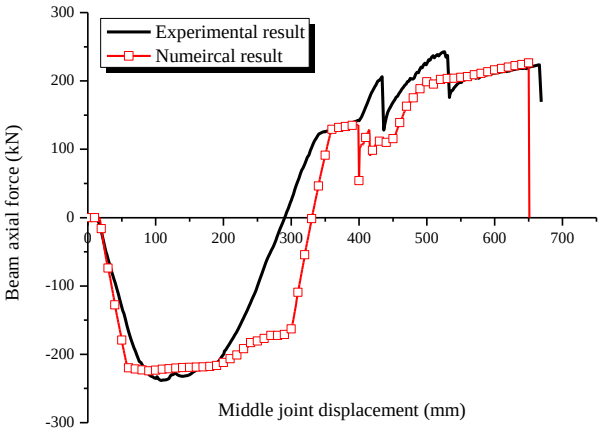

(d) S5- Axial force vs. MJD

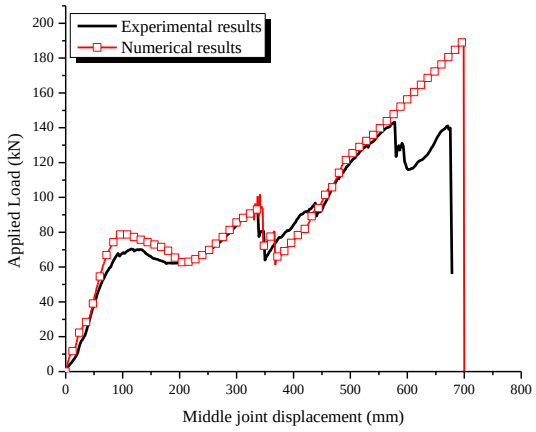

(e) S6-Applied load vs. MJD

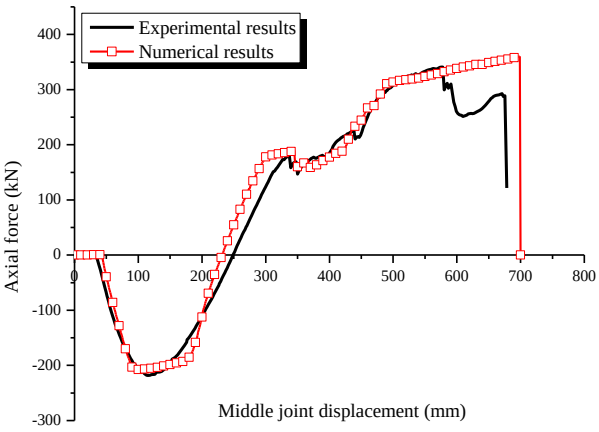

(f) S6-Applied load vs. MJD

Fig. 7.18: Validation of the proposed component-based joint model (MJD denotes middle joint displacement)

In summary, by incorporating the proposed component-based joint model into macro-FEA, structural deformation due to large slips at the joint and the end-column-stub interfaces and the discontinuity due to bar fracture can be considered. Consequently, predictions agree well with experimental results. Moreover, the macro-FEA by combining fiber elements and component-based joint models are computationally efficient to simulate structural behavior of beam-column sub-assemblages subjected to large deformations and severe discontinuity. Therefore, this numerical approach is a feasible alternative to the extensive 3-D continuum-based FEA.

7.4 Discussions

Currently, available test results to calibrate the average bond strength are based on pullout tests with most bar strains at elastic and early post-yield stage. However, bars at the joint and the end-column-stub interfaces of sub-assemblages were subjected to coupled tension and shear. Furthermore, large tensile strains were mobilized up to bar fracture and bond deterioration could extend from interfaces to a certain embedment length. As a result, the average bond strength of a bar exceeding tensile yield strength (i.e, τ_{YT}) is capped to $0.2\sqrt{f_c'}$.

To formulate the compressive spring properties before macro-FEA on structures, some assumptions have to be introduced, as discussed in the section "*compressive spring force-slip model*". In the tests, crushing of concrete at the joint and the end-column-stub interfaces resulted in sub-assemblages failing to sustain axial compression, and axial force gradually changed from compression to tension. Because compressive springs have been assigned a priori to the centroid of compression steel at the interfaces without considering concrete crushing, the joint model was unable to simulate the deterioration of compression zone near the joint interfaces, leading to inaccurate prediction of the descending part of compressive arch action. However, the 2^{nd}-order (three node isoparametric) fiber elements adjacent to interface springs can capture the crushing of concrete, to some extent compensating for the weakness of compressive springs. For example, the rapid reduction of beam axial compression, as shown in **Fig. 7.18(b)**, results from

concrete crushing at the 2nd-order fiber beam elements near the end-column-stub interfaces. As a result, the transition of applied loads and beam axial forces from CAA to catenary action stage can be reasonably simulated. If the major concerns are the capacities of compressive arch action and catenary action, then the inaccurate prediction at the transition stage becomes insignificant.

7.5 Conclusions

The structural behavior of RC beam-column sub-assemblages under a middle column removal scenario involves large deformations and severe discontinuity. To capture the combined effects of large slips at the joint and the end-column-stub interfaces and discontinuity due to bar fracture or pullout on structural behavior, a component-based joint model is proposed in this chapter. The components in the joint model function as equivalent nonlinear springs. Then the joint model is incorporated into macromodel-based finite element analysis (macro-FEA) with fiber beam elements. Numerical results agree well with experimental results in terms of load vs. MJD relationship and beam axial force vs. MJD. This indicates that the macro-FEA is able to characterize the essential structural mechanisms, including compressive arch action and catenary action. With the joint model, bar fracture can be predicted so that structural resistance at catenary action will not be overestimated. However, it is challenging to precisely predict the MJD corresponding to bar fracture. Typically, the prediction is conservative.

With careful calibrations on each nonlinear spring of the component-based joint model, the structural capacities of compressive arch action and catenary action corresponding to a large MJD as well as maximum axial compression can be reasonably predicted. To calibrate the spring properties, a systematic calibration procedure for each component is presented. Since tensile springs at the joint interfaces are mostly dominant, in particular at catenary action stage, a new bar stress-slip model is proposed to calibrate the bar stress-slip relationship to a very large tensile strain even up to bar fracture or pullout. This bar stress-slip model is based on the assumption of respective uniform bond stress over the elastic and the inelastic development length of a reinforcing bar. Then this model is validated by limited pullout test results and is further verified with Shima's local bond-slip

model. The validation and the verification studies indicate that the model is able to predict the bar stress-slip relationship under large tensile strain with good fidelity.

CHAPTER 8 CONCLUSIONS AND FUTURE WORK

8.1 Conclusions

This research program experimentally investigated the structural behavior of reinforced concrete (RC) sub-assemblages and frames subjected to a middle column removal scenario. Thereafter, an analytical model was developed for investigating compressive arch action (CAA) of RC sub-assemblages and a component-based joint model was proposed to facilitate structural analysis under column loss scenarios.

In terms of load-deflection histories of sub-assemblages and frames, with increasing middle joint displacement (i.e. deflection of the two-bay beam above the removed column), flexural action, CAA and catenary action were mobilized sequentially. Each of them can be regarded as one alternate load path (ALP) to mitigate progressive collapse. The commencement of catenary action is defined at the moment of beam axial force changing from compression to tension. Provided that shear failure of RC beams can be prevented, *one beam depth* can approximately be regarded as the deflection corresponding to the onset of catenary action. However, there is no clear demarcation between flexural action and CAA of RC beams because axial force can develop with increasing middle joint displacement (MJD). Therefore, flexural capacity that is determined based on conventional plastic-hinge mechanisms without considering beam axial force, is specified as an artificial demarcation between flexural action and CAA. Moreover, flexural capacity can be used as a baseline to evaluate the enhancement of structural resistance due to CAA and catenary action.

Similarities between the test results of two series of specimens

The *similarities* of the test results of eight sub-assemblages and seven frames are summarized as follows:

(1) The development of CAA heavily depends on the stiffness of axial and rotation restraints imposed at both ends of two-bay beams. The development

of catenary action depends on both axial stiffness of restraints and rotation ductility of beam-column connections.

(2) With adequate axial and rotational restraints, CAA capacities of sub-assemblage specimen S1 to S8 were 13.5%~43.2% larger than their flexural action capacity, and catenary action capacities of S1 to S7 were 28%~128% greater than their CAA capacities. However, CAA is a favorable ALP for both sub-assemblages and frames because it attains its capacity at a MJD of 0.18~0.46 beam depth, whereas catenary action achieves its capacity at a MJD greater than *two* beam depth.

(3) Failure was mainly concentrated at the *beam-column connections* rather than at the *joint panels*. Near the interfaces of the middle joints of sub-assemblages and frames, large cracking, severe concrete crushing and bottom bar fracture occurred. However, no cracks can be observed at the panels of the middle joints. For the interior side joints of RC frames, a few cracks occurred at the joint panels, and for the exterior side joints, such as joints in F3, extensive shear cracks formed at one joint panel, but the final failure was controlled by the column failure. Also, the specimens designed according to ACI 318-05 had adequate anchorage length for reinforcing bars even under catenary action.

(4) Seismic detailing in terms of arrangement of the stirrups in RC members and the hoops in joint cores did not benefit the structural behavior of sub-assemblages and frames significantly, in particular at catenary action stage. This is because the structural behavior of specimens was dominated by flexural and axial action instead of shear. Moreover, wide and concentrated cracking near the joint interfaces weakened the confinement effect from closed stirrups.

Differences between the test results of two series of specimens

The evident *differences* between the test results of the RC frames and the sub-assemblages resulted from different boundary conditions:

(1) Compared with the sub-assemblages, top bars of the RC frames with conventional detailing fractured at the side joint interfaces when the MJDs

were relatively small, significantly wrecking the development of catenary action. This was because in the side joints of the RC frames, physical embedment lengths of top bars was shorter compared to the sub-assemblage tests, and axial loads in the side columns resulted in higher bond stress, leading to smaller ultimate slips at the joint interfaces and thus reducing rotation capacities of beam-column connections adjacent to the joint interfaces. As a result, it is reasonable to follow the recommendations in UFC 4-023-03 that internal ties (i.e. bars) be placed on either side of beams rather than within beams or within the area directly above beams, unless the beams can achieve large rotations (say, 0.2 rad) without bar fracture.

(2) The equivalent restraint stiffness to two-bay beams in sub-assemblages was greater than that in frames. However, the stiffer boundary restraints resulted in a more rapid decline of structural resistance after CAA capacity.

Other findings in each series of tests

Other than the comparisons between the test results of two series of specimens, the design and analyses of each series of specimens also shed light on the structural behavior of RC framed structures subjected to a middle column removal scenario.

From the sub-assemblage tests, the force transfer mechanism at catenary action stage was clarified and the effects of key parameters on CAA and catenary action were investigated:

(1) At catenary action stage, structural resistance is contributed by both beam axial tension and shear force (or bending moment). Furthermore, the contribution from beam axial tension keeps increasing whereas that from shear keeps decreasing. Whether catenary action can increase structural resistance beyond the CAA capacity depends on whether the contribution of beam axial tension can exceed the loss in shear. After fracture of all bottom reinforcing bars, structural resistance is solely contributed from beam axial tension.

(2) CAA can significantly increase structural resistance of the sub-assemblages with small span-to-depth ratio and low longitudinal reinforcement ratio, and

catenary action can significantly increase structural resistance of sub-assemblages with large span-to-depth ratio and high longitudinal reinforcement ratio, particularly with high top reinforcement ratio. This is because bottom reinforcement typically fractures following the descending of CAA and catenary action development has to be solely depends on the strength and the amount of top reinforcement near the joint regions. However, a higher bottom reinforcement ratio corresponds to the fracture of bottom bars near the middle joint at a relatively larger MJD, which in turn large structural resistance due to catenary action may be attained at a relatively smaller MJD. In particular, when the detailing with symmetrical longitudinal reinforcement is employed, e.g. specimen S5-1.24/1.24/23, catenary action capacity achieved its capacity when bottom bars fractured. For slender beams (i.e. such as single beam span-to-depth ratio greater than 8.6), structural resistance due to flexure is smaller than that due to shear. Accordingly, structural response is dominant by flexural and axial behavior, and catenary action can significantly increase structural resistance. However, when the beam span-to-depth ratio is reduced to 7.6, e.g. specimen S8-1.24/0.82/13.4, shear failure occurs first, resulting in catenary action mobilized at a relatively smaller MJD. However, catenary action may not be able to compensate for the loss in shear. Consequently, structural resistance keeps decreasing after the first peak capacity.

Three different special detailing techniques in RC frames, including additional middle reinforcement layer in beams, partial debonding of bottom reinforcement at the joint regions and partial hinges at a beam depth away from the joint interfaces, were able to increase rotation capacities of the beam-column connections and yet without premature fracture of top bars. As a result, large resistance due to catenary action of RC beams can be used to mitigate progressive collapse. Also, it is noteworthy that for two-bay beams restrained by columns without lateral supports, catenary action is not a preferred option unless the stability of columns can be guaranteed.

Analytical model on CAA of two-bay RC sub-assemblages

Because CAA is a favorable ALP to mitigate progressive collapse with limited deflections of RC beams, it could be used in the ALP method. Accordingly, an analytical model was proposed to predict CAA capacity and maximum axial compression of RC sub-assemblages under a middle column removal scenario. The model considers imperfect boundary conditions, stress state of compressive reinforcement at critical beam sections, geometric and material properties of RC beams. The validations of the model indicate that the proposed model is able to predict the capacity of CAA and the maximum axial compression along the beams with satisfactory accuracy and reliability.

The parametric studies on the axial and rotational stiffness of restraints suggest that only when both relative axial and rotational stiffness are *not less than one,* CAA can be considered as a beneficial ALP to mitigate progressive collapse. The relative stiffness is a ratio of restraint stiffness to the corresponding stiffness of restrained uncracked beams. The parametric studies also suggest that for beams under adequate axial and rotational restraints, a lower reinforcement ratio and a lower span-to-depth ratio will enhance structural resistance from CAA.

Component-based joint model and bar stress-slip spring

Under a middle column removal scenario, structural behavior of RC beam-column sub-assemblages involves large deformations and even severe discontinuity. To capture the effects of large slips at the joint interfaces and the discontinuity due to bar fracture or pullout on structural behavior, a component-based joint model was proposed. The components in the joint model function as equivalent nonlinear springs. The validations based on sub-assemblage tests indicate that the macromodel-based finite element analysis incorporating fiber elements and the proposed component-based joint model is capable of characterizing the essential structural mechanisms, including CAA and catenary action. With the joint model, bar fracture can be predicted so that the structural resistance at catenary action stage will not be overestimated. With careful calibrations on each nonlinear spring, the structural capacities of CAA and catenary action, as well as maximum axial compression, can be accurately predicted.

Since tensile springs at the joint interfaces played the most dominant role in the ultimate resistance, in particular at catenary action stage, a new bar stress-slip model was proposed to calibrate the bar force-slip relationship to a very large tensile strain until bar fracture or pullout occurs. This bar stress-slip model is based on the assumption that uniform bond stress is respectively distributed over the elastic and inelastic development length of a reinforcing bar. The validation and verification indicates that the model is able to predict the bar stress (force)-slip relationship under large tensile strain with good fidelity.

8.2 Future work

In RC structures, RC beams contain many longitudinal reinforcing bars, and the bars can be counted as effective ties to develop catenary action if RC beams can achieve large rotation capacity (say, 0.2 rad) without fracture of bars. Typically, at each beam-column joint, the bottom reinforcement is not greater than the top reinforcement. Therefore, under a middle column removal scenario, the fracture of bottom reinforcement in the joint above the removed column is very likely to occur. Even so, the top longitudinal reinforcement, which is approximately at the same layer of slab reinforcement, can still be expected for catenary action. Currently, UFC 4-023-03 only allows placing ties beside beams because the design guideline is not clear whether beams are able to provide axial tension under large rotations. This necessitates the research to evaluate the ultimate rotation capacities of RC beams and to investigate the effect of axial tension on ultimate rotation capacity. On the other hand, future work can also be dedicated to increasing rotation capacity of RC beams by using special detailing, as shown in Chapter 5 in this thesis.

Rotation capacities of RC beams are affected by bond-slip behavior of reinforcing bars. During the process of validating the proposed bar stress-slip model, it is found that there is very limited data to demonstrate bond-slip behavior under large post-yield strains even to bar fracture. Moreover, in both the sub-assemblage and frame tests, longitudinal bars in beams were subjected to combined action of tension and shear. Therefore, more detailed component tests should be conducted to consider these effects. Accordingly, the component-based joint model can be improved.

The magnitude of tie forces in UFC 4-023-03 is specified without seemingly any apparent support from experimental data. Moreover, the tie force method mainly depends on catenary action and tensile membrane action. Therefore, further experiments should be dedicated to study the holistic behavior of RC buildings subjected to column loss scenarios. That is, specimens should include multiple bays, three dimensional action and typical floor systems. Also, experiments should be conducted to large deformations to achieve both material and geometric nonlinearities of RC structures. The corresponding test results can then be used to validate the magnitudes of tie forces.

In the sub-assemblage tests, it was found that the structural mechanisms of all the specimens are quite similar. As a result, to identify considerable variation in the structural response at critical limit states, the variation of beam-span-to depth ratio should be larger than those used in the sub-assemblage tests. For example, transfer girders are used in many tall buildings, the removal of columns under transfer girders may significantly undermine structural resistance against progressive collapse. Moreover, the public buildings designed according to old design codes, in which the structural integrity is not as strictly required as that in modern design codes, are more vulnerable to progressive collapse. It is necessary to investigate structural responses of this type of buildings under a column removal scenario.

Progressive collapse is a nonlinear and dynamic event. To more accurately evaluate the structural resistance against progressive collapse, it is necessary to convert nonlinear static structural behavior into dynamic behavior by introducing dynamic increase factors (DIF). However, the determination of DIFs in UFC 4-023-03 is mainly based on numerical analysis. Therefore, dynamic tests are needed to validate DIFs.

REFERENCES

Abrams, D. P. (1987). "Scale Relations for Reinforced Concrete Beam-Column Joints." *ACI Structural Journal*, 84(6), 502-512.

Allen, D. E., and Schriever, W. R. (1972). "Progressive Collapse, Abnormal Loads, and Building Codes." *Proceedings ASCE National Meeting on Structural Engineering*, Cleveland, Ohio, 21-47.

Alsiwat, J. M., and Saatcioglu, M. (1992). "Reinforcement Anchorage Slip under Monotonic Loading." *Journal of Structural Engineering-ASCE*, 118(9), 2421-2438.

Altoontash, A., and Deierlein, G. D. (2003). "A versatile model for beam-column joints." Structural Congress ASCE, Seattle, WA.

American Concrete Institute. (2005). "ACI 318-05: Building Code Requirements for Structural Concrete." Farmington Hills,, Michigan.

American Society of Civil Engineers (ASCE). (2005). "Minimum Design Loads for Buildings and Other Structures." American Society of Civil Engineers, Reston, Virginia.

American Society of Civil Engineers (ASCE). (2007). "Seismic Rehabilitation of Existing Buildings." SEI 41-06.

Bao, Y. H., Kunnath, S. K., EI-Tawil, S., and Lew, H. S. (2008). "Macromodel-Based Simulation of Progressive Collapse: RC Frame Structures." *Journal of Structural Engineering*, 134(7), 1079-1091.

British Standards Institute. (1997). "Structural Use of Concrete, Part 1: Code of Practice for Design and Construction." BS 8110:1997.

Byfield, M. P., Matteis, G. D., and Dinu, F. (2007). "Robust design of steel framed buildings against extreme loading." *Urban Habitat Constructions under Catastrophic Events Proceedings of Workshop*, Prague.

Byfield, M. P., and Paramasivam, S. (2007a). "Catenary action in steel-framed buildings." *Structures & Buildings*, 160(5), 247-257.

Byfield, M. P., and Paramasivam, S. (2007b). "The prevention of disproportionate collapse using catenary action." *Urban Habitat Constructions under Catastrophic Events Proceedings of Workshop*, Prague.

CEB-FIP. (2000). "Bond of reinforcement in concrete: state-of-art report." *FIB Bulletin 10*, CEB-FIP.

Ciampi, V., Eligehausen, R., Bertero, V. V., and Popov, E. P. (1982). "Analytical model for concrete anchorage of reinforcing bar under eneralized excitation." *UCB/EERC-82/23*, University of California, Berkeley, California.

Corley, W. G. (2002). "Applicability of seismic design in mitigating progressive collapse." National Workshop on Prevention of Progressive Collapse in Rosemont, Ill, Multihazard Mitigation Council of the National Institute of Building Sciences, Washington,D.C.

Corley, W. G., Mlakar, P. F., Sozen, M. A., and Thornton, C. H. (1998). "The Oklahoma City Bombing: summary and recommendations for multihazard mitigation." *Journal of Performance of Constructed Facilities*, 12(3), 100-112.

Demonceau, J. F. (2007). "Steel and composite building frames: sway response under conventional loading and development of membrane effects in beams further to an exceptional action," University of Liege, Liege, Belgium.

Department of Defense (DOD). (2005). "Design of buildings to resist progressive collapse." Unified Facilities Criteria (UFC) 4-023-03, 25 January 2005.

Department of Defense (DOD). (2010). "Design of Buildings to Resist Progressive Collapse." Unified Facilities Criteria (UFC) 4-023-03, 27 January, 2010.

Dusenberry, D. O., and Juneja, G. (2002). "Review of existing guidelines and provisions related to progressive collapse." National Workshop on Prevention of Progressive Collapse in Rosemont, Ill., Multihazard Mitigation Council of the National Institute of Building Sciences., Washington, D.C.

Eligehausen, R., Popov, E. P., and Bertero, V. V. (1983). "Local Bond Stress-Slip Relationships of Deformed Bars Under Generalized Excitations." *Report UCB/EERC-83/23*, EERC, Univeristy of California, Berkeley.

Ellingwood, B., and Leyendecker, E. V. (1978). "Approaches for design against progressive collapse." *Journal of the Structural Division, ASCE*, 18(ST3), 413-423.

Ellingwood, B., Marjanishvili, S., Mlakar, P., and Sasani, M. W., E. (2009). "Disproportionate Collapse Research Needs." *Structures Congress 2009 Proceedings, ASCE*, Austin, Texas, 1896-1907.

European Committee for Standardization. (2004). "EN 1992-1-1: Eurocode 2: Design of concrete structures -- Part 1.1: General rules and rules for buildings." CEN, Brussels.

European Committee for Standardization. (2006). "EN 1991-2-7: Eurocode 1 - Actions on structures - Part 1-7: General actions - Accidental actions." CEN, Brussels.

FERGAN. (2011). "http://teamsites.ntu.edu.sg/cee/FERGAN." Fire Engineering Research Group At NTU, Nanyang Technological University, Singapore.

Filippou, F. C. (1985). "A simple model for reinforcing bar anchorages under cyclic excitations." *UCB/EERC-85/05*, University of California, Berkeley, California.

Filippou, F. C., Popov, E. P., and Bertero, V. V. (1983). "Effects of Bond Deterioration on Hysteretic Behaivor of Reinforced Concrete Joints." *Reprot No. UCB/EERC 83/19*, EERC, University of California, Berkeley.

Fleury, F., Reynouard, J. M., and Merabet, O. (2000). "Multicomponent model of reinforced concrete joints for cyclic loading." *Journal of Engineering Mechanics, ASCE*, 126(8), 804-811.

Forum8. (2008). "Engineers' Studio, (http://www.forum8.co.jp/english/uc-win/EngineersStudio-1e.htm)."

Foster, S., Bailey, G., Burgess, I., and Plank, J. (2004). "Experimental behaviour of concrete floor slabs at large displacements." *Engineering Structures*, 26(9), 1231-1247.

General Services Administration (GSA). (2003). "Progressive Collapse Analysis and Design Guidelines for New Federal Office Buildings and Major Modernization Projects."

Guice, L. K., and Rhomberg, E. J. (1988). "Membrane Action in Partially Restrained Slabs." *ACI Structural Journal*, 85(3), 365-373.

Gurley, C. R. (2008). "Progressive Collapse and Earthquake Resistance." *Practice Periodical on Structural Design and Construction*, 13(1), 19-23.

Hawkins, N. M., Lin, I. J., and Jeang, F. L. (1982). "Local bond strength of concrete for cyclic reversed loadings." *Bond in Concrete*, Paisley College of Technology, Scotland, 151-161.

Hayes Jr., J. R., Woodson, S. C., Pekelnicky, R. G., Poland, C. D., Corley, W. G., and Sozen, M. (2005). "Can Strengthening for Earthquake Improve Blast and Progressive Collapse Resistance?" *Journal of Structural Engineering*, 131(8), 1157-1177.

Izzuddin, B. A. (2005). "A simplified model for axially restrained beams subjected to extreme loading." *Steel Structures*, 5, 421-429.

Izzuddin, B. A., and Elghazouli, A. Y. (2004). "Failure of lightly reinforced concrete members under fire I: analytical model." *Journal of Structural Engineering*, 130(1).

Izzuddin, B. A., and Nethercot, D. A. (2009). "Design-Oriented Approaches for Progressive Collapse Assessment: Load-Factor vs Ductility-Centred Methods." *Structures Congress 2009 Proceedings, ASCE*, Austin, Texas, USA, 1791-1800.

Izzuddin, B. A., Vlassis, A. G., Elghazouli, A. Y., and Nethercot, D. A. (2008). "Progressive collapse of multi-storey buildings due to sudden column loss -- Part I: Simplified assessment framework." *Engineering Structures*, 30, 1308-1318.

Jaspart, J. P. (2000). "General report: session on connections." *Journal of Constructional Steel Research*, 55, 69-89.

Khandelwal, K., EI-Tawil, S., Kunnath, S. K., and S., L. H. (2008). "Macromodel-Based Simulation of Progressive Collapse: Steel Frame Structures." *Journal of Structural Engineering*, 134(7), 1070-1078.

Kim, J., and Yu, J. (2012). "Analysis of reinforced concrete frames subjected to column loss." *Magazine of Concrete Research*, 64(1), 21-33.

Krauthammer, T. (2003). "AISC research on structural steel to resist blast and progressive collapse." *Proceedings: Steel Building Symposium: Blast and Progressive Collapse Resistance*, New York City, NY, 67-81.

Krauthammer, T., Hall, R. L., Woodson, S. C., Baylot, J. T., Hayes, J. R., and Sohn, Y. (2002). "Development of progressive collapse analysis procedure and condition assessment for structures." National Workshop on Prevention of Progressive Collapse in Rosemont, Ill., Multihazard Mitigation Council of the National Institute of Building Sciences., Washington, D.C.

Krawinkler, H. (1988). "Scale effects in static and dynamic model testing of structures." *Proc. 9th Wold Conf. on Earthquake Engineering*, Tokyo-Kyoto, Japan, 865-876.

Lee, C. H., Kim, S., and Lee, K. (2010). "Parallel Axial-Flexural Hinge Model for Nonlinear Dynamic Progressive Collapse Analysis of Welded Steel Moment Frames." *Journal of Structural Engineering*, 136(2), 165-173.

Lowes, L. N., and Altoontash, A. (2003). "Modeling Reinforced-Concrete Beam-Column Joints Subjected to Cyclic Loading." *Journal of Structural Engineering*, 129(12), 1686-1697.

Lowes, L. N., Mitra, N., and Altoontash, A. (2003). "A beam-column joint model for simulating the earthquake response of reinforced concrete frames." *Technical Rep. No. PEER 2003/10*, PEER,Berkeley, Calif.

MacGregor, J. G., and Wight, J. K. (2005). *Reinforced Concrete Mechanics and Design*, Prentice Hall Pearson Education South Asia Pte Ltd.

Maekawa, K., Pimanmas, A., and Okamura, H. (2003). *Nonlinear Mechanics of Reinforced Concrete*, Spon Press Taylor & Francis Group.

Marchand, K., McKay, A., and Stevens, D. (2009). "Development and Application of Linear and Non-Linear Static Approaches in UFC 4-023-03." *Structures Congress 2009 Proceedings, ASCE*, Austin, Texas, 1729-1738.

Marjanishvili, S. M. (2004). "Progressive Analysis Procedure for Progressive Collapse." *Journal of Performance of Constructed Facilities*, 18(2), 79-85.

Mazonni, S., McKenna, F., Scott, M. H., and Fenves, G. L., etc.,. (2006). "OpenSees user command language manual."

Ministry of Hoursing and Local Government. (1968). "Report of the Inquiry into the Collapse of Flats at Ronan Point." Canning Town. HM Stationery Office, London.

Mitra, N. (2007). "An analytical study of reinforced concrete beam-column joint behavior under seismic loading," University of Washington, Washington, D. C., USA.

Mitra, N., and Lowes, L. N. (2007). "Evaluation, calibration and verification of a reinforced concrete beam-column joint model." *Journal of Structural Engineering*, 133(1), 106-120.

Moore, D. B. (2002). "The UK and European Regulations for Accidental Actions." *NIST/NIBS Multihazard Mitigation Council National Workshop on Prevention of Progressive Collapse*, Chicago.

National Institute Standard and Test (NIST). (2007). "Best Practices for Reducing the Potential for Progressive Collapse in Buildings."

Ockleston, A. J. (1958). "Arching Action in Reinforced Concrete Slabs." *The Structural Engineer*, 36(6), 197-201.

Orton, S., Jirsa, J., and Bayrak, O. (2009). "Carbon Fiber-Reinforced Polymer for Continuity in Existing Reinforced Cocnrete Buildings Vulnerable to Collapse." *ACI Structural Journal*, 106(5), 608-616.

Orton, S. L. (2007). "Development of a CFRP System to Provide Continuity in Existing Reinforced Concrete Buildings Vulnerable to Progressive Collapse," University of Texas, Austin.

Park, R., and Gamble, W. L. (2000). *Reinforced Concrete Slabs*, John Wiley & Sons, Inc.

Park, R., and Paulay, T. (1975). *Reinforced Concrete Structures*, John Wiley & Sons.

Qureshi, J., and Maekawa, K. (1993). "Computational model for steel embedded in concrete under combined axial pullout and transverse shear displacement." *Proceedings of the JCI*, 1249-1254.

Regan, P. E. (1975). "Catenary Action in Damaged Concrete Structures." *Industrialization in Concrete Building Construction, ACI Special Publication SP-48*, American Concrete Institute, Detroit, Michigan, 191-224.

Santaf é Iribarren, B., Berke, P., Bouillard, P., Vantomme, J., and Massart, T. J. (2011). "Investigation of the influence of design and material parameters in

the progressive collapse analysis of RC structures." *Engineering Structures*, 33(10), 2805-2820.

Sasani, M., Bazan, M., and Sagiroglu, S. (2007). "Experimental and analytical progressive collapse evaluation of actual reinforced concrete structure." *ACI Structural Journal*, 104(6), 731-739.

Sasani, M., Kazemi, A., Sagiroglu, S., and Forest, S. (2011). "Progressive Collapse Resistance of an Actual 11-Story Structure Subjected to Severe Initial Damage." *Journal of Structural Engineering*, 137(9), 893.

Sasani, M., and Kropelnicki, J. (2008). "Progressive collapse analysis of an RC structure." *The Structural Design of Tall and Special Buildings*, 17(4), 757-771.

Sasani, M., and Sagiroglu, S. (2008). "Progressive collapse resistance of hotel San Diego." *Journal of Structural Engineering*, 134(3), 474-488.

Sezen, H., and Setzler, E. J. (2008). "Reinforcement Slip in Reinforced Concrete Columns." *ACI Structural Journal*, 105(3), 280-289.

Shima, H., Chou, L., and Okamura, H. (1987). "Micro and macro model for bond behavior in RC." *Journal of the Faculty of Engineering, The University of Tokyo(B)*, 39(2), 133-194.

Sozen, M. A., and Moehle, J. P. (1990). "Development and Lap-Splice Lengths for Deformed Reinforcing Bars in Concrete." Report to the Portland Cement Association and Concrete Reinforcing Steel Institute.

Sozen, M. A., Thornton, C. H., Corley, W. G., and Mlakar, P. F. (1998). "The Oklahoma City Bombing: Structure and mechanisms of the Murrah Building." *Journal of Performance of Constructed Facilities*, 12(3), 120-136.

Stevens, D., Crowder, B., Sunshine, D., Marchand, K., Smilowitz, R., Williamson, E., and Waggoner, M. (2011). "DoD Research and Criteria for the Design of Buildings to Resist Progressive Collapse." *Journal of Structural Engineering*, 137(9), 870-880.

Stevens, D., Hewitt, O., Campbell, T., and Marchand, K. (2009a). "Overview of the Revised DoD Progressive Collapse Design Requirements." *Structures Congress 2009 Proceedings, ASCE*, Austin, Texas, 1718-1722.

Stevens, D., Marchand, K., and McKay, A. (2009b). "Revision of the Tie Force and Alternate Path Approaches in the DoD Progressive Collapse Design Requirements." *Structures Congress 2009 Proceedings, ASCE*, Astin, Texas, 1723-1728.

Su, Y., P., Tian, Y., and Song, X. S. (2009). "Progressive collapse resistance of axially-restrained frame beams." *ACI Structural Journal*, 106(5), 600-607.

Tschemmernegg, F., and Humer, C. (1988). "The design of structural steel frames under consideration of the nonlinear behaviour of joints." *Journal of Constructional Steel Research*, 11, 73-103.

Ueda, T., Lin, I., and Hawkins, N. M. (1986). "Beam Bar Anchorage in Exterior Beam-Column Connections." *ACI Journal, Proceedings*, 83(3), 412-422.

Vecchio, F. J., and Collins, M. P. (1986). "The modified compression-field theory for reinforced concrete elements subjected to shear." *ACI Structural Journal*, 83(22), 219-231.

Viawanthanatepa, S., Popov, E. P., and Bertero, V. V. (1979). "Effects of Generalized Loadings on Bond of Reinforcing Bars Embedded in Confined

Concrete Blocks." *Report UCB/EERC-79/22*, EERC, University of California, Berkeley.

Welch, R. W. (2000). "Compressive membrane capacity estimates in laterally edge restrained reinforced concrete one-way slabs," University of Illinois, Urbana, Illinois.

Yi, W. J., He, Q. F., Xiao, Y., and Kunnath, S. K. (2008). "Experimental study on progressive collapse-resistant behavior of reinforced concrete frame structures." *ACI Structural Journal*, 105(4), 433-439.

Yin, Y. Z., and Wang, Y. C. (2005). "Analysis of catenary action in steel beams using a simplified hand calculation method, Part 1: theory and validation for uniform temperature distribution." *Journal of Constructional Steel Research*, 61(2), 183-211.

Youssef, M., and Ghobarah, A. (2001). "Modeling of RC beam-column joints and structural walls." *Journal of Earthquake Engineering*, 5(1), 93-111.

Yu, J., and Tan, K. H. (2010a). "Macromodel-based simulation of catenary action of RC beam-column sub-assemblages." *The Third International fib Congress and Exhibition*, Gaylord National Resort, Washington, D.C., Paper #208 in Proceedings Disc.

Yu, J., and Tan, K. H. (2010b). "Progressive collapse resistance of RC beam-column sub-assemblages." *The Third International Conference of Design and Analysis of Protective Structures*, Singapore, 74-83.

Yu, J., and Tan, K. H. (2011a). "Experimental and numerical investigation on progressive collapse resistance of reinforced concrete beam column sub-assemblages." *Engineering Structures*, (Accepted).

Yu, J., and Tan, K. H. (2011b). "Experimental and numerical investigation on progressive collapse resistance of reinforced concrete beam column sub-assemblages." *Engineering Structures*, (Online).

Yu, J., and Tan, K. H. (2012a). "Compressive arch action of reinforced concrete beam-column sub-assemblages I: Analytical modeling." *Journal of Structural Engineering*, (submitted).

Yu, J., and Tan, K. H. (2012b). "Structural behavior of reinforced concrete beam-column sub-assemblages under a middle column removal scenario." *Journal of Structural Engineering*, (Online).

Zhao, J., and Sritharan, S. (2007). "Modeling of Strain Penetration Effects in Fiber-Based Analysis of Reinforced Concrete Structures." *ACI Structural Journal*, 104(2), 133-141.

Zoetemeijer, P. (1983). "Summary of the Research on Bolted Beam-to-Column Connections (period 1978-1983)." *No. 6-85-M*, Seven Laboratory, Delft.

APPENDIX A: DETERMINATION OF RESTRAINT STIFFNESS

During the tests on the reinforced concrete (RC) beam-column sub-assemblages and the RC frames, the reaction force and the corresponding end movement at each restraint were measured. As a result, based on the relationship of the reaction force and the end movement, the stiffness of each restraint can be evaluated. To more precisely simulate structural behavior of a specimen, the stiffness should be assessed on individual restraint that was used to connect the specimen to an A-Frame and a reaction wall in laboratory. On the other hand, structural mechanisms were mainly developed throughout the two-bay beam in each test, and the remaining structure functioned as restraints to the beam. Therefore, to simplify analysis, the restraint stiffness can be evaluated as equivalent restraint stiffness to the two-bay beam.

A.1 Stiffness of each individual restraint

A.1.1 Stiffness of restraints to sub-assemblages

Fig. A.1(a) shows the reaction forces (i.e. H_1, H_2 and R_1) at each end-column stub of the sub-assemblages. Since vertical reactions were eventually transferred to a solid ground through steel plates, a pin and rollers, vertical settlements of the end-column stubs could be ignored. As indicated in **Fig. A.2(a)**, horizontal movements Δ_1 and Δ_2 corresponded to reactions H_1 and H_2, respectively. Based on the relationships of H_1 and Δ_1 as well as H_2 and Δ_2, the stiffnesses of the top and the bottom horizontal restraints can be evaluated by linear regression. The slopes of linear functions are the values of restraint stiffness in tension and compression. As a result, each horizontal restraint can be regarded as a linear elastic spring. During the tests, the horizontal restraints were connected to a reaction wall (RW) or an A-frame (AF) at both ends of a specimen. Accordingly, the restraints are denoted as Top-RW, Btm-RW, Top-AF and Btm-AF.

Figs. A.3(a) to **(f)** show the relationships of horizontal reaction force vs. end movement. It can be seen that gaps (corresponding to zero force and non-zero

movement) existed in connections between the horizontal restraints and the specimen ends. Since the connections were designed to allow manufacturing errors of the specimens and to facilitate specimen installation, they were very flexible so that the gaps were not identical for all the tests. In addition, the tension and the compression stiffness of each horizontal restraint may not be equal. The values of the stiffness and gaps for the horizontal restraints are listed in **Figs. A.3(a)** to **(f)** as well. Therefore, the boundary conditions of the sub-assemblages can be more accurately represented and the experimental data can be used to validate relevant numerical models. **Figs. A.3(a)** to **(f)** also indicate that *top horizontal restraints (i.e. Top-RW and Top-AF) hardly provided horizontal reactions to the sub-assemblages at compressive arch action (CAA) stage but they played dominant roles at catenary action stage.*

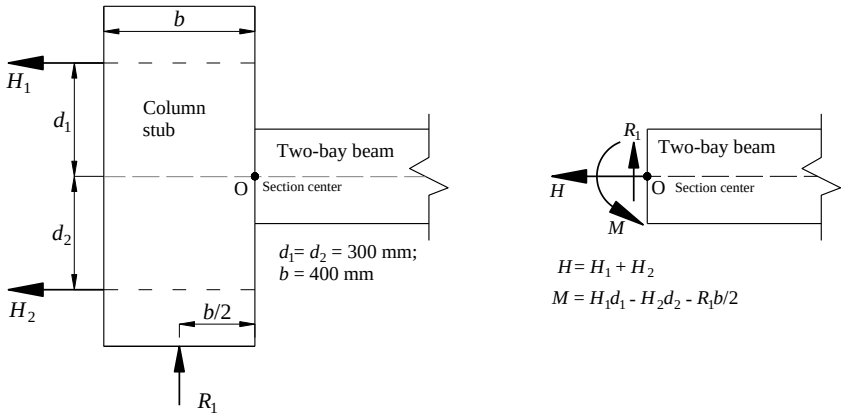

(a) Reactions at end stubs (b) Equivalent Forces at beam ends

Fig. A.1: Reaction forces to sub-assemblages

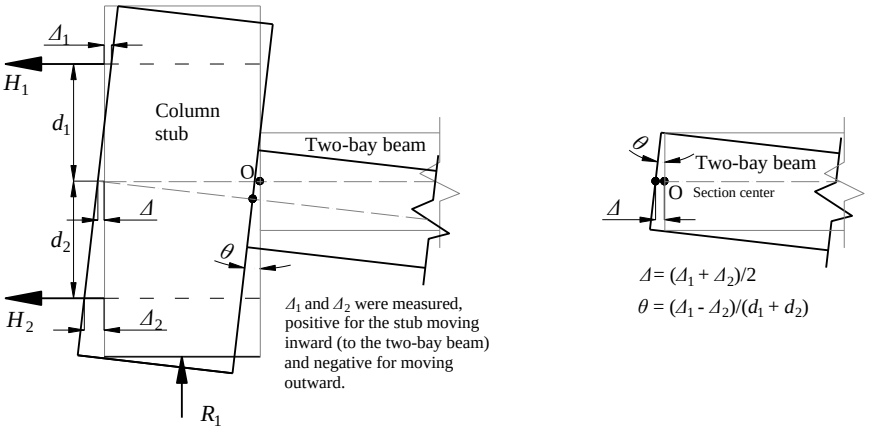

(a) Translation and rotation of end stubs (b) movements at beam ends

Fig. A.2: End movements of sub-assemblages

Due to improper operation, the measurement for specimen S5 was not very successful. However, the stiffness at CAA stage can be correctly assessed. The values of tension stiffness, which were uncertain as shaded in **Fig. A.3(c)**, can be referred to the values of S4 and S6.

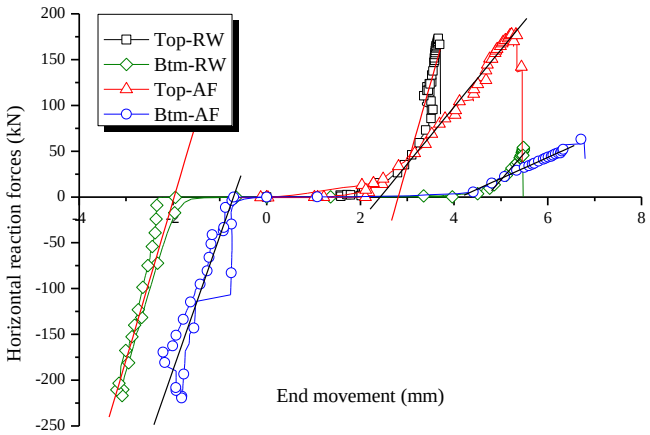

Horizontal restraints	Tension stiffness(kN/m)	Compression stiffness (kN/m)	Tension Gap (mm)	Compression Gap (mm)
Top-RW	143744.60	–	2.6	–
Btm-RW	58523.14	173352.0	4.7	– 2.0
Top-AF	62413.11	–	2.4	–
Btm-AF	23050.53	146390.7	4.1	– 0.7

(a) Specimen S3-1.24/0.49/23

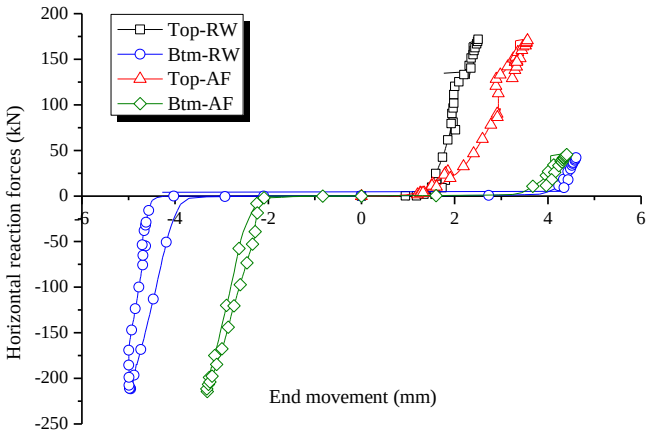

Horizontal restraints	Tension stiffness(kN/m)	Compression stiffness (kN/m)	Tension Gap (mm)	Compression Gap (mm)
Top-RW	160392.93	–	1.4	–
Btm-RW	82649.59	254494.5	4.1	– 4.3
Top-AF	100571.92	–	1.8	–
Btm-AF	49255.37	175277.46	3.5	– 2.1

(b) Specimen S4-1.24/0.82/23

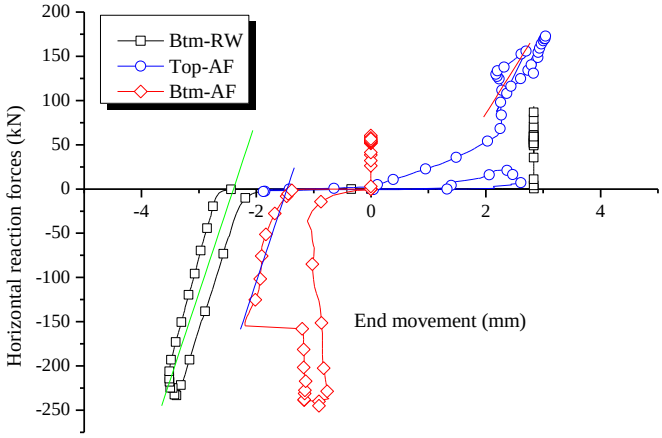

Horizontal restraints	Tension stiffness(kN/m)	Compression stiffness (kN/m)	Tension Gap (mm)	Compression Gap (mm)
Top-RW	160834.3	–	3.0	–
Btm-RW	82649.59	195634.09	4.1	– 2.4
Top-AF	103620.12	–	1.2	–
Btm-AF	82649.59	195343.58	3.5	– 1.5

(c) Specimen S5-1.24/1.24/23

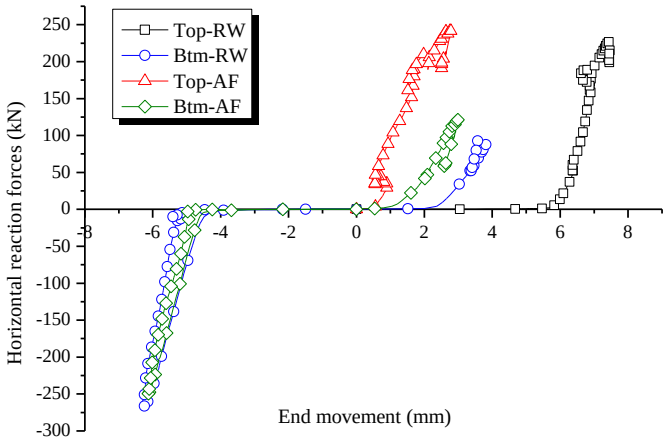

Horizontal restraints	Tension stiffness (kN/m)	Compression stiffness (kN/m)	Tension Gap (mm)	Compression Gap (mm)
Top-RW	142143.51	–	5.8	–
Btm-RW	67813.18	204321.78	2.5	– 5.0
Top-AF	90793.58	–	0	–
Btm-AF	80139.36	175093.03	1.5	– 4.8

(d) Specimen S6-1.87/0.82/23

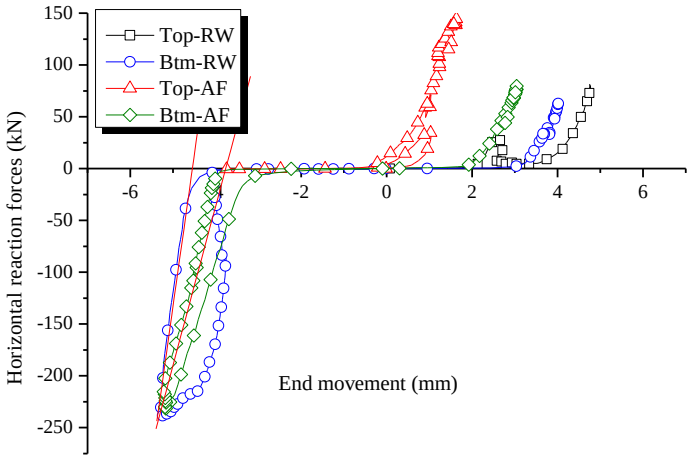

Horizontal restraints	Tension stiffness (kN/m)	Compression stiffness (kN/m)	Tension Gap (mm)	Compression Gap (mm)
Top-RW	75615.00	–	3.8	–
Btm-RW	71217.04	311843.04	3.2	– 4.6
Top-AF	108723.92	–	0.3	–
Btm-AF	72955.43	157282.14	2.0	– 3.8

(e) Specimen S7-1.24/0.82/18.2

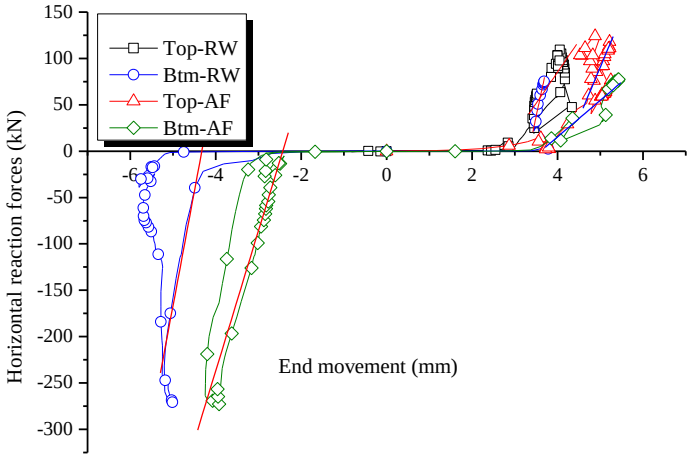

Horizontal restraints	Tension stiffness (kN/m)	Compression stiffness (kN/m)	Tension Gap (mm)	Compression Gap (mm)
Top-RW	67339.76	–	2.7	–
Btm-RW	215412.25	247304.83	3.3	– 4.3
Top-AF	109849.12	–	4.2	–
Btm-AF	39366.97	151016.56	3.6	– 2.4

(f) Specimen S8-1.24/0.82/13.4

Fig. A.3: Stiffness of horizontal restraints to RC sub-assemblages S3 to S8

Table A.1 listed the average stiffness of each horizontal restraint during the tests on sub-assemblages S3 to S8. Note that the average values of tension stiffness do not include the one of S5. The tension stiffness of Btm-RW for S8 was extremely larger than the counterparts for the other tests, so it is not included as well. **Table A.1** indicates that the restraints at both ends were quite symmetrical in terms of the order of magnitude.

Table A.1 Average stiffness and gap of each horizontal restraint

Horizontal restraints	Tension stiffness (kN/m)	Compression stiffness (kN/m)	Tension Gap (mm)	Compression Gap (mm)
Top-RW	117847	–	3.3	–
Btm-RW	75796	231158	3.6	–3.8
Top-AF	95995	–	1.7	–
Btm-AF	52954	166734	2.9	–2.6

Prior to the tests on sub-assemblages S3 to S8, the tests on S1 and S2 were conducted. **Fig. A.4** shows the relationships of horizontal reactions to the end movements at restraints Top-AF and Btm-AF for S1 and S2.

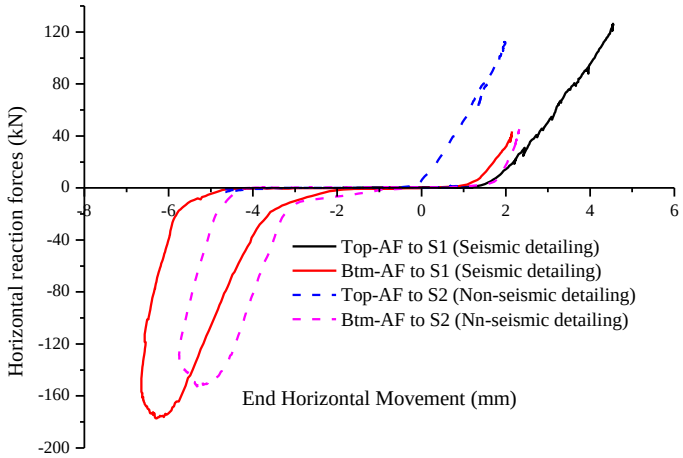

Fig. A.4: Stiffness of horizontal restraints to sub-assemblages S1 and S2

Table A.2 lists the values of restraint stiffness and connection gaps. However, the measurement at RW side was not successful. In numerical validation, the boundary conditions could be assumed symmetrical because **Table A.1** suggests that the restraints at both ends were symmetrical in terms of the order of magnitude and

structural response of the sub-assemblages is actually not sensitive to the values of restraint stiffness at this order.

Table A.2: Results of the boundary conditions for S1 and S2

Specimen	Horizontal restraints	Tension stiffness (kN/m)	Compression stiffness (kN/m)*	Tension Gap (mm)	Compression Gap (mm)
S1-0.90/0.49/23S	Top-AF	43234.25	--	1.8	--
	Btm-AF	42589.05	122601.52	1.2	–4.6
S2-0.73/0.49/23	Top-AF	55957.26	--	0.0	--
	Btm-AF	63942.28	102326.82	1.7	–3.9

* Average value of loading and unloading stiffness

A.1.2 Stiffness of restraints to RC frames

At each end of an RC frame, there were three horizontal restraints applied to a side column, as shown in **Fig. A.5(a)**. A pin, a permanent part of the test set-up and corresponding to H_3, was seated beneath the bottom of the side column. Therefore, the pin was designed with a little tolerance and could be regarded as an idealistic pin. That is, the values of vertical and horizontal stiffness at the pin are infinite.

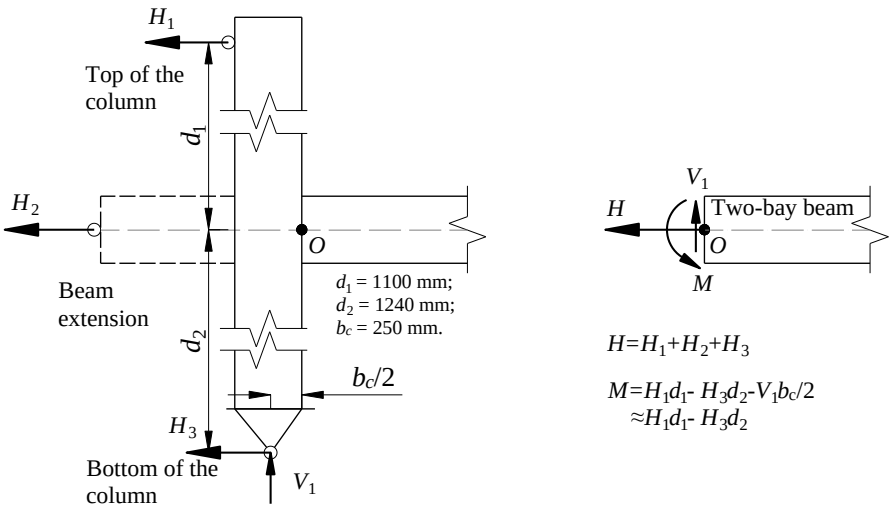

(a) Reactions at end (b) Equivalent Forces at beam ends

Fig. A.5: Reaction forces to frames

However, according to manufacturing errors of the frame specimens, the lengths of horizontal restraints corresponding to H_1 and H_2 were required to adjust slightly during installation. The flexibility of horizontal restraints at H_1 and H_2 could result

in the existence of connection gaps. Moreover, after installation of each frame specimen, prescribed axial loads were applied onto two side columns. Small lateral deflections of the columns caused by axial loads could increase gaps in a certain direction.

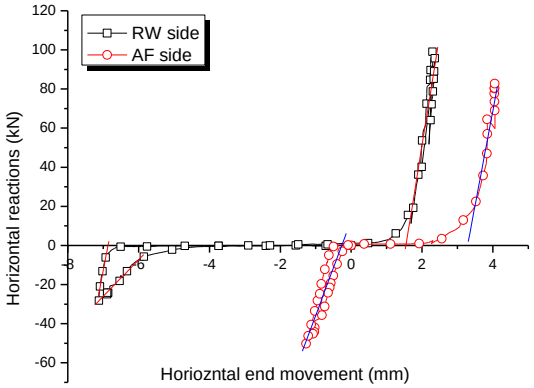

(a) Specimen F1-CD-NS

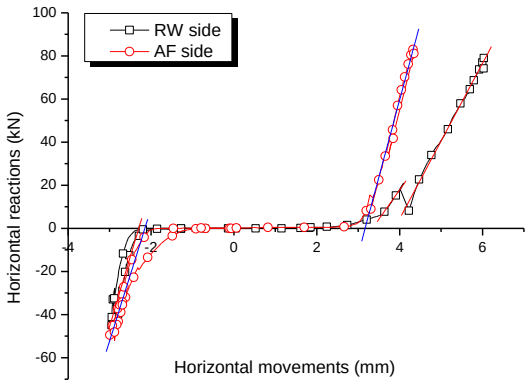

(b) Specimen F2-CD-WS

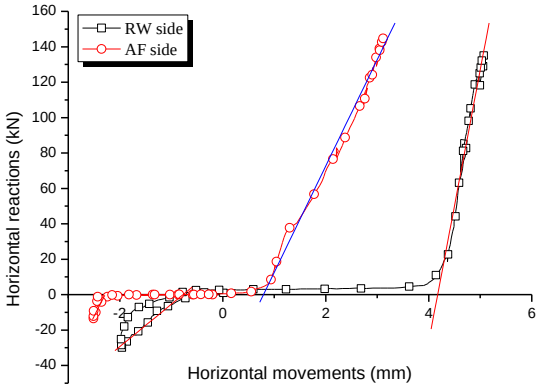

(c) Specimen F5-SD-MR

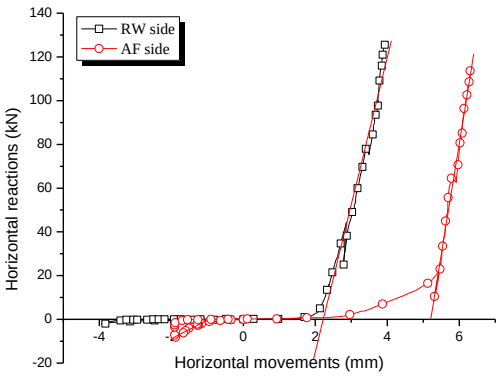

(d) Specimen F6-SD-PD

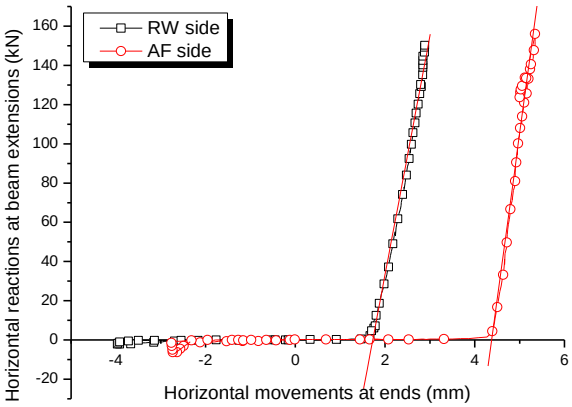

(e) Specimen F7-SD-PH

Fig. A.6: Spring properties of the horizontal restraints at the end of beam extensions

Specimens F1, F2, F5, F6 and F7 had beam extensions. The reaction forces and the corresponding movements at the ends of beam extensions were recorded during the tests. Their relationships are shown in **Figs. A.6(a)** to **(e)**. It can be seen that only for specimens F1, F2 and F5, the horizontal restraints at the ends of beam extensions (i.e. H_2 in **Fig. A.5**) contributed reactions at CAA stage. In contrast, H_2 contributed to catenary action for all specimens. Based on linear regressions in **Figs. A.6(a)** to **(e)**, the values of restraint stiffness and gaps are summarized in **Table A.3**.

Table A.3 Values of stiffness and gaps of horizontal restraints at beam extension ends

Specimen	At Reaction Wall (RW) side				At A-Frame (AF) side			
	Compression stiffness (kN/m)	Compression gap (mm)	Tension stiffness (kN/m)	Tension gap (mm)	Compression stiffness (kN/m)	Compression gap (mm)	Tension stiffness (kN/m)	Tension gap (mm)
F1-CD-NS	18671	-5.6	112755	1.5	48637	-0.3	96635	3.3
F2-CD-WS	64578	-2.3	36089	3.3	61358	-2.1	71561	3.2
F5-SD-MR	23941	-0.8	153678	4.2	57985	-2.3	60055	0.8
F6-SD-PD	N.A.	-4	67332	2.2	N.A.	-1	101526	5.2
F7-SD-PH	N.A.	-4	121661	1.7	N.A.	-2.3	168161	4.4
Average	35730	-3.3	98303	2.6	55993	-1.6	99588	3.4

For specimens F3, F4 and F7, the horizontal reaction forces and the corresponding movements at the top of side columns were measured during the tests. Their relationships are shown in **Fig. A.7**. The top horizontal restraints (i.e. H_1 in **Fig. A.5**) hardly provided any reactions to the RC frames at CAA stage but significantly contributed to cateanry action. **Table A.4** summarizes the values of restraint stiffness and gaps.

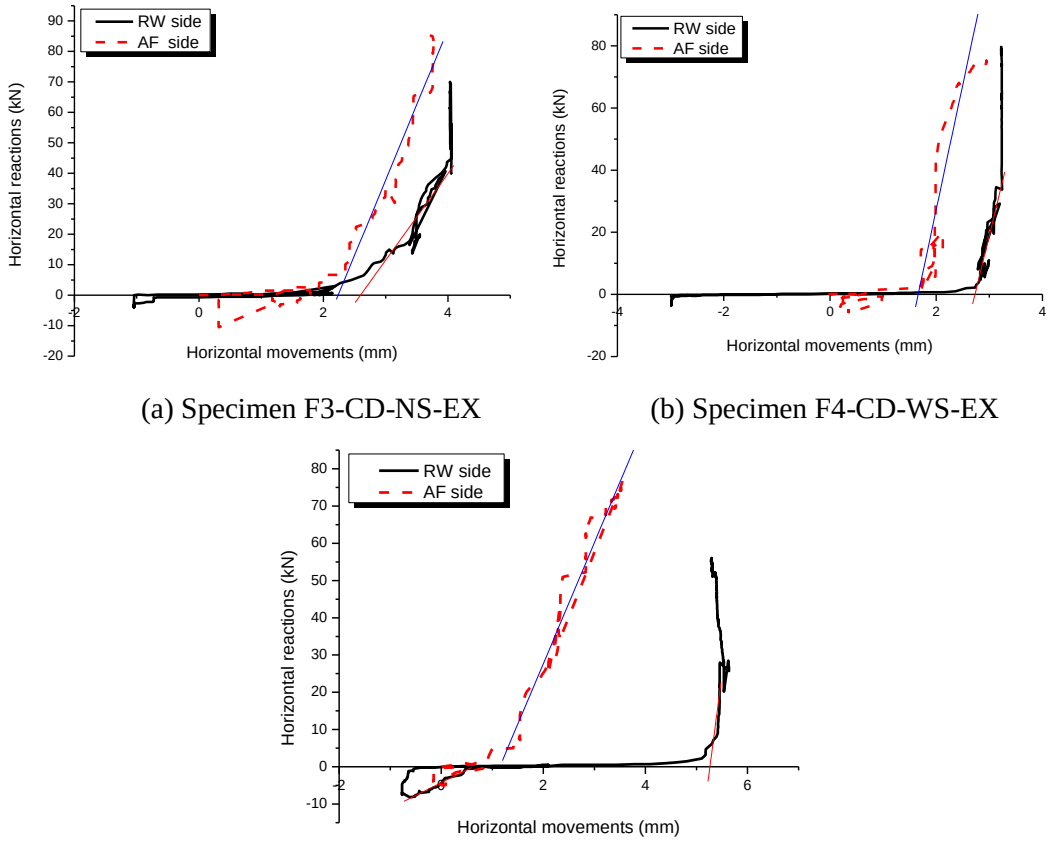

(a) Specimen F3-CD-NS-EX

(b) Specimen F4-CD-WS-EX

(c) Specimen F7-SD-PH

Fig. A.7: Spring properties of the horizontal restraints at the top of side columns

Table A.4 Values of stiffness and gaps of horizontal restraints at the top of side columns

Specimen	At Reaction Wall (RW) side				At A-Frame (AF) side			
	Comp.* stiffness (kN/m)	Comp. gap (mm)	Tension stiffness (kN/m)	Tension gap (mm)	Comp. stiffness (kN/m)	Comp. gap (mm)	Tension stiffness (kN/m)	Tension gap (mm)
F3-CD-NS-EX	N.A.	-1.1	28399	2.6	N.A.	0	49488	2.2
F4-CD-WS-EX	N.A.	-3.5	70190	2.7	N.A.	0	80375	1.7
F7-SD-PH	6853.49	-1	104312	5.3	6853.49	-1	32479	1.1
Average	N.A.	-1.9	67634	3.5	N.A.	-0.3	54114	1.7

*: Comp. indicates compression

Development of catenary action depends on rotation ductility of RC beam-column connections, continuity of reinforcing bars at the connections and external axial restraints. However, the restraint stiffness is evaluated based on structural response that involved contribution from both connections and axial restraints. Therefore, the relationship of reaction force vs. end movement is significantly affected by damage at beam-column connections, such as bar fracture, as shown in **Figs. A.7(a)** and **(b)**. Although the restraint stiffness should be independent of the specimens, it is hard to differentiate the distinct effects of beam-column connections and external restraints on the recorded structural response.

A.2 Equivalent stiffness to the two-bay beams

Fig. A.8 shows that all the restraints at each end of a two-bay beam can be converted to an equivalent axial restraints K_a, an equivalent rotational restraints K_r and a vertical roller support. In vertical direction, it is assumed that there is no settlement. In addition, due to manufacturing errors and specified tolerance in connections, there existed gaps in axial restraints. As a result, equivalent connection gaps may also exist.

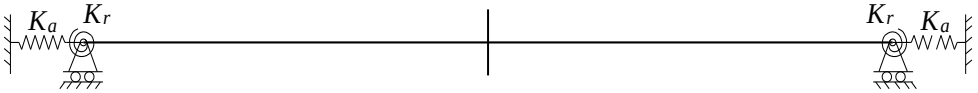

Fig. A.8: Equivalent boundary conditions for a two-bay beam

A.2.1 Two-bay beams in RC beam-column sub-assemblages

Fig. A.1(a) shows the boundary restraints at one end stub. Based on static equilibrium, they can be converted to equivalent forces (i.e. H, M, and R_1) acting at the end section center of the two-bay beam, as illustrated in **Fig. A.1(b)**. Assuming that the end column stub moves and rotates as a rigid body, horizontal movements of the restraints (as shown in **Fig. A.2(a)**) could be converted to an equivalent translation and rotation (i.e. Δ and θ) of the beam end section, as elucidated in **Fig. A.2(b)**. The typical properties of equivalent axial springs to two-bay beams in the sub-assemblages are represented in terms of relationships of H and Δ, as shown in **Fig. A.9**.

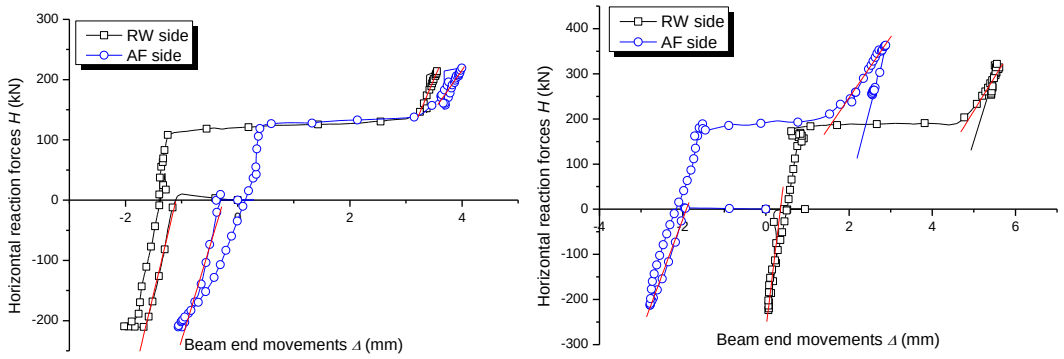

(a) Specimen S4 (b) Specimen S6

Fig. A.9: Properties of equivalent axial springs to two-bay beams in sub-assemblages

Based on linear regression, **Table A.5** summarizes the equivalent axial stiffness and gaps at the ends of the two-bay beams. It can be seen that the axial stiffness is at the order of 10^5 kN/m and may not be equal at both sides. When the analytical model proposed in chapter 6 is used, the axial restraint stiffness at both beam ends is assumed to be identical. According to Eq. (6-21), the equivalent equal stiffness at both ends of the two-bay beams can be obtained, as highlighted in **Table A.5**.

Table A.5 Equivalent axial stiffness and gaps to two-bay beams in the sub-assemblages

Specimen No.	Compression stiffness (kN/m)		Compression Gap (mm)	Tension stiffness (kN/m)	
	RW side	AF side		RW side	AF side
S3-1.24/0.49/23	438087.12	--	1.0	230383.28	69702.23
S4-1.24/0.82/23	388103.93	309640.0	0.8	219889.87	132653.8
S5-1.24/1.24/23	--	--	0.8	--	--
S6-1.87/0.82/23	761832.25	248551.38	1.0	149665.65	134788.05
S7-1.24/0.82/18.2	1048047.9	189140.07	1.2	141230.29	138268.67
S8-1.24/0.82/13.4	700867.85	517983.29	0.8	--	--
Average	667387.8	316328.7	0.9	185292	118853
Equivalent stiffness	**429000**		--	**145000**	

Likewise, **Table A.6** summarizes the rotational stiffness at both beam ends. It indicates that the values of rotational stiffness at both ends are quite close to each other. Approximately, the equivalent rotational stiffness, which can be used in the proposed analytical model in Chapter 6, is taken as 30000 kN·m/rad.

Table A.6 Equivalent rotational stiffness to two-bay beams in the sub-assemblages

Specimen No.	Rotational stiffness (kN·m/rad)	
	RW side	AF side
S3-1.24/0.49/23	26624.97	21417.94
S4-1.24/0.82/23	30121.59	38437.83
S5-1.24/1.24/23	--	--
S6-1.87/0.82/23	19481.22	34803.49
S7-1.24/0.82/18.2	31333.30	28086.18
S8-1.24/0.82/13.4	35884.02	35070.32
Average	28689.02	31563.15
Equivalent stiffness	**30000**	

Table A.7 shows the values of equivalent restraint stiffness to the two-bay beams for specimens S1 and S2. During the tests on S1 and S2, only the stiffness of the restraints at AF side could be accurately evaluated because the measurement at RW side was not successful. As indicated in **Table A.5**, the axial stiffness at AF side is typically smaller than that at RW side. Therefore, the axial stiffness at AF side could be taken as the equivalent stiffness to the two-bay beams for conservatism. On the other hand, **Table A.6** indicates that the rotational stiffness at both sides is quite similar. As a result, the rotational stiffness at AF side could be regarded as the equivalent rotational stiffness that is identical at both ends of the two-bay beam.

Table A.7 Equivalent restraint stiffness to two-bay beams in sub-assemblages S1 and S2

Specimen No.	Compression stiffness (kN/m)	Compression Gap (mm)	Tension stiffness (kN/m)	Rotational stiffness (kN·m/rad)
S1-0.90/0.49/23S	106425.15	0.5	91035.84	25403.00
S2-0.73/0.49/23	109370.90	1.2	138574.71	28027.19
Average	107898.02	0.9	114805.28	26715.1
Equivalent stiffness	**108000**	--	**115000**	**25000**

A.2.2 Two-bay beam in RC beam-column frames

Fig. A.5(a) shows the reactions at one side of a frame specimen. **Fig. A.5(b)** illustrates the approaches to convert these reactions to an equivalent axial force and bending moment at the end of the two-bay beam.

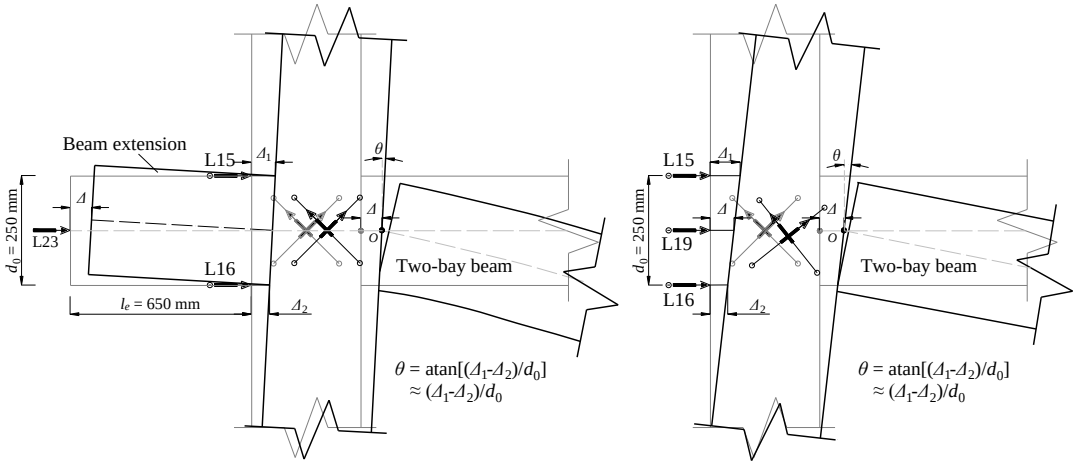

(a) Specimens with beam extensions (b) Specimens without beam extensions

Fig. A.10: Measurement at side columns

Joint rotation consists of joint panel deformation and rigid joint rotation. The former results from shear stress transferred into joint panels and geometric and material properties of joint panels. The latter mainly derives from deformations of side columns. **Figs. A.10(a)** and **(b)** elucidate how to determine the joint rotation in an RC frame with and without beam extensions, respectively. The joint rotation calculated in **Fig. A.10** includes both rigid joint rotation and joint panel deformation. Note that axial restraints at the beam extensions shown in **Fig. 3.9(a)** could not restrain vertical movement of the beam extensions. That is, they could not restrain rotations of the side joints. As deformations in the beam extensions caused by bending moment and shear force were extremely small (at the order of 10^{-4} mm), the effects of beam extension deformations on vertical movement at the end of the beam extensions (at the order of 1 mm) are negligible. Therefore, the beam extensions roughly rotated as rigid bodies, and rotations of the beam extensions can be approximately used to estimate joint rotations. Due to nonlinear response of the joint panels, it is impossible to formulate linear rotation springs at both ends of the two-bay beam throughout the whole load-deflection histories of RC frames. To

simplify the analysis at compressive arch action stage, the corresponding equivalent rotational springs at CAA stage are investigated. However, to simulate the whole load-deflection histories of RC frames, it is suggested to model the entire frames.

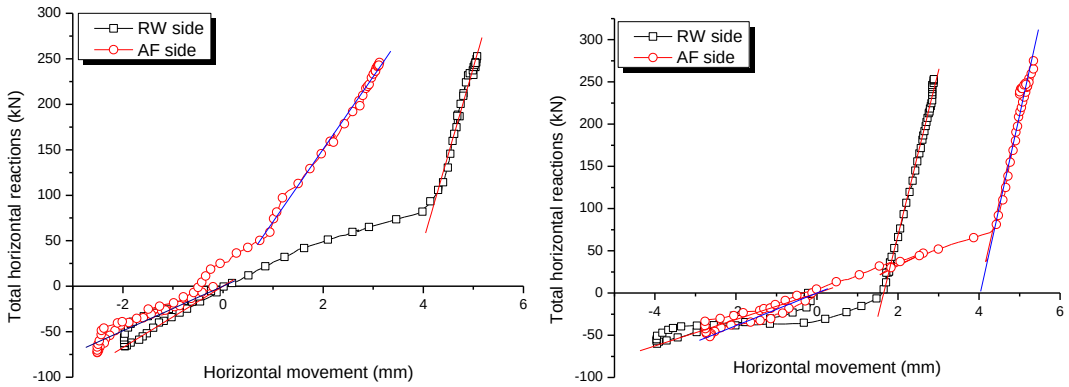

(a) Specimen F5 (b) Specimen F7

Fig. A.11: Properties of equivalent axial springs to two-bay beams in frames

Table A.8 Equivalent axial stiffness to two-bay beams in frames

Specimen types	Specimen No.	Compression stiffness (kN/m)		Tension stiffness (kN/m)†	
		RW side	AF side	RW side	AF side
With beam extensions	F1-CD-NS	10601	70507	--	--
	F2-CD-WS	26330	28480	--	--
	F5-SD-MR	33722	24540	191026	79746
	F6-SD-PD	25527	26373	97202	131483
	F7-SD-PH	15654	19323	194739	217857
	Average	22367	24679*	160989	143029
	Equivalent stiffness	**23500**		**151500**	
Without beam extensions	F3-CD-NS-EX	13648	15448	--	--
	F4-CD-WS-EX	13083	13740	--	--
	Average	13366	14594	--	--
	Equivalent stiffness	**13950**		--	

*: The compression stiffness at AF side for F1 was much larger than the rest, so it was not included to determine the average stiffness;

†: For specimens F1 to F4, development of catenary action was not successful due to prematurely consecutive fracture of top bars at interfaces of the side joints.

Fig. A.11 shows the typical properties of equivalent axial springs to the two-bay beams in frames. For both specimens F5 and F7, the axial restraints at the end of beam extensions did not provide large horizontal reactions at CAA stage, but they exerted large horizontal reactions at catenary action stage so that the equivalent

restraint stiffness was increased significantly, as shown in **Fig. A.11**. Based on linear regression, the values of equivalent axial stiffness are obtained, as summarized in **Table A.8**.

The equivalent rotational stiffnesses to two-bay beams in the frames at CAA stage are summarized in **Table A.9**. The values of rotational stiffness for the frame specimens with and without beam extensions are at the same order of 10^4 kN m/rad.

Table A.9: Equivalent rotational stiffness to two-bay beams in frames at CAA stage

Specimen types	Specimen No.	Rotational stiffness (kN·m/rad)	
		RW side	AF side
With beam extensions	F1-CD-NS	--	41429
	F2-CD-WS	--	20071
	F5-SD-MR	--	37796
	F7-SD-PH	--	32329
	Average	--	32906
	Equivalent stiffness	**32900**	
Without beam extensions	F3-CD-NS-EX	20927	17184
	F4-CD-WS-EX	17616	22942
	Average	19272	20063
	Equivalent stiffness	**20000**	